



PhD-FSTM-2025-127  
The Faculty of Science, Technology and Medicine

## DISSERTATION

Defence held on 10/11/2025 in Esch-sur-Alzette

to obtain the degree of

DOCTEUR DE L'UNIVERSITÉ DU LUXEMBOURG

EN *BIOLOGIE*

by

**Jeff DIDIER**

Born on 22 October 1993 in Luxembourg City (Luxembourg)

MACHINE LEARNING-BASED IDENTIFICATION OF  
BIOMARKERS IN CLINICAL COHORT AND CANCER  
CELL LINE DATA

### Dissertation defence committee

Dr-Ing. Thomas SAUTER (dissertation supervisor)

*Professor, Université du Luxembourg*

Dr-Ing. Martin THEOBALD (defence chairman)

*Professor, Université du Luxembourg*

Dr med. Jochen KLUCKEN

*Professor, Université du Luxembourg*

Dr Fabian MÜLLER

*Junior Professor, Universität des Saarlandes*

Giltæe SONG, Ph.D.

*Associate Professor, Pusan National University*



## Affidavit / Statement of originality



*I declare that this thesis:*

- is the result of my own work. Any contribution from any other party, and any use of generative artificial intelligence technologies have been duly cited and acknowledged;
- is not substantially the same as any other that I have submitted, and;
- is not being concurrently submitted for a degree, diploma or other qualification at the University of Luxembourg or any other University or similar institution except as specified in the text.

*With my approval I furthermore confirm the following:*

- I have adhered to the rules set out in the University of Luxembourg's Code of Conduct and the Doctoral Education Agreement (DEA)<sup>1</sup>, in particular with regard to Research Integrity.
- I have documented all methods, data, and processes truthfully and fully.
- I have mentioned all the significant contributors to the work.
- I am aware that the work may be screened electronically for originality.

I acknowledge that if any issues are raised regarding good research practices based on the review of the thesis, the examination may be postponed pending the outcome of any investigation of such issues. If a degree was conferred, any such subsequently discovered issues may result in the cancellation of the degree.

---

**Approved on 2025-10-01**

<sup>1</sup> If applicable (DEA is compulsory since August 2020)



## Acknowledgements

First and foremost, I would like to communicate my deepest acknowledgement to my supervisor Prof. Dr-Ing. Thomas Sauter for his firm support, thoughtful feedback, and invaluable guidance throughout the course of my PhD. I am also grateful to my dissertation supervision committee chair Prof. Dr-Ing. Martin Theobald and committee member Prof. Dr med. Jochen Klucken and for their insightful suggestions and encouragement.

I would like to extend my appreciation to the external members of my Dissertation Defence Committee Assoc. Prof. Giltae Song, PhD and Jun.-Prof. Dr Fabian Müller for kindly agreeing to contribute as evaluators of this dissertation.

Special thanks to the members of the Systems Biology and Epigenetics Group of the Department of Life Sciences and Medicine at the University of Luxembourg for their camaraderie and collaborative spirit.

I gratefully acknowledge the financial support of the doctoral training unit data-driven computational modelling and applications (DRIVEN) by the Luxembourg National Research Fund under the PRIDE program (PRIDE17/12252781).

I also appreciate the administrative support provided by the Office of Doctoral Education and the administration of the Doctoral School in Science and Engineering at the University of Luxembourg.

I am grateful to the International Society for Computational Biology Student Council (ISCB-SC) and its Regional Student Groups (RSGs), particularly the ISCB RSG Luxembourg, for providing me with opportunities to take on leadership roles and to engage with one of the largest communities in computational biology. These experiences have given me valuable connections and unforgettable memories over the past years.

Finally, I want to deeply thank my family for their unconditional love and remarkably continuous support, as well as to my friends for their solid patience and consistent encouragement through the highs and lows of this exceptional journey.



## Dedications

*For those who made me who I am. Those still here, and those who've drifted:*

*Your presence, your absence, and your silence, all were teachers.*

*I carry your imprint with gratitude, as life unfolds in its own time.*



## Table of content

|   |     |
|---|-----|
| Affidavit / Statement of originality .....  | i   |
| Acknowledgements .....  | ii  |
| Dedications .....   | iii |
| Table of content.....   | iv  |
| List of figures and tables .....  | vii |
| List of abbreviations .....   | ix  |
| List of publications .....  | xi  |
| Abstract.....   | 1   |
| Aims and objectives .....   | 3   |
| Materials and methods.....  | 5   |
| Materials and methods for biomarker detection in clinical cohort data using<br>machine learning .....     | 5   |
| - BASE-II participants and the Fried et al. frailty phenotype .....                                       | 5   |
| - Inferential and descriptive analysis of clinical cohort data .....                                      | 6   |
| - Machine learning algorithms and pipeline setup .....  | 7   |
| - Model performance and feature contribution analysis .....   | 9   |
| - Post-dissertation follow-up of the BASE-II project outcomes.....  | 10  |
| Materials and methods for drug sensitivity prediction for time-of-day<br>cancer treatment profiling ..... | 12  |
| - Cancer cell lines, drugs, core clock genes and circadian parameters .....                               | 12  |
| - Inferential and descriptive analysis of cancer cell line circadian data .....                           | 14  |
| - Machine learning algorithms for circadian subtyping.....  | 16  |
| - Chronosensitivity index for model evaluation and validation .....                                       | 17  |
| - Post-dissertation follow-up of the circadian subtyping framework .....                                  | 18  |
| Materials and methods for machine learning integration in systems<br>biology education .....              | 20  |

- Literature research strategy screening systems biology study lines .....20
- Study lines organization and data characterization .....20
- Descriptive and thematic analysis of today’s systems biology education .....21
- Synopsis .....22
- Chapter 1: Biomarker detection in clinical cohort data using machine learning .....22
  - Scientific context and motivation of the study .....22
  - Key findings and observations of sex-specific pre-frailty .....26
    - Sex-specific clinical characteristics and physical frailty profiles .....26
    - Mixed-sex model outperformed by context- and sex- specific tailored models .....29
    - Body composition in men and physiological anomalies in women most predictive of their respective frailty profiles .....33
  - Insights and implications of the research outcomes .....38
- Chapter 2: Drug sensitivity prediction for time-of-day cancer treatment profiling ....41
  - From circadian drug profiling to functional cancer subtyping.....41
  - Main findings of circadian-based cancer phenotyping.....44
    - How core clock genes shape time-of-day drug sensitivity .....44
    - Detailed example and evaluation of the methodological approach.....46
    - Circadian-based subtyping of breast cancer cell lines driving drug sensitivities ....48
  - Interpretation and consequences of the study’s findings .....53
- Chapter 3: Machine learning integration in systems biology education .....57
  - Challenges and opportunities for machine learning in systems biology education .....57
  - Study lines, perspectives, and machine learning in systems biology education .....59
    - Systems biology Master Programs: strong diversity but lack common framework .....59
    - Students and alumni highlight strengths in training but gap in quantitative skills .....63
    - Machine learning still underrepresented despite clear demand .....65
  - From student feedback to future directions in systems biology education .....66

|  |         |
|--|---------|
| Conclusions and perspectives.....  | 70      |
| Linking sex-specific pre-frailty, circadian oncology, and educational practice .....     | 70      |
| - Sex-specific profiling improves pre-frailty prediction and understanding .....         | 70      |
| - Circadian phenotyping exposes functional diversity in breast cancer models ..          | 71      |
| - Evolving systems biology education to integrate machine learning<br>meaningfully.....  | 73      |
| From signals to stratification: next steps in cohorts, cell models, and classrooms ..... | 73      |
| References .....   | 76      |
| Appendix of original publications .....  | I       |
| Appendix A1: BASE-II.....  | I       |
| Appendix A2: TOD .....   | XX      |
| Appendix A3: TNBC.....   | XXXVII  |
| Appendix A4: Neuroblastoma .....   | LXIV    |
| Appendix A5: Systems Biology .....   | LXXXIII |
| Appendix A6: Example of course material .....  | XCIV    |

## List of figures and tables

|                   |  |    |
|-------------------|--|----|
| <b>Figure 1:</b>  | Pipeline setup and context-specific model configurations.....  | 8  |
| <b>Figure 2:</b>  | Biomarker detection pipeline adjustments in the BASE-II<br>follow-up project.....  | 11 |
| <b>Figure 3:</b>  | Strategic framework for determining ideal treatment times in both cancer<br>and healthy tissue systems .....   | 16 |
| <b>Figure 4:</b>  | Summary of the machine learning-based method for novel circadian<br>subtyping in triple negative breast cancer .....                                 | 17 |
| <b>Figure 5:</b>  | A chronosensitivity index based on LDA-transformed space for scoring<br>circadian dependency in the triple negative breast cancer cell lines.....    | 18 |
| <b>Figure 6:</b>  | Frailty development versus healthy ageing.....   | 23 |
| <b>Figure 7:</b>  | Sex-specific frailty profiles of the BASE-II participants call for<br>contextualized modelling.....  | 27 |
| <b>Figure 8:</b>  | Sex-specific machine learning models outperform mixed-sex approaches<br>and uncover distinct predictors of pre-frailty in BASE-II.....               | 31 |
| <b>Figure 9:</b>  | Model-specific frailty predictions stratified by the Fried frailty phenotype<br>levels in the complete BASE-II cohort .....                          | 33 |
| <b>Figure 10:</b> | Increasing cluster separation revealed through post hoc analysis of top<br>feature combinations compared to the best single predictive feature ..... | 35 |
| <b>Figure 11:</b> | Introducing the contributions to triple negative breast cancer subtyping<br>using circadian-based deep phenotyping .....                             | 43 |
| <b>Figure 12:</b> | Analysis on how core clock genes shape time-of-day sensitivity .....   | 45 |
| <b>Figure 13:</b> | Example and evaluation of methodological approaches .....  | 47 |
| <b>Figure 14:</b> | Defining circadian phenotypes and genetic profiles in breast<br>cancer cell lines .....  | 49 |
| <b>Figure 15:</b> | Circadian features shape variability in drug sensitivity across cell lines ....  | 52 |

|                     |  |         |
|---------------------|--|---------|
| <b>Figure 16:</b>   | Reflections from active students in the University of Luxembourg’s Master’s tracks in Integrated Systems Biology and International Biomedicine ..... | 64      |
| <b>Figure 17:</b>   | Reflections of alumni from the Master’s programmes in Integrated Systems Biology and Biomedicine at the University of Luxembourg .....               | 65      |
| <b>Table 1:</b>     | Characteristics, measurables and definitions of the 5-item Fried et al. frailty phenotype including adjustments for BASE-II .....                    | 6       |
| <b>Table 2:</b>     | Key characteristics of cell lines, drugs, and data used in the circadian project .....   | 13-14   |
| <b>Table 3:</b>     | Heterogeneous prevalence of frailty level by the most applied frailty measurements .....   | 24      |
| <b>Table 4:</b>     | BASE-II cohort description of the main hall marks related to frailty .....   | 28      |
| <b>Table 5:</b>     | Cohort characteristics of the ten most predictive features in subgroup-specific data-driven models in the BASE-II cohort .....                       | 37      |
| <b>Table 6:</b>     | Systems biology Master’s in Europe, North America, and Caribbean ..  | 60-62   |
| <b>Appendix A1:</b> | Clinical data-driven classification of pre-frailty reveals sex-specific patterns – Data from the Berlin Aging Study II (BASE-II) .....               | I       |
| <b>Appendix A2:</b> | Time-of-day effects of cancer drugs revealed by high-throughput deep phenotyping .....   | XX      |
| <b>Appendix A3:</b> | Circadian clock features define novel subtypes among breast cancer cells and shape drug sensitivity .....  | XXXVII  |
| <b>Appendix A4:</b> | Circadian rhythm heterogeneity modulates drug response variations in neuroblastoma models .....  | LXIV    |
| <b>Appendix A5:</b> | Challenges and opportunities in systems biology education .....  | LXXXIII |
| <b>Appendix A6:</b> | Drug Target Prediction Using Context-Specific Metabolic Models Reconstructed from rFASTCORMICS .....   | XCIV    |

**List of abbreviations**

|         |   |      |  |
|---------|---|------|--|
| AC      | auto-correlation                        | DDR  | DNA-damaging response                            |
| AIC     | Akaike information criterion            | DOR  | diagnostics odds ratio                           |
| ALM     | appendicular lean mass                  | ECTS | European credit transfer and accumulation system |
| AUC     | area under the curve                    | EX   | exhaustion                                       |
| BASE-II | Berlin Aging Study II                   | FPR  | false positive rate                              |
| BCD     | between cluster distance                | GA   | gait   |
| BF      | body fluids                             | G    | growth   |
| BIC     | Bayesian information criterion          | GD   | grouped devices                                  |
| BMC     | bone mineral content                    | GM   | grouped medications                              |
| BMD     | bone mineral density                    | GR   | growth rate                                      |
| BL      | basal-like                              | GS   | grip strength                                    |
| BMI     | body mass index                         | HDL  | high density lipoprotein                         |
| CATS    | credit accumulation and transfer scheme | HER  | human epidermal growth factor receptor           |
| CCLE    | cancer cell line encyclopedia           | ID   | individual devices                               |
| CG      | cognition                               | IM   | individual medications                           |
| CH      | chronic morbidity                       | IQR  | inter quartile range                             |
| CI      | confidence interval                     | KO   | knock-out  |
| CV      | cross-validation                        | L1   | lasso regularization                             |
| CWT     | continuous wavelet transform            | L2   | ridge regularization                             |
|         |   | LAR  | luminal androgen receptor                        |
|         |   | LDA  | linear discriminant analysis                     |

|        |  |        |                                   |
|--------|--|--------|-----------------------------------|
| LDL    | low density lipoprotein                    | TOD    | time-of-day                       |
| LOOCV  | leave-one-out cross-validation             | TOD-MR | time-of-day maximal drug response |
| MANOVA | multivariate analysis of variance          | TP     | true positive                     |
| MES    | mesenchymal                                | WC     | within cluster distance           |
| MRA    | multiresolution analysis                   | WHR    | waist-hip ratio                   |
| NB     | neuroblastoma                              | WL     | weight loss                       |
| NT     | nutrients                                  | WT     | wild type                         |
| PA     | physical activity                          |        |                                   |
| PCA    | principal component analysis               |        |                                   |
| PD     | Parkinson's disease                        |        |                                   |
| PM     | physical measurements                      |        |                                   |
| PR     | precision-recall                           |        |                                   |
| RBF    | radial basis function                      |        |                                   |
| ROC    | receiver operating characteristics         |        |                                   |
| RUS    | random under-sampling                      |        |                                   |
| SD     | standard deviation                         |        |                                   |
| SMOTE  | synthetic minority over-sampling technique |        |                                   |
| SV     | surveys                                    |        |                                   |
| SVM    | support vector machines                    |        |                                   |
| TN     | true negative                              |        |                                   |
| TNBC   | triple negative breast cancer              |        |                                   |



## List of publications

### - 2026

[published] Ector, C., Schmal, C., **Didier, J.**, De Landtsheer, S., Schulte, H. J., Keilholz, U., Sauter, T., Kramer, A., Herzel, H., & Granada, E. A. Circadian rhythm heterogeneity modulates drug response variations in neuroblastoma models. *Cell Reports* 45, 116975. <https://doi.org/10.1016/j.celrep.2026.116975>

### - 2025

[published] **Didier, J.**, De Landtsheer, S., Pacheco, M. P., Kishk, A., Schneider, J. G., Goldeck, D., Pawelec, G., Spira, D., Demuth, I., & Sauter, T. Clinical data-driven classification of pre-frailty reveals sex-specific patterns – Data from the Berlin Aging Study II (BASE-II). *Mechanisms of Ageing and Development*, 228. <https://doi.org/10.1016/j.mad.2025.112114>

[published] Ector, C., **Didier, J.**, De Landtsheer, S., Nordentoft, S. M., Schmal, C., Keilholz, U., Herzel, H., Kramer, A., Sauter, T., & Granada, E. A. Circadian clock features define novel subtypes among breast cancer cells and shape drug sensitivity. *Molecular Systems Biology*, 21(4). <https://doi.org/10.1038/s44320-025-00092-7>

[published] **Didier, J.**, Croce, S., Bayoumi, S., Valceschini, E., Escoffier, H., Gonzalez, E., Kishk, A., Badkas, A., De Landtsheer, S., & Sauter, T. Challenges and opportunities in systems biology education. *Endocrine-Related Cancer*, 32(6). <https://doi.org/10.1530/ERC-25-0024>

### - 2024

[published] Ector, C., Schmal, C., **Didier, J.**, De Landtsheer, S., Finger, A., Müller-Marquardt, F., Schulte, H. J., Sauter, T., Keilholz, U., Herzel, H., Kramer, A., & Granada, E. A. Time-of-day effects of cancer drugs revealed by high-throughput deep phenotyping. *Nature Communications* 15, 7205. <https://doi.org/10.1038/s41467-024-51611-3>

### - 2022

[published] Bintener, T., Pacheco, M. P., Kishk, A., **Didier, J.**, & Sauter, T. Drug Target Prediction Using Context-Specific Metabolic Models Reconstructed from rFASTCORMICS. In: Baiocchi, M. (eds) *Cancer Drug Resistance. Methods in Molecular Biology*, vol 2535. Humana, New York, NY. [https://doi.org/10.1007/978-1-0716-2513-2\\_17](https://doi.org/10.1007/978-1-0716-2513-2_17)



## Abstract

This dissertation is an illustrative example of how computational biology can be applied in interdisciplinary settings to identify prognostic biomarkers in clinical cohort and cancer cell line data and highlights the potential for integrating these methodologies into modern systems biology curricula. While the first two chapters of this dissertation are focusing on applied computational biology, the third chapter is exploring the integration of these machine learning approaches into current systems biology education.

The first chapter entitled 'Biomarker detection in clinical cohort data using machine learning' showcases how data-driven computational biology can be applied for exploratory and hypothesis-generating research in biomedical clinical cohort data. In the context of the geriatric condition of frailty, *post-hoc* interpretable machine learning applications reveal that men and women show distinct frailty phenotype profiles, linked to body composition in men and physiological anomalies in women. In fact, (pre-)frailty prediction performance improved with sex-specific tailored machine learning models. These revealed that the physical frailty profile in men is characterised by high fat and low body lean mass, whereas the female physical frailty is more linked to vitamin D deficiency and increased concentrations of monocytes, leukocytes and eosinophils in blood. Furthermore, *post-hoc* analysis indicates that the combinations of such features, not single markers, best capture these sex-specific pre-frailty patterns. Eventually, these findings led to follow-up research on validating and further investigating these intriguing physical pre-frailty patterns in a Luxembourgish Parkinson's Disease study.

The second chapter, 'Drug sensitivity prediction for time-of-day cancer treatment profiling', concentrates on hypothesis-driven approaches to predict time-dependent drug sensitivity in cancer cell line expression data. The projects in this chapter underscore circadian dynamics as critical factor influencing overall cancer drug responsiveness, and our approaches significantly contributed to the development and validation of a robust quantitative phenotyping platform to evaluate drug timing effects and predict drug sensitivity, resulting in the introduction of the chronotherapeutic index and the chronosensitivity index to assess timing effect and sensitivity of cancer drugs. Additionally, these applications help leveraging circadian characteristics to stratify cancer cell lines into new subtypes with high predictive value, this in the context of triple negative breast cancer and neuroblastoma. For example, new circadian-related subtypes were identified in triple negative breast cancer, separating them in unstable, weak, dysfunctional, and functional

Abstract

circadian state. Overall, these contributions helped building an interdisciplinary and translational framework where cellular clock phenotypes effectively could shape chronotherapy design in oncological treatments. The projects presented in this chapter were initiated and led by the Granada Lab of the Charité Comprehensive Cancer Center of the Medical University of Berlin with close collaboration of the Systems Biology and Epigenetics Team of the Department of Life Sciences and Medicine at the University of Luxembourg.

Finally, the third chapter is focusing on 'Machine learning integration in systems biology education'. This chapter attempts to lay out the status quo of machine learning in current systems biology study lines. It aligns the importance of interdisciplinary collaborations and the integration of computational biology to respond to the current opportunities and challenges in this field of study. In a recently published review, we realised that systems biology education must combine deep biological knowledge with computational and technological methods, yet current graduate programs still struggle to deliver this integration effectively. Insufficient exposure to multimodal data integration (*e.g.*, clinical cohort data and cell line data coupled with machine learning approaches) adds to the consequences of this lack. As a result, we concluded that without early and sustained institutional commitment, the field risks producing graduates underprepared for translational bioinformatics and precision systems applications anticipated to shape the future of the field. A good example to mitigate such consequences is the careful design of adaptive and interdisciplinary educational material that can be used in classrooms to, for example, predict drug targets and candidate drugs for repurposed cancer therapies in the context of metabolic modelling, machine learning, and expression data.

In conclusion, this dissertation exhibits how computational biology can drive discovery in both research and education. From identifying prognostic biomarkers in geriatric conditions to shaping cancer treatment strategies, and from data integration to curriculum design, it underscores the power and necessity of bridging biology and machine learning in today's scientific landscape.

## **Aims and objectives**

The key aim and objective are to leverage interpretable machine learning algorithms to identify prognostic biomarkers. The focus is on conceptually evolving medical conditions where diagnostic criteria are fragmented, and biomedical or cellular insights may guide therapeutic stratification. While these objectives constitute the core of the first two chapters, their achievement eventually influenced the setup of the third chapter, attempting to lay out the status quo of machine learning in current systems biology education.

More precisely, chapter one is tackling the following research questions in the context of the geriatric condition of frailty and rich biomedical and clinical data: which biomedical and clinical biomarkers are the most reliable predictors of pre-frailty in older adults; how can a multidimensional model including physiological, clinical, and functional indicators improve the identification and understanding of frailty as a systemic condition; and what are the sex-specific differences in the biological and clinical presentation of pre-frailty and how might these differences inform more effective, stratified interventions. The objectives achieved in this chapter resulted in new and intriguing insights into how biological sex influences physical frailty patterns and revealed potential avenues for better stratified prevention and treatment approaches.

In chapter two, the main thread spans tightly around the context of optimal timing windows for anti-cancer drugs and cell-specific characteristics such as their circadian rhythm and circadian-related gene expression profiles. More specifically, this chapter is posing the following research questions: what is the optimal time-of-day (TOD) window for drug efficacy across cancer cell types; which cellular or genetic features (circadian strength, circadian gene signatures) best predict time-dependent drug responses; and can circadian clock phenotypes classify subtypes and explain differential drug sensitivity. In response, the contributions to the projects in this chapter resulted in the establishment of a high-throughput circadian drug profiling framework in cancer cell lines able to identify cell line-specific determinants of chronosensitivity. This framework was then applied to reveal various circadian phenotypes in the context of triple negative breast cancer (TNBC) and neuroblastoma (NB) that can be used for subtyping and therapeutic stratification.

These chapter-wise aims and objectives then coalesced into the motivations illustrated by the third chapter. Here, the main research questions revolve around systems biology education and how machine learning-based approaches, as shown in the previous two

Aims and objectives

chapters, can be integrated earlier and more efficiently into current study lines. This chapter is treating the following research question: how can graduate-level systems biology curricula best integrate disciplinary content bridging biology and computational tools; what are the main educational obstacles experienced by students and alumni in systems biology programs and what best teaching approaches address these; and how is interdisciplinary teaching and computational biology applied in various universities around the world. The achievements highlighted in this chapter indicate that the educational infrastructure is adapting to best foster interdisciplinary research and the foundation of future biomedical training that involves interpretable computational tools coupled with quantitative methods, yet the field must keep pace with the constant evolution of the methods in computational and systems biology.

Together, these chapters showcase how interpretable machine learning approaches can improve biomarker discovery, guide cancer therapy and treatment timing, and shape systems biology education. This progression highlights both the scientific value of data-driven approaches and their growing role in shaping future biomedical education.

## Materials and methods

*This section summarizes the main materials and methods used in the projects presented in this manuscript. For a more detailed description of the applied techniques, please kindly refer to the respective manuscripts appended to this dissertation. Recently adapted methodologies that are employed in ongoing follow-up projects are described in the respective paragraphs.*

### **Materials and methods for biomarker detection in clinical cohort data using machine learning**

#### **- BASE-II participants and the Fried et al. frailty phenotype**






The Berlin Aging Study II (BASE-II) is a clinical observational study of 2200 participants in ageing groups of 20 to 35 and 60 to 85. The recruitment happened in the greater Berlin area, Germany, during the period of 2009 to 2015 and was carefully designed to ensure age and sex matching (<https://www.base2.mpg.de/en>, and references [1–3]). Written informed consent was obtained during enrolment, and the clinical study was carried out in accordance with the Declaration of Helsinki and received ethical approval from the Ethics Committee of Charité - Universitätsmedizin Berlin (approval number: EA2/029/09; date: 19 March 2009). Most importantly, in this study, participants completed diverse medical examinations that resulted in a rich collection of psychological, genetic, medical, socioeconomic, and immunological data.

Frailty in BASE-II was defined by the 5-item *Fried et al.* frailty phenotype [4], comprised of the clinical variables weight loss (WL), physical activity (PA), exhaustion (EX), grip strength (GS), and gait (GA), with adjustments to the BASE-II cohort as detailed by *Spira et al.* [5] (see **Tab. 1**). The presence of frailty was assessed using the below equation (1) as the sum of positive frailty-related phenotypes to give a frailty score ( $FR_{score}$ ).

$$FR_{score} = WL + PA + EX + GS + GA \quad (1)$$

## Materials and methods

From the resulting  $FR_{score}$ , the *Fried et al.* frailty phenotype is derived, labelling participants as non-frail (level 0,  $FR_{score} = 0$ ), pre-frail (level 1,  $FR_{score} \in \{1; 2\}$ ), or frail (level 2,  $FR_{score} \geq 3$ ).

| A) Characteristics of Frailty  | B) Cardiovascular Health Study Measure [4], and BASE II adjustments [5]   |
|--|---|
| <b>Shrinking</b><br>- Weight loss (unintentional)<br>- Sarcopenia (muscle mass loss)  | <b>Weight loss</b><br>- >10 lbs (4.5 kg) lost unintentionally in the prior year<br>- <b>BASE II:</b> > 5% of the body weight lost unintentionally in the prior year       |
| <b>Weakness</b><br>   | <b>Grip strength</b><br>- lowest 20% (by sex and BMI)<br>- <b>BASE II:</b> no adjustments   |
| <b>Poor endurance</b><br>   | <b>Exhaustion</b><br>- self-report<br>- <b>BASE II:</b> no adjustments  |
| <b>Slowness</b><br>  | <b>Gait</b><br>- walking time/15 feet (4.6 m); slowest 20% (by sex and BMI)<br>- <b>BASE II:</b> timed Up & Go test, subjects needing >10 seconds                         |
| <b>Low activity</b><br>   | <b>Physical activity</b><br>- lowest 20%; ♂ < 383 Kcals/week; ♀ < 270 Kcals/week<br>- <b>BASE II:</b> self-report, question: 'Are you seldom or never physically active?' |
| <b>C) Presence of Frailty</b>  | <b>≥ 3 positive criteria:</b> positive for frailty phenotype<br><b>1 or 2 positive criteria:</b> intermediate frail or pre-frail  |

**Table 1: Characteristics, measurables and definitions of the 5-item Fried et al. frailty phenotype including adjustments for BASE-II.** As defined by *Fried et al.* in 2001 [4] (A-C), adjustments for the BASE-II clinical cohort by *Spira et al.* in 2015 [5] (C). BMI body mass index

### - Inferential and descriptive analysis of clinical cohort data

This study analysed a subset of the BASE-II cohort ( $n = 1512$ ), restricted to participants aged 60 years and above with sufficient data to compute frailty phenotypes [6–13]. Data preprocessing included the removal of features with more than 20% missing values, except for sparse binary variables related to medication and device use, which were aggregated into summary metrics (e.g., total medications, total devices). Participants lacking any of the key frailty criteria were excluded ( $n = 159$ ). Remaining missing values were imputed separately in the training and test sets (80% training, 20% hold-out test) using the mode for categorical and the mean for continuous variables, based on training-set statistics [14].

## Materials and methods

Due to the heavy class imbalance between the three level of *Fried et al.*'s frailty phenotype in BASE-II (non-frail:  $n = 1028$ ; pre-frail:  $n = 470$ ; frail:  $n = 14$ ), the pre-frail and frail participants were merged into the group of pre-frail/frail. Key clinical variables were engineered, including polypharmacy [15–17], cumulative side-effects and allergies, poly-dependency [18,19], and vitamin D deficiency [20–22]. As an example of such feature engineering, two vitamin D assay variables with complementary missingness were merged and standardized to form a continuous z-score, with deficiency status defined by the Institute of Medicine's threshold of  $<50$  nmol/L [22,23]. Main descriptive statistics and group comparisons were performed using Welch's unequal variance T-test for continuous variables [24] with variance homogeneity assessed by Levene's T-test, and corrected Cramér's V for categorical features [25,26]. Prior to model training, redundant, and low-variance features were removed across sex-specific and subgroup-specific partitions, based on feature pair-wise correlation, variance-to-mean ratios and minimum case thresholds aligned with 10-fold cross-validation (CV) splits. More detailed descriptions of the applied inferential and descriptive methods can be found in the appended manuscript **A1**.

#### - **Machine learning algorithms and pipeline setup**

Classification tasks were conducted using a structured machine-learning pipeline implemented in Python and executed on the University of Luxembourg's High-Performance Computing infrastructure [27]. To address frailty class imbalance, datasets were resampled using both Random Under-sampling (RUS) and the Synthetic Minority Over-sampling Technique (SMOTE) [28]. The order of operations, resampling followed by feature transformation, was found to improve performance across contexts [29]. Feature scaling was applied using one of three approaches (min-max, standard, or robust), selected per dataset based on downstream performance. Dimensionality reduction techniques, such as principal component analysis (PCA), linear discriminant analysis (LDA), and kernel PCA were used for continuous features while discrete features were ranked by chi-squared ( $\chi^2$ ) and Cramér's V statistics corrected for data type [26]. Support Vector Machines (SVM) were then employed as classifiers with linear and radial basis function (RBF) kernels [30] since SVMs are well-suited to detect biomarkers in clinical cohort data, especially due to their effectiveness in high-dimensional context and the level of generalization [31,32]. Linear SVM was primarily employed to enable interpretability of the feature contributions, as the decision function provides direct insight into feature importance through the weight

Materials and methods

vector  $w$  and the bias term  $b$  (see equation 2). The amplitude and sign of each  $w_i$  reflects the contribution of feature  $x_i$  to the classification decision.

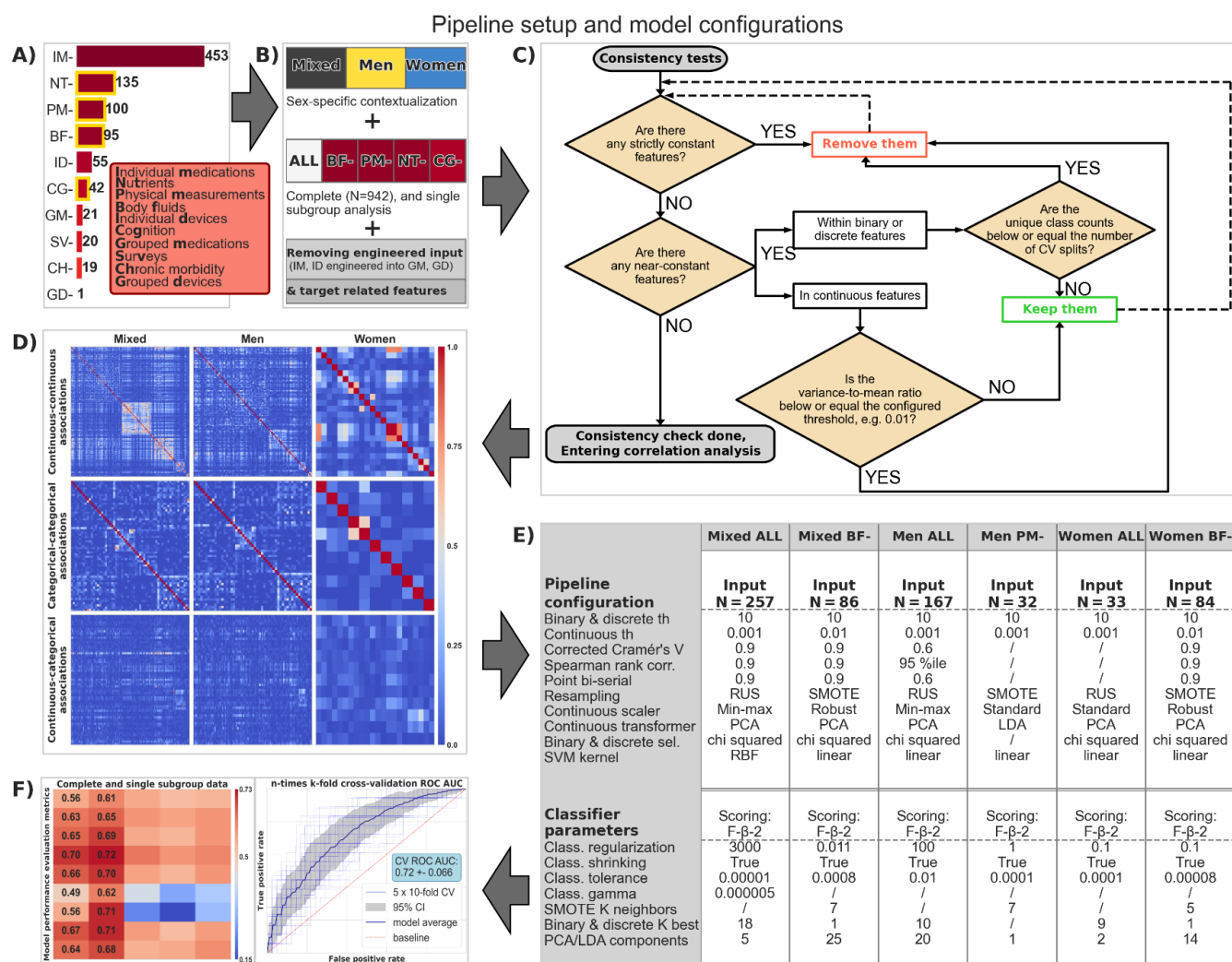
$$f(x) = w^T + b \tag{2}$$

Hyperparameter tuning was carried out with exhaustive grid search over predefined parameter ranges (see supplementary data in appendix **A1**), using stratified 10-fold CV with the F- $\beta$ -2 scoring function (see equation 3).

$$F_\beta = (1 + \beta^2) * \frac{precision*recall}{(\beta^2 * precision)+recall} \tag{3}$$

This scoring metric with  $\beta = 2$  weights recall more heavily than precision, an approach suitable for imbalanced clinical data where the condition of interest is underrepresented.

The overall pipeline setup and model configurations are summarised in the **Fig. 1**.



Materials and methods

**Figure 1: Pipeline setup and context-specific model configurations.** (A) The biomedical dataset from BASE-II was organized into 10 subgroups based on the type of information contained. (B) Analyses were conducted separately for mixed-sex, men, and women datasets, using either the complete feature set or 4 selected subgroups (highlighted in A), excluding features used to derive engineered variables or directly related to the frailty target. (C) A consistency check was applied to remove constant and near-constant features, with thresholds defined by each sex- and context-specific configuration. (D) Remaining features underwent correlation analysis tailored to data type, and highly correlated variables were filtered out to reduce redundancy. (E) The cleaned dataset was then processed through the machine-learning pipeline using predefined settings; shown here are only the configurations for the best-performing models in each context. (F) Final models were evaluated across multiple performance metrics, and feature importance was estimated by repeated permutation testing, capturing each feature's effect on cross-validated prediction performance. IM individual medications, NT nutrients, PM physical measurements, BF body fluids, ID individual devices, CG cognition, GM grouped medications, SV surveys, CH chronic morbidity, GD grouped devices, th threshold, corr correlation, sel selection, SVM Support Vector Machine, SMOTE synthetic minority oversampling technique, PCA principal component analysis, LDA linear discriminant analysis, RUS random under-sampling, RBF radial basis function, CV cross-validation, ROC receiver operating characteristics, DOR diagnostics odds ratio, TP true positive, TN true negative

- **Model performance and feature contribution analysis**

Each model was evaluated using stratified 10-fold CV and a 20% hold-out test set. Primary evaluation metrics included the F- $\beta$ -2 and F- $\beta$ -1 score, receiver operating characteristic (ROC) and precision-recall (PR) curves, diagnostics odds ratio (DOR), accuracy, and confusion matrix components (true positives (TP) and true negatives (TN)). Given the clinical priority of minimizing false negatives in (pre-)frailty detection, the F- $\beta$ -2 scorer was chosen to emphasize recall during hyperparameter optimization. Additional performance validation was conducted with five repetitions of stratified 10-fold CV using ROC and PR curves to verify the stability of model performance across folds.

Feature importance was assessed through systematic permutation testing. Each input variable was individually permuted (500 iterations for men and women models, 1000 iterations for the mixed-sex models), and the resulting drop in cross-validated F- $\beta$ -2 scores was used to estimate the feature's contribution to the model performance. Results were standardized to express statistical significance (z-score) in the top 30 most influential features per model. To better understand how these features function in combination, not just in isolation, a *post-hoc* multivariate contribution analysis was performed. This included both univariate group (e.g., vitamin D deficiency, sarcopenia, heart insufficiency) and

## Materials and methods

pairwise comparisons of the most influential continuous features stratified by sex. For discrete features, adjusted Cramér's  $V$  coefficients were calculated, with Bonferroni-corrected p-value thresholds. Continuous features underwent Welch's unequal variance T-test after assessing the variance equality with the Levene's T-test (see appendix **A1**).

Feature combinations were further examined using linear multivariate analysis of variance (MANOVA) models to assess joint discriminatory capacity (see equation 3), reporting 1 - Wilks' lambda as the measure of separation. In specific cases (*e.g.*, best performing men or women subgroup models), combinations of 2, 5, and 10 top features were also projected using PCA and LDA to visually inspect class separation in reduced dimensions. These analyses were designed to highlight context-specific interactions and additive effects that might not be apparent from univariate rankings alone [33]. Further methodological details, including code and preprocessing steps, are documented in the associated manuscript (appendix **A1**) and a public GitHub repository ([https://github.com/sysbiolux/Clinical\\_Biomarker\\_Detection](https://github.com/sysbiolux/Clinical_Biomarker_Detection)).

$$feature_1 + feature_2 + feature_3 + \dots + feature_n \sim pre-frail + frail \quad (3)$$

#### - **Post-dissertation follow-up of the BASE-II project outcomes**

The intriguing outcomes of this major project in BASE-II then led to a follow-up project involving the Luxembourg Parkinson's disease (PD) clinical cohort by the NCER-PD consortium [34]. In a first step, the *Fried et al.* frailty phenotype was integrated in that cohort using known close proxies of these frailty items in close concordance with medical experts. Although the project is still ongoing and not included in this dissertation, an improved strategic feature pooling and machine learning pipeline was established (**Fig. 2**) to effectively mitigate the technical limitations introduced in the BASE-II project and described in more detail in the synopsis section. The implemented adjustments in this follow-up projects help to minimize most common forms of selection bias and information leakage, while maximizing the generalizability and interpretability of the selected best performing models. In short, this pipeline will use 3 CV-aware strategic approaches (univariate, wrapper model, and embedded models) to pool a subset of the most important features. From this subset, exhaustive feature selection coupled to SVM classifier is performed to identify the top combination of 2 to 10 features to predict frailty. Within the training set only, the best performing combination is then selected based on multiple information criteria of the model performance and complexity (log loss, Akaike and Bayesian information

criterion). Only after this selection will the final model be validated on the hold-out validation set to ensure the model's generalizability.

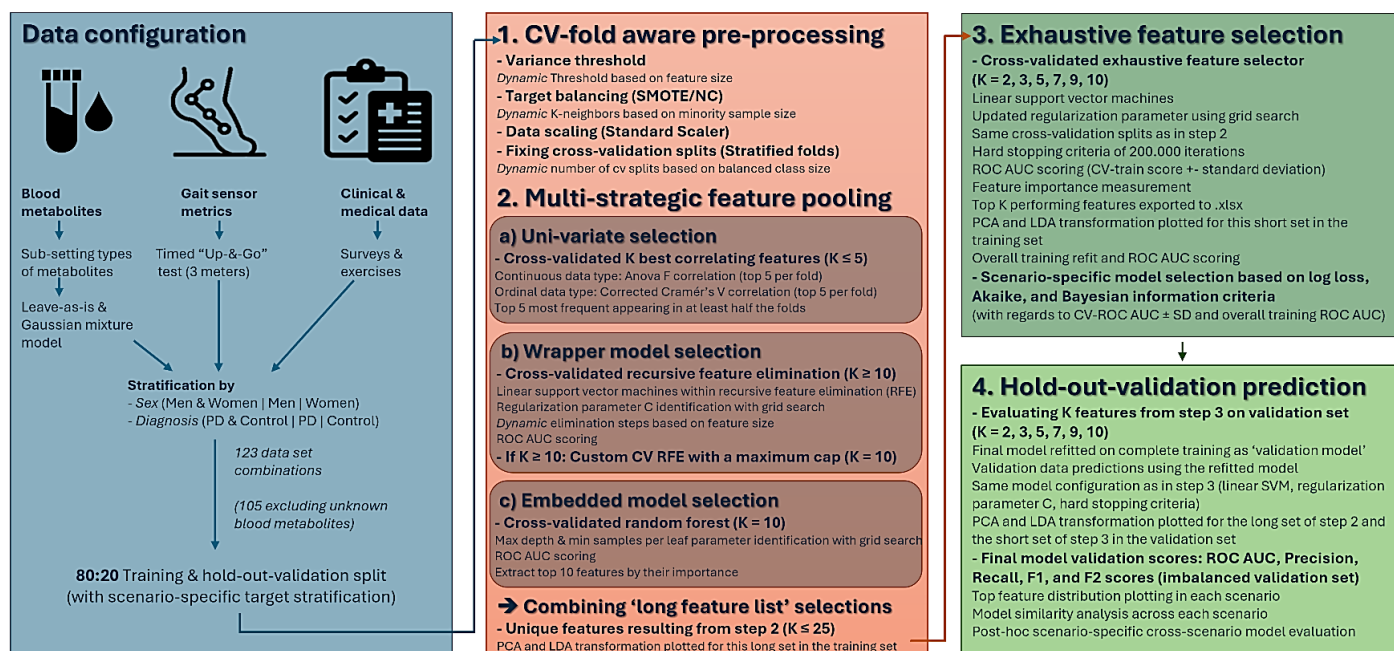


**Figure 2: Biomarker detection pipeline adjustments in the BASE-II follow-up project.** The workflow begins with data configuration and preprocessing, including stratified splitting based on sex and diagnosis (left panel). In Step 1, CV-aware preprocessing is applied, including variance filtering, class balancing, and standard scaling. Step 2 involves multi-strategic feature pooling through univariate selection, wrapper-based recursive feature elimination, and embedded model selection using random forests. Features from these strategies are combined to create a candidate feature list. In Step 3, an exhaustive feature selector performs cross-validated evaluation of multiple feature subset sizes using linear SVM, and the model selection is done based on ROC score and information criteria (log loss, AIC, BIC). Step 4 evaluates selected feature subsets on the hold-out validation set, reporting final model metrics (ROC, F-β-1, F-β-2, precision, and recall). CV cross-validation, ROC receiver operating characteristics, AIC Akaike information criterion, BIC Bayesian information criterion

## ***Materials and methods for drug sensitivity prediction for time-of-day cancer treatment profiling***

*This section illustrates the materials and methods used in the framework of a close collaboration with the Granada Lab of the Charité Comprehensive Cancer Center of the Medical University of Berlin that led to the fruition of a research trilogy, with two research articles published [35–37] (appendix **A2**, **A3**, and **A4**). Since they all are closely related in terms of data profiles and approach, all methods that resulted in the significant contributions are merged in the sections below.*

### **- Cancer cell lines, drugs, core clock genes and circadian parameters**

The following table (**Tab. 2**) summarises the key characteristics of the data used in this project. It lists the names and cancer type of the investigated cell lines (A), the name, type, and target pathway of the tested drugs (B), the name and function or pathway role of the analysed core clock genes (C), as well as the metrics and details of the main circadian parameter classes used (D). The cancer cell line origins, circadian parameter generation, and some drug sensitivity measurements (cisplatin) initiated from the Granada Lab are described in more detail in the related appended manuscripts **A2** and **A3**. The expressions of core clock genes and their somatic mutation information in the selected cell lines, as well as the drug sensitivity measurements of a larger panel of anti-cancer drugs were all obtained from the Cancer Cell Line Encyclopedia Dependency Map (CCLE DepMap, see <https://sites.broadinstitute.org/ccle/datasets>). Gene expression data was obtained from the 2022-Q2/Q4 version, mutation profiles are from 2023-Q2, and drug sensitivities are from the 2015-Q1 version) [38]. A binary approach based on the median was applied to categorize cell lines into high and low drug sensitivity for each of the available drug data. Circadian parameters for the biological and technical replicates of cell lines by the collaborators were characterized by their median.

## Materials and methods

| <b>A) Cancer cell lines</b> |                                |                                 |
|-----------------------------|--------------------------------|---------------------------------|
| <b>Cell line</b>            | <b>Cancer type</b>             |                                 |
| MCF10A                      | Non-malignant epithelial       |                                 |
| U-2 OS (WT)                 | Osteosarcoma                   |                                 |
| U-2 OS single KO            | Osteosarcoma (BMAL1-only KO)   |                                 |
| U-2 OS double KO            | Osteosarcoma (BMAL1 & PER2 KO) |                                 |
| MDAMB468                    | TNBC-BL1                       |                                 |
| HCC1937                     | TNBC-BL1                       |                                 |
| HCC1143                     | TNBC-BL1                       |                                 |
| HCC38                       | TNBC-BL1                       |                                 |
| HCC1806                     | TNBC-BL2                       |                                 |
| SUM149PT                    | TNBC-BL2                       |                                 |
| HCC70                       | TNBC-BL2                       |                                 |
| MDAMB436                    | TNBC-MES                       |                                 |
| BT549                       | TNBC-MES                       |                                 |
| MDAMB231                    | TNBC-MES                       |                                 |
| CAL51                       | TNBC-MES                       |                                 |
| HCC1428                     | Luminal A                      |                                 |
| MCF7                        | Luminal A                      |                                 |
| T47D                        | Luminal A                      |                                 |
| <b>B) Drugs</b>             |                                |                                 |
| <b>Drug</b>                 | <b>Type</b>                    | <b>Target pathway</b>           |
| Adavosertib                 | WEE1 inhibitor                 | Cell cycle checkpoint           |
| Doxorubicin                 | Chemotherapy (anthracycline)   | DNA intercalation / Topo-II     |
| Paclitaxel                  | Chemotherapy (taxane)          | Microtubule stabilizer          |
| 5-FU                        | Antimetabolite                 | Thymidylate synthase inhibition |
| Torin2                      | mTOR inhibitor                 | mTORC1/2                        |
| Alisertib                   | Aurora A kinase inhibitor      | Mitosis regulation              |
| Alpelisib                   | PI3K $\alpha$ inhibitor        | PI3K/AKT signalling             |
| Cisplatin                   | Platinum-based chemotherapy    | DNA crosslinking agent          |
| 17-AAG                      | HSP90 inhibitor                | Chaperone inhibition            |
| Erlotinib                   | EGFR TKI                       | EGFR signalling                 |
| Nilotinib                   | BCR-ABL inhibitor              | Tyrosine kinases                |
| AZD0530                     | Src inhibitor                  | Src-family kinases              |
| PD0325901                   | MEK inhibitor                  | MAPK pathway                    |
| PHA665752                   | MET inhibitor                  | MET RTK                         |
| L685458                     | $\gamma$ -secretase inhibitor  | Notch signalling                |
| Lapatinib                   | EGFR/HER2 inhibitor            | HER2 signalling                 |
| Panobinostat                | HDAC inhibitor                 | Epigenetic regulation           |
| Irinotecan                  | Topoisomerase I inhibitor      | DNA replication                 |
| ZD6474                      | EGFR/VEGFR inhibitor           | Dual receptor inhibition        |

## Materials and methods

|           |                           |                     |
|-----------|---------------------------|---------------------|
| PF2341066 | MET inhibitor             | MET RTK             |
| RAF265    | RAF kinase inhibitor      | MAPK/ERK signalling |
| TKI258    | FGFR inhibitor            | RTK pathway         |
| AEW541    | IGF-1R inhibitor          | IGF signalling      |
| Sorafenib | Multi-kinase inhibitor    | RAF/VEGFR/PDGFR     |
| TAE684    | ALK inhibitor             | ALK fusion kinases  |
| Topotecan | Topoisomerase I inhibitor | DNA replication     |

**C) Circadian clock genes**

| <b>Gene</b>               | <b>Function or pathway role</b>                 |
|---------------------------|---|
| BMAL1                     | Core activator (forms complex with CLOCK/NPAS2) |
| CLOCK                     | Core activator with BMAL1                       |
| NPAS2                     | Alternative activator (especially in brain)     |
| PER1/2/3                  | Negative feedback regulators                    |
| CRY1/2                    | Feedback repressors                             |
| REV-ERB $\alpha/\beta$    | Nuclear receptors repressing BMAL1              |
| ROR $\alpha/\beta/\gamma$ | Nuclear receptors activating BMAL1              |
| CSNK1D/E                  | Kinases regulating PER protein stability        |
| DBP                       | Output gene; rhythmic transcription factor      |

**D) Circadian parameters**

| <b>Metric domain</b>                     | <b>Description</b>  |
|--|---|
| Autocorrelation analysis                 | Measures rhythmic repeatability, period consistency, and lag coherence between the clock reporters                                    |
| Continuous wavelets transformation (CWT) | Extracts dominant frequencies and rhythms from noisy time-series defined as ridge length  |
| Multiresolution analysis (MRA)           | Decomposes signals to quantify circadianity into noise (1-4h), ultradian (4-16h), circadian (16-32h), and infradian (32-256h) rhythms |
| Growth rate coefficients                 | Measures drug effects on proliferation across circadian phases in multiple growth rate coefficients                                   |

**Table 2: Key characteristics of cell lines, drugs, and data used in the circadian project.** This table summarises the cancer cell lines (A), drugs (B), circadian core clock genes (C), and circadian parameters (D) used in this project. WT wild type, KO knock-out, CWT continuous wavelet transform

### - Inferential and descriptive analysis of cancer cell line circadian data

To explore the relationships between circadian biology and drug sensitivity in cancer cell lines, a series of unsupervised and inferential analyses was conducted across the studies of this project. Circadian gene expression patterns were first analysed using hierarchical

Materials and methods

clustering based on Euclidean distance and a complete linkage. Latter defines the distance between two clusters as the maximum distance between any two data points (one from each cluster). This was applied to core clock gene expression data to identify similarities across the cancer cell lines. In parallel, mutation scores for the selected circadian genes were quantified and clustered using the Hamming distance to reflect mutational burden stratified by circadian phenotype. Correlative relationships between circadian parameters, gene expression, and drug sensitivity were evaluated using Spearman and Pearson rank correlation coefficients, with statistical significance assessed through p-values. Regression plots of the strongest correlating genes illustrated the associations between them and time-of-day (TOD) drug sensitivity in the tested cancer cell lines, including confidence intervals (CI) and correlation metrics.

For the triple negative breast cancer (TNBC) analyses (appendix **A2**), dimensionality reduction using PCA was applied to min-max scaled circadian parameters derived from Bmal1 and Per2 luciferase reporters. PCA revealed key features driving phenotypic variation, enabling a reduction of the dataset into three representative parameters: period, phase difference variability, and circadian component strength. These features were visualized in a 3D space and subsequently used for k-means clustering, with optimal cluster number determined by elbow plots using the KneeLocator algorithm. **Fig. 3** presents the analytical framework used in the TOD article (appendix **A2**), outlining the full pipeline from circadian parameter and core clock gene expression input to predictive stratification of cancer cell line drug sensitivity.

## Materials and methods

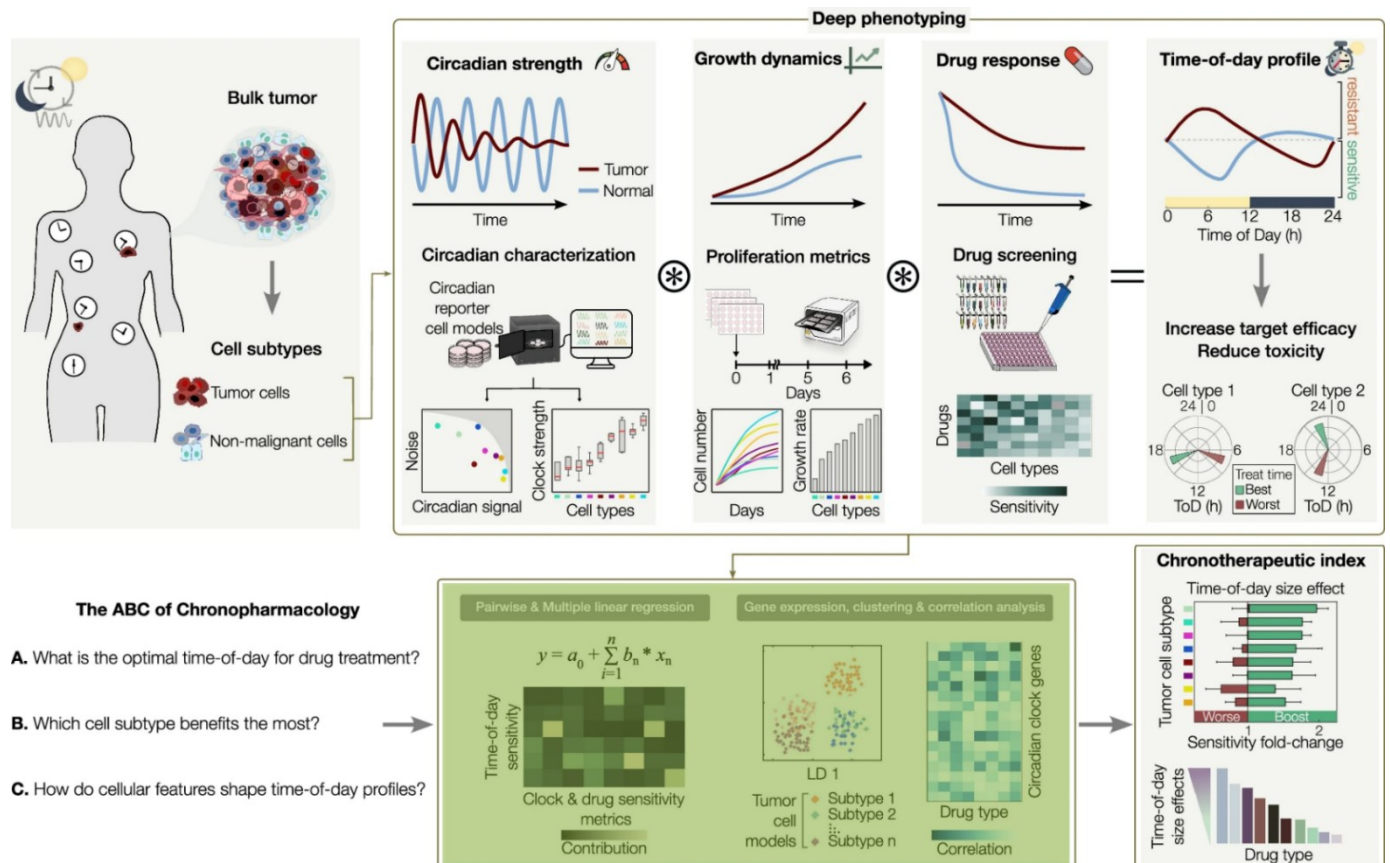


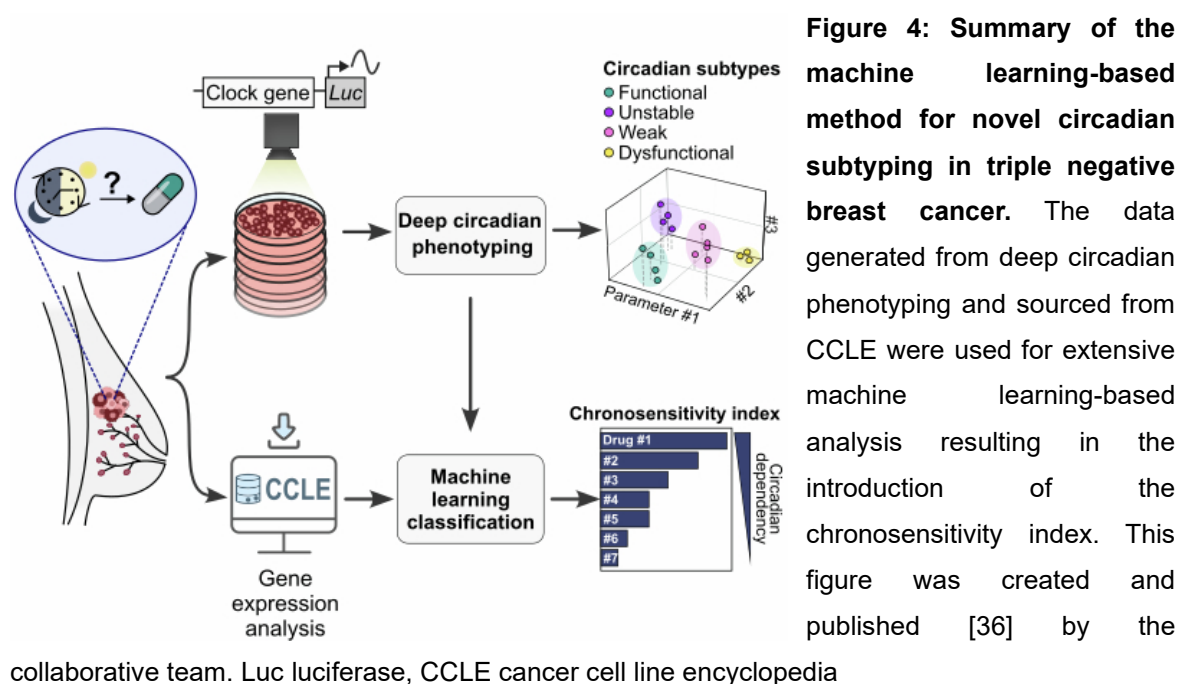
**Figure 3: Strategic framework for determining ideal treatment times in both cancer and healthy tissue systems.** The upper panels outline the circadian parameter and drug sensitivity data generation framework established by the collaborative team of the Granada Lab of the Charité Comprehensive Cancer Center of the Medical University of Berlin. Our contributions (highlighted in green) significantly complemented this strategic framework with computational biology applications to find the answers to the following chrono-pharmacology questions: what is the optimal TOD for drug treatment; which cell subtype benefits the most; and how do cellular features shape TOD profiles. This figure was created and published [35] by the collaborative team before the highlighted adaptations. TOD time-of-day

### - Machine learning algorithms for circadian subtyping

Both supervised and unsupervised machine learning approaches were applied to extract structure from circadian datasets and stratify breast cancer models according to drug response and their circadian rhythms. PCA was used to reduce high-dimensional circadian gene expression profiles into interpretable axes. Loadings of individual genes on the first two components were visualized to understand the contribution of each feature and highlight patterns associated with drug response. Supervised learning with LDA was conducted using median-binarized drug sensitivity as the target variable, resulting in a

## Materials and methods

single discriminant axis directly comparing across the high or low drug sensitive groups. To prevent data overlap in visualization, results were jittered along the y-axis. The model's feature contributions were reported as percentages summing to 100%, allowing for straightforward biological interpretation of circadian clock gene importance. **Fig. 4** provides the methodological flowchart and core of our contribution to the TNBC-related article (appendix **A3**), detailing data input, transformation steps, and integration into the classification model to define a chronosensitivity index.



### - Chronosensitivity index for model evaluation and validation

To ensure model robustness and interpretability, we employed systematic evaluation strategies combining cluster-based discriminative metrics and CV. Model performance in classifying drug sensitivity based on circadian parameters or gene expression was quantified using the chronosensitivity index based on the between cluster distance (BCD) to within cluster distance (WCD) ratio in the one-dimensional LDA-transformed space. A threshold of  $BCD/WCD \geq 2$  was used to indicate meaningful separation between sensitive and insensitive groups, reflecting a minimum of twofold separation between group centres relative to internal dispersion. This is a heuristic criterion for meaningful separation where the clusters are not just statistically distinguishable, but substantively far apart relative to their noise within clusters.

To validate generalizability, we applied leave-one-out CV (LOOCV), particularly suited for our limited sample sizes of cell lines. LOOCV was used across both LDA and regression-based models such as multi-dimensional Lasso (L1) and Ridge (L2) regression analyses to identify circadian features most strongly associated with drug sensitivity. Regularization parameters were chosen to enhance feature selection and reduce overfitting ( $\alpha = 0.1$  for L1 regularization;  $\alpha = 1.0$  for L2 regularization). **Fig. 5** illustrates the calculation and interpretation of the chronosensitivity index, showing how LDA-transformed circadian features lead to class separation and model evaluation.

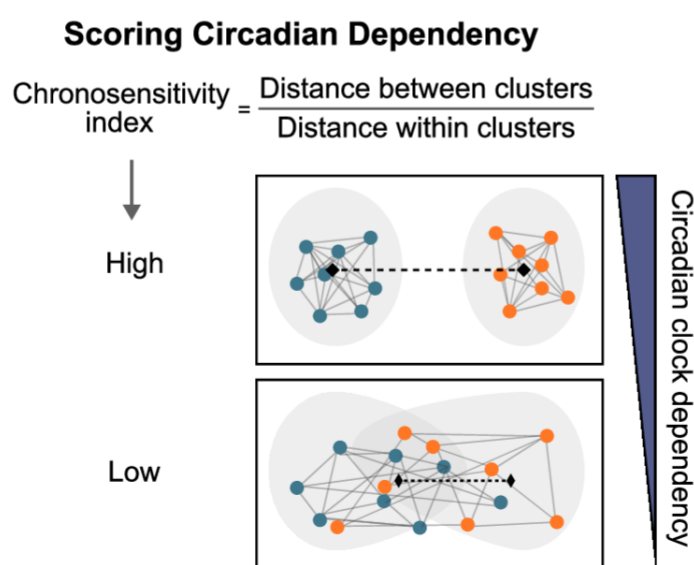


**Figure 5: A chronosensitivity index based on the LDA-transformed space for scoring circadian dependency in the triple negative breast cancer cell lines.** The chronosensitivity index (drug sensitivity) is a metric for each drug based on the between cluster distance to within cluster distance ratio in the LDA-transformed space. It reflects the circadian clock dependency for a given drug. This excerpt was created and published [36] by the collaborative

team. LDA linear discriminant analysis

### - Post-dissertation follow-up of the circadian subtyping framework

In this follow-up study on neuroblastoma (NB), we examined the relationship between circadian gene expression and drug sensitivity across several pharmacological metrics, namely activity area, IC50, and EC50 (see appendix **A4**). Spearman rank correlation was used to analyse associations between the circadian genes and drug sensitivity, with the statistical significances adjusted for multiple testing using the Bonferroni method [39]. Correlation matrices were hierarchically clustered using Euclidean distance and complete linkage to mirror the structure observed in the gene expression profiles. Significant gene-drug associations were further examined through pairwise linear regression and visualized with 95% CI. To identify circadian or NB-specific gene signatures predictive of drug response, we applied LDA transformation to min-max scaled expression data comprising

Materials and methods

the same 16 circadian clock genes (**Tab. 2C**) and, in parallel, 11 NB-related genes (MYCN, ALK, PHOX2B, CHD5, TP53, TERT, ATRX, BIRC5, CADM1, NTRK1, NTRK2). Drug sensitivity values were median-binarized for supervised classification in one dimension. LDA performance was assessed with the log-transformed BCD-WCD ratio to assess the chronosensitivity index. Subsets of genes were systematically tested to identify optimal discriminatory combinations, and the most informative transformations were validated using LOOCV to ensure model generalizability.

## ***Materials and methods for machine learning integration in systems biology education***

### **- Literature research strategy screening systems biology study lines**

This review was conducted as a focused, narrative inquiry into the current landscape of Master's-level systems biology education (see appendix **A5**). Rather than adopting a systematic review framework, educational programs were selected based on the authors' institutional knowledge and familiarity with the respective countries. Sources were identified through academic publications, program websites, and internal documentation of teaching practices across 11 institutions. The selection was not exhaustive, nor was it intended to cover all existing programs, but rather to represent illustrative examples of different pedagogical approaches, structural models, and teaching philosophies [40]. Here, we focused on a combination of publicly available curriculum data, our own experience designing and delivering systems biology courses, and the feedback of alumni to highlight current challenges and opportunities in systems biology education. This perspective enabled both descriptive documentation and critical reflection on common challenges, such as managing disciplinary heterogeneity among students' educational background or aligning computational and experimental content across modules. As an addition to this recent review, this dissertation will attempt to specifically map the current state of interdisciplinary machine learning training and application in systems biology education and propose suggestions on how their integration can be further improved to primarily mitigate the presented challenges while exploiting the currently available opportunities.

### **- Study lines organization and data characterization**

Study lines were characterized according to their structural organization, disciplinary composition, the degree of integration between experimental and computational components, and seminar costs. Special attention was given to how foundational competencies in programming and mathematical modelling were introduced and distributed throughout the curriculum. Course formats, credit distributions, and educational objectives were examined qualitatively across the different institutional settings. Another source of data used to gain insight into current systems biology education was the analysis of responses from a round table involving active students and a structured online SV. The round table titled 'Struggles in bioinformatics education' welcomed undergraduate,

graduate, and PhD candidates, while the SV was specifically distributed to enrolled students and alumni of the systems biology Master's programs at the University of Luxembourg. For example, the alumni were asked to evaluate their program's strengths and limitations across areas such as interdisciplinary integration, workload, skill acquisition, and preparation for research or industry. The SV feedback provided valuable first-hand perspectives on the practical outcomes of different teaching models and helped contextualize institutional designs considering former student experience.

Taken together, the documentary evidence of the current systems biology study lines, and the first-hand student and alumni data contributed to a comparative understanding of how diverse programs attempt to meet the pedagogical and logistical demands of interdisciplinary education in systems biology, and how these could be further expanded and improved.

#### - **Descriptive and thematic analysis of today's systems biology education**

A descriptive synthesis was then used to identify recurring themes in systems biology education. These included common challenges in managing disciplinary diversity, aligning instructional content across domains, and ensuring continuity between theoretical instruction and applied skill development. Particular attention was given to pedagogical tensions that emerge in programs with mixed student cohorts from life sciences, mathematics, and computer science.

Examples were used to illustrate how specific programs address these tensions, through modular course design, preparatory training in quantitative methods, or collaborative, integrative project work [41]. Broader structural barriers, such as the lack of formal teaching recognition for interdisciplinary efforts and limited institutional support for cross-departmental collaboration, were also highlighted as factors that continue to shape the development of systems biology education [40]. A good example for preparatory training in quantitative methods is the careful design of adaptive and interdisciplinary educational material that can be used in classrooms to, for example, predicting drug targets and candidate drugs for repurposed cancer therapies in the context of metabolic modelling and expression data [42] (see appendix **A6**).

## Synopsis

### ***Chapter 1: Biomarker detection in clinical cohort data using machine learning***

*This chapter refers to the manuscript presented in appendix A1.*

#### **- Scientific context and motivation of the study**

Frailty is a geriatric condition strongly associated with age and age-related pathologies [6–10]. It is described as increased vulnerability to internal and external stressors, often manifesting as chronic or inflammatory diseases [8,11,12], and contributes to a higher likelihood of institutionalisation. Two large-scale systematic reviews, analysing 21 and 46 studies respectively, reported weighted frailty prevalences of 10.7% and 13.6% among community-dwelling individuals aged 65 years and older [43,44]. Demographic projections from both the European Commission and the United Nations anticipate a significant increase in the number and proportion of older adults by 2050, from 90.5 million (20.3%) to 129.8 million (29.4%) in Europe, and from 727 million (9.3%) to 1.5 billion (16.0%) globally [45]. If the biological and systemic underpinnings of frailty are not adequately addressed, this demographic shift may exert considerable strain on healthcare systems.

Since the 1990s, numerous conceptual frameworks have been proposed to characterise the frailty phenotype, yet a widely accepted consensus has not been reached [19]. Different models describe frailty either as an independent phenotype [4,7,9], a clinical syndrome [46,47], or the consequence of deficit accumulations over the life course [48]. These divergent perspectives of characterising frailty reflect the heterogeneous and multifaceted nature of the condition. Consequently, the literature is focusing on categorising frailty into subtypes based on predominant manifestations, including physical [49,50], cognitive [51,52], or system-specific impairments of liver, gut, oral cavity, metabolism, and renal or respiratory functions [49,53–58].

Despite variations in these subtypes of frailty, most share the same fate of accelerated and disproportionate decline in physiological reserve compared to healthy ageing (see **Fig. 6**, inspired by *Patel et al.* [59]). This process is influenced by many different biological risk factors potentially facilitating frailty development. Among the most frequently reported are



However, in most studies, physiological reserve is assessed through physical characteristics such as GS, various parameters of the limbs or other body parts, and cardio-vascular or -pulmonary exercise, using a wide range of instruments [62,63] (**Tab. 3**).

| <b>Frailty assessment tool</b>            | <b>Frail (95% CI)<br/>Data sets (N individuals)</b> | <b>Pre-frail (95% CI)<br/>Data sets (N individuals)</b> |
|---|---|---|
| FRAIL scale                               | 8% (4% - 14%)<br>11 (19772)                         | 36% (27% - 46%)<br>11 (19772)                           |
| <b>Fried and modified versions</b>        | 13% (4% - 25%)<br>169 (348472)                      | 47% (46% - 49%)<br>138 (294068)                         |
| Physical frailty                          | 12% (11% - 13%)<br>186 (372440)                     | 46% (44% - 48%)<br>155 (318036)                         |
| <b>Frailty index (Rockwood)</b>           | 24% (22% - 26%)<br>71 (1334964)                     | 49% (46% - 52%)<br>29 (1193745)                         |
| Clinical frailty scale                    | 17% (3% - 37%)<br>4 (5982)                          | 15% (0% - 46%)<br>3 (4277)                              |
| Groningen frailty indicator               | 51% (37% - 65%)<br>7 (5148)                         | N/A   |
| Tilburg frailty indicator                 | 38% (27% - 49%)<br>13 (56394)                       | N/A   |
| Other frailty scales                      | 29% (26% - 32%)<br>66 (160043)                      | 21% (15% - 28%)<br>14 (45851)                           |
| <b>All tools tested in the study [63]</b> | <b>18% (17% - 19%)<br/>323 (1867447)</b>            | <b>45% (43% - 46%)<br/>198 (1557632)</b>                |

**Table 3: Heterogeneous prevalence of frailty level by the most applied frailty measurements.**

Excerpt of prevalence values adapted from the meta-analysis by O’Caoimh *et al.* [63]. CI confidence interval, N/A not available

As the development of these assessments has primarily focused on such physical characteristics at singular time points, they lack the sensitivity required to capture underlying physiological aspects, including age- or muscle-related biochemical markers. As pointed out in a 2021 review by Howlett *et al.* [64], the various frailty assessment tools each have specific advantages and limitations depending on their methodology and scope. This has led to therapies and treatments mostly targeting only the symptoms based on the specific assessment tool used, rather than addressing underlying biological mechanisms of frailty [6]. Furthermore, existing frailty assessment instruments rarely consider frailty-associated biological markers including vitamin D deficiency [20–22,65], polypharmacy [15,16], comorbidities [2,60], sarcopenia [5,59], diabetes [66], or chronic inflammation [61]. These are often linked to detrimental effects on the physiological reserve and the individual’s ability to recover from insults. In this study, we focus on data of older people aged 60 years and above from the observational BASE-II study [2]. Frailty in BASE-II was

defined according to *Fried et al.*'s 5-item frailty phenotype [4] (**Tab. 1**), and showed associations with low lean mass, physical performance, sex-specific vitamin D deficiency, metabolic syndrome, use of potentially inappropriate medication, and mortality [5,22,56,67,68]. Using this established definition of frailty, we applied explainable machine learning techniques to identify biomedical and clinical variables that best reflect the physical frailty phenotype in BASE-II [69].

Although not yet undertaken within BASE-II, previous studies have demonstrated the utility of machine-learning in frailty research. For instance, *Gomez-Cabrero et al.* identified protective biomarkers and key risk factor for frailty across four European ageing cohorts [70]. The protective factors included vitamin D and lutein zeaxanthin (carotenoid, and precursor of vitamin A), while troponin T, a protein in the heart muscle responsible for calcium binding, was found to be main risk factor. *Park et al.* explored the minimal set of digital biomarkers needed to classify frailty according to *Fried et al.*'s criteria [71]. *Akbari et al.* quantified the risk of frailty in older people based on real-time skeletal motion data collected by Kinect sensors during simple physical tasks (sit-and-stand, arm curls, ...) [72]. More recently, *Da Cunha Leme et al.* applied machine-learning to the English Longitudinal Study of Aging to determine the most predictive features of frailty which included age, balance, socioeconomic status, alcohol use, and depression [73].

In this study, we leveraged the rich biomedical and clinical data of BASE-II to identify prognostic biomarkers of pre-frailty and contribute new insights to the existing body of knowledge. Given the expected rise in the older population and the continued lack of a universally accepted frailty definition, we aimed to prioritise relevant biomedical and clinical features, including blood-based biomarkers, disease status, and functional measures. This approach considers frailty as a systemic condition spanning physiological, clinical, and functional domains, requiring a broad set of input variables to identify meaningful and clinically useful markers. We also investigated factors related to sex-specific pre-frailty, an underexplored topic, as biological sex differences in hormonal regulation, inflammatory responses, and body composition may influence frailty development and expression. Recognising these patterns could improve early detection, risk stratification, and support the development of more tailored interventions.

- **Key findings and observations of sex-specific pre-frailty**

*The analyses and results presented here focus on pre-frail participants, that is, individuals at the initial stage of a trajectory that may eventually lead to fully developed frailty. Throughout the text and figures, the label ‘pre-frail/frail’ refers overwhelmingly to pre-frail participants ( $n = 470$ ), with only a very small subset of frail participants ( $n = 14$ ,  $<1\%$ ). Consequently, all findings should be interpreted as reflecting predictors of pre-frailty, and no conclusions can be drawn about fully developed frailty from this data.*

**Sex-specific clinical characteristics and physical frailty profiles**

Sex-specific differences were examined across *Fried et al.*'s frailty score, frailty phenotype, and its five individual items. While no significant differences were found in overall frailty scores ( $p$ -value =  $7.03e-01$ ) or phenotype classifications ( $p$ -value =  $5.23e-01$ ), four of the five items showed sex-specific patterns. EX ( $p$ -value =  $2.94e-03$ ) and weak GS ( $p$ -value =  $5.77e-04$ ) were more common in women, whereas GA ( $p$ -value =  $1.34e-02$ ) and low PA ( $p$ -value =  $3.88e-02$ ) were more frequently observed in men. WL was evenly distributed ( $p$ -value =  $5.61e-01$ ) and had the lowest overall prevalence. GS demonstrated the largest sex difference, with a corrected Cramér's  $V$  of 0.09 (small association with one degree of freedom) (more details in appendix **A1**). These observations first suggest that *Fried et al.*'s frailty phenotype manifests differently in men and women by means of diverging pre-frailty profiles.

Across frailty groups, men and women were nearly equally represented, with non-frail individuals comprising the majority (**Fig. 7A**). Most participants (97.1%) were affected by one or two frailty items, and only 14 participants (3.9%) met three or more criteria (**Fig. 7B**). The distribution of individual and combined frailty items further confirmed the sex-specific patterns, and visualisations confirm once again how GA and PA are more frequently affected in men, while women are more affected by EX and GS (**Fig. 7C-D**). Although WL was rare, its distribution was balanced across sexes (37 total cases of WL compared to the 115, 133, 137, and 168 cases of GS, PA, EX, and GA, respectively). To explore whether these differences extended beyond phenotype-level traits, we performed PCA on the continuous biomedical variables. The resulting clustering revealed a clear separation by sex (**Fig. 7E**), suggesting that sex-specific characteristics are also reflected in underlying clinical and laboratory data. Finally, as frailty is age-associated, we examined age distributions across groups. Pre-frail/frail participants were slightly older than non-frail

individuals, particularly among men ( $p$ -value =  $8.62e-04$ ) and to a lesser extent among women ( $p$ -value =  $2.77e-02$ ) (**Fig. 7F**). Overall, these initial descriptive results by sex show solid evidence for considering sex-specific modelling of the pre-frailty phenotype as observed in the BASE-II cohort.

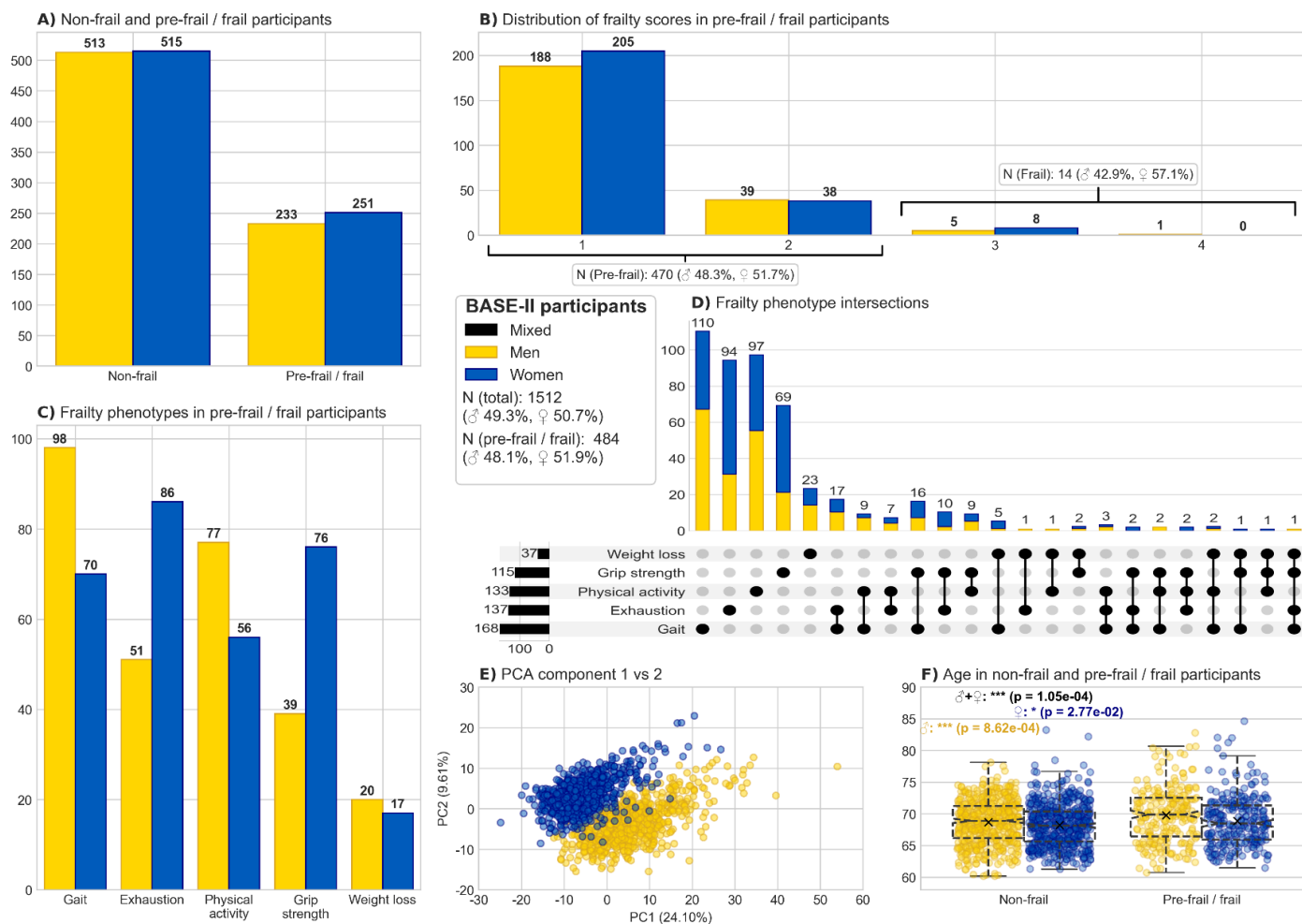


**Figure 7: Sex-specific frailty profiles of the BASE-II participants call for contextualized modelling.** (A) shows the distribution of the non-frail and pre-frail/frail participants. The underlying *Fried et al.* frailty score equal or above 1 are displayed in (B). Sex-specific profiles first appear at the level of the individual items composing the *Fried et al.* frailty phenotype (C) and the intersections thereof (D). The first two principal components (E) reveal clear separation of sex in the biomedical data. Significant differences are also observed in age between non-frail and pre-frail/frail participants (F). Statistical significance obtained from Welch's unequal variance T-test. Illustrated are mixed-sex (black), men (yellow), and women (blue) participants of BASE-II. PCA principal component analysis,  $0.01 < * < 0.05$ ,  $0.001 < ** < 0.01$ ,  $0.0001 < *** < 0.001$ ,  $0.00001 < **** < 0.0001$

In addition to the *Fried et al.* frailty items, the description of general frailty-related features in the BASE-II cohort such as sex (biological men and women), age, body mass index (BMI), waist-hip ratio (WHR), appendicular lean mass (ALM), sarcopenia, morbidity index, and polypharmacy, revealed interesting differences between non-frail and pre-frail/frail participants when stratified by sex (**Tab. 4**). Although sex itself was not significant in the mixed-sex analysis (p-value = 5.23e-01), distinct contrasts emerged between men and women across multiple characteristics. WHR showed significance in men only (p-value = 9.48e-03), while ALM was significantly different in men (p-value = 3.04e-03) and the mixed-sex group (p-value = 2.84e-02). The morbidity index was significant in women (p-value = 1.43e-04) and mixed-sex (p-value = 1.72e-04), as was polypharmacy with differences in women (p-value = 1.43e-03) and the mixed-sex group (p-value = 3.39e-04). Detailed visualizations of the frailty-related characteristics and their distributions can be found in the manuscript of appendix **A1**.

| Cohort characteristics        | Non-frail mixed (N=1028, 67.99%) | Pre-frail / frail mixed (N=484, 32.01%) | P-value         | Non-frail men (N=513, 33.93%) | Pre-frail / frail men (N=233, 15.41%) | P-value         | Non-frail women (N=515, 34.06%) | Pre-frail / frail women (N=251, 16.60%) | P-value         |
|-------------------------------|----------------------------------|---|-----------------|-------------------------------|---------------------------------------|-----------------|---------------------------------|---|-----------------|
| <b>Sex</b>                    |                                  |   | 5.23e-01 (ns)   |                               |                                       |                 |                                 |   |                 |
| men N (%)                     | 513 (33.93%)                     | 233 (15.41%)                            |                 | /                             | /                                     |                 | /                               | /                                       |                 |
| women N (%)                   | 515 (34.06%)                     | 251 (16.60%)                            |                 |                               |                                       |                 |                                 |   |                 |
| <b>Age (years)</b>            |                                  |   | 1.05e-04 (****) |                               |                                       | 8.62e-04 (****) |                                 |   | 2.77e-02 (*)    |
| mean ± SD                     | 68.46 ± 3.44                     | 69.31 ± 4.16                            |                 | 68.68 ± 3.46                  | 69.76 ± 4.33                          |                 | 68.25 ± 3.41                    | 68.89 ± 3.96                            |                 |
| [min, max]                    | [60.16, 83.25]                   | [60.74, 84.63]                          |                 | [60.16, 78.12]                | [60.74, 82.79]                        |                 | [61.29, 83.25]                  | [61.46, 84.63]                          |                 |
| <b>BMI (kg/m<sup>2</sup>)</b> |                                  |   | 4.73e-08 (****) |                               |                                       | 2.13e-04 (****) |                                 |   | 1.99e-05 (****) |
| mean ± SD                     | 26.37 ± 3.79                     | 27.73 ± 4.72                            |                 | 26.93 ± 3.45                  | 27.97 ± 3.77                          |                 | 25.82 ± 4.03                    | 27.50 ± 5.45                            |                 |
| [min, max]                    | [17.03, 44.24]                   | [17.94, 47.68]                          |                 | [19.13, 44.24]                | [19.97, 42.61]                        |                 | [17.03, 40.4]                   | [17.94, 47.68]                          |                 |
| <b>Waist/Hip ratio</b>        |                                  |   | 3.35e-01 (ns)   |                               |                                       | 9.36e-03 (**)   |                                 |   | 6.88e-01 (ns)   |
| mean ± SD                     | 0.96 ± 0.08                      | 0.96 ± 0.08                             |                 | 1.01 ± 0.05                   | 1.02 ± 0.05                           |                 | 0.90 ± 0.07                     | 0.91 ± 0.06                             |                 |
| [min, max]                    | [0.57, 1.44]                     | [0.74, 1.21]                            |                 | [0.81, 1.25]                  | [0.88, 1.17]                          |                 | [0.57, 1.44]                    | [0.74, 1.21]                            |                 |
| <b>Height (cm)</b>            |                                  |   | 1.07e-04 (****) |                               |                                       | 1.46e-03 (**)   |                                 |   | 1.68e-04 (****) |
| mean ± SD                     | 169.74 ± 8.81                    | 167.84 ± 8.94                           |                 | 176.09 ± 6.17                 | 174.53 ± 6.21                         |                 | 163.41 ± 6.06                   | 161.63 ± 6.18                           |                 |
| [min, max]                    | [146.0, 194.8]                   | [144.0, 191.0]                          |                 | [160.0, 194.8]                | [156.3, 191.0]                        |                 | [146.0, 182.5]                  | [144.0, 176.0]                          |                 |
| <b>ALM (kg)</b>               |                                  |   | 3.05e-02 (*)    |                               |                                       | 2.62e-03 (**)   |                                 |   | 3.99e-01 (ns)   |
| mean ± SD                     | 21.38 ± 4.95                     | 20.80 ± 4.77                            |                 | 25.49 ± 3.06                  | 24.75 ± 3.17                          |                 | 17.29 ± 2.46                    | 17.13 ± 2.56                            |                 |
| [min, max]                    | [9.28, 35.1]                     | [11.97, 35.82]                          |                 | [18.91, 35.1]                 | [17.42, 35.82]                        |                 | [9.28, 25.31]                   | [11.97, 26.18]                          |                 |
| <b>ALM/BMI ratio</b>          |                                  |   | 1.54e-08 (****) |                               |                                       | 3.65e-10 (****) |                                 |   | 3.19e-07 (****) |
| mean ± SD                     | 0.82 ± 0.18                      | 0.76 ± 0.17                             |                 | 0.96 ± 0.13                   | 0.89 ± 0.11                           |                 | 0.68 ± 0.10                     | 0.64 ± 0.11                             |                 |
| [min, max]                    | [0.42, 1.47]                     | [0.38, 1.31]                            |                 | [0.63, 1.47]                  | [0.59, 1.31]                          |                 | [0.42, 1.03]                    | [0.38, 0.93]                            |                 |
| <b>Heart insufficiency</b>    |                                  |   | 1.16e-07 (****) |                               |                                       | 2.37e-03 (**)   |                                 |   | 1.73e-05 (****) |
| unaffected                    | 863                              | 350                                     |                 | 451                           | 185                                   |                 | 412                             | 165                                     |                 |
| affected                      | 165                              | 134                                     |                 | 62                            | 48                                    |                 | 103                             | 86                                      |                 |
| median (IQR)                  | 0 (0.0, 0.0)                     | 0 (0.0, 1.0)                            |                 | 0 (0.0, 0.0)                  | 0 (0.0, 0.0)                          |                 | 0 (0.0, 0.0)                    | 0 (0.0, 1.0)                            |                 |
| <b>Vitamin D deficiency</b>   |                                  |   | 1.02e-05 (****) |                               |                                       | 5.35e-03 (**)   |                                 |   | 5.96e-04 (****) |
| unaffected                    | 537                              | 194                                     |                 | 270                           | 97                                    |                 | 267                             | 97                                      |                 |
| affected                      | 491                              | 290                                     |                 | 243                           | 136                                   |                 | 248                             | 154                                     |                 |
| median (IQR)                  | 0 (0.0, 1.0)                     | 1 (0.0, 1.0)                            |                 | 0 (0.0, 1.0)                  | 1 (0.0, 1.0)                          |                 | 0 (0.0, 1.0)                    | 1 (0.0, 1.0)                            |                 |
| <b>Sarcopenia</b>             |                                  |   | 8.69e-08 (****) |                               |                                       | 2.57e-02 (*)    |                                 |   | 6.57e-09 (****) |
| unaffected                    | 968                              | 416                                     |                 | 468                           | 200                                   |                 | 500                             | 216                                     |                 |
| affected                      | 60                               | 68                                      |                 | 45                            | 33                                    |                 | 15                              | 35                                      |                 |
| median (IQR)                  | 0 (0.0, 0.0)                     | 0 (0.0, 0.0)                            |                 | 0 (0.0, 0.0)                  | 0 (0.0, 0.0)                          |                 | 0 (0.0, 0.0)                    | 0 (0.0, 0.0)                            |                 |
| <b>Morbidity Index</b>        |                                  |   | 1.72e-04 (****) |                               |                                       | 2.11e-01 (ns)   |                                 |   | 1.98e-04 (****) |
| unaffected                    | 427                              | 168                                     |                 | 205                           | 82                                    |                 | 222                             | 86                                      |                 |
| only one                      | 295                              | 128                                     |                 | 133                           | 62                                    |                 | 162                             | 66                                      |                 |
| two - four                    | 294                              | 168                                     |                 | 169                           | 82                                    |                 | 125                             | 86                                      |                 |
| five or more                  | 12                               | 20                                      |                 | 6                             | 7                                     |                 | 6                               | 13                                      |                 |
| median (IQR)                  | 1 (0.0, 2.0)                     | 1 (0.0, 2.0)                            |                 | 1 (0.0, 2.0)                  | 1 (0.0, 2.0)                          |                 | 1 (0.0, 2.0)                    | 1 (0.0, 2.0)                            |                 |
| <b>Polypharmacy</b>           |                                  |   | 3.39e-04 (****) |                               |                                       | 6.72e-02 (ns)   |                                 |   | 1.43e-03 (**)   |
| unaffected                    | 203                              | 64                                      |                 | 116                           | 35                                    |                 | 87                              | 29                                      |                 |
| one                           | 157                              | 56                                      |                 | 73                            | 31                                    |                 | 84                              | 25                                      |                 |
| two                           | 460                              | 230                                     |                 | 216                           | 107                                   |                 | 244                             | 123                                     |                 |
| three or more                 | 208                              | 134                                     |                 | 108                           | 60                                    |                 | 100                             | 74                                      |                 |
| median (IQR)                  | 2 (1.0, 4.0)                     | 3 (2.0, 5.0)                            |                 | 2 (1.0, 4.0)                  | 2 (1.0, 5.0)                          |                 | 2 (1.0, 4.0)                    | 3 (2.0, 5.0)                            |                 |

**Table 4: BASE-II cohort description of the main hall marks related to frailty.** In relation to the frailty phenotype, mixed-sex, men, and women show distinct correlative responses for various

Synopsis: Chapter 1 – Biomarker detection in clinical cohort data using machine learning

features associated to frailty. P-values for binary and discrete data types were obtained with the corrected Cramér's V correlation algorithm. For features of continuous data type, Welch's unequal variance T-test after assessing the equality of variances with the Levene's test between the non-frail and pre-frail/frail group were calculated. SD standard deviation, BMI body mass index, ALM appendicular lean mass, WHR waist-hip ratio, IQR inter quartile range, ns non-significant,  $0.01 < * < 0.05$ ,  $0.001 < ** < 0.01$ ,  $0.0001 < *** < 0.001$ ,  $0.00001 < **** < 0.0001$

### ***Mixed-sex model outperformed by context- and sex- specific tailored models***

Using the complete set of biomedical data as input (denoted by the affix ALL), sex-stratified models were trained for the mixed-sex, men-only, and women-only population of BASE-II. Following preprocessing, the number of features was reduced to 257 for the mixed-sex model, 167 for men, and 33 for women. Despite differing in scaling approaches (min-max scaling for mixed-sex and men, standard scaling for women) and in the SVM kernel used (RBF for mixed-sex, linear for both men and women), all models shared key architectural elements: RUS resampling technique to address class imbalance, PCA for dimensionality reduction, and  $\chi^2$  for discrete feature selection (see **Fig. 1E** for a summary of the best configurations and parameters). As shown in **Fig. 8A**, the best-performing ALL models reached mean CV receiver operating characteristics area under the curve (ROC, AUC) scores of  $0.665 \pm 0.057$  for mixed-sex (95% CI: [0.551 – 0.779]),  $0.705 \pm 0.069$  for men (95% CI: [0.567 – 0.843]), and  $0.693 \pm 0.071$  for women (95% CI: [0.551 – 0.835]), with respective hold-out ROC AUC scores of 0.63, 0.66, and 0.66. The men-ALL and women-ALL models slightly outperformed the mixed-sex model, with improved classification of both non-frail and pre-frail/frail individuals. Specifically, the men-ALL model correctly identified 64.29% of non-frail and 67.27% of pre-frail/frail participants, while the women-ALL model achieved 69.00% and 63.27%, respectively. These results suggest that sex-specific modelling, even using the same full biomedical dataset, improves predictive performance over a mixed-sex approach.

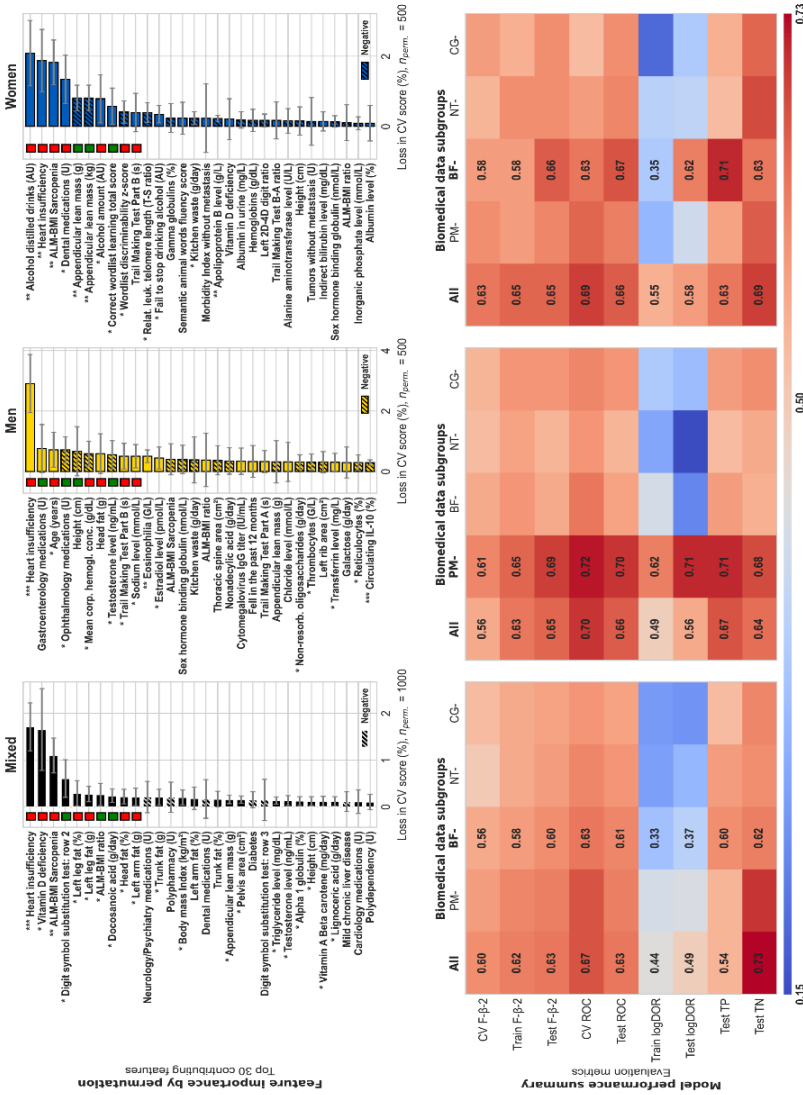
Building on this, a second experiment focused on subgroup-specific input features derived from four predefined biomedical domains: physical measurement (PM), body fluids (BF), nutrients (NT), and cognition (CG) (as illustrated in **Fig. 1A**). The best performing subgroup model for each context was selected, resulting in the three following configurations denoted below: mixed-BF, men-PM, and women-BF. After preprocessing, the feature sets were reduced to 86 (mixed-BF), 32 (men-PM), and 84 (women-BF) features. Notably, SMOTE resampling technique was used in all three subgroup models, replacing RUS and leading to improved performance. Additionally, all subgroup models achieved their best results

Synopsis: Chapter 1 – Biomarker detection in clinical cohort data using machine learning

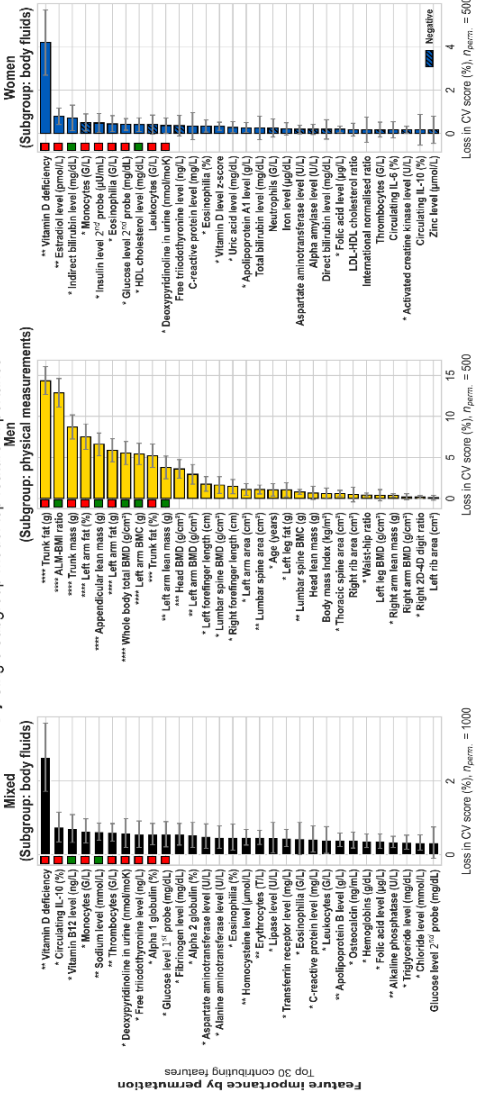
using a linear SVM kernel. While mixed-BF and women-BF shared several preprocessing steps, including robust scaling, PCA, and  $\chi^2$ -based feature selection, the men-PM model differed significantly, using standard scaling and LDA to reduce the input to a single discriminating feature. As shown in **Fig. 8B**, the mixed-BF model reached a CV ROC AUC of  $0.629 \pm 0.047$  (95% CI: [0.535 – 0.723]) with a hold-out ROC AUC of 0.61. In comparison, the men-PM model significantly outperformed it, achieving a CV ROC AUC of  $0.721 \pm 0.066$  (95% CI: [0.619 – 0.853]) and a hold-out ROC AUC of 0.70. The women-BF model showed moderate improvement, with a CV ROC AUC of  $0.633 \pm 0.068$  (95% CI: [0.497 – 0.769]) and hold-out ROC AUC of 0.67. In terms of classification accuracy, the men-PM model correctly identified 68.37% of non-frail and 70.91% of pre-frail/frail individuals, whereas the women-BF model achieved 63.00% and 71.43%, respectively.

These results suggest that using targeted biomedical domains, particularly PM for men and BF for women, lead to improved performance over models trained on the mixed-sex data set. Feature importance, based on permutation scores, is visualised in **Fig. 8C** for the best performing ALL models. The top thirty features are shown with their average contribution and standard deviation (SD) across permutations ( $n = 1000$  for mixed-sex, 500 for men and women), showing the overall CV score loss or gain when a particular variable is shuffled. Directionality of each feature's influence is also highlighted for the top ten, using red (high value in frail participants) and green (low value in frail participants) indicators to support biological interpretation of the findings. In parallel, the heatmaps in **Fig. 8C** provide an overview of performance across subgroup models, comparing the complete set with the best performing domain-specific models for each sex. Further details on the top contributing features for the subgroup-based models are shown in **Fig. 8D**. Like for the complete models, the thirty most influential features are depicted based on their permutation scores, with more detailed results available in Appendix **A1**. These analyses provide valuable insight into how biomedical domains and sex-specific feature patterns shape pre-frailty prediction and form the basis for contextual interpretation in the following section.

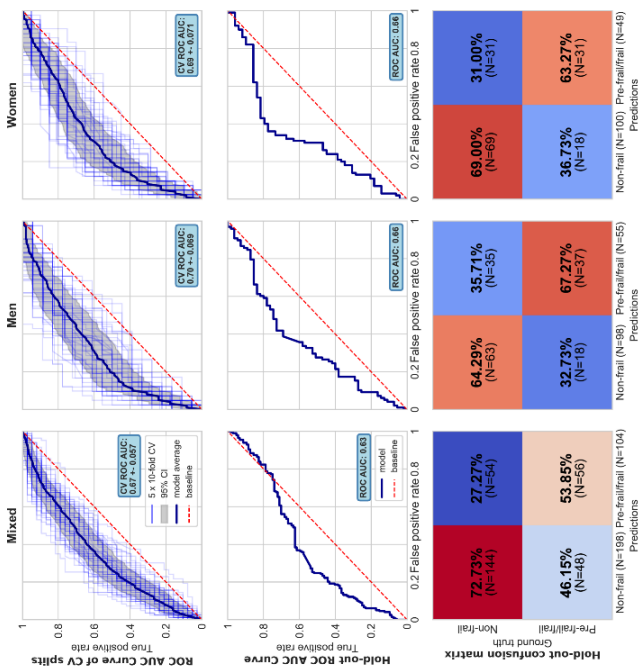
C) Complete model top contributing feature importance and single subgroup performance



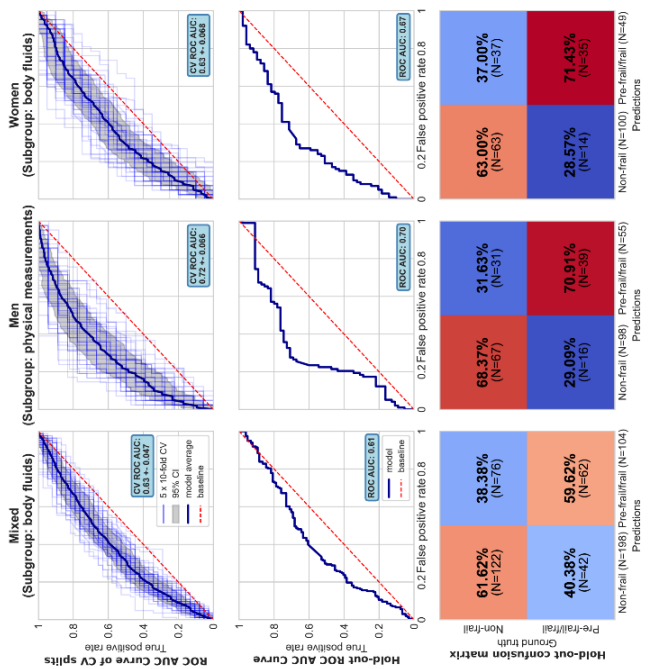
D) Single subgroup model top feature importance



A) Complete input model performances



B) Subgroup input model performances



Synopsis: Chapter 1 – Biomarker detection in clinical cohort data using machine learning

**Figure 8: Sex-specific machine learning models outperform mixed-sex approaches and uncover distinct predictors of pre-frailty in BASE-II.** (A) Performance of sex-specific and mixed-sex models trained on the full dataset, evaluated using ROC AUC scores from a 5 times 10-fold CV process, with the following results: mixed-sex:  $0.665 \pm 0.057$ , men:  $0.705 \pm 0.069$ , women:  $0.693 \pm 0.071$ ; and on the hold-out test set: mixed-sex: 0.61, men: 0.65, women: 0.68. (B) Results from subgroup-specific models trained separately for each sex, showing ROC AUC scores from CV: mixed-sex:  $0.629 \pm 0.047$ , men:  $0.721 \pm 0.066$ , women:  $0.633 \pm 0.068$ ; and test set performance: mixed-sex: 0.60, men: 0.68, women: 0.71. Confusion matrices on the test set are shown in the bottom row. (C) Key predictive features for each sex in the full data models, ranked by average CV score loss from multiple feature permutations. Non-hatched bars indicate features that worsened model performance when permuted. Color-coded squares interpretation: green for features lower in frail-predicted participants, red for higher. Asterisks denote associated absolute z-score levels across permutations. (D) Displays sex-specific predictive features from the subgroup-only models, presented using the same conventions as in panel C. The middle row shows a heatmap summarizing evaluation metrics across complete and subgroup-specific models. CV cross-validation, ROC receiver operating characteristics, AUC area under the curve, ALM appendicular lean mass, BMI body mass index, T-S telomere-single gene ratio, 2D-4D digit 2-to-digit 4 ratio, ROC receiver operating characteristics, DOR diagnostics odds ratio, TP true positive, TN true negative, BMC bone mineral content, BMD bone mineral density, HDL high density lipoprotein, LDL low density lipoprotein

Model interpretability was further enhanced by stratifying predictions according to the original *Fried et al.* frailty levels, rather than the combined pre-frail/frail group. As shown in **Fig. 9**, model performance improves with increasing frailty severity. The best mixed-BF model identified pre-frail and frail participants with sensitivities of 60.0% and 85.7%, respectively. Similarly, the men-PM model achieved sensitivities of 70.5% and 83.3%, while the women-BF model reached 63.8% and 87.5%, respectively. False positive rate (FPR) among non-frail individuals were 41.4% (mixed-BF), 35.5% (men-PM), and 41.9% (women-BF), with specificities of 58.9%, 64.5%, and 58.1%. These results demonstrate that the selected predictors retain discriminative power even in the smaller frail subgroup and suggest a graded model response aligned with clinical frailty progression.

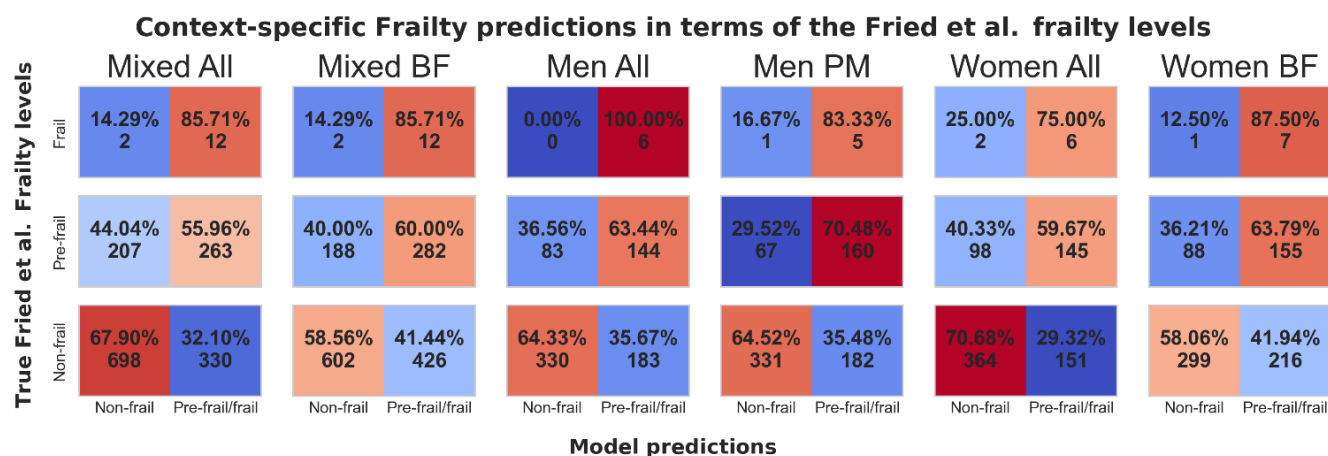


**Figure 9: Model-specific frailty predictions stratified by the Fried frailty phenotype levels in the complete BASE-II cohort.** Model performance is presented across the three frailty categories defined by the *Fried et al.* phenotype (non-frail, pre-frail, and frail), expressed as absolute numbers and percentages within the full BASE-II cohort (training and test sets combined). The best-performing *mixed-BF* model achieves a sensitivity of 60.0% for pre-frail and 85.7% for frail individuals, with a FPR of 41.4% and a specificity of 58.9%. The top *men-PM* model shows improved sensitivity at 70.5% (pre-frail) and 83.3% (frail), alongside a lower FPR of 35.5% and a specificity of 64.5%. The best *women-BF* model reaches sensitivities of 63.8% for pre-frail and 87.5% for frail participants, with an FPR of 41.9% and a specificity of 58.1%. FPR false positive rate

### ***Body composition in men and physiological anomalies in women most predictive of their respective frailty profiles***

Sex-specific classification models revealed that body composition played a significant role in pre-frail/frail men, while physiological and biochemical anomalies were more important in pre-frail/frail women. Although a few predictors were shared across sex, most notably heart insufficiency, model behaviour and feature contributions strongly differed. This pattern persisted across the complete- and subgroup-driven models.

In men, models limited to PM showed the strongest improvements compared to all other subgroups tested. Here, nine of the top ten features caused a CV score drop of 5-15% during permutation (**Fig. 8D**). Key contributors included higher trunk fat mass, left arm fat percentage and mass, and lower lean mass features (ALM, ALM-to-BMI ratio, left arm lean mass). Bone mineral content and density (BMD, BMC) were also lower in pre-frail/frail men, hinting to structural vulnerability. These imbalances portrait a male pre-frailty profile where older men with high fat accumulation in limbs and trunk, reduced lean mass, and low skeletal density are more likely to be pre-frail/frail. In terms of feature transformation, the

best separation between non-frail and pre-frail/frail men was observed with LDA on the top 5-10 features, with a peak BCD-WCD ratio of 1.03 (**Fig. 10A**).

For women, pre-frailty was driven less by external body composition and more by physiological anomalies. The most impactful feature in the women-BF model was vitamin D deficiency, which substantially reduced CV score during permutation (**Fig. 8D**). Multiple immune-related features (white cell counts of monocyte, leukocyte, eosinophil) were elevated in pre-frail/frail women. Metabolic and hormonal markers, including increased insulin, glucose, oestradiol, and urinary deoxypyridinoline (a bone resorption marker), as well as decreased high density lipoprotein (HDL) cholesterol and indirect bilirubin, further differentiated pre-frail/frail women. These markers suggest a complex interplay between inflammation, metabolic imbalance, and hormonal regulation in the female pre-frailty profile. Unlike the men-PM model, the best separation in the women-BF model was yielded with PCA on the top five features (BCD-WCD ratio: 0.54), and LDA applied to all ten features yielded a slightly higher BCD-WCD ratio of 0.78 (**Fig. 10B**).

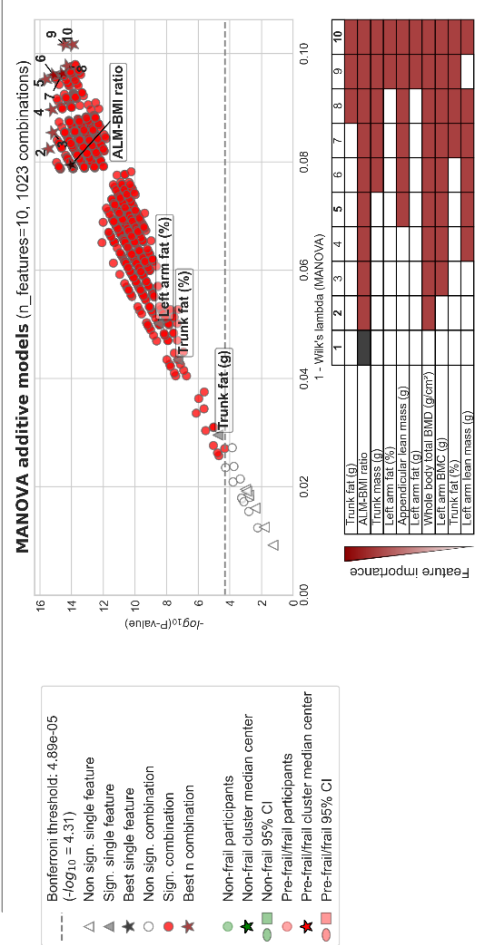
While heart insufficiency was a consistently strong feature, its relative influence and permutation effect differed (**Fig. 8C**). For example, in men-ALL, heart insufficiency showed even stronger detrimental permutation impact than in the mixed-sex model, where it was still ranked highest. The mixed-ALL model also captured sarcopenia and cognitive test performance (*e.g.*, low digit symbol substitution scores) as relevant features, although with less specificity than the sex-stratified models. In general, mixed-sex overlapped partially with sex-specific models but failed to highlight their most defining features.

To assess whether these models identified individual or aggregated predictors, MANOVA was conducted using combinations of top-ranked features from the best-performing models. Results showed increasing statistical significance and higher 1 – Wilk's lambda scores as more features were included (**Fig. 10A-B**). This pattern held true across models and supports the notion that predictive strength lies in feature combinations rather than isolated variables. Clustering analyses using LDA, PCA, and raw values further validated this. In men, LDA transformation yielded the clearest group separation, especially when using 5-10 top features. For raw and PCA-transformed values, the best-performing features were ALM-BMI ratio and total body BMD. In contrast, clustering performance in women was more modest, with no single method or feature set achieving clear separation.

Synopsis: Chapter 1 – Biomarker detection in clinical cohort data using machine learning

Post-hoc feature combination analysis

A) Men PM (SMOTE resampled, standard scaled)



B) Women BF (SMOTE resampled, robust scaled)

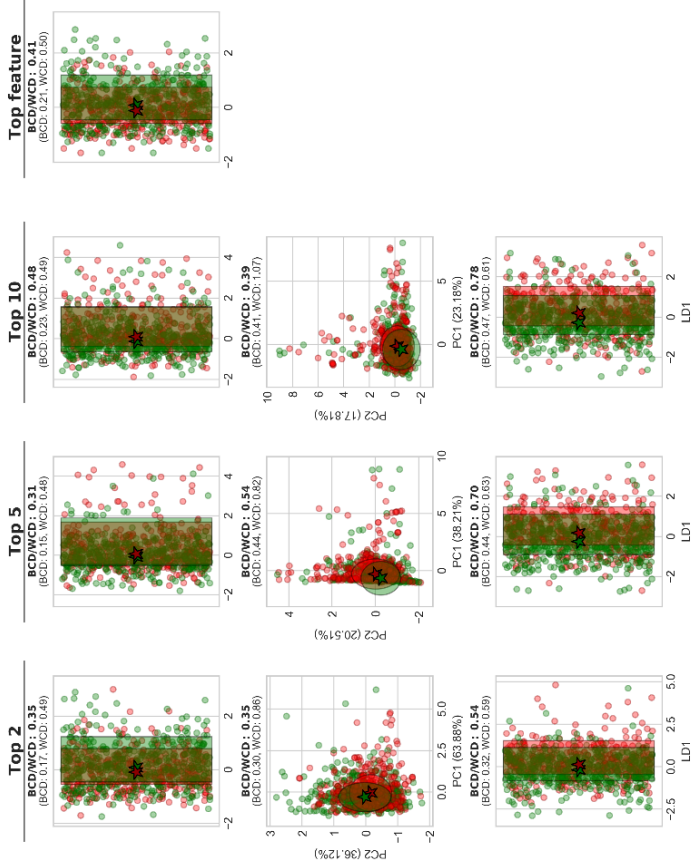
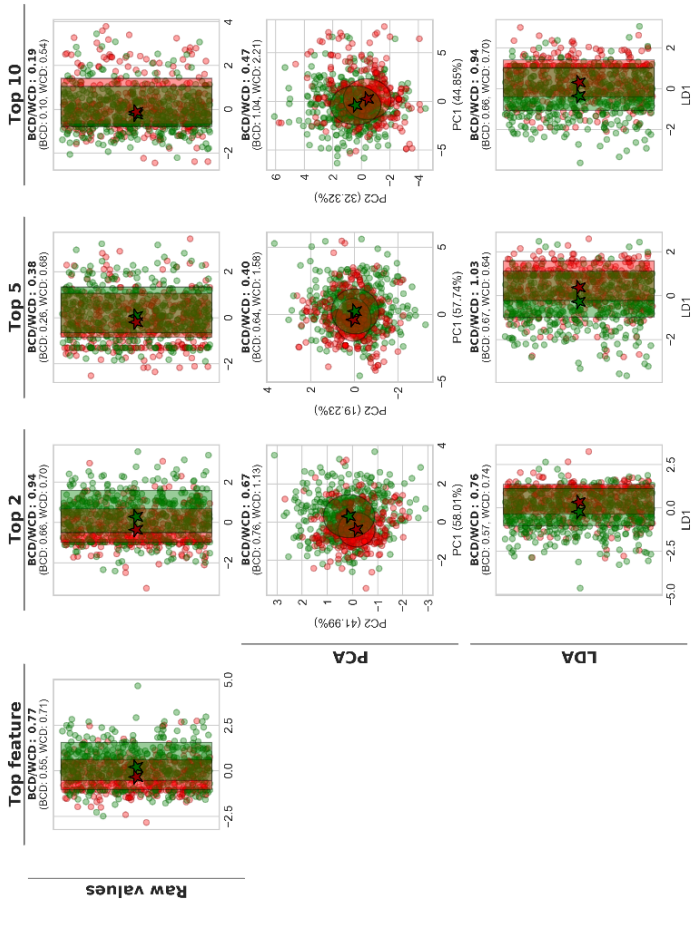
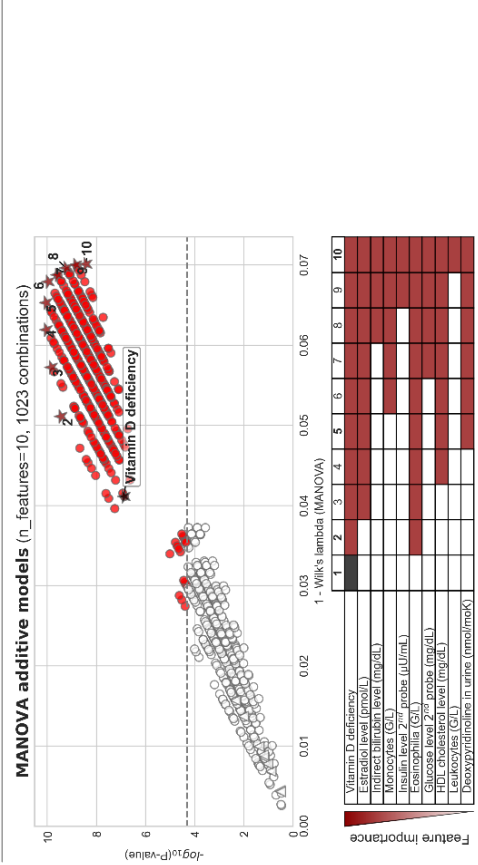


**Figure 10: Increasing cluster separation revealed through post hoc analysis of top feature combinations compared to the best single predictive feature.** Data-driven models for the men (A) and women (B) subgroups were processed using corresponding sampling and scaling methods (see **Fig. 1**) prior to MANOVA analysis. All possible combinations of one to ten features (1,023 total) were evaluated for their discriminatory power using Wilks' lambda, expressed as  $1 - \text{Wilks' lambda}$ , with statistical significance assessed by base-10 log-transformed p-values. Significant combinations are marked in red, while the best-performing combination at each feature count (n) is denoted by a dark red star and annotated accordingly. Single features are represented by triangles, with significant ones highlighted in black. The underlying table ranks the top ten features by performance, with components of the best-performing combinations highlighted in dark red (or black for top single features). Bonferroni-adjusted significance threshold is indicated by a dashed horizontal line. Below the table, visualizations of the raw data, PCA, and LDA are shown for the best single feature and the best combinations of two, five, and all ten features. Each representation includes annotations describing cluster separation and compactness between non-frail (green) and frail (red) groups, with 95% CI applied. Median cluster centres are marked with star symbols. BF body fluids, PM physical measurements, RUS random under-sampling, SMOTE synthetic minority over-sampling technique, sign. Significant, BCD between cluster distance, WCD within cluster distance, CI confidence interval

Complementing these results, statistical testing of the top ten and top thirty model features revealed that only a subset was significantly associated with the pre-frail/frail groups when tested in the combined training and test dataset (**Tab. 5**). In the men-PM model, 9 out of the top 10 features, most notably body composition and BMD, were significantly different between non-frail and pre-frail/frail (complete table of the top 10 and top 30 contributing features of all models can be found within the manuscript in appendix **A1**). However, in women-BF, fewer features reached statistical significance, especially when accounting for p-value correction across variables (see appendix **A1**). This divergence highlights that some of the most contributing features may not show strong individual associations but still contribute meaningfully to the aggregation of biomedical features that are associated to pre-frail/frail. Indeed, comparing z-score differences (continuous features) and corrected Cramér's V (categorical and binary features) across the full BASE-II cohort confirmed that model-relevant features often derive their value from aggregated patterns, rather than isolated statistical strength (see appendix **A1**).

## Synopsis: Chapter 1 – Biomarker detection in clinical cohort data using machine learning

| A) Most important men-PM features                      | Non-frail<br>(N=513, 33.93%)               | Pre-frail / frail<br>(N=233, 15.41%)       | P-value            | B) Most important women-BF features                                   | Non-frail<br>(N=515, 34.06%)    | Pre-frail / frail<br>(N=251, 16.60%) | P-value           |
|--|--|--|--------------------|---|---------------------------------|--------------------------------------|-------------------|
| Trunk fat (g)<br>mean ± SD; [min, max]                 | 13812.02 ± 4071.45<br>[3965.92, 28361.59]  | 15024.44 ± 4742.30<br>[4878.38, 33258.54]  | 3.72e-04<br>(***)  | Vitamin D deficiency  | 0: 267<br>1: 248                | 0: 97<br>1: 154                      | 5.96e-04<br>(***) |
| ALM BMI ratio<br>mean ± SD; [min, max]                 | 0.96 ± 0.13<br>[0.63, 1.47]                | 0.89 ± 0.11<br>[0.59, 1.31]                | 3.65e-10<br>(****) | Estradiol (pmol/L)<br>mean ± SD; [min, max]                           | 35.73 ± 59.27<br>[9.2, 817.2]   | 44.03 ± 60.11<br>[9.2, 471.4]        | 7.03e-02<br>(ns)  |
| Trunk mass (g)<br>mean ± SD; [min, max]                | 41614.36 ± 6726.38<br>[24496.4, 72459.25]  | 42853.48 ± 8159.18<br>[25029.34, 74016.79] | 4.34e-02<br>(*)    | Indirect bilirubin (mg/dL)<br>mean ± SD; [min, max]                   | 0.44 ± 0.15<br>[0.18, 1.22]     | 0.42 ± 0.15<br>[0.11, 1.04]          | 8.40e-02<br>(ns)  |
| Left arm fat (%)<br>mean ± SD; [min, max]              | 31.03 ± 5.85<br>[13.71, 52.38]             | 33.04 ± 5.82<br>[16.98, 51.9]              | 1.53e-05<br>(****) | Monocytes (G/L)<br>mean ± SD; [min, max]                              | 0.40 ± 0.14<br>[0.16, 1.1]      | 0.43 ± 0.16<br>[0.13, 1.51]          | 2.41e-02<br>(*)   |
| ALM (g)<br>mean ± SD; [min, max]                       | 25486.42 ± 3064.90<br>[18910.53, 35100.72] | 24747.02 ± 3173.83<br>[17423.04, 35815.85] | 2.62e-03<br>(**)   | Insulin 2 <sup>nd</sup> probe (µU/mL)<br>mean ± SD; [min, max]        | 59.35 ± 50.15<br>[5.45, 460.1]  | 62.76 ± 52.07<br>[6.86, 502.5]       | 3.83e-01<br>(ns)  |
| Left arm fat (g)<br>mean ± SD; [min, max]              | 1422.53 ± 405.07<br>[445.24, 3374.5]       | 1494.40 ± 435.79<br>[615.73, 3556.75]      | 2.86e-02<br>(*)    | Eosinophilia (G/L)<br>mean ± SD; [min, max]                           | 0.15 ± 0.10<br>[0.01, 0.9]      | 0.18 ± 0.15<br>[0.01, 1.46]          | 4.30e-03<br>(**)  |
| Body BMD (g/cm <sup>2</sup> )<br>mean ± SD; [min, max] | 1.24 ± 0.11<br>[0.94, 1.62]                | 1.23 ± 0.10<br>[0.96, 1.65]                | 1.11e-01<br>(ns)   | Glucose 2 <sup>nd</sup> probe (mg/dL)<br>mean ± SD; [min, max]        | 109.05 ± 29.00<br>[38.0, 278.0] | 114.24 ± 37.36<br>[56.0, 333.0]      | 3.53e-02<br>(*)   |
| Left arm BMC (g)<br>mean ± SD; [min, max]              | 206.54 ± 33.64<br>[115.55, 484.77]         | 199.43 ± 33.22<br>[121.59, 314.21]         | 7.43e-03<br>(**)   | High density lipoprotein cholesterol (mg/dL)<br>mean ± SD; [min, max] | 70.18 ± 16.03<br>[35.0, 134.0]  | 67.68 ± 16.98<br>[32.0, 153.0]       | 4.81e-02<br>(*)   |
| Trunk fat (%)<br>mean ± SD; [min, max]                 | 32.62 ± 5.57<br>[14.66, 47.71]             | 34.39 ± 5.36<br>[17.46, 51.87]             | 5.02e-05<br>(****) | Leukocytes (G/L)<br>mean ± SD; [min, max]                             | 5.56 ± 1.44<br>[2.7, 11.8]      | 5.92 ± 2.02<br>[2.1, 24.4]           | 4.95e-03<br>(**)  |
| Left arm lean mass (g)<br>mean ± SD; [min, max]        | 3123.96 ± 487.39<br>[1737.97, 4738.63]     | 2991.33 ± 504.83<br>[1911.19, 4546.69]     | 6.95e-04<br>(***)  | Deoxyypyridinoline in urine (nmol/moK)<br>mean ± SD; [min, max]       | 59.34 ± 24.88<br>[1.0, 191.0]   | 60.55 ± 25.29<br>[3.5, 152.0]        | 5.27e-01<br>(ns)  |

**Table 5: Cohort characteristics of the ten most predictive features in subgroup-specific data-driven models in the BASE-II cohort.** Displayed are the cohort-level characteristics of the top ten most predictive features derived from the single subgroup models for men (A) and women (B), respectively. For binary and categorical variables, p-values were calculated using Cramér's V, adjusted for data type. Continuous variables were assessed with Welch's t-test for unequal variances, following evaluation of variance homogeneity between non-frail and pre-frail/frail groups using the Levene's test. SD standard deviation, BMI body mass index, ALM appendicular lean mass, BMD bone mineral density, BMC bone mineral content, ns non-significant, 0.01 < \* < 0.05, 0.001 < \*\* < 0.01, 0.0001 < \*\*\* < 0.001, 0.00001 < \*\*\*\* < 0.0001

Together, these findings form a strong argument for sex-specific modelling in frailty-related research. The observed sex-specific profiles, externally visible in men and internally in women, reflect both biological differences and measurement bias in frailty assessment tools. Machine-learning helped identify meaningful feature combinations that escape detection in univariate testing but offer new opportunities for targeted (pre-)frailty screening and intervention.

### - Insights and implications of the research outcomes

Our findings show that physical pre-frailty, as defined by the *Fried et al.* frailty phenotype, presents differently in men and women despite the similar overall prevalence in both sex (**Fig. 7A**). While sex was not significantly correlated with pre-frailty in the full cohort, several frailty-related risk factors differed between men and women in strength and direction (**Tab 4**). For example, polypharmacy and morbidity index showed different associations across groups. More importantly, the five items that define the *Fried et al.* frailty phenotype revealed clear sex-specific patterns: men were more likely to have reduced PA and GA speed, while women more often reported EX and lower GS (**Fig. 7C-D**). These differences occurred even though the frailty scores were similar between men and women (**Fig. 7A-B**), pointing toward different underlying mechanisms. Sex differences in continuous biomedical features were also visible regardless of frailty status (**Fig. 7E**), suggesting a broader pattern of physiological differences. These observations support earlier studies that linked EX and psychological aspects to pre-frailty in women, and performance-related decline to pre-frailty in men [13,15,74–78]. However, few studies have analysed these effects in direct relation to a shared frailty definition, particularly not in the context of applied machine learning.

When comparing model performance, sex-specific models outperformed the mixed-sex model (**Fig. 8A**). The mixed-sex model predicted fewer pre-frail/frail participants correctly and tended to classify many as non-frail. In contrast, the sex-specific models were better at identifying participants of the pre-frail/frail group, especially in cases where contributing features were unequally distributed between sexes. Most top-ranked features were specific to one sex. For example, vitamin D deficiency, alcohol consumption, and sarcopenia were important in women, while body fat mass, height, and age were more important in men (**Fig. 8C**). Only heart insufficiency appeared as a strong predictor across all models, supporting its known association with frailty in both sexes [79,80]. Some cognitive features, such as the trail-making test, were also present in both men and women models, although cognitive performance alone explained little variance in contribution (**Fig. 8C**). This is in line with previous work suggesting that cognitive frailty may be a separate construct [52,74]. While we rank features based on their relative importance, we avoid over-interpreting single features, as their individual effects are often weak.

When we restricted the models to specific subgroups of data, clearer patterns emerged. For men, the model based only on PM performed significantly better than the complete data-driven model, while for women, the model based on BF markers showed a moderate improvement (**Fig. 8B**). These results support the idea that pre-frailty manifests differently

in men and women, and that different domains carry more predictive value depending on sex. In men, frailty was associated with traits like low ALM-BMI ratio, high trunk fat mass, and low bone density (**Fig. 8D, Tab. 5A**), which supports a body composition-driven men pre-frailty profile. In women, vitamin D deficiency was the most important predictor, followed by elevated white blood cell counts such as eosinophils and monocytes (**Tab. 5B**). These physiological differences suggest that pre-frailty in men may be more closely linked to body composition and physical shape, while it may involve immune or hormonal changes in women. Although these associations have been reported separately [20–22,81–83], our results show that their importance varies depending on sex, and they should be interpreted in that context.

To better understand how these features interact, we explored combinations of the top ten features for the best-performing subgroup models (men-PM and women-BF). In both cases, adding more features gradually improved the separation between pre-frail/frail and non-frail participants (**Fig. 10A-B**). For men, the strongest separation was reached with five features related to lean mass and bone density. The ALM-BMI ratio alone already showed a strong separation. For women, the best combination included vitamin D deficiency, oestradiol levels, eosinophil count, HDL cholesterol, and deoxypyridinoline in urine. Again, vitamin D deficiency was the strongest single contributor. Although this simplified method does not fully reflect the model's inner workings, it supports the idea that different combinations of deficits best describe frailty in men and women. These findings align with the view that frailty results from the accumulation of different physiological impairments [48,84], and that this accumulation looks different depending on sex.

Despite these findings, there are several limitations. First, the cross-sectional design limits any interpretation about the direction of effects. We do not know whether the identified markers predict future frailty or are consequences of it. Longitudinal data would be needed to test this. Second, the low number of frail participants in the dataset (14 individuals) forced us to merge pre-frail and frail participants into one category. As a result, we could not investigate the full transition from pre-frail to frail in detail, and some markers relevant for advanced frailty may have been missed. Thus, the present results reflect biomarkers of pre-frailty. Pre-frail and frail are distinct clinical stages, and future studies with larger frail cohorts will be required to extend these findings to fully developed frailty. Still, the models performed well when tested on the original three *Fried et al.* physical frailty phenotype labels, correctly predicting nearly all frail and most pre-frail individuals (**Fig. 9**). Third, missing data required imputation to keep enough participants. Although we used separate imputation for training and testing to avoid data and information leakage, this process can

still introduce a source of bias. Fourth, the dataset is imbalanced, with more than twice as many non-frails as pre-frail/frail participants. To deal with this, we used the F- $\beta$ -2 score to prioritize recall and applied under- and over-sampling techniques during the cross-validated model training. However, imbalanced datasets always carry a risk of skewed model performance. Fifth, while the *Fried et al.* frailty phenotype was used to define frailty, many predictors reflect domains more aligned with the *Rockwood* frailty index, such as chronic diseases, inflammation, or cognitive function. This mismatch between outcome and feature space could lead to overfitting or misinterpretation. Lastly, the analysis of additive feature combinations (**Fig. 10**) does not capture the complexity of the original models, which include non-linear interactions and classifier-specific behaviour.

Our findings support the idea that sex-specific profiling improves the prediction and understanding of frailty development. The models reveal that different physiological systems contribute to pre-frailty in men and women. This suggests that future frailty screening and prevention could benefit from being sex specific. For example, screening older men for sarcopenia, fat gain or lean mass loss, and screening older women for inflammation, vitamin D deficiency, or hormonal imbalances, may help detect early development of frailty. These findings also suggest that generic frailty models, which treat all individuals the same, may miss important risk patterns. Future studies should validate these results in other populations and across time to test if these predictors remain relevant and can anticipate future frailty.

Future perspectives of this project involve addressing the above-mentioned limitations and simultaneously validating the claimed findings in another European population. For this, we are following a more rigid and generalizable workflow (**Fig. 2**) applied in the largest Luxembourg-based PD cohort [34]. Other than blood metabolites, the biomedical data of this cohort is enriched by clinical data (SV and medical examinations) and GA sensor parameters, which potentially could shed light on even more sex- and PD-specific frailty biomarkers. Besides mitigating the limitations and increase generalizability, one additional intention of this follow-up project is the investigation of PD-specific physical frailty on top of the sex-specific differences observed in BASE-II. This additional dimension of research is based on the heavy overlap between physical frailty risk factors, such as depression, fatigue, postural instability, or GA impairment, and the observed motoric and non-motoric symptoms during the various stages of PD development [85–87].

## ***Chapter 2: Drug sensitivity prediction for time-of-day cancer treatment profiling***

*This chapter refers to the manuscripts presented in appendix A2, A3, and A4.*

### **- From circadian drug profiling to functional cancer subtyping**

The circadian clock controls essential physiological and behavioural functions in nearly all living beings. In mammals, it is organised hierarchically with a main pacemaker in the suprachiasmatic nucleus of the brain's hypothalamus with the role to regulate peripheral clocks among different tissues [88,89]. In fact, around 40% of all genes show a tissue-specific rhythmic expression [90], which is affecting major biological functions such as metabolism [91,92], cell proliferation [93], immune responses [94], and DNA repair [95]. This rhythmic regulation is maintained through interlocking transcriptional-translational feedback loops [96] which are highly sensitive to environmental factors like light and temperature. Disruptions to this system, be it through lifestyle, environmental factors, or genetic mutations, are associated with a range of diseases including cancer [97]. In fact, circadian dysfunction has already been linked to tumour progression, lower survival rates [98] and altered sensitivity to anti-cancer drugs at given timepoints [99].

To better understand how circadian rhythms affect drug efficacy, we contributed to the development of an experimental and computational pipeline to characterise TOD responses in tumour and non-tumour cell lines (see appendix **A2**) [35]. This approach combines deep phenotyping of circadian clock function, growth dynamics, and drug response features, using both experimental measurements and high-throughput screens. The pipeline is illustrated in **Fig. 3** and includes the analysis of TOD profiles of multiple tumour and non-tumour cell lines across a large panel of drugs, allowing for the identification of treatment times that maximise efficacy while reducing toxicity. By integrating this deep phenotyping data with publicly available transcriptomic datasets, our contributions (highlighted in green in **Fig. 3** and **Fig. 11**) mainly addressed central questions in chronopharmacology: which treatment times are optimal, which cancer types benefit most, and how cellular features shape TOD profiles. As part of this effort, a chronotherapeutic index was developed that quantifies the possible benefits of circadian-based treatments across different compounds and models.

In a second step, we applied this framework to breast cancer (see appendix **A3** and reference [36]), the most frequently diagnosed cancer in women and a highly

heterogeneous disease [100]. We focused on TNBC, an aggressive subtype lacking oestrogen, progesterone, and HER2 receptor expression, the three major breast cancer type markers (**Fig. 11A**). Since this classification is based on the absence of these markers, it inevitably groups together biologically diverse tumours. Hence, TNBC is further divided into distinct molecular subtypes, namely basal-like (BL1, BL2), mesenchymal (MES), immunomodulatory, and luminal androgen receptor (LAR), each manifesting different growth characteristics and drug sensitivities [101,102]. Although circadian rhythms have been shown to persist in some breast cancer models [103,104], the overall more aggressive subtypes are thought to have weaker or more disrupted clocks [105]. However, this assumption has rarely been tested systematically across multiple subtypes and cell lines.

To fill this gap, we contributed to a comprehensive circadian profiling of breast cancer cell lines to determine their circadian phenotype and to research the association between these phenotypes, drug sensitivity and tumour growth (**Fig. 11B**) applying the same pipeline introduced in the TOD study [35]. Circadian rhythms were characterised using bioluminescence-based measurements and quantification methods (**Fig. 11C-D**), cell growth dynamics were assessed (**Fig. 11F**), and drug sensitivity across time points was quantified with both stationary and non-stationary analysis (**Fig. 11G**). The obtained circadian parameters were then analysed for their correlation strength (**Fig. 11E**). In addition, we included genomic expression data of core clock-related genes and highlighted the mutational burden of these genes in the tested breast cancer cell lines (**Fig. 11H**). By integrating all these cellular features, we identified clusters of cell lines with distinct circadian phenotypes (**Fig. 11I**), effectively defining novel circadian-based subtypes of breast cancer with functional, unstable, weak, or dysfunctional circadian phenotype. These subtypes were predictive of drug response patterns, highlighting candidate compounds for further chronotherapeutic investigation.

Together, these studies demonstrate the significant value and potential impact of circadian profiling across cancer cell lines and drug panels. The general TOD framework [35] enables the systematic identification of drug timing strategies and circadian vulnerabilities, while its application to breast cancer provides a proof-of-concept for circadian-based subtyping [36]. Such approaches could clinically complement existing molecular classifications and uncover treatment windows not apparent through conventional methods. These insights may help refine future treatment approaches, especially in cancers with poor prognosis like TNBC, where additional therapeutic stratification is urgently needed.

Synopsis: Chapter 2 – Drug sensitivity prediction for time-of-day cancer treatment profiling

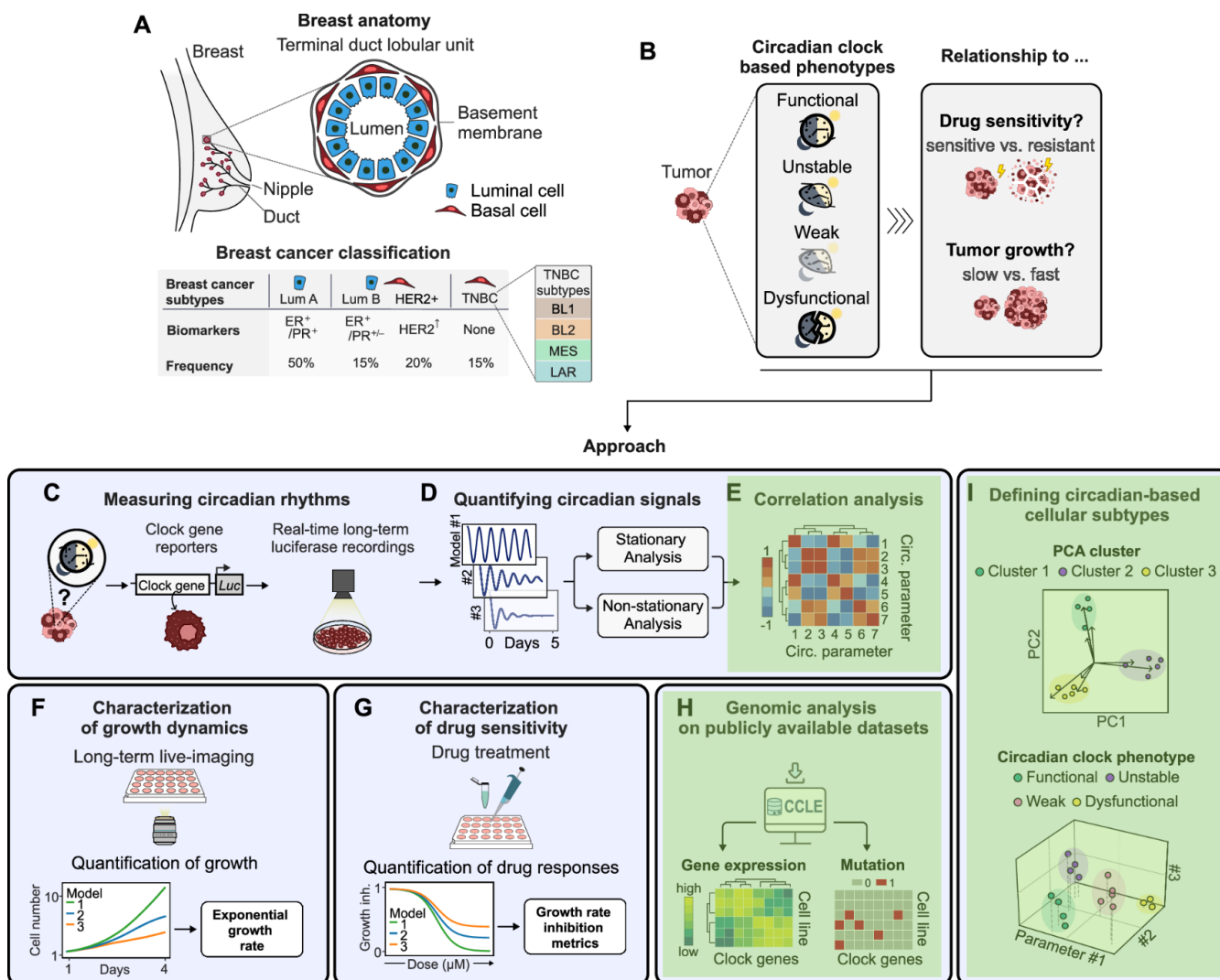


**Figure 11: Introducing the contributions to triple negative breast cancer subtyping using circadian-based deep phenotyping.** Breast anatomy and breast current breast cancer subtype classification (A). Leading hypothesis of relationship between circadian clock-based phenotypes (functional, unstable, weak, dysfunctional), and specific drug sensitivity together with tumour growth (B). The panels C, D, F, and G summarize the quantification and characterization of key circadian factors to capture the circadian rhythms of each tested TNBC cell line. Panels E, H, and I highlight our contributions towards the data analysis and validation of TNBC subtyping using circadian-based deep phenotyping data. This figure was created and published [36] by the collaborative team before the highlighting of our contributions in green (E, H, and I). TNBC triple negative breast cancer, Lum luminal, HER human epidermal growth factor receptor, BL basal-like, MES mesenchymal, LAR luminal androgen receptor, luc luciferase, CCLC cancer cell line encyclopedia, PCA principal component analysis

- **Main findings of circadian-based cancer phenotyping**

***How core clock genes shape time-of-day drug sensitivity***

To explore if circadian gene expression relates to TOD-dependent differences in drug sensitivity, we analysed transcriptomic data from a panel of 8 TNBC cell lines with known TOD maximal drug response (TOD-MR) values. The heatmap in **Fig. 11A** displays the normalized expression of 16 core clock genes across these lines, revealing marked heterogeneity. Hierarchical clustering suggested the presence of two distinct groups, with several genes including ROR $\alpha$ , CLOCK, NPAS2, REV-ERBs, PERs, and CRY1 showing high variance across cell lines. Potential links between TOD-MR and gene expression are summarized by their absolute correlations, either categorized by drug or gene (**Fig. 11B**). When stratified by drug (**Fig. 11B**, left), the strongest correlations were observed for DNA-damaging response (DDR) drugs such as cisplatin and adavosertib, but also the PI3K/AKT/mTOR inhibitors alpelisib and torin2. Stratification by gene (**Fig. 11B**, right) identified Per2, DBP, ROR $\beta$ , PER3, and REV-ERB $\alpha$  (NR1D1) among the genes most frequently correlated with TOD-modulated drug sensitivity.

We then focused on cisplatin, a DDR drug, and used LDA to evaluate if cell lines could be separated by their TOD-MR values (**Fig. 11C**). The left panel shows the TOD-MR values varying across lines (threshold = 0.30, and LDA transformation shows a clear separation between high and low TOD-MR. Genes contributing most to this separation (**Fig. 11C**, right) included ROR $\beta$  and DBP, followed by NPAS2, PER3, and CRY2, suggesting that these genes may be informative in the context of DDR-related TOD effects. We then applied PCA to evaluate if similar patterns can be observed for different drugs. Using paclitaxel, a mitosis inhibitor, we again stratified cell lines by TOD-MR (**Fig. 11D**, left). The first two principal components explained 44.8% and 28.9% of the variance (sum = 73.7%), and partial grouping by TOD-MR status. The loadings (**Fig. 11D**, right) indicate that CSNK1D, CRY1, CLOCK, and PER1 contributed mostly to PC1, while CLOCK, ROR $\alpha$ , DBP, NPAS2 and REV-ERB $\alpha$  were leading PC2, supporting that distinct circadian genes are associated with time-dependent responses to different drug classes likely driven by the drug's mechanism.

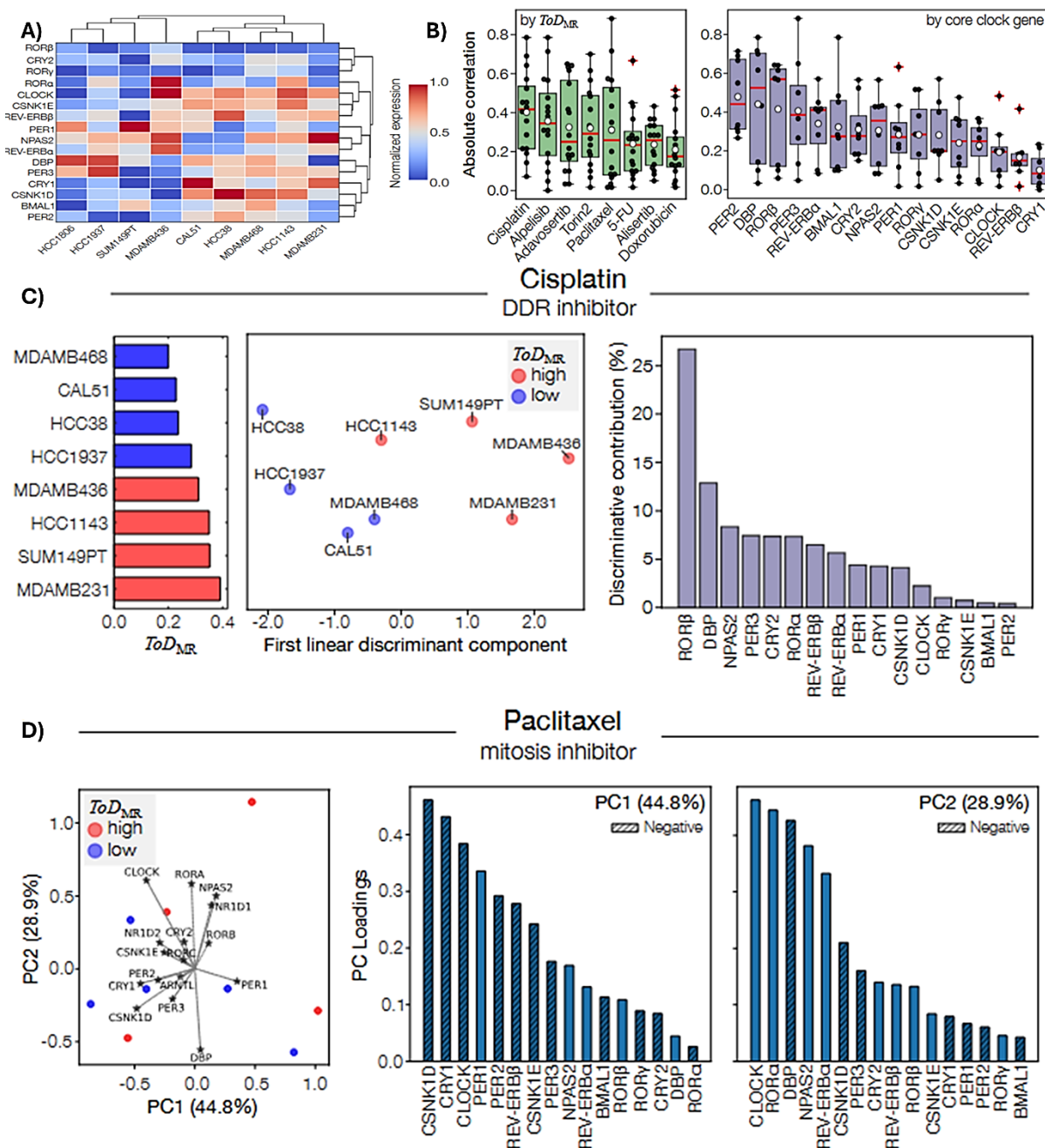


**Figure 12: Analysis on how core clock genes shape time-of-day sensitivity.** Gene expression of core clock genes for the different cell models used in the framework project [35] (A). The boxplots show the mean ranking of the absolute spearman rank correlations between the TOD median values and circadian clock gene expression, either by drug ( $n = 8$ ) or circadian clock gene ( $n = 16$ ). The boxplots display the 25<sup>th</sup> and 75<sup>th</sup> percentiles with their edges, median by red lines, mean by white circles, and outliers with red crosses (B). LDA transformation was applied on median-binarized TOD-MR values for the DDR drug cisplatin, colour coded as blue (low) and red (high). Contributions of core clock genes for this discrimination of low and high TOD-MR are shown as percentage in the right panel (C). To emphasize on drug-specificity, a PCA biplot of the first two components is depicted for the mitosis inhibitor drug paclitaxel. Merged to that panel are the normalized loadings (arrows) to

show their relative contribution to the TOD-MR separation (left panel). The ranked contribution of the circadian clock genes to the first and second PCA components are shown in the lower central and right panels (D). TOD time-of-day, LDA linear discriminant analysis, TOD-MR time-of-day maximal response, DDR DNA-damage response, PCA principal component analysis

### ***Detailed example and evaluation of the methodological approach***

To explore whether circadian clock gene expression shapes TOD drug responses, we selected 16 core clock genes that are central to molecular clock feedback loops and known to disrupt circadian rhythms when altered [96,106] and examined them across a panel of up to 9 TNBC cell lines. The main metric TOD-MR was compared with gene expression using three approaches: linear correlation, LDA, and PCA (**Fig. 13A**). Correlation analysis suggested only moderate links between individual genes and TOD-MR, with cisplatin showing the highest mean correlation ( $r = 0.40 \pm 0.21$ ) and PER2 ranking highest among genes ( $r = 0.48 \pm 0.20$ ) (**Fig. 13B**, and appendix **A2**). For paclitaxel, stronger negative correlations appeared for PER3 ( $r = -0.88$ ) and DBP ( $r = -0.72$ ) (**Fig. 13B-C**). LDA was then applied after grouping cell lines median-binarized into high or low TOD-MR by drug. In paclitaxel, separation was clear (**Fig. 13D**, left), and CRY2, DBP, and PER3 together contributed ~46% of the discriminative power (**Fig. 13D**, right). Importantly, gene contributions varied by drug, hinting at drug- or target-specific interactions with the clock. When gene effects were combined across all drugs, overall contributions were small, with ROR $\beta$  leading at  $10.5\% \pm 9.6\%$  (**Fig. 13E**, and appendix **A2**). Besides linear regression and LDA analysis, PCA was also able to separate low from high TOD-MR and revealed for example that paclitaxel-treated cell lines clustered along two principal components with 73.7% of variability, where CSNK1D dominated PC1 and CLOCK PC2 (appendix **A2**). This suggests that while no single gene consistently predicts TOD-MR, combined expression profiles may still capture relevant structure.

We also compared TOD-MR values from the raw data points vs. derived smoothed spline fits (using the moving average method) with the concern that this processing of the response data could have introduced artifacts into the final TOD-MR estimates. Linear regression analysis was performed between TOD-MR values from raw and smoothed data and found to be close to a perfect agreement ( $R^2 = 0.99$ ) across all drug-cell combinations (**Fig. 13F**). Finally, the LDA models were validated using LOOCV and showed varying predictive accuracy across the tested drugs. Some drugs (*e.g.*, torin2, adavosertib, cisplatin) classified all cell lines correctly, while others (*e.g.*, alisertib, 5-FU) performed poorly (**Fig. 13G**). Overall, while single-gene correlations with TOD-MR were limited,

multivariate patterns suggested that the collective circadian machinery may influence drug-specific TOD sensitivities in TNBC cell lines.

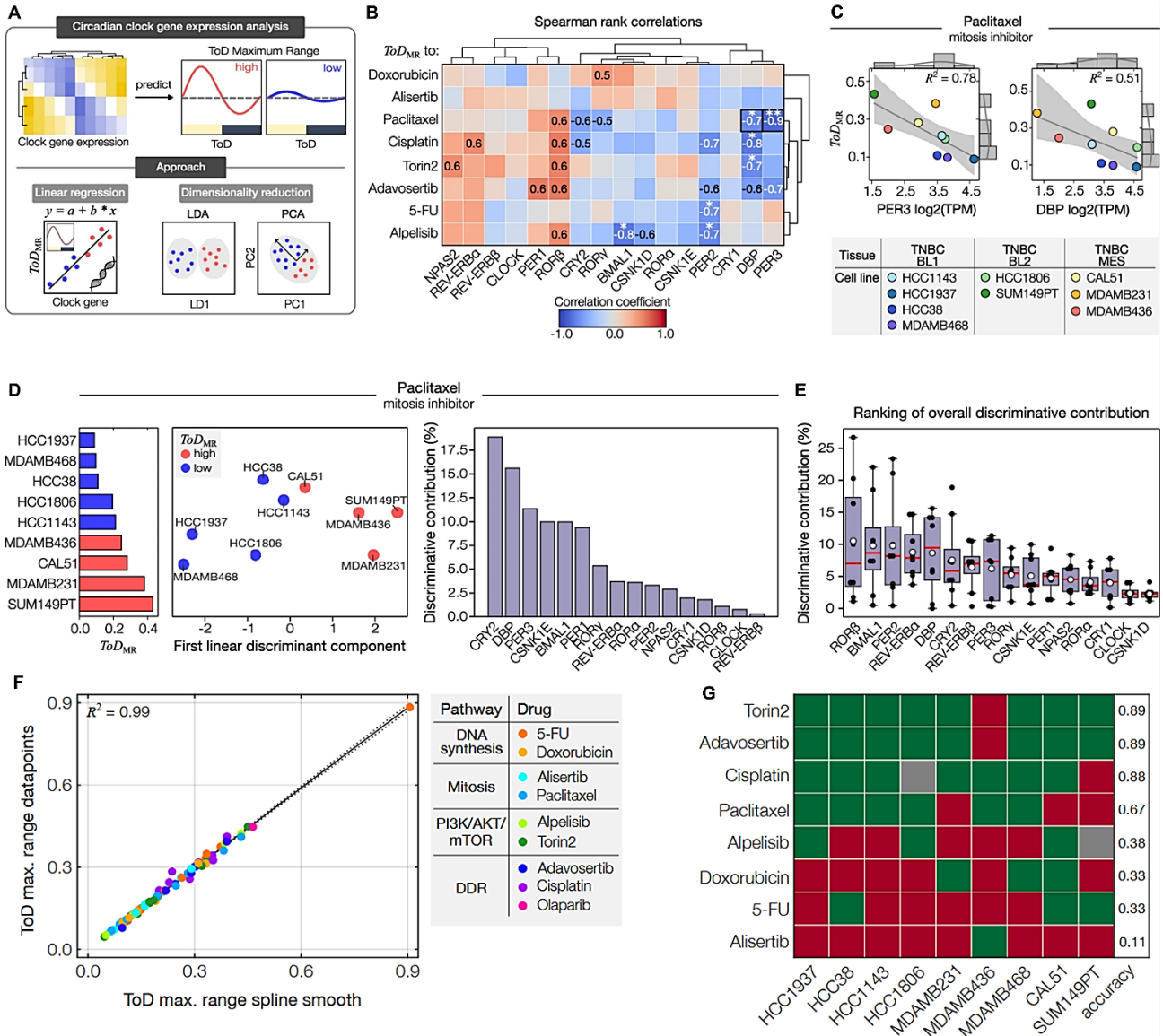


**Figure 13: Example and evaluation of methodological approaches.** Workflow to assess whether core clock genes modulate TOD drug sensitivity (A). Spearman correlations between TOD-MR and gene expression, clustered by drug (rows) and gene (columns) (B). Cisplatin/alpelisib:  $n = 8$ ; others:  $n = 9$  cell lines. Example correlations for paclitaxel with PER3 and DBP ( $\log_2$  TPM); shaded = 95% CI (C). LDA separation of high (red) vs. low (blue) TOD-MR for paclitaxel; right: gene contributions (%) (D). Boxplot of mean discriminative contributions across 8 drugs (E). TOD-MR from discrete vs. spline fits ( $n = 80$  drug-cell combinations) (F). LOOCV accuracy for LDA models; green: correct, red: incorrect; grey: not available) (G). TOD, time-of-day; TOD-MR, TOD maximal response; TPM, transcripts per million; LDA, linear discriminant analysis; LOOCV, leave-one-out cross-validation. \*  $p \leq 0.05$ , \*\*  $p \leq 0.01$

***Circadian-based subtyping of breast cancer cell lines driving drug sensitivities***

With the main framework of circadian-based deep phenotyping set up and the TOD effects of cancer drugs revealed, the next step was to exploit the gained knowledge in a particular condition to exemplify the added value. For this, we focused on TNBC cell lines to investigate whether circadian-based parameters can reveal a new way of subtyping a specific cancer type and how they can predict cancer drug sensitivities (see [36], and appendix **A3**).

We first examined how circadian clock parameters and growth rate (GR) relate to one another across breast cancer cell lines. Pairwise Pearson correlations revealed a strong positive relationship between different circadian metrics, but mostly weaker, negative associations between these parameters and GR. By contrast, circadian instability markers, such as period or phase-difference variability, showed positive correlations with faster growth (**Fig. 14A**). Using PCA, we identified 3 circadian-based clusters capturing 54.7% and 21.1% of the variance along PC1 and PC2, respectively (**Fig. 14B**). Infradian and circadian components contributed most to PC1, marking them as potential key indicators of circadian behaviour. Interestingly, this grouping did not align with the classical breast cancer subtypes, suggesting that circadian-based clustering could instead offer complementary information. To assign functional meaning, we selected the strongest representative circadian parameter from each PCA cluster; namely the period scale, the variability of BMAL1-PER2 phase-difference, and circadian scale; and performed k-means clustering ( $k = 4$  by elbow method; silhouette score 0.445, see appendix **A3**). This yielded four circadian phenotypes, namely functional (strong and stable rhythms), unstable (high instability), weak (low strength), and dysfunctional (low strength and long periods) (**Fig. 14C**). Functional models included MCF10A, 2 LumA, and 2 TNBC-BL1 lines; the dysfunctional group contained only 2 models, SUM149PT and HCC38.

Next, analysis of the mutational burden in 16 core and 44 related clock genes [38] showed heterogeneous patterns across cell lines. Most carried at least one mutation, while five had none (**Fig. 14D**, only showing genes which have at least one mutation in one of the cell lines). Mutation burden scores were attributed as 1 for silent (least damaging), 2 for missense, and 3 for nonsense/frameshift mutation (most damaging). Highest scores were observed in the unstable phenotype, while the functional phenotype had the lowest score. Interestingly, damaging mutations appeared to concentrate more likely in unstable and weak phenotypes (**Fig. 14E**). Dysfunctional models, had low mutation scores, hinting that factors beyond mutational burden may drive loss of circadianicity. These results outline a circadian-based subtyping framework that differs from classical classification and captures

variation in circadian strength, stability, and genetic disruption, features that may influence drug response.

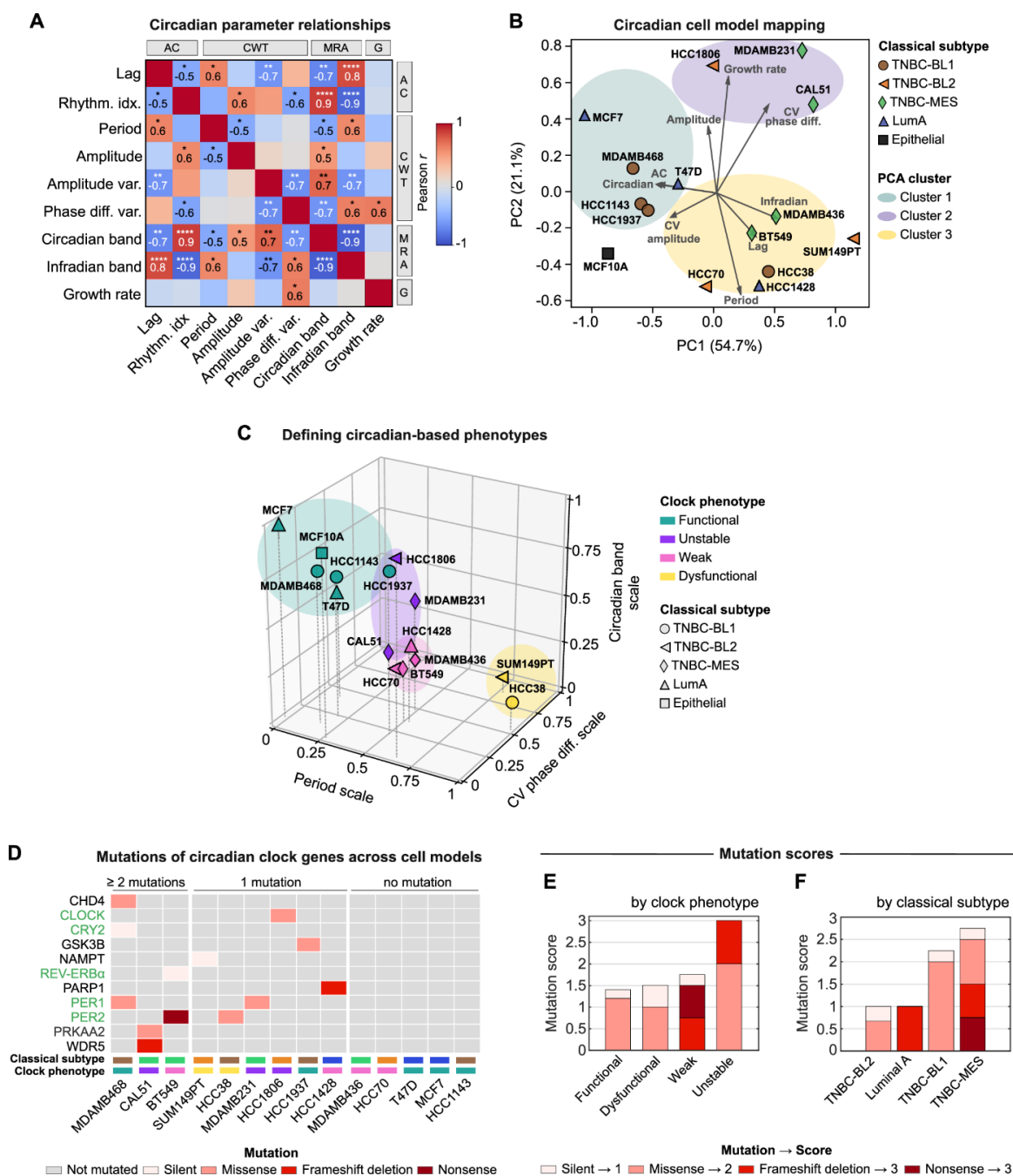


**Figure 14: Defining circadian phenotypes and genetic profiles in breast cancer cell lines.**

Pearson correlations between circadian parameters and growth rate; clock-strength measures positively correlate with each other and inversely with growth, while instability metrics (period/phase-difference variability) correlate positively with growth (A). PCA of circadian and growth parameters showing three clusters; PC1 (54.7% variance) driven mainly by infradian and circadian components (B). K-means clustering ( $k = 4$ ; silhouette score = 0.445, see appendix A3) of selected parameters defines 4 phenotypes, namely functional, unstable, weak, and dysfunctional (C). Mutation profiles of

Synopsis: Chapter 2 – Drug sensitivity prediction for time-of-day cancer treatment profiling

16 core and 44 related circadian genes; scores: silent = 1, missense = 2, nonsense/frameshift = 3, only genes with at least 1 mutation across cell lines are shown (D). Mutation scores by phenotype: unstable highest, functional lowest; damaging mutations occur in unstable and weak phenotypes (E, F). PCA principal component analysis, AC auto-correlation, CWT continuous wavelet transform, MRA multiresolution analysis, G growth

Circadian regulation and drug response seem connected in ways that are still not fully mapped out. Prior work has shown that timing drug delivery with the body's internal clock can sometimes amplify therapeutic effects [98,99,107]. To see how intrinsic circadian features might relate to drug sensitivity, we compared multiple drug response parameters with metrics of circadian oscillation using Pearson correlations and linear regression. Drug sensitivity was assessed with the normalized growth rate inhibition method [108], which corrects for cell division during assays and is generally more stable than raw viability measures.

The drug panel covered a broad pharmacological range, from DNA synthesis blockers (5-FU, doxorubicin) and mitosis inhibitors (alisertib, paclitaxel) to agents that are targeting specific pathways (PI3K inhibitor alpelisib, mTOR inhibitor torin2) and DDR inducers such as adavosertib and cisplatin. One striking relationship emerged for cisplatin as its maximal inhibitory effect (GRinf) showed a clear negative correlation with the autocorrelation rhythmicity index ( $r = -0.64$ ; **Fig. 15A**). In other words, strongly rhythmic cell lines tended to be more affected by cytotoxicity, whereas weaker rhythmicity was linked with cytostatic or milder responses. Similar trends appeared for other circadian parameters, including amplitude and ridge length, while markers of clock instability (*e.g.*, variability in period length) pointed in the opposite direction.

This wasn't unique to cisplatin, as several drugs displayed meaningful links between GRinf and circadian features. Alpelisib, for example, showed the highest median correlation ( $r = 0.82$ ), suggesting PI3K inhibitor responses may be especially sensitive to circadian state. When flipping the perspective, amplitude emerged as the circadian parameter most often associated with maximal drug effect (median  $r = 0.74$ ). Other sensitivity metrics, such as GR50 and the Hill coefficient, were also correlated with certain clock parameters, but overall patterns were weak. This hinted that single-parameter correlations might be too simplistic given the clock's multi-layered architecture.

To capture these combined effects, we applied LDA to both our own data and public datasets (**Fig. 15B**). In our cisplatin screen, LDA separated cell lines into cytostatic versus

cytotoxic drug response (**Fig. 15C**). The rhythmicity index and ridge length together accounted for roughly a quarter of the separation, making them the top discriminators (**Fig. 15D**). Moving from phenotypes to genes, our analysis showed that circadian clock gene expression also can classify cisplatin sensitivity where  $ROR\alpha$  and  $CRY2$  stood out, contributing ~34% of the discriminative signal (appendix **A3**). Given our limited sample size, we tested alternative models (L1/L2 regression, logistic regression) to see if they could match LDA's performance. Classification methods generally outperformed regression, but accuracies remained moderate (0.42 to 0.51 for regression methods), likely reflecting the heterogeneity of cell lines and metric dependencies (appendix **A3**). Still, the classification-based results were consistent enough to justify continuing with LDA for broader screening.

Expanding to the public CCLE dataset, the HSP90 inhibitor 17-AAG emerged as especially circadian-sensitive, with clock stability parameters driving the distinction between high and low sensitivity (**Fig. 15E-F**). To quantify this separation, we used the ratio of BCD to WCD, calling it the chronosensitivity index (**Fig. 15G**) [109]. Nearly all 19 drugs tested had chronosensitivity indices above our chosen threshold of 2 (**Fig. 15H**). Consistent with that, 17-AAG achieved the highest classification accuracy in LOOCV (71%), while topotecan performed worst (14%). Some other agents (e.g., erlotinib, nilotinib, AZD0530) scored high on the index but had varying classification accuracy depending on method, hinting at context-specific dependencies.

Clock gene expression offered a complementary view. For about half the drugs, the gene-based chronosensitivity index was above threshold, and for some (topotecan, lapatinib, paclitaxel) it outperformed circadian parameter-based classification (**Fig. 15I**). Interestingly, topotecan's poor parameter-based separation improved substantially when gene expression was used, suggesting the two approaches capture partly distinct biology. High gene-based chronosensitivity tended to align with better LDA classification accuracy (71-86% for the top three drugs), though logistic regression didn't always replicate these gains (appendix **A3**).

Taken together, these results suggest the circadian clock have a broad but variable influence on drug sensitivity. No single feature explained the patterns; rather, combinations of rhythmicity, stability, and specific clock gene expression contributed to separating drug effectiveness. The chronosensitivity index provides a straightforward way to flag drugs that may be time- or circadian-dependent, potentially guiding future chronotherapy strategies.

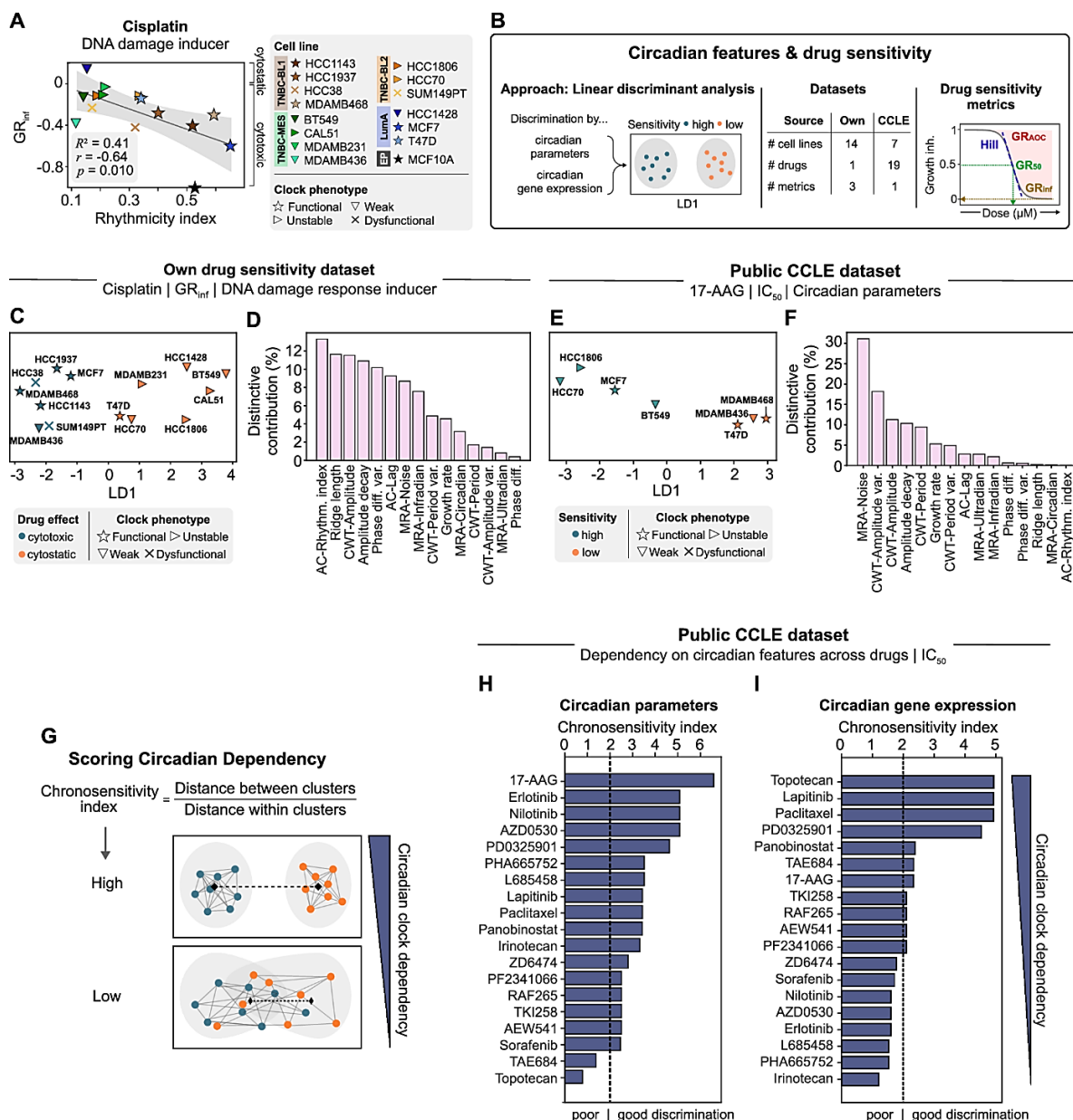


**Figure 15: Circadian features shape variability in drug sensitivity across cell lines.** Linear regression between cisplatin GR<sub>inf</sub> values (absolute drug effect, right axis annotation) and rhythmicity indices from autocorrelation analysis. Symbols indicate cell lines, with shapes denoting circadian phenotype; grey shading = 95% CI. R<sup>2</sup>, Pearson r, and p-values shown (A). Overview of the LDA-based workflow and datasets used to assess circadian contributions to drug sensitivity. Sketch illustrates dose-response curves, and the sensitivity parameters analysed (B). LDA using median-binarized cisplatin GR<sub>inf</sub> values and 15 circadian/growth parameters as predictors. Cell lines below and above median are shown in blue or orange, respectively. LD1 captures the main variance between groups (C). Ranked contributions of circadian and growth parameters to discrimination (D). LDA on median-binarized IC<sub>50</sub> values for 17-AAG (E). Parameter contribution ranking (F). Schematic of the chronosensitivity index, calculated as the BCD/WCD ratio. Higher values indicate stronger circadian influence on drug sensitivity classification (G). Chronosensitivity index ranking for

Synopsis: Chapter 2 – Drug sensitivity prediction for time-of-day cancer treatment profiling

multiple drugs based on circadian oscillation parameters (H). Chronosensitivity index ranking for multiple drugs based on circadian gene expression (I). Dashed line at  $y = 2$  marks the threshold for good vs. poor separation in LDA space. GR growth rate, LDA linear discriminant analysis, BCD between cluster distance, WCD within cluster distance

### - Interpretation and consequences of the study's findings

The idea that cancer inevitably erodes circadian timing turns out to be far less universal than often claimed. In the datasets treated in this chapter, strong oscillations appeared not only in non-malignant MCF10A and luminal cell lines like MCF7 and T47D, but also in several TNBC lines and their current clinical subtypes (**Tab. 2**). This goes against the common view that highly transformed tumours usually lose their circadian rhythms [98,110]. Instead, our results align with reports that clock functionality can be subtype-dependent and modulated by hormonal status [104], with oestrogen responsiveness acting as a regulatory factor. What stood out here was that even within a single molecular subtype, clock behaviour varied widely. Using PCA on our circadian parameter dataset on the combined period, amplitude, rhythmicity index, BMAL1-PER2 phase-difference variability, and circadian/infradian spectral components, we retained >75% of the variance in the first 3 components. From there, k-means clustering (elbow method,  $k = 4$ , silhouette score 0.445) separated the models into functional, unstable, weak, and dysfunctional phenotypes (**Fig. 14**) which did not overlap with the classical breast cancer categories. Functional clocks appeared in both hormone-positive and -negative models, while some oestrogen-positive lines fell into the weak group. The phenotypes themselves carried distinct biological signatures, including functional models with high amplitude and stability and low mutation burden; unstable models showing high variability and the heaviest mutation load; weak models having reduced rhythmic strength; and dysfunctional models combining long periods with low amplitude but minimal genomic damage. These findings not only echo earlier observations in non-malignant and luminal models [103,111–113], but also extend them to aggressive TNBC contexts, suggesting that circadian profiling exposes hidden heterogeneity that molecular markers alone cannot detect. This was already emphasised in other tumour subtype-specific rhythm studies [104].

The framework that enabled this classification was designed to integrate multiple data types while preserving their relationships (**Fig. 11**). In our part of the work, we analysed the circadian parameter sets that had been generated from raw luminescence traces and applied several processing and statistical approaches to link them with growth dynamics and drug sensitivity metrics (**Fig. 12**). This led us to the development of the

chronosensitivity index as a new way to classify cell models into high and low sensitivity groups with circadian features (**Fig. 15**). For context, the chronotherapeutic index [97,110,114], which reflects TOD variation in drug effects across malignant and non-malignant models, was introduced by our collaborators and is discussed here alongside our results. This index confirmed expected TOD effects for DNA synthesis inhibitors 5-FU and doxorubicin [114–117] and the DNA intercalator cisplatin [114,117], but also highlighted new candidates. The chronosensitivity index, in turn, quantified the degree to which circadian state predicts drug response, not just in timing terms, but as a static classifier. For example, cisplatin and adavosertib scored high on both TOD variation and circadian classification, while 17-AAG emerged as particularly circadian sensitive, with stability parameters dominating the separation (**Fig. 15**). These observations match earlier hints from HSP90 literature linking its inhibition to clock control of the cell cycle [99] but here emerged from a deliberate, large-scale, multi-parametric screen. Even more revealing was the comparison between parameter-based and gene expression-based classification. For most drugs the results aligned, but for topotecan, a poor parameter-based separation improved remarkably when clock gene expression was used (**Fig. 15**). This divergence suggests that parameter and expression data capture partly distinct aspects of circadian biology, an insight that may guide which data type to prioritise in future modelling. The flexibility of the framework means it could, in principle, be extended to other cancer types or even non-oncological systems, as argued in prior chronotherapy reviews [97,114].

Our correlation and classification analyses, run on a drug-by-drug basis, revealed just how context dependent these relationships are. For DDR agents like cisplatin, the rhythmicity index and amplitude were top predictors, with higher values linked to stronger cytotoxic responses (**Fig. 15**). This is consistent with prior demonstrations that DNA repair efficiency and chemotherapy toxicity can be clock-phase dependent [96,97,105]. For paclitaxel, the strongest signal came from individual genes, such as PER3 and DBP, showing strong negative correlations with TOD-MR ( $r = -0.88$ , and  $r = -0.72$ , respectively) (**Fig. 13**) that are consistent with known circadian regulation of mitotic processes [96,106]. The LDA gene contribution profiles reinforced this specificity: ROR $\beta$  and DBP dominated cisplatin separation, while CRY2 featured for paclitaxel, and CSNK1D/CLOCK for other agents (**Fig. 13**). Pooling drugs diluted these effects, as no gene explained more than 10% of discriminative power across the board likely due to redundancy and compensation within the clock network. This mosaic pattern was also observed in our mutation analysis. Unstable phenotypes carried high burdens of damaging mutations, often missense or nonsense changes, whereas dysfunctional phenotypes sometimes had few, hinting at non-genetic routes to circadian loss such as epigenetic modifications or altered protein turnover.

From a predictive point of view, these results suggest not relying on single markers and instead favour multi-feature models, exactly the rationale behind our chronosensitivity index. Classification performance underscored this. Some drugs (torin2, adavosertib, cisplatin) achieved perfect LOOCV accuracy, others (alisertib, 5-FU) performed poorly, and several pathway inhibitors (e.g., erlotinib, nilotinib) scored high on the index but showed variable CV accuracy, suggesting context-specific dependencies that need further mechanistic work.

Several of our contributions went into strengthening the robustness of these conclusions. We directly addressed potential artefacts from data smoothing by comparing TOD-MR from raw data points and spline fits. The correlation showed to be essentially perfect ( $R^2 = 0.99$ ) across 80 drug-cell combinations (**Fig. 13**), indicating our downstream associations were not biased by this method. We considered fibroblast and other non-malignant comparators as baselines for interpreting tumour chronotherapeutic indices given their consistently strong rhythms [118–120]. Early comparisons hinted at meaningful healthy-tumour differences in TOD sensitivity patterns, though we remain cautious about generalising fibroblast behaviour to in vivo tissue contexts. We also acknowledged possible bidirectional effects, where drugs might themselves alter circadian parameters, thereby influencing their own efficacy in subsequent cycles [121]. Such effects are currently not captured by the design of this framework. Moreover, the multiresolution analysis (MRA) detected alternate ultradian rhythms (~12 h) in BMAL1 and PER2 oscillations also observed in a previous work, showing that ultradian rhythms contribute to stress responses [122]. While not the focus here, these rhythms could partially explain drug response patterns that seem decoupled from classic 24 hours timing. Capturing such layers would require time-series designs with pre- and post-treatment phenotyping, ideally at the single-cell level to distinguish proliferation-driven changes from clock-driven ones.

That said, important limitations remain. All experiments were in vitro, without modelling tumour-host interactions, systemic hormonal rhythms, or immune modulation. These factors are known to influence both circadian timing and therapy outcomes [123]. GR differences could confound both clock metrics and drug response [124,125] as well, and although population-based luciferase assays help avoid clonal artefacts, they cannot eliminate random reporter insertion effects. Sample sizes for some drug-cell combinations were rather small, limiting statistical power and producing classification accuracies ranging from 14% (topotecan) to 71% (17-AAG). The mutation screen, while informative, was restricted to a small set of clock-related genes; other regulators such as metabolic, stress-response, or DNA-repair genes, may also shape the phenotypes we observed. Our

analysis also did not incorporate potential circadian misalignment effects from external factors like temperature cycles or nutrient timing, which can influence peripheral clocks independently of the light-dark cycle [88]. These caveats mean that while our framework is ready for application to more complex cancer models, translation to clinical recommendations should proceed with caution and with validation in organoid or animal systems first.

Even with those caveats, the implications are substantial. By profiling circadian function alongside drug sensitivity, we could identify phenotypes within and across tumour types that predict drug sensitivity in ways unrelated to classical subtype. The chronotherapeutic and chronosensitivity indices offer a way to quantify and compare these relationships across models and drugs, helping to flag timing-sensitive compounds and match them to the tumour phenotypes most likely to benefit. The data also suggest that personalising drug timing will require a multi-parametric view including rhythmicity, stability, gene expression, mutation status, and potentially even ultradian components, rather than reliance on any single feature. This approach aligns with calls for tumour subtype-specific circadian analysis [104] and with the broader vision of integrating circadian biology into pharmacology [97,114]. Building on these insights, we have initiated a follow-up project on NB cell lines (see appendix **A4**) to test whether this framework remains as performant in other cancer cell line examples (including testing of random selected gene sets as additional validation) and to show that circadian-guided therapy can move from an intriguing laboratory observation to a practical tool in clinical oncology.

## **Chapter 3: Machine learning integration in systems biology education**

*This chapter refers to the manuscripts presented in appendix A5 and A6.*

### **- Challenges and opportunities for machine learning in systems biology education**

Systems biology has grown into a major branch of biological and biomedical research, driven by advances in high-throughput sequencing, the expanding scope of bioinformatics, and the accelerating influence of machine learning. These tools have not only expanded the scale at which data can be collected but also the complexity of the questions that can be asked. With new data types and integrative analytical pipelines, researchers can now carry out large-scale investigations that were previously impossible, leading to discoveries that reshape biological theory and open entirely new lines of inquiry. This growth is reflected in publication trends, rising from roughly 6,400 papers in 2003 to over 35,000 in 2023 (scholar search, input 'systems biology'). Notable examples from recent years include the identification of new RNA functions [126,127], large-scale prediction of protein structures [128], and refined understanding of genomic and epigenetic regulation [129].

While these developments create opportunities for innovation, they also put pressure on educational systems. Traditional biology curricula, rooted in qualitative reasoning and hands-on experimentation, and standard computer science programs, which rarely address biological complexity, leave many students without the interdisciplinary mindset needed to connect molecular details to system-level behaviours. Academic and industry roles increasingly demand not just isolated technical competence, but the ability to merge biological insight with computational reasoning as a form of systems thinking that remains difficult to foster within existing course structures.

In response, various authors have suggested ways to blend advanced biology content with computational modelling and data analysis training, equipping students to conceptualise living systems in terms of components, interactions, and emergent behaviours [130–137]. Some have proposed specific course structures, while others focus on the conceptual hurdles students face when trying to master complex biological systems alongside quantitative methods. Several articles have highlighted the issues of systems biology education, and a number of case studies illustrated these approaches: the *Bulletin of Mathematical Biology* examined cross-disciplinary challenges for mathematics and biology

students [133]; *Feenstra et al.* described the structure, evolution, and lessons from a joint systems biology course at the Vrije Universiteit and University of Amsterdam [131]; *Momsen et al.* outlined a framework to shift classical biology teaching toward systems perspectives, including system components, architecture, environmental interactions, and emergent outcomes [135]; and *Dale et al.* demonstrated how combining biochemical experiments (e.g., enzyme kinetics) with coding exercises can strengthen modelling skills [134].

Recent commentaries have expanded the scope of systems biology education further, proposing integration with public health and computer science [138], advocating for broader computational competencies and public outreach [130,139], and reviewing progress in modelling methodologies [140]. However, many of these perspectives are anchored in the experience of individual institutions or focus on high-level aspirations, often without detailed comparisons across different program designs or practical barriers faced in diverse educational settings.

In the corresponding review (see appendix **A5**), we aim to complement such perspectives by mapping how systems biology is taught across a wide set of institutions. It offers a comparative view of program content, identifies challenges reported by students and graduates, and considers practical factors such as skill heterogeneity, prerequisite structures, interdisciplinary balance, adoption of AI tools, and student well-being. The intention is to connect strategic vision with real-world implementation, and to inform a more adaptive and inclusive approach to systems biology training.

In the final part of this chapter, I build on that foundation to discuss how machine learning, as used throughout this dissertation, could be embedded more efficiently into systems biology education to strengthen interdisciplinarity and applied problem-solving. As one example, I refer to in-house course material [42] (see appendix **A6**, and the course repository available on GitHub: <https://github.com/sysbiolux/ISB705MetabolicNetworkModeling>), which illustrates how students could be introduced to practical machine learning applications in metabolic network modelling. This example represents just one of many potential pathways for integrating these methods into the training of the next generation of systems biologists.

- **Study lines, perspectives, and machine learning in systems biology education**

***Systems biology Master Programs: strong diversity but lack common framework***

Most systems biology courses are currently offered at the master's level [141], although a small but growing set of initiatives aim to engage undergraduate students, particularly since the COVID-19 period, through hybrid workshops, crash courses, or newly introduced Bachelor's programs in systems and computational biology [142,143]. These are often organised by university departments, learned societies, or graduate student groups. At the master's level, programs may appear as stand-alone systems biology degrees or as specialised tracks within broader fields such as bioinformatics, molecular biology, biochemistry, or computational biomedicine.

For the academic year 2024/2025, we sampled program descriptions from universities in Europe, North America, and the Caribbean (**Tab. 6**). Across most European countries, a standard of 120 ECTS (European credit transfer and accumulation system) over two years (~60 US semester credit hours, or 240 UK CATS (credit accumulation and transfer scheme)) is common. Exceptions reflect national structures, for example, France offers independent M1 and M2 stages of 60 ECTS each, while in the UK some programs are 90 ECTS/180 CATS over the same period. Curricula generally blend biological, computational, and quantitative content, often combining lectures, seminars, and practical work. Some follow a fixed curriculum with a set thesis track, while others offer flexible elective options.

Specialisation approaches vary widely. In some cases, systems biology is one of several interdisciplinary tracks; in others, it is embedded in more targeted domains such as cardiovascular systems, neurobiology, or synthetic biology. Project-based learning is common in some institutions, whereas others retain a traditional lecture-based format. Tuition fees show stark variation from no fees in Sweden and Finland to €800 in Luxembourg, up to £15,000 GBP (€17,500) in the UK for national students, and as high as £37,000 GBP (~€43,000) in the UK for international students. In fact, it appeared more common in European institutions to differentiate between national and international tuition, while North American and Caribbean universities generally have higher, but uniform rates.

Entry requirements typically include a Bachelor's in life sciences or a related field, alongside demonstrable experience in bioinformatics skills such as coding, statistical analysis, working with large datasets, data visualisation, or practices in reproducibility. A few

## Machine Learning-based Identification of Biomarkers in Clinical Cohort and Cancer Cell Line Data

Synopsis: Chapter 3 – Machine learning integration in systems biology education

programs request a minimum number of credits in mathematics, molecular biology, or computer programming, and occasionally a minimum Bachelor's grade (e.g.,  $\geq 70\%$  in Ottawa, Canada). English-language proficiency requirements usually range from CEFR B1 to C1. These findings highlight the structural diversity in program delivery and the lack of a unified framework for systems biology education worldwide. More details on each study line can be reviewed in appendix **A5**.

| Program name (degree)  | Credits (duration) | Program structure   | Specialization tracks   |
|--|--------------------|---|---|
| <i>University of Luxembourg (Esch-sur-Alzette, Luxembourg)</i> |                    |   |   |
| Molecular and Computational Biomedicine (MSc)                  | 120 ECTS (2 years) | <ul style="list-style-type: none"> <li>- Four semesters with around 15 weeks of full-time courses, plus additional time required for the exam preparation</li> <li>- The first semesters are course-based, mainly with block-courses of 2 weeks</li> <li>- The last 8 months individual research work is performed</li> <li>- The course content is around 1/3 lectures in biology and bio-medicine, 1/3 experimental and 1/3 computational practical</li> </ul> <p><a href="https://www.uni.lu/fstm-en/study-programs/master-in-molecular-and-computational-biomedicine">https://www.uni.lu/fstm-en/study-programs/master-in-molecular-and-computational-biomedicine</a></p>   | <ul style="list-style-type: none"> <li>- Systems Biology</li> <li>- Biomedicine</li> </ul>  |
| <i>Maastricht University (Maastricht, Netherlands)</i>         |                    |   |   |
| Systems Biology (MSc)  | 120 ECTS (2 years) | <ul style="list-style-type: none"> <li>- Year 1, periods 1 and 2: problem-based learning followed by compulsory courses, depending on background: biology and physiology or mathematics of biological systems</li> <li>- Mandatory courses: systems biology, modelling biosystems, experimental design and data management</li> <li>- Periods 3 and 6: project I and project II</li> <li>- Periods 4 and 5: elective choices among omics, cardiovascular systems biology, or dynamical systems and non-linear dynamics, fundamental and systems neuroscience, modelling metabolism, or machine learning and multivariate statistics</li> <li>- Year 2, period 1: two elective courses from computational neuroscience, network biology, scientific programming, or commercialization and entrepreneurship</li> <li>- Periods 2–6: Master's thesis</li> </ul> <p><a href="https://curriculum.maastrichtuniversity.nl/education/master/systems-biology">https://curriculum.maastrichtuniversity.nl/education/master/systems-biology</a></p> | <ul style="list-style-type: none"> <li>- Omics</li> <li>- Cardiovascular Systems Biology</li> <li>- Dynamical Systems &amp; Non-Linear Systems</li> <li>- Fundamental &amp; Systems Neuroscience</li> <li>- Modelling Metabolism</li> <li>- Machine Learning &amp; Multivariate Statistics</li> </ul> |
| <i>Ghent University (Ghent, Belgium)</i>                       |                    |   |   |
| Bioinformatics (MSc)   | 120 ECTS (2 years) | <ul style="list-style-type: none"> <li>- Common package (33 ECTS) of applied bioinformatics, including theoretical deepening and data analytical/problem-solving skills</li> <li>- Systems biology specialization module (28 ECTS)</li> <li>- Applied mathematics and informatics module (20 ECTS)</li> <li>- Optional courses (9 ECTS)</li> </ul> <p><a href="https://studiekiezer.ugent.be/2023/master-of-science-in-bioinformatics-systems-biology-en">https://studiekiezer.ugent.be/2023/master-of-science-in-bioinformatics-systems-biology-en</a></p>   | <ul style="list-style-type: none"> <li>- Systems Biology</li> <li>- Bioscience Engineering</li> <li>- Engineering</li> </ul>  |

Machine Learning-based Identification of Biomarkers in Clinical Cohort and Cancer Cell Line Data

Synopsis: Chapter 3 – Machine learning integration in systems biology education

| Program name (degree)   | Credits (duration)           | Program structure  | Specialization tracks  |
|---|------------------------------|--|--|
| <i>Université Paris-Saclay/Université d'Evry-Val-d'Essonne (Evry-Courcouronnes, France)</i> |                              |  |  |
| Systems and Synthetic Biology (M2 level) (MSc)  | 60 ECTS (1 year)             | <ul style="list-style-type: none"> <li>- Five core compulsory modules</li> <li>- Five selection modules (among 11)</li> <li>- Six-month research internship</li> </ul> <a href="https://www.mssb.fr">https://www.mssb.fr</a>   | <ul style="list-style-type: none"> <li>- Systems Biology</li> <li>- Synthetic Biology</li> </ul>   |
| <i>Technical University of Denmark (Copenhagen, Denmark)</i>                                |                              |  |  |
| Bioinformatics and Systems Biology (MSc)  | 120 ECTS (2 years)           | <ul style="list-style-type: none"> <li>- Polytechnical foundation courses (5 ECTS)</li> <li>- Program specific courses (55 ECTS, of which five in innovation courses, ten in mandatory courses, 40 in chosen program-specific courses)</li> </ul> <a href="https://www.dtu.dk/english/education/graduate/msc-programmes/bioinformatics-and-systems-biology">https://www.dtu.dk/english/education/graduate/msc-programmes/bioinformatics-and-systems-biology</a>  | <ul style="list-style-type: none"> <li>- Biomedical Bioinformatics</li> <li>- Infectious Disease Health Informatics</li> <li>- Bioinformatic Methods in Life Sciences</li> </ul> |
| <i>Imperial College London (South Kensington, UK)</i>                                       |                              |  |  |
| Bioinformatics and Theoretical Systems Biology (MSc)  | 90 ECTS or 180 CATS (1 year) | <ul style="list-style-type: none"> <li>- Composed of two core modules: bioinformatics and theoretical systems biology, and mathematics and computing</li> <li>- Computing project reinforcing programming skills through group project over 11 weeks</li> <li>- Bioinformatics and systems biology project applying course skills in research environment over 22 weeks</li> <li>- Lectures, computing labs, practical classes, presentations and seminars, group work</li> <li>- 30% projects; 70% examinations and coursework</li> <li>- Coursework, written exams, dissertation, computer and mathematics assignments</li> <li>- Individual research project, presentations, group report, and oral exam</li> </ul> <a href="https://www.imperial.ac.uk/study/courses/postgraduate-taught/bioinformatics">https://www.imperial.ac.uk/study/courses/postgraduate-taught/bioinformatics</a>                                   | No specialization tracks   |
| <i>Karolinska Institute (Stockholm, Sweden)</i>   |                              |  |  |
| Molecular Techniques in Life Science (MSc)  | 120 ECTS (2 years)           | <ul style="list-style-type: none"> <li>- First year advanced level courses in genetics and genomics, translational medicine, applied communication, and molecular life science methods, as well as the foundations of biostatistics, programming, bioinformatics, and comparative genomics</li> <li>- Second year mandatory courses in applied gene technology with bioinformatics analysis of large-scale data, and applied proteomics</li> <li>- The second half of the autumn semester offers three courses, of which the student should select two: systems biology, drug development, and a project course</li> <li>- During the spring semester, the individual degree project is performed</li> </ul> <a href="https://education.ki.se/programme/5mt23-masters-programme-in-molecular-techniques-in-life-science">https://education.ki.se/programme/5mt23-masters-programme-in-molecular-techniques-in-life-science</a> | <ul style="list-style-type: none"> <li>- Systems Biology</li> <li>- Drug Development</li> </ul>  |

| Program name (degree)  | Credits (duration)           | Program structure  | Specialization tracks  |
|--|------------------------------|--|--|
| <i>University of Turku (Turku, Finland)</i>  |                              |  |  |
| Molecular Systems Biology (MSc)  | 120 ECTS (2 years)           | <ul style="list-style-type: none"> <li>- Common courses</li> <li>- Track-specific major subject studies</li> <li>- Selectable studies</li> <li>- Master's thesis</li> </ul> <p><a href="https://www.utu.fi/en/study-at-utu/masters-degree-programme-in-biosciences-molecular-systems-biology">https://www.utu.fi/en/study-at-utu/masters-degree-programme-in-biosciences-molecular-systems-biology</a></p>   | <ul style="list-style-type: none"> <li>- Molecular Systems Biology</li> <li>- Evolutionary Biology</li> </ul>  |
| <i>University of Ottawa (Ottawa, Canada)</i>   |                              |  |  |
| Biology (MSc)  | 60 ECTS (1 year)             | <ul style="list-style-type: none"> <li>- Multiple lecture and seminar available (63 in total) giving each 3 units/credits</li> <li>- No clear structure requirement given</li> <li>- Possible course components: lecture, theory and laboratory, magistral courses, and seminars</li> </ul> <p><a href="https://catalogue.uottawa.ca/en/graduate/master-science-biology-specialization-bioinformatics">https://catalogue.uottawa.ca/en/graduate/master-science-biology-specialization-bioinformatics</a></p>   | <ul style="list-style-type: none"> <li>- Bioinformatics</li> </ul>   |
| <i>George Washington University School of Medicine and Health Sciences – Graduate School of Columbian College of Arts and Sciences (Washington, DC, USA)</i> |                              |  |  |
| Bioinformatics and Molecular Biochemistry (MSc)  | 30 credits (1–2 years)       | <ul style="list-style-type: none"> <li>- Thesis and non-thesis tracks</li> <li>- Eleven credits in required courses, 6 credits in required track, and 13 credits of electives (non-thesis option) or 6 credits in thesis and 7 credits of electives (thesis option)</li> <li>- Schedule flexibility, with 1-year or 2-year program option</li> <li>- Hands-on experience in a myriad of laboratories and research initiatives</li> <li>- Diverse elective course pool to choose from</li> </ul> <p><a href="https://bulletin.gwu.edu/arts-sciences/biochemistry-molecular-medicine/ms-bioinformatics-molecular-biochemistry">https://bulletin.gwu.edu/arts-sciences/biochemistry-molecular-medicine/ms-bioinformatics-molecular-biochemistry</a></p>   | <ul style="list-style-type: none"> <li>- Cancer Biology</li> <li>- Inflammation</li> <li>- Pathobiology</li> <li>- Computational Genomics</li> </ul>             |
| <i>University of Havana (Havana, Cuba)</i>   |                              |  |  |
| Biochemistry (MSc)   | 60 credits (3 years, hybrid) | <ul style="list-style-type: none"> <li>- Basic mandatory courses: biomolecules, enzymology, immunology, biochemical method, metabolic biochemistry, research work</li> <li>- Research work evaluation: two research seminars in 4th and 5th semesters (8 credits each), pre-defence act before scientific council for thesis endorsement and writing (8 credits), remaining credits awarded upon thesis defence (8 credits)</li> <li>- Credit accumulation: minimum of 60 total credits required, maximum 24 credits per course (18 mandatory, 6 optional), 32 credits for research work, minimum 4 credits for non-lecture activities</li> </ul> <p><a href="https://serviciosacademicos.fundacion.uh.cu/slides/maestria-en-bioquimica-91">https://serviciosacademicos.fundacion.uh.cu/slides/maestria-en-bioquimica-91</a></p> | <ul style="list-style-type: none"> <li>- Biochemistry and Systems Biology</li> <li>- Immunology</li> <li>- Biotechnology</li> <li>- Molecular Biology</li> </ul> |

**Table 6: Systems biology Master's in Europe, North America, and Caribbean.** Summary of the main characteristics in various European, north America, and Caribbean study lines that lead to a master's degree linked to systems biology. See appendix **A5** for a more detailed table. CATS: Credit Accumulation and Transfer Scheme; ECTS: European Credit Transfer and Accumulation System; M2: second year in the French Master's program system; MSc: Master of Science

***Students and alumni highlight strengths in training but gap in quantitative skills***

To complement the institutional overview, we gathered feedback from students enrolled in the University of Luxembourg's Master's in Integrated Systems Biology (MISB), now renamed to the Master's in Molecular and Computational Biomedicine (MMCB), and the International Master's in Biomedicine (IMBM). Both are two-year, 120 ECTS programs, sharing a common first semester of experimental and computational training including genomics, transcriptomics, proteomics, and R programming, alongside lectures in biology, biomedicine, and systems biology. The curriculum is organised into two-week thematic blocks, such as our project-based metabolic network modelling course [41], allowing intensive immersion in each topic and enabling laboratory practical training that require extended sessions. This structure also enables closer interaction with faculty and visiting researchers.

IMBM students complete their second and third semesters at partner universities in Strasbourg (France) and Mainz (Germany) to deepen their clinical and biomedical training, while MISB/MMCB students remain in Luxembourg to focus on systems biology, omics, and molecular medicine. Programming instruction for biology-trained students is scaffolded: exercises start with familiar biological questions and datasets, gradually introducing statistical and scripting concepts. Peer-assisted learning, interactive coding platforms, and integrated workshops link coding directly with biological data interpretation.

From 21 student questionnaires (**Fig. 16**), challenges reported were highly individual but often related to learning programming (particularly R) without a strong computational background, handling the inherent complexity of biological systems, and coping with the interdisciplinary scope. The abundance of available resources, combined with a dense first-semester schedule, sometimes led to a stressful start, a concern addressed by offering certain courses as optional and introducing two lecture-free weeks. Students especially valued traditional in-person lectures, computational exercises, project-based learning, and early access to course material, whereas group work and pre-recorded lectures received more mixed feedback, often due to uneven prior knowledge within groups.

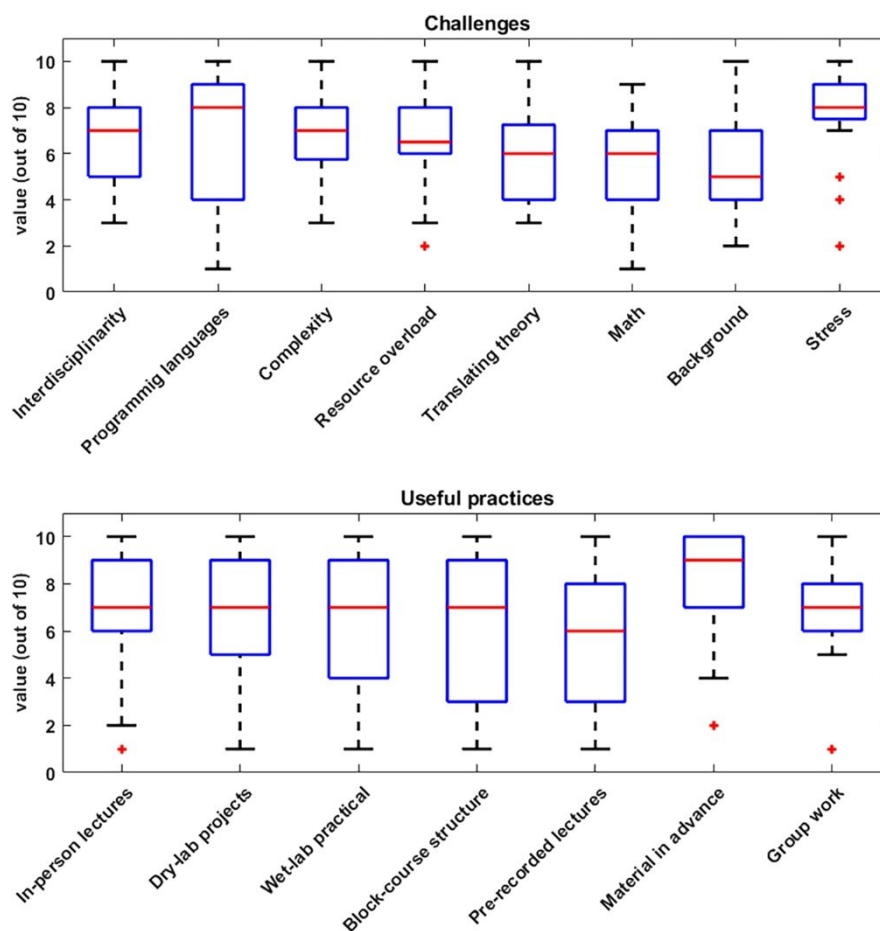
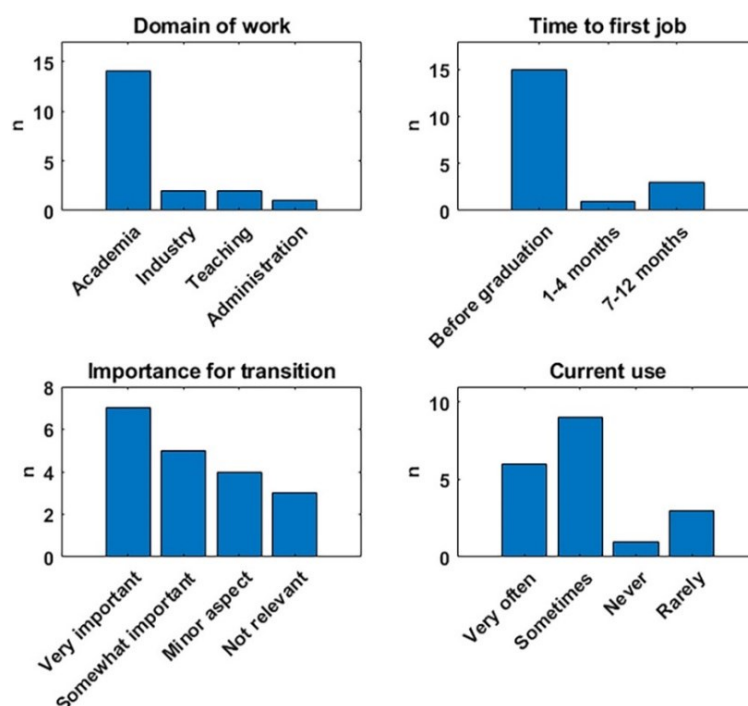


Figure 16: **Reflections from active students in the University of Luxembourg’s Master’s tracks in Integrated Systems Biology and International Biomedicine.** Questionnaires collected from students in early 2024 are summarized in this figure with questions listed in Supplementary Appendix A5.

Further insight came from a networking event titled ‘Struggles in Bioinformatics Education’ and organised by the ISCB-SC RSG Luxembourg (<https://www.uni.lu/life-en/social-life/student-associations-clubs/rsg/>). Topics ranged from UNIX navigation and programming languages (with Python favoured) to advanced concepts such as Singularity containers and R Markdown. Preferences leaned toward project-based learning but with concerns about workload and the scarcity of relevant programming courses at the Bachelor’s level. Students also noted a lack of master’s-level offerings in transferable skills like scientific practice, data visualisation in Python, and science communication.

Alumni responses (**Fig. 17**) showed most graduates in academic research, with others in industry, teaching, or administration. Many secured employments before graduation or within a year. Systems biology and bioinformatics training were widely regarded as critical for career transitions, with alumni reporting frequent or occasional use of computational

methods. Skills applied in the workplace spanned multi-omics analysis, image and clinical data processing, metabolic and protein network modelling, dynamical pharmacokinetic modelling, machine learning, and statistics, using R, Python, or MATLAB. Interestingly, some alumni apply R programming in school teaching, indirectly introducing systems biology concepts to younger students and colleagues. Alumni also highlighted the value of a broad methodological introduction, while noting areas needing deeper coverage, particularly programming, statistics, mathematics, and machine learning.



**Figure 17: Reflections of alumni from the Master's programmes in Integrated Systems Biology and Biomedicine at the University of Luxembourg.** This survey was addressed to alumni and with the following questions (top left to bottom right) about their current field, the time it took to ensure their first job, the perceived importance of study courses for career, and the current use of systems biology/bioinformatics in their current occupation.

### ***Machine learning still underrepresented despite clear demand***

Across the programs surveyed, the formal integration of machine learning into systems biology curricula remains limited. Where present, machine learning content is often confined to optional modules, short workshops, or single lectures, rather than embedded in core course sequences. This is more common at the graduate level than at the undergraduate level, but even in master's programs, sustained machine learning instruction is not universal. Several challenges were cited by educators, including the rapid pace of change in machine learning tools, a shortage of instructors with both biological and

computational expertise, and concerns about overloading students who are already adapting to interdisciplinary demands.

Student and alumni feedback echoes these concerns, with many reporting that their first significant exposure to machine learning occurred in research projects rather than formal coursework. As a result, self-directed learning is common, which risks uneven skill development. Alumni working in fields where machine learning is applied, such as omics-based classification, predictive modelling, and image analysis, emphasised the importance of earlier and more structured machine learning training.

In this context, targeted, applied machine learning training within existing systems biology courses can serve as a practical entry point. Our in-house metabolic network modelling course [42] (see appendix **A6**, and <https://github.com/sysbiolux/ISB705MetabolicNetworkModeling>) illustrates such an approach, introducing machine learning concepts through biologically relevant tasks. Students use Python-based workflows to build network models, estimate parameters, and perform predictive analyses, thereby learning computational methods in a domain-specific context. By embedding machine learning in a problem-driven framework, students can appreciate its utility without the abstraction that often alienates those from purely biological backgrounds.

The SV findings suggest that wider adoption of such integrated models could bridge current gaps. Rather than treating machine learning as an isolated computational discipline, positioning it as a natural extension of systems thinking may help foster the interdisciplinary fluency that modern research demands. This also aligns with alumni calls for deeper training in machine learning and related quantitative skills, reinforcing its relevance for both academic and industry careers.

### **- From student feedback to future directions in systems biology education**

Student feedback, whether provided directly or by representatives, offered complementary perspectives on program strengths and weaknesses. More sensitive or critical points often emerged through representatives rather than direct SV, highlighting their role as intermediaries who can collect honest input without students fearing negative repercussions on grades or evaluations. This difference emphasises the value of having multiple feedback channels, including informal peer-mediated routes.

From the combined student and alumni insights, and our own teaching experience, several recurring themes can be identified. Systems biology master's cohorts often bring together students from biology, biotechnology, pharmacy, engineering, and computer science backgrounds. This diversity enriches interdisciplinarity but also poses challenges in bringing all students to a shared baseline. Literature in systems biology education has long recognised this tension, stressing the need for depth in core topics alongside broad exposure to related fields [131]. Foundational bridging courses, such as math for biologists or molecular biology for engineers, could help address these gaps, although faculty expertise, teaching resources, and curriculum time are often limiting factors. Summer boot camps in mathematics, biology, or programming, already used in other interdisciplinary programs, could be a practical way to ensure standardised entry-level skills before formal coursework begins.

Technical infrastructure is another consideration. While many analyses can be performed on standard laptops, access to high-performance computing, reliable IT support, and appropriate software remains important. Public repositories containing exercises and teaching materials, such as our publicly available GitHub resource for metabolic modelling (<https://github.com/sysbiolux/ISB705MetabolicNetworkModeling>), reduce barriers and encourage collaborative curriculum development across institutions.

Our block-course format of two-week thematic modules allows deep immersion and close integration of theory and practice, but some students find the pace intense and prefer more time for review. As shown in the SV results (**Fig. 16**), programming, especially R, remains a common hurdle, amplified by the complexity of biological systems and the breadth of interdisciplinary skills required. Introducing lecture-free weeks and optional courses in the first semester has helped reduce the initial workload. Feedback from the ISCB-SC RSG Luxembourg networking event confirmed the value of project-based learning, while also pointing to persistent issues such as an overwhelming workload, limited prior exposure to programming at the bachelor's level, and the need for transferable skills training, including data visualisation and science communication, earlier in the curriculum. These observations align with broader calls for active learning strategies [41,144] and avoiding superficial coding practices that rely on pre-filled scripts.

True interdisciplinarity in systems biology requires more than adding biological examples to quantitative problems. Students benefit most when they generate their own data, analyse it computationally, and interpret the results within the context of current literature. The development of systems medicine illustrates how far this integration has progressed, with graduate-level programs at institutions such as the Institute for Systems Biology and

Georgetown University linking systems-level analysis directly to patient care. In Europe, governmental and EU-level funding has supported the development of interdisciplinary graduate schools and infrastructure, though the extent of support varies between countries.

Assessment remains another area of challenge. Single final grades often fail to capture uneven progress across disciplines. A more constructive approach combines multiple formats, including rubrics that separately evaluate coding, mathematics, biological reasoning, and communication; peer evaluations; and portfolios documenting project work. Our programs now blend these with classical exams and quizzes to provide a fuller picture of student performance.

Educational system differences between countries add complexity when considering standardisation. US undergraduates often receive broader, more flexible training, while European systems tend to specialise earlier. Nevertheless, a shared framework focused on key competencies and learning outcomes could offer consistency while allowing institutions to adapt content locally.

While alumni report using a wide range of computational tools (**Fig. 17**), including machine learning, program analysis (**Tab. 6**) and course SV show that machine learning remains underrepresented in many systems biology curricula. This is despite its growing role in omics analysis, network modelling, and predictive biology. The gap partly reflects the pace of machine learning development and the difficulty of teaching coding and machine learning concepts simultaneously to students still building foundational programming skills. In our own teaching, we integrate approachable machine learning examples within familiar biological contexts, as in our metabolic network modelling course [42], where scaffolded exercises guide students from simple simulation problems to more complex applications. This approach helps demystify machine learning and illustrates its relevance to biological research.

The seemingly exponential growth of AI-driven coding tools such as GitHub Copilot and ChatGPT adds another layer of complexity. These tools can speed up learning and debugging but risk fostering overreliance. Responsible integration will require guidelines, an emphasis on understanding outputs, and potentially dedicated modules on AI in computational biology. Alumni who have taken R coding into high-school classrooms show that early exposure to computational biology could smooth the later transition into advanced programs.

Finally, bridging the gap between academia and industry remains an important consideration. Industrial environments often rely on proprietary tools and workflows,

requiring graduates to adapt quickly. Greater collaboration, for example through joint teaching modules, industry-led workshops, or co-supervised thesis projects, could help prepare students for this shift.

Overall, the results from this chapter indicate that while systems biology education is already producing graduates who transition successfully into research and industry roles, challenges remain in balancing depth and breadth, integrating machine learning more fully, assessing interdisciplinary skills, and supporting student well-being alongside technical mastery. By refining curricula, expanding early computational exposure, and fostering a mindset of lifelong learning, programs can better prepare students for the evolving demands at the intersection of systems biology and machine learning.

## Conclusions and perspectives

### ***Linking sex-specific pre-frailty, circadian oncology, and educational practice***

#### **- Sex-specific profiling improves pre-frailty prediction and understanding**

Across BASE-II, frailty looked similar in prevalence for men and women, yet the composition of the frailty phenotype strongly differed. Four of the five *Fried et al.* items diverged by sex: reduced PA and slower GA were more common in men, whereas EX and lower GS were more common in women (**Fig. 7C-D**) despite similar overall scores (**Fig. 7A-B**). These contrasts at the phenotype level were supported by the clear separation of sex in the underlying biomedical features (PCA in **Fig. 7E**), which suggested that a mixed-sex model would likely blur such sex-specific signals.

Sex-specific models trained on the complete feature space (men-ALL, women-ALL) outperformed the mixed-sex model, and, when we moved from the ALL-feature set to specific clinical subgroups, model performances further increased, most notably for men using physical measurements (men-PM), and for women using body fluid markers (women-BF) (**Fig. 8A-B**). As such, model performance reflected the differing contexts of physical pre-frailty men and women. In men, lean mass and skeletal health features (e.g., ALM-BMI ratio, trunk fat, BMD/BMC) dominated (**Fig. 8D; Tab. 5A**), which is consistent with a body composition driven profile of physical frailty development. In women, the best signal came from physiological and biochemical anomalies (e.g., vitamin D deficiency, eosinophils and monocytes, insulin and glucose, oestradiol) (**Fig. 8D; Tab. 5B**) [13,15,20–22,74–83]. Individually, these markers were not uniformly strong, and we resisted over-interpreting single coefficients. Rather, combinations of a few top features produced much clearer separation (MANOVA;  $1 - \text{Wilks' lambda}$  rises with added features; **Fig. 10A-B**), which aligns with the accumulation of deficits views of frailty [48,84].

There were several limitations to this study, for example the cross-sectional design of the available BASE-II cohort data. Moreover, low numbers in the frail class forced us to combine pre-frail and frail as one group, given that imputation plus imbalance handling, although carefully done (F- $\beta$ -2 emphasis, resampling, CV), can still skew performance.

However, as the merged category is dominated by pre-frail participants, the present results reflect biomarkers of pre-frailty, not frailty. Pre-frail and frail are distinct clinical stages, and future studies with larger frail cohorts will be required to extend these findings to fully developed frailty. We also acknowledge a feature source mismatch (*Fried et al.* outcome vs many *Rockwood*-aligned predictors), which could bias feature ranking. Still, several *post-hoc* analysis showed that the models are on the right track. First, sensitivity rose with the severity of the frailty phenotype when predictions were stratified into the initial non-frail, pre-frail, and frail (**Fig. 9**). Second, we validated that feature effects aggregated meaningfully, rather than hinging on single variables (**Fig. 10**). Third, we recorded convergence in a few consistent hallmark features across settings (*e.g.*, heart insufficiency in both sexes [79,80]), which further adds validity. Methodologically, the pipeline choices (resampling before transformation, linear SVM for interpretability,  $\chi^2$  and variance filtering, and cross-validated permutation importance) are defensible for clinical cohort biomarker discovery (**Fig. 1**).

Taken together, this chapter's dissertation is simple but consequential. Sex-specific modelling captures distinct physiological pathways to frailty that blurred the mixed-sex model performances. Practically, men may benefit from earlier screening for sarcopenia, lean-mass loss, and bone health, and women from screening for vitamin D deficiency, immune dysregulation, and metabolic or hormonal anomalies. These aren't prescriptions so much as pointers. The signal appears real, but prospective validation and harmonised longitudinal designs are needed to see which feature sets truly anticipate the transition from the pre-frail to the frail state [13,15,20–22,48,74–84].

#### - **Circadian phenotyping exposes functional diversity in breast cancer models**

The second chapter focuses on whether circadian biology is present and structured enough in cancer cell models to assess therapy sensitivity. Contrary to the common assumption that advanced tumours lack coherent oscillators, we observed a spectrum of clock phenotypes across non-malignant, luminal, and TNBC lines. Using multiresolution analysis (MRA) and auto-correlation (AC) metrics including BMAL1-PER2 phase relationships, PCA retained >75% of variance in 3 components, and k-means ( $k = 4$  by elbow; silhouette score 0.45) separated models into functional, unstable, weak, and dysfunctional phenotypes (**Fig. 14**). These circadian phenotypes did not recapitulate molecular subtypes one-to-one, instead, they appeared to cut across them, with distinct amplitude, stability patterns and

## Conclusions and perspectives

mutation burdens (cell lines with unstable and weak circadian strength showed higher mutation burdens in core clock and clock related genes, while dysfunctional had fewer mutations, hinting at non-genetic factors) [96,103,104,111–113].

From there, we linked clock features to TOD response. Two complementary ideas helped, namely the collaborator-introduced chronotherapeutic index (how much a drug's efficacy varies by dosing time) and our chronosensitivity index (how well circadian state parameters or gene expression classifies high vs low drug sensitivity), both embedded in a high-throughput deep phenotyping and data-integration pipeline (**Figs. 3-5**). DDR agents, such as cisplatin, tended to associate with rhythmicity and amplitude metrics such as stronger clocks, but also stronger cytotoxicity (**Fig. 15A**), which is in line with clock control of DNA repair and cell cycle [95,98,99,107]. However, paclitaxel for example looked different. Gene-level signals (*e.g.*, PER3, DBP) showed the clearest associations with TOD maximal response (**Fig. 13B-D**), consistent with clock-mitosis coupling [96,106]. For a subset (Torin2, adavosertib, cisplatin), LOOCV was perfect (**Fig. 13G**). For others (alisertib, 5-FU), it was not, which underlines context-dependence and suggests a natural ceiling on static predictors. And yet, the index did what we needed. It revealed drug-model pairs where circadian features are likely to matter, and it offered a compact way to compare separation strength across drugs and feature types (circadian parameters vs gene expression), with some divergences (*e.g.*, topotecan's poor parameter-based separation improved with gene expression) (**Figs. 12-15**) [97,108,114–117].

Control analyses confirmed that the pre-processing of drug sensitivity values did not introduce artifacts (**Fig. 13F**). We also noted biological factors that our pipeline did not yet capture, for example drug-induced clock changes that may alter next-cycle efficacy [121], ultradian (~12 h) components detectable in oscillations that could interact with dosing patterns [122], and missing host-level coupling (hormonal and immune effects) that in vivo can reshape both clock state and drug response [123]. Those gaps are both opportunities and limitations. They invite for richer experimental designs (pre- and post-drug time series at single-cell resolution), and for translational layers such as chrono-toxicities in healthy tissue vs therapeutic windows in tumours by co-phenotyping malignant and non-malignant contexts. Methodologically, the framework is extensible (we have already ported it to NB in follow-up analyses), and the results are very insightful. As the circadian profiling gives an orthogonal axis to stratify models beyond classical markers, the two chrono-based indices offer a practical means for comparing how much timing matters across settings [88–92,95–99,103–109,111–117,121–123].

- **Evolving systems biology education to integrate machine learning meaningfully**

The third chapter treated education as a systems problem. Diverse cohorts, uneven baselines, compressed timelines, and curricula must keep pace with fast-moving methods. Student and alumni feedback converged on a predictable set of obstacles, for example programming (especially R and python) as a bottleneck early on, block formats that some find intense, and assessment that doesn't always reflect the uneven progress across domains. Several remedies appear to help, such as preparatory bridging (for example boot camps before the first term), and publicly available repositories for exercises and projects. Other institutions already partially implemented project-based modules where students generate data and then analyse and interpret it, and multi-component assessment that separates coding, math, biological reasoning, and communication (rather than a single catch-all grade). These are consistent with broader calls for active learning and educational research [41,141–144].

In the context of machine learning for example, it is present in many programs but remains underrepresented relative to its impact in omics, network modelling, and predictive biology, often because it is introduced before students are comfortable with the programming substrate (**Tab. 6**). A pragmatic path we tested is to embed approachable machine learning use-cases in courses students already take (e.g., metabolic network modelling), moving from transparent baselines to slightly more complex models and algorithms while insisting on explanation and uncertainty. The alumni reports further suggest graduates can adapt to diverse academic and industry toolchains, but the slope is gentler when exposure to machine learning comes early and is threaded through real biological problems. This chapter's point is not a grand theory, rather it's a handful of concrete patterns that, when implemented, appear to make the next generation of systems biology students' climb a bit less steep [40–42,130–144].

***From signals to stratification: next steps in cohorts, cell models, and classrooms***

Building on the BASE-II findings presented in chapter 1, the immediate next step is to move from cross-sectional signal to longitudinal prediction and external validation. We have already re-designed the pipeline for the Luxembourg PD cohort (NCER-PD) with CV-aware

## Conclusions and perspectives

feature pooling (univariate, wrapper, embedded) and exhaustive subset selection before final validation (**Fig. 2**). This setup reduces selection bias and information leakage, and lets us ask a sharper question: which combinations of 2 to 10 features (different by sex, and potentially by PD status) consistently anticipate transition to pre-frail or frail? Alongside blood and clinical markers, we will add GA and wearable-derived mobility features that may complement biochemical and hormonal markers, especially in women where metabolic features were dominant and in men more affected by postural instability or GA impairment [34,85–87,145,146].

For chapter 2, two priorities emerge. First, extend circadian phenotyping into designs that can separate cell-intrinsic clock effects from drug-induced clock resetting. That means time-series before and after dosing, ideally at single-cell resolution, using methods that quantify both oscillation quality and growth behaviour [121–123]. Second, bridge the in vitro-translation gap with patient-level timing data. There is now accumulating evidence that TOD can shape outcomes for certain therapies, including immune checkpoint inhibitors (ICI), where better survival rate was observed when the first ICI dose was given in the early morning [147,148]. Reviews also point to plausible mechanisms and emerging clinical signals for chrono-immunotherapy [149,150]. These new references should be read alongside the classic chrono-chemotherapy literature [110,114–117] and our own TOD and chronosensitivity results, because they collectively argue for a pragmatic translational path based on quantifying a tumour's circadian state (parameters and gene expression), a person's circadian phase (wearables), and then test timing windows for agents that our index already identified as likely time-sensitive.

A second translational opportunity sits in paediatric oncology. Our NB follow-up (see appendix **A4**) uses the same 16-gene clock gene panel plus NB-specific genes to classify drug sensitivity and assess chronosensitivity in a biologically different system. There are also disease-specific mechanistic hints worth exploring, for example, genomic changes that use circadian mechanisms to drive oncogenesis or metastasis. A recent study for example showed that chromosomal breakage during telomere crisis can be temporally gated by the circadian clock [151–153]. While not NB-specific, it illustrates the kind of clock-genome interactions that might explain why certain DDR agents become time-dependent in particular paediatric tumours. The near-term deliverable, though, is straightforward: replicate the two indices (chronotherapeutic and chronosensitivity) in NB cell lines and patient-derived models, quantify when parameter- vs gene-based classification diverges, and pre-register a small, timing-aware experimental setup for one agent in an appropriate setting. This could for example include timing the delivery of irinotecan (a topoisomerase I

inhibitor with known chronotherapeutic effects) under controlled light-dark cycles in NB organoids that are amplified in the oncogene MYCN.

The curriculum thread exposed in chapter 3 now ties back into the science. The same pipelines we use for BASE-II/NCER-PD and circadian drug screens are teachable, such as CV-aware preprocessing, transparent linear models first, feature importance techniques, and tight coupling to domain questions. Three concrete steps feel worth institutionalising: (i) introduce bridge-weeks with structured programming and math refreshers; (ii) a required first-term module that embeds machine learning inside a biological modelling course (e.g., constraint-based or ordinary differential equation models) so that coding and inference are applied immediately; and (iii) multi-component grade assessment that separately score code, inference, biological interpretation, and communication. These steps are modest, affordable, and in line with calls for active and research-driven learning [41,141–144].

Two kinds of uncertainty will remain even after the proposed follow-ups. First, cohort-level machine learning risks entangling biology with measurement practice. Some sex differences almost certainly reflect tooling and questionnaire bias, e.g., self-reported EX vs instrumented gait, the PD study is our chance to triangulate with sensors and harmonised labels. Second, circadian-timing signals will vary by mechanism, half-life, and schedule. Our indices help prioritise but do not replace mechanistic work, and any clinical use must be sensitive to practicalities (nurse shift patterns, infusion logistics) and equity (who can realistically wear devices, how phase is inferred, etc.). Encouragingly, these constraints are tractable design problems rather than blockers.

If, two years from now, we can show that (i) small, interpretable feature sets stratify sex-specific frailty risk in NCER-PD and generalise out-of-sample; (ii) chronosensitivity and circadian-based subtyping in NB replicates and points to one or two timing-aware and mechanism-consistent drug hypotheses; (iii) and that the implementation of a first-term ‘machine learning inside biology’ module measurably reduces the programming bottleneck reported by current students, then this dissertation won’t just have argued for the integration of biology and machine learning, it will have operationalised it.

## References

1. Baltés PB, Mayer KU, editors. The Berlin Aging Study: Aging from 70 to 100 [Internet]. Cambridge: Cambridge University Press; 1998 [cited 2023 Sep 21]. Available from: <https://www.cambridge.org/core/books/berlin-aging-study/B1641E71F86F59A1A20BBE8824CB2EE5>
2. Bertram L, Böckenhoff A, Demuth I, Düzel S, Eckardt R, Li SC, et al. Cohort Profile: The Berlin Aging Study II (BASE-II). *Int J Epidemiol*. 2014 Jun 1;43(3):703–12.
3. Demuth I, Banszerus V, Drewelies J, Düzel S, Seeland U, Spira D, et al. Cohort profile: follow-up of a Berlin Aging Study II (BASE-II) subsample as part of the GendAge study. *BMJ Open*. 2021 Jun 1;11(6):e045576.
4. Fried LP, Tangen CM, Walston J, Newman AB, Hirsch C, Gottdiener J, et al. Frailty in Older Adults: Evidence for a Phenotype. *J Gerontol Ser A*. 2001 Mar 1;56(3):M146–57.
5. Spira D, Buchmann N, Nikolov J, Demuth I, Steinhagen-Thiessen E, Eckardt R, et al. Association of Low Lean Mass With Frailty and Physical Performance: A Comparison Between Two Operational Definitions of Sarcopenia—Data From the Berlin Aging Study II (BASE-II). *J Gerontol Ser A*. 2015 Jun 1;70(6):779–84.
6. Lally F, Crome P. Understanding frailty. *Postgrad Med J*. 2007 Jan 1;83(975):16–20.
7. Clegg A, Young J, Iliffe S, Rikkert MO, Rockwood K. Frailty in elderly people. *The Lancet*. 2013 Mar 2;381(9868):752–62.
8. Fulop T, Larbi A, Witkowski JM, McElhaney J, Loeb M, Mitnitski A, et al. Aging, frailty and age-related diseases. *Biogerontology*. 2010 Oct 1;11(5):547–63.
9. Rockwood K, Fox RA, Stolee P, Robertson D, Beattie BL. Frailty in elderly people: an evolving concept. *CMAJ Can Med Assoc J*. 1994 Feb 15;150(4):489–95.
10. Abizanda P, Romero L, Sánchez-Jurado PM, Ruano TF, Ríos SS, Sánchez MF. Energetics of Aging and Frailty: The FRADEA Study. *J Gerontol Ser A*. 2016 Jun 1;71(6):787–96.

References

11. Holliday R. Understanding Ageing [Internet]. Cambridge: Cambridge University Press; 1995 [cited 2023 Sep 21]. (Developmental and Cell Biology Series). Available from: <https://www.cambridge.org/core/books/understanding-ageing/7C795DA1F52124A30E0F6A6278A4C8E8>
12. Fedarko NS. The Biology of Aging and Frailty. *Clin Geriatr Med*. 2011 Feb 1;27(1):27–37.
13. Fhon JRS, Rodrigues RAP, Santos JLF, Diniz MA, dos Santos EB, Almeida VC, et al. Factors associated with frailty in older adults: a longitudinal study. *Rev Saúde Pública*. 2018 Jul 13;52:74.
14. Amballa A. Feature Engineering Part-1 Mean/ Median Imputation. [Internet]. Analytics Vidhya. 2020 [cited 2023 Sep 21]. Available from: <https://medium.com/analytics-vidhya/feature-engineering-part-1-mean-median-imputation-761043b95379>
15. Gutiérrez-Valencia M, Izquierdo M, Cesari M, Casas-Herrero Á, Inzitari M, Martínez-Velilla N. The relationship between frailty and polypharmacy in older people: A systematic review. *Br J Clin Pharmacol*. 2018;84(7):1432–44.
16. Nwadiugwu MC. Frailty and the Risk of Polypharmacy in the Older Person: Enabling and Preventative Approaches. *J Aging Res*. 2020 Jun 29;2020:e6759521.
17. König M, Spira D, Demuth I, Steinhagen-Thiessen E, Norman K. Polypharmacy as a Risk Factor for Clinically Relevant Sarcopenia: Results From the Berlin Aging Study II. *J Gerontol Ser A*. 2018 Jan 1;73(1):117–22.
18. Tomita MR, Mann WC, Fraas LF, Stanton KM. Predictors of the Use of Assistive Devices that Address Physical Impairments Among Community-Based Frail Elders. *J Appl Gerontol*. 2004 Jun 1;23(2):141–55.
19. Morley JE, Vellas B, van Kan GA, Anker SD, Bauer JM, Bernabei R, et al. Frailty Consensus: A Call to Action. *J Am Med Dir Assoc*. 2013 Jun;14(6):392–7.
20. Shardell M, Hicks GE, Miller RR, Kritchevsky S, Andersen D, Bandinelli S, et al. Association of Low Vitamin D Levels With the Frailty Syndrome in Men and Women. *J Gerontol Ser A*. 2009 Jan 1;64A(1):69–75.

References

21. Zhou J, Huang P, Liu P, Hao Q, Chen S, Dong B, et al. Association of vitamin D deficiency and frailty: A systematic review and meta-analysis. *Maturitas*. 2016 Dec 1;94:70–6.
22. Spira D, Buchmann N, König M, Rosada A, Steinhagen-Thiessen E, Demuth I, et al. Sex-specific differences in the association of vitamin D with low lean mass and frailty: Results from the Berlin Aging Study II. *Nutrition*. 2019 Jun 1;62:1–6.
23. Ross AC, Manson JE, Abrams SA, Aloia JF, Brannon PM, Clinton SK, et al. The 2011 Report on Dietary Reference Intakes for Calcium and Vitamin D from the Institute of Medicine: What Clinicians Need to Know. *J Clin Endocrinol Metab*. 2011 Jan 1;96(1):53–8.
24. WELCH BL. THE GENERALIZATION OF 'STUDENT'S' PROBLEM WHEN SEVERAL DIFFERENT POPULATION VARLANCES ARE INVOLVED. *Biometrika*. 1947 Jan 1;34(1–2):28–35.
25. Cramér H. *Mathematical Methods of Statistics*. Princeton University Press; 1946. 598 p.
26. Bergsma W. A bias-correction for Cramér's V and Tschuprow's T. *J Korean Stat Soc*. 2013 Sep 1;42(3):323–8.
27. Varrette S, Cartiaux H, Peter S, Kieffer E, Valette T, Olloh A. Management of an Academic HPC & Research Computing Facility: The ULHPC Experience 2.0. In: *Proceedings of the 2022 6th High Performance Computing and Cluster Technologies Conference [Internet]*. New York, NY, USA: Association for Computing Machinery; 2022 [cited 2023 Oct 27]. p. 14–24. (HPCCT '22). Available from: <https://doi.org/10.1145/3560442.3560445>
28. Chawla NV, Bowyer KW, Hall LO, Kegelmeyer WP. SMOTE: synthetic minority over-sampling technique. *J Artif Int Res*. 2002 Jun 1;16(1):321–57.
29. Zhang C, Bi J, Soda P. Feature selection and resampling in class imbalance learning: Which comes first? An empirical study in the biological domain. In: *2017 IEEE International Conference on Bioinformatics and Biomedicine (BIBM) [Internet]*. 2017 [cited 2023 Oct 27]. p. 933–8. Available from: <https://ieeexplore.ieee.org/abstract/document/8217782>

References

30. Boser BE, Guyon IM, Vapnik VN. A training algorithm for optimal margin classifiers. In: Proceedings of the fifth annual workshop on Computational learning theory [Internet]. New York, NY, USA: Association for Computing Machinery; 1992 [cited 2023 Oct 31]. p. 144–52. (COLT '92). Available from: <https://dl.acm.org/doi/10.1145/130385.130401>
31. Rouzbahani AK, Khalili-Tanha G, Rajabloo Y, Khojasteh-Leylakoochi F, Garjan HS, Nazari E, et al. Machine learning algorithms and biomarkers identification for pancreatic cancer diagnosis using multi-omics data integration. *Pathol - Res Pract*. 2024 Nov 1;263:155602.
32. Sahoo B, Pinnix Z, Sims S, Zelikovsky A. Identifying Biomarkers Using Support Vector Machine to Understand the Racial Disparity in Triple-Negative Breast Cancer. *J Comput Biol*. 2023 Apr;30(4):502–17.
33. Beam AL, Motsinger-Reif AA, Doyle J. An investigation of gene-gene interactions in dose-response studies with Bayesian nonparametrics. *BioData Min*. 2015 Feb 6;8(1):6.
34. Hipp G, Vaillant M, Diederich NJ, Roomp K, Satagopam VP, Banda P, et al. The Luxembourg Parkinson's Study: A Comprehensive Approach for Stratification and Early Diagnosis. *Front Aging Neurosci*. 2018 Oct 29;10:326.
35. Ector C, Schmal C, Didier J, De Landtsheer S, Finger AM, Müller-Marquardt F, et al. Time-of-day effects of cancer drugs revealed by high-throughput deep phenotyping. *Nat Commun*. 2024 Aug 22;15(1):7205.
36. Ector C, Didier J, De Landtsheer S, Nordentoft MS, Schmal C, Keilholz U, et al. Circadian clock features define novel subtypes among breast cancer cells and shape drug sensitivity. *Mol Syst Biol*. 2025 Apr 2;21(4):315–40.
37. Ector C, Schmal C, Didier J, Landtsheer SD, Schulte JH, Keilholz U, et al. Circadian rhythm heterogeneity modulates drug response variations in neuroblastoma models. *Cell Rep* [Internet]. 2026 Feb 24 [cited 2026 Feb 12];45(2). Available from: [https://www.cell.com/cell-reports/abstract/S2211-1247\(26\)00053-7](https://www.cell.com/cell-reports/abstract/S2211-1247(26)00053-7)
38. Barretina J, Caponigro G, Stransky N, Venkatesan K, Margolin AA, Kim S, et al. The Cancer Cell Line Encyclopedia enables predictive modelling of anticancer drug sensitivity. *Nature*. 2012 Mar;483(7391):603–7.

References

39. Armstrong RA. When to use the Bonferroni correction. *Ophthalmic Physiol Opt J Br Coll Ophthalmic Opt Optom*. 2014 Sep;34(5):502–8.
40. Didier J, Croce S, Bayoumi S, Valceschini E, Escoffier H, Gonzalez E, et al. Challenges and opportunities in systems biology education. *Endocr Relat Cancer* [Internet]. 2025 Jun 1 [cited 2025 Jul 31];32(6). Available from: <https://erc.bioscientifica.com/view/journals/erc/32/6/ERC-25-0024.xml>
41. Sauter T, Bintener T, Kishk A, Presta L, Prohaska T, Guignard D, et al. Project-based learning course on metabolic network modelling in computational systems biology. Palagi PM, editor. *PLOS Comput Biol*. 2022 Jan 27;18(1):e1009711.
42. Bintener T, Pacheco MP, Kishk A, Didier J, Sauter T. Drug Target Prediction Using Context-Specific Metabolic Models Reconstructed from rFASTCORMICS. In: Baiocchi M, editor. *Cancer Drug Resistance: Methods and Protocols* [Internet]. New York, NY: Springer US; 2022 [cited 2025 Jul 31]. p. 221–40. Available from: [https://doi.org/10.1007/978-1-0716-2513-2\\_17](https://doi.org/10.1007/978-1-0716-2513-2_17)
43. Collard RM, Boter H, Schoevers RA, Oude Voshaar RC. Prevalence of Frailty in Community-Dwelling Older Persons: A Systematic Review. *J Am Geriatr Soc*. 2012;60(8):1487–92.
44. Ofori-Asenso R, Chin KL, Mazidi M, Zomer E, Ilomaki J, Zullo AR, et al. Global Incidence of Frailty and Prefrailty Among Community-Dwelling Older Adults: A Systematic Review and Meta-analysis. *JAMA Netw Open*. 2019 Aug 2;2(8):e198398.
45. Abreu W, Tolson D, Jackson GA, Staines H, Costa N. The relationship between frailty, functional dependence, and healthcare needs among community-dwelling people with moderate to severe dementia. *Health Soc Care Community*. 2019;27(3):642–53.
46. Chen X, Mao G, Leng SX. Frailty syndrome: an overview. *Clin Interv Aging*. 2014 Mar 19;9:433–41.
47. Xue QL. The Frailty Syndrome: Definition and Natural History. *Clin Geriatr Med*. 2011 Feb 1;27(1):1–15.
48. Rockwood K, Mitnitski A. Frailty in Relation to the Accumulation of Deficits. *J Gerontol Ser A*. 2007 Jul 1;62(7):722–7.

References

49. Fried LP, Cohen AA, Xue QL, Walston J, Bandeen-Roche K, Varadhan R. The physical frailty syndrome as a transition from homeostatic symphony to cacophony. *Nat Aging*. 2021 Jan;1(1):36–46.
50. Liu LK, Guo CY, Lee WJ, Chen LY, Hwang AC, Lin MH, et al. Subtypes of physical frailty: Latent class analysis and associations with clinical characteristics and outcomes. *Sci Rep*. 2017 Apr 11;7(1):46417.
51. Idris S, Badruddin N. Classification of Cognitive Frailty in Elderly People from Blood Samples using Machine Learning. In: 2021 IEEE EMBS International Conference on Biomedical and Health Informatics (BHI). 2021. p. 1–4.
52. Panza F, Seripa D, Solfrizzi V, Tortelli R, Greco A, Pilotto A, et al. Targeting Cognitive Frailty: Clinical and Neurobiological Roadmap for a Single Complex Phenotype. *J Alzheimers Dis*. 2015 Jan 1;47(4):793–813.
53. Di Sabatino A, Lenti MV, Cammalleri L, Corazza GR, Pilotto A. Frailty and the gut. *Dig Liver Dis*. 2018 Jun 1;50(6):533–41.
54. Wang CW, Lebsack A, Chau S, Lai JC. The Range and Reproducibility of the Liver Frailty Index. *Liver Transpl*. 2019;25(6):841–7.
55. Dibello V, Zupo R, Sardone R, Lozupone M, Castellana F, Dibello A, et al. Oral frailty and its determinants in older age: a systematic review. *Lancet Healthy Longev*. 2021 Aug 1;2(8):e507–20.
56. Buchmann N, Spira D, König M, Demuth I, Steinhagen-Thiessen E. Frailty and the Metabolic Syndrome — Results of the Berlin Aging Study II (BASE-II). *J Frailty Aging*. 2019 Oct 1;8(4):169–75.
57. Laur CV, McNicholl T, Valaitis R, Keller HH. Malnutrition or frailty? Overlap and evidence gaps in the diagnosis and treatment of frailty and malnutrition. *Appl Physiol Nutr Metab*. 2017 May;42(5):449–58.
58. Vaz Fragoso CA, Enright PL, McAvay G, Van Ness PH, Gill TM. FRAILTY AND RESPIRATORY IMPAIRMENT IN OLDER PERSONS. *Am J Med*. 2012 Jan;125(1):79–86.
59. Patel HP, Clift E, Lewis L, Cooper C, Patel HP, Clift E, et al. Epidemiology of Sarcopenia and Frailty. In: *Frailty and Sarcopenia - Onset, Development and Clinical Challenges*

References

- [Internet]. IntechOpen; 2017 [cited 2023 Nov 7]. Available from: <https://www.intechopen.com/chapters/56116>
60. Espinoza SE, Quiben M, Hazuda HP. Distinguishing Comorbidity, Disability, and Frailty. *Curr Geriatr Rep*. 2018 Dec 1;7(4):201–9.
61. Puts MTE, Visser M, Twisk JWR, Deeg DJH, Lips P. Endocrine and inflammatory markers as predictors of frailty. *Clin Endocrinol (Oxf)*. 2005;63(4):403–11.
62. Linn N, Goetzinger C, Regnaud JP, Schmitz S, Dessenne C, Fagherazzi G, et al. Digital Health Interventions among People Living with Frailty: A Scoping Review. *J Am Med Dir Assoc*. 2021 Sep 1;22(9):1802-1812.e21.
63. O’Caoimh R, Sezgin D, O’Donovan MR, Molloy DW, Clegg A, Rockwood K, et al. Prevalence of frailty in 62 countries across the world: a systematic review and meta-analysis of population-level studies. *Age Ageing*. 2021 Jan 1;50(1):96–104.
64. Howlett SE, Rutenberg AD, Rockwood K. The degree of frailty as a translational measure of health in aging. *Nat Aging*. 2021 Aug;1(8):651–65.
65. Murad MH, Elamin KB, Abu Elnour NO, Elamin MB, Alkatib AA, Fatourechi MM, et al. The Effect of Vitamin D on Falls: A Systematic Review and Meta-Analysis. *J Clin Endocrinol Metab*. 2011 Oct 1;96(10):2997–3006.
66. Strain WD, Down S, Brown P, Puttanna A, Sinclair A. Diabetes and Frailty: An Expert Consensus Statement on the Management of Older Adults with Type 2 Diabetes. *Diabetes Ther*. 2021 May 1;12(5):1227–47.
67. Toepfer S, König M, Spira D, Drewelies J, Kreutz R, Bolbrinker J, et al. Sex Differences in Characteristics Associated with Potentially Inappropriate Medication Use and Associations with Functional Capacity in Older Participants of the Berlin Aging Study II. *Gerontology*. 2021 Sep 17;68(6):664–72.
68. Koenig M, Malsch C, Marino J, Vetter VM, Komleva Y, Demuth I, et al. Nocturia as a Risk Factor for Developing Frailty in Older Adults: Results of the Berlin Aging Study II [Internet]. medRxiv; 2024 [cited 2024 Sep 24]. p. 2024.09.20.24313292. Available from: <https://www.medrxiv.org/content/10.1101/2024.09.20.24313292v1>

References

69. Didier J, De Landtsheer S, Pacheco MP, Kishk A, Schneider JG, Goldeck D, et al. Clinical data-driven classification of pre-frailty reveals sex-specific patterns – Data from the Berlin Aging Study II (BASE-II). *Mech Ageing Dev.* 2025 Dec 1;228:112114.
70. Gomez-Cabrero D, Walter S, Abugessaisa I, Miñambres-Herraiz R, Palomares LB, Butcher L, et al. A robust machine learning framework to identify signatures for frailty: a nested case-control study in four aging European cohorts. *GeroScience.* 2021 Jun 1;43(3):1317–29.
71. Park C, Mishra R, Golledge J, Najafi B. Digital Biomarkers of Physical Frailty and Frailty Phenotypes Using Sensor-Based Physical Activity and Machine Learning. *Sensors.* 2021 Jan;21(16):5289.
72. Akbari G, Nikkhoo M, Wang L, Chen CPC, Han DS, Lin YH, et al. Frailty Level Classification of the Community Elderly Using Microsoft Kinect-Based Skeleton Pose: A Machine Learning Approach. *Sensors.* 2021 Jan;21(12):4017.
73. Leme DE da C, de Oliveira C. Machine Learning Models to Predict Future Frailty in Community-Dwelling Middle-Aged and Older Adults: The ELSA Cohort Study. *J Gerontol Ser A.* 2023 May 20;glad127.
74. Karanth SD. Sex-specific association of physical frailty and cognitive function in a population-based cross-sectional study of American older adults. *Alzheimers Dement.* 2023;19(S6):e068336.
75. Wang H yu, Zhang M, Sun X. Sex-Specific Association Between Socioeconomic Status, Lifestyle, and the Risk of Frailty Among the Elderly in China. *Front Med [Internet].* 2021 Nov 18 [cited 2024 May 28];8. Available from: <https://www.frontiersin.org/articles/10.3389/fmed.2021.775518>
76. Gordon EH, Peel NM, Samanta M, Theou O, Howlett SE, Hubbard RE. Sex differences in frailty: A systematic review and meta-analysis. *Exp Gerontol.* 2017 Mar 1;89:30–40.
77. Uchai S, Andersen LF, Hopstock LA, Hjartåker A. Body mass index, waist circumference and pre-frailty/frailty: the Tromsø study 1994–2016. *BMJ Open.* 2023 Feb 1;13(2):e065707.
78. Yarnall AJ, Sayer AA, Clegg A, Rockwood K, Parker S, Hindle JV. New horizons in multimorbidity in older adults. *Age Ageing.* 2017 Nov 1;46(6):882–8.

References

79. Uchmanowicz I, Łoboz-Rudnicka M, Szelağ P, Jankowska-Polańska B, Łoboz-Grudzień K. Frailty in Heart Failure. *Curr Heart Fail Rep*. 2014 Sep 1;11(3):266–73.
80. Sze S, Pellicori P, Zhang J, Weston J, Clark AL. Identification of Frailty in Chronic Heart Failure. *JACC Heart Fail*. 2019 Apr;7(4):291–302.
81. Reid N, Young A, Hanjani LS, Hubbard RE, Gordon EH. Sex-specific interventions to prevent and manage frailty. *Maturitas*. 2022 Oct 1;164:23–30.
82. Xu L, Zhang J, Shen S, Hong X, Zeng X, Yang Y, et al. Association Between Body Composition and Frailty in Elder Inpatients. *Clin Interv Aging*. 2020 Mar 4;15:313–20.
83. Mitchell E, Spencer Chapman M, Williams N, Dawson KJ, Mende N, Calderbank EF, et al. Clonal dynamics of haematopoiesis across the human lifespan. *Nature*. 2022 Jun;606(7913):343–50.
84. Lachmann R, Stelmach-Mardas M, Bergmann MM, Bernigau W, Weber D, Pischon T, et al. The accumulation of deficits approach to describe frailty. *PLOS ONE*. 2019 Oct 15;14(10):e0223449.
85. Poewe W, Seppi K, Tanner CM, Halliday GM, Brundin P, Volkman J, et al. Parkinson disease. *Nat Rev Dis Primer*. 2017 Mar 23;3(1):17013.
86. Belvisi D, Canevelli M, Costanzo M, Giangrosso M, Fabbrini A, Borraccino A, et al. The role of frailty in Parkinson's disease: a cross-sectional study. *J Neurol*. 2022 Jun 1;269(6):3006–14.
87. McMillan JM, Michalchuk Q, Goodarzi Z. Frailty in Parkinson's disease: A systematic review and meta-analysis. *Clin Park Relat Disord*. 2021 Jan 1;4:100095.
88. Chaix A, Zarrinpar A, Panda S. The circadian coordination of cell biology. *J Cell Biol* [Internet]. 2016;215. Available from: <https://doi.org/10.1083/jcb.201603076>
89. Golombek DA, Bussi IL, Agostino PV. Minutes, days and years: molecular interactions among different scales of biological timing. *Philos Trans R Soc Lond B Biol Sci*. 2014 Mar 5;369(1637):20120465.
90. Zhang R, Lahens NF, Ballance HI, Hughes ME, Hogenesch JB. A circadian gene expression atlas in mammals: implications for biology and medicine. *Proc Natl Acad Sci USA* [Internet]. 2014;111. Available from: <https://doi.org/10.1073/pnas.1408886111>

References

91. Saini C. A functional circadian clock is required for proper insulin secretion by human pancreatic islet cells. *Diabetes Obes Metab* [Internet]. 2016;18. Available from: <https://doi.org/10.1111/dom.12616>
92. Neufeld-Cohen A. Circadian control of oscillations in mitochondrial rate-limiting enzymes and nutrient utilization by PERIOD proteins. *Proc Natl Acad Sci USA* [Internet]. 2016;113. Available from: <https://doi.org/10.1073/pnas.1519650113>
93. Chakrabarti S, Michor F. Circadian clock effects on cellular proliferation: Insights from theory and experiments. *Curr Opin Cell Biol* [Internet]. 2020;67. Available from: <https://doi.org/10.1016/j.ceb.2020.07.003>
94. Scheiermann C, Kunisaki Y, Frenette PS. Circadian control of the immune system. *Nat Rev Immunol* [Internet]. 2013;13. Available from: <https://doi.org/10.1038/nri3386>
95. Sancar A. Circadian clock control of the cellular response to DNA damage. *FEBS Lett* [Internet]. 2010;584. Available from: <https://doi.org/10.1016/j.febslet.2010.03.017>
96. Takahashi JS. Transcriptional architecture of the mammalian circadian clock. *Nat Rev Genet* [Internet]. 2017;18. Available from: <https://doi.org/10.1038/nrg.2016.150>
97. Sulli G, Lam MTY, Panda S. Interplay between circadian clock and cancer: New frontiers for cancer treatment. *Trends Cancer* [Internet]. 2019;5. Available from: <https://doi.org/10.1016/j.trecan.2019.07.002>
98. Ye Y. The genomic landscape and pharmacogenomic interactions of clock genes in cancer chronotherapy. *Cell Syst* [Internet]. 2018;6. Available from: <https://doi.org/10.1016/j.cels.2018.01.013>
99. Lee Y. Time-of-day specificity of anticancer drugs may be mediated by circadian regulation of the cell cycle. *Sci Adv* [Internet]. 2021;7. Available from: <https://doi.org/10.1126/sciadv.abd2645>
100. Bray F, Laversanne M, Sung H, Ferlay J, Siegel RL, Soerjomataram I, et al. Global cancer statistics 2022: GLOBOCAN estimates of incidence and mortality worldwide for 36 cancers in 185 countries. *CA Cancer J Clin*. 2024;74(3):229–63.
101. Lehmann BD, Jovanović B, Chen X, Estrada MV, Johnson KN, Shyr Y, et al. Refinement of Triple-Negative Breast Cancer Molecular Subtypes: Implications for Neoadjuvant Chemotherapy Selection. *PLOS ONE*. 2016 Jun 16;11(6):e0157368.

References

102. Lehmann BD, Bauer JA, Chen X, Sanders ME, Chakravarthy AB, Shyr Y, et al. Identification of human triple-negative breast cancer subtypes and preclinical models for selection of targeted therapies. *J Clin Invest*. 2011 Jul;121(7):2750–67.
103. Lellupitiyage Don SS. Circadian oscillations persist in low malignancy breast cancer cells. *Cell Cycle* [Internet]. 2019;18. Available from: <https://doi.org/10.1080/15384101.2019.1648957>
104. Li SY, Hammarlund JA, Wu G, Lian JW, Howell SJ, Clarke RB, et al. Tumor circadian clock strength influences metastatic potential and predicts patient prognosis in luminal A breast cancer. *Proc Natl Acad Sci U S A*. 2024 Feb 13;121(7):e2311854121.
105. Rida P, Syed MI, Aneja R. Time will tell: Circadian clock dysregulation in triple negative breast cancer. *Front Biosci Sch Ed* [Internet]. 2019;11. Available from: <https://doi.org/10.2741/s533>
106. Ko CH, Takahashi JS. Molecular components of the mammalian circadian clock. *Hum Mol Genet* [Internet]. 2006;15. Available from: <https://doi.org/10.1093/hmg/ddl207>
107. Dallmann R, Brown SA, Gachon F. Chronopharmacology: New insights and therapeutic implications. *Annu Rev Pharmacol Toxicol* [Internet]. 2014;54. Available from: <https://doi.org/10.1146/annurev-pharmtox-011613-135923>
108. Hafner M, Niepel M, Chung M, Sorger PK. Growth rate inhibition metrics correct for confounders in measuring sensitivity to cancer drugs. *Nat Methods* [Internet]. 2016;13. Available from: <https://doi.org/10.1038/nmeth.3853>
109. Tibshirani R, Walther G, Hastie T. Estimating the number of clusters in a data set via the gap statistic. *J R Stat Soc Ser B Stat Methodol*. 2001;63(2):411–23.
110. Mormont M. C, Levi F. Cancer chronotherapy: Principles, applications, and perspectives. *Cancer* [Internet]. 2003;97. Available from: <https://doi.org/10.1002/cncr.11040>
111. Börding T, Abdo AN, Maier B, Gabriel C, Kramer A. Generation of human CRY1 and CRY2 knockout cells using duplex CRISPR/Cas9 technology. *Front Physiol* [Internet]. 2019;10. Available from: <https://doi.org/10.3389/fphys.2019.00577>

References

112. Lin HH, Qraitem M, Lian Y, Taylor SR, Farkas ME. Analyses of BMAL1 and PER2 Oscillations in a Model of Breast Cancer Progression Reveal Changes With Malignancy. *Integr Cancer Ther*. 2019;18:1534735419836494.
113. Baggs JE. Network features of the mammalian circadian clock. *PLOS Biol* [Internet]. 2009;7. Available from: <https://doi.org/10.1371/journal.pbio.1000052>
114. Lévi F, Okyar A, Dulong S, Innominato PF, Clairambault J. Circadian timing in cancer treatments. *Annu Rev Pharmacol Toxicol* [Internet]. 2010;50. Available from: <https://doi.org/10.1146/annurev.pharmtox.48.113006.094626>
115. Wood PA, Du-Quiton J, You S, Hrushesky WJM. Circadian clock coordinates cancer cell cycle progression, thymidylate synthase, and 5-fluorouracil therapeutic index. *Mol Cancer Ther* [Internet]. 2006;5. Available from: <https://doi.org/10.1158/1535-7163.MCT-06-0177>
116. Lévi FA. Chronomodulated versus fixed-infusion—rate delivery of ambulatory chemotherapy with oxaliplatin, fluorouracil, and folinic acid (Leucovorin) in patients with colorectal cancer metastases: a randomized multi-institutional trial. *J Natl Cancer Inst* [Internet]. 1994;86. Available from: <https://doi.org/10.1093/jnci/86.21.1608>
117. Sothorn RB, Lévi F, Haus E, Halberg F, Hrushesky WJ. Control of a murine plasmacytoma with doxorubicin-cisplatin: dependence on circadian stage of treatment. *J Natl Cancer Inst* [Internet]. 1989;81. Available from: <https://doi.org/10.1093/jnci/81.2.135>
118. Nagoshi E. Circadian gene expression in individual fibroblasts: cell-autonomous and self-sustained oscillators pass time to daughter cells. *Cell* [Internet]. 2004;119. Available from: <https://doi.org/10.1016/j.cell.2004.11.015>
119. Izumo M, Johnson CH, Yamazaki S. Circadian gene expression in mammalian fibroblasts revealed by real-time luminescence reporting: Temperature compensation and damping. *Proc Natl Acad Sci USA* [Internet]. 2003;100. Available from: <https://doi.org/10.1073/pnas.2536313100>
120. Balsalobre A, Damiola F, Schibler U. A serum shock induces circadian gene expression in mammalian tissue culture cells. *Cell* [Internet]. 1998;93. Available from: [https://doi.org/10.1016/S0092-8674\(00\)81199-X](https://doi.org/10.1016/S0092-8674(00)81199-X)

References

121. Manella G, Aizik D, Aviram R, Golik M, Asher G. Circa-SCOPE: high-throughput live single-cell imaging method for analysis of circadian clock resetting. *Nat Commun*. 2021 Oct 8;12(1):5903.
122. Zhu B. A cell-autonomous mammalian 12 hr clock coordinates metabolic and stress rhythms. *Cell Metab* [Internet]. 2017;25. Available from: <https://doi.org/10.1016/j.cmet.2017.05.004>
123. Anafi RC, Francey LJ, Hogenesch JB, Kim J. CYCLOPS reveals human transcriptional rhythms in health and disease. *Proc Natl Acad Sci U S A*. 2017 May 16;114(20):5312–7.
124. Bieler J. Robust synchronization of coupled circadian and cell cycle oscillators in single mammalian cells. *Mol Syst Biol* [Internet]. 2014;10. Available from: <https://doi.org/10.15252/msb.20145218>
125. Gutu N, Nordentoft MS, Kuhn M, Ector C, Möser M, Finger AM, et al. Circadian coupling orchestrates cell growth. *Nat Phys*. 2025 May;21(5):768–77.
126. Memczak S, Jens M, Elefsinioti A, Torti F, Krueger J, Rybak A, et al. Circular RNAs are a large class of animal RNAs with regulatory potency. *Nature*. 2013 Mar;495(7441):333–8.
127. Conn SJ, Pillman KA, Toubia J, Conn VM, Salmanidis M, Phillips CA, et al. The RNA Binding Protein Quaking Regulates Formation of circRNAs. *Cell*. 2015 Mar;160(6):1125–34.
128. Jumper J, Evans R, Pritzel A, Green T, Figurnov M, Ronneberger O, et al. Highly accurate protein structure prediction with AlphaFold. *Nature*. 2021 Aug 26;596(7873):583–9.
129. Bujold D, Morais DADL, Gauthier C, Côté C, Caron M, Kwan T, et al. The International Human Epigenome Consortium Data Portal. *Cell Syst*. 2016 Nov;3(5):496-499.e2.
130. Cvijovic M, Höfer T, Aćimović J, Alberghina L, Almaas E, Besozzi D, et al. Strategies for structuring interdisciplinary education in Systems Biology: an European perspective. *Npj Syst Biol Appl*. 2016 May 26;2(1):16011.

References

131. Anton Feenstra K, Abeln S, Westerhuis JA, Brancos Dos Santos F, Molenaar D, Teusink B, et al. Training for translation between disciplines: a philosophy for life and data sciences curricula. *Bioinformatics*. 2018 Jul 1;34(13):i4–12.
132. Attwood TK, Blackford S, Brazas MD, Davies A, Schneider MV. A global perspective on evolving bioinformatics and data science training needs. *Brief Bioinform*. 2019 Mar 25;20(2):398–404.
133. Jungck JR, Robeva R, Gross LJ. Mathematical Biology Education: Changes, Communities, Connections, and Challenges. *Bull Math Biol*. 2020 Sep;82(9):117, s11538-020-00793–0.
134. Dale R, Craig S. Integrating Math Modeling, Coding, and Biology in a CURE Lab [Internet]. *Scientific Communication and Education*; 2022 Jan [cited 2024 Feb 14]. Available from: <http://biorxiv.org/lookup/doi/10.1101/2022.01.20.477155>
135. Momsen J, Speth EB, Wyse S, Vilaprinyo E, Alves R, Sorribas A, et al. Integrating math modeling, coding, and biology in a CURE lab (preprint). *CBE Life Sci Educ*. 2022;50:131–6.
136. Smith RW, Garcia-Morales L, Martins Dos Santos VAP, Saccenti E. Research-driven education: An introductory course to systems and synthetic biology. *Front Syst Biol*. 2022 Sep 23;2:981800.
137. Tamir R, Ben-Zvi Assaraf O, Maman S. System-thinking progress in engineering programs: A case for broadening the roles of students. *Front Educ*. 2023 Apr 20;8:1138503.
138. EO Voit. Systems biology beyond biology. *Front Syst Biol*. 2022;2.
139. EO Voit, MA Shah, D Olivença. What's next for computational systems biology? *Front Syst Biol*. 2023;3.
140. AZupanic, HC Bernstein, I Heiland. Systems biology: current status and challenges. *Cell Mol Life Sci*. 2020;3:379–80.
141. Vilaprinyo E, Alves R, Sorribas A. Teaching systems biology. *IET Syst Biol*. 2011 Mar 1;5(2):131–6.

References

142. Mulder N, Schwartz R, Brazas MD, Brooksbank C, Gaeta B, Morgan SL, et al. The development and application of bioinformatics core competencies to improve bioinformatics training and education. Troyanskaya OG, editor. *PLOS Comput Biol*. 2018 Feb 1;14(2):e1005772.
143. K LaTourrette, A Stengel, J Clarke. Student-led workshops: filling skills gaps in computational research for life scientists. *Nat Sci Educ*. 2021;50.
144. Sauter T, Albrecht M. Introduction to Systems Biology: Workbook for Flipped-classroom Teaching [Internet]. 1st ed. Cambridge, UK: Open Book Publishers; 2023 [cited 2024 May 24]. Available from: <https://www.openbookpublishers.com/books/10.11647/obp.0291>
145. Del Din S, Elshehabi M, Galna B, Hobert MA, Warmerdam E, Suenkel U, et al. Gait analysis with wearables predicts conversion to Parkinson disease. *Ann Neurol*. 2019;86(3):357–67.
146. Mirelman A, Bonato P, Camicioli R, Ellis TD, Giladi N, Hamilton JL, et al. Gait impairments in Parkinson's disease. *Lancet Neurol*. 2019 Jul 1;18(7):697–708.
147. Huang Z, Karaboué A, Zeng L, Lecoeuvre A, Zhang L, Li XM, et al. Overall survival according to time-of-day of combined immuno-chemotherapy for advanced non-small cell lung cancer: a bicentric bicontinental study. *eBioMedicine*. 2025 Feb 20;113:105607.
148. Catozzi S, Assaad S, Delrieu L, Favier B, Dumas E, Hamy AS, et al. Early morning immune checkpoint blockade and overall survival of patients with metastatic cancer: An In-depth chronotherapeutic study. *Eur J Cancer*. 2024 Mar 1;199:113571.
149. Karaboué A, Innominato PF, Wreglesworth NI, Duchemann B, Adam R, Lévi FA. Why does circadian timing of administration matter for immune checkpoint inhibitors' efficacy? *Br J Cancer*. 2024 Sep;131(5):783–96.
150. Fey RM, Billo A, Clister T, Doan KL, Berry EG, Tibbitts DC, et al. Personalization of Cancer Treatment: Exploring the Role of Chronotherapy in Immune Checkpoint Inhibitor Efficacy. *Cancers*. 2025 Feb 21;17(5):732.
151. Dewhurst SM. Chromothripsis and telomere crisis: engines of genome instability. *Curr Opin Genet Dev*. 2020 Feb;60:41–7.

References

152. Vainshelbaum NM, Salmina K, Gerashchenko BI, Lazovska M, Zayakin P, Cragg MS, et al. Role of the Circadian Clock “Death-Loop” in the DNA Damage Response Underpinning Cancer Treatment Resistance. *Cells*. 2022 Jan;11(5):880.
153. Chen W. D. The circadian rhythm controls telomeres and telomerase activity. *Biochem Biophys Res Commun* [Internet]. 2014;451. Available from: <https://doi.org/10.1016/j.bbrc.2014.07.138>



## Appendix of original publications

### **Appendix A1: BASE-II**

Article title: **Clinical data-driven classification of pre-frailty reveals sex-specific patterns – Data from the Berlin Aging Study II (BASE-II)**

Contributions: Material preparation

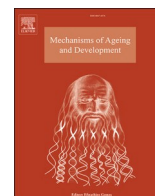
Data analysis

Manuscript writing and revision

All figures and tables

DOI link: <https://doi.org/10.1016/j.mad.2025.112114>

Published in: Mechanisms of Ageing and Development



## Clinical data-driven classification of pre-frailty reveals sex-specific patterns – Data from the Berlin Aging Study II (BASE-II)

Jeff Didier <sup>a</sup>, Sébastien De Landtsheer <sup>a</sup>, Maria Pires Pacheco <sup>a</sup>, Ali Kishk <sup>a</sup>,  
Jochen G. Schneider <sup>b,c,d</sup>, David Goldeck <sup>e</sup>, Graham Pawelec <sup>f</sup>, Dominik Spira <sup>g</sup>,  
Ilja Demuth <sup>g,h</sup>, Thomas Sauter <sup>a,\*</sup>

<sup>a</sup> Systems Biology & Epigenetics Group, Department of Life Sciences and Medicine, University of Luxembourg, Esch-sur-Alzette, Luxembourg

<sup>b</sup> Medical Translational Research Group, Luxembourg Centre for Systems Biomedicine, University of Luxembourg, Esch-sur-Alzette, Luxembourg

<sup>c</sup> Department of Life Sciences and Medicine, University of Luxembourg, Esch-sur-Alzette, Luxembourg

<sup>d</sup> Department of Internal Medicine, Saarland University Hospital and Saarland University Faculty of Medicine, Homburg, Germany

<sup>e</sup> Department of Internal Medicine 2, University of Tübingen, Tübingen, Germany

<sup>f</sup> Department of Immunology, University of Tübingen, Tübingen, Germany

<sup>g</sup> Division of Lipid Metabolism, Department of Endocrinology and Metabolic Diseases, Corporate Member of Freie Universität Berlin and Humboldt-Universität zu Berlin, Charité – Universitätsmedizin Berlin, Berlin, Germany

<sup>h</sup> Berlin Institute of Health at Charité – Universitätsmedizin Berlin, BCRT-Berlin Institute of Health Center for Regenerative Therapies, Berlin, Germany

### ARTICLE INFO

#### Keywords:

Ageing  
Frailty  
Classification  
Prognostic biomarkers  
Machine-learning  
BASE-II

### ABSTRACT

Frailty is a geriatric condition with multidimensional consequences that strongly affect older adults' quality of life. The lack of a universal standard to describe, diagnose, and treat frailty further complicates this situation. Nowadays, multitudinous frailty assessment tools are applied depending on the regional and clinical context, adding complexity by increasing heterogeneity in the definition and characterization of frailty. Better insights into the causes and pathophysiology of frailty and its early stages are required to establish strong and accurately tailored treatment rationales for frail patients. We analysed participants aged 60 and above using cross-sectional biochemical and survey data from the Berlin Aging Study II (BASE-II, N = 1512, pre-frail=470, frail=14), applying machine-learning techniques to investigate determinants of physical frailty measured by Fried et al.'s 5-item frailty phenotype. Our findings highlight new prognostic sex-specific biomarkers of pre-frailty (the early stage of frailty) with possible clinical applications, enriching the current sex-agnostic diagnostic scores with easy monitorable physical and physiological characteristics. Low appendicular lean mass and high fat composition in men, or vitamin D deficiency and high white blood cell counts in women, emerged as strong indicators of the respective pre-frailty profiles. Because the number of fully frail individuals was extremely small (n = 14, <1%), our findings should be interpreted as reflecting predictors of pre-frailty, not of frailty itself. We conclude that understanding the development of frailty remains a complex challenge, and that sex-specific differences must be considered by clinical geriatricians and researchers.

**Abbreviations:** BASE-II, Berlin Aging Study II; BMI, body mass index; WHR, waist-to-hip ratio; ALM, appendicular lean mass; EX, exhaustion; GA, gait; GS, grip strength; PA, physical activity; WL, weight loss; PCA, principal component analysis; RUS, random under-sampling; SVM, support vector machine; ROC, receiver operating characteristics; CV, cross-validation; CI, confidence interval; PM, physical measurements; BF, body fluids; CG, cognition; SMOTE, synthetic minority over-sampling technique; LDA, linear discriminant analysis; BMD, bone mineral density; BMC, bone mineral content; HDL, high-density lipoprotein; MANOVA, multivariate analysis of variance; BCD, between-cluster distance; WCD, within-cluster distance; IM, individual medications; ID, individual devices; GM, grouped medications; SV, surveys; CH, chronic morbidity; GD, grouped devices; HPC, high-performance computing; DOR, diagnostics odds ratio; TP, true positive; TN, true negative; PR, precision-recall; FPR, false positive rate.

\* Corresponding author.

*E-mail addresses:* [jeff.didier@uni.lu](mailto:jeff.didier@uni.lu) (J. Didier), [sebastien.delandtsheer@uni.lu](mailto:sebastien.delandtsheer@uni.lu) (S. De Landtsheer), [maria.pacheco@uni.lu](mailto:maria.pacheco@uni.lu) (M.P. Pacheco), [ali.kishk@icloud.com](mailto:ali.kishk@icloud.com) (A. Kishk), [jochen.schneider@uni.lu](mailto:jochen.schneider@uni.lu) (J.G. Schneider), [dgoldeck@yahoo.de](mailto:dgoldeck@yahoo.de) (D. Goldeck), [graham.pawelec@uni-tuebingen.de](mailto:graham.pawelec@uni-tuebingen.de) (G. Pawelec), [dominik.spira@charite.de](mailto:dominik.spira@charite.de) (D. Spira), [ilja.demuth@charite.de](mailto:ilja.demuth@charite.de) (I. Demuth), [thomas.sauter@uni.lu](mailto:thomas.sauter@uni.lu) (T. Sauter).

<https://doi.org/10.1016/j.mad.2025.112114>

Received 3 June 2025; Received in revised form 16 September 2025; Accepted 18 September 2025

Available online 24 September 2025

0047-6374/© 2025 The Authors. Published by Elsevier B.V. This is an open access article under the CC BY license (<http://creativecommons.org/licenses/by/4.0/>).



2012; Espinoza et al., 2018; Puts et al., 2005; Spira et al., 2015; Fhon et al., 2018), and the word cloud in Fig. 1). However, measurement of physiological reserve is often limited to physical characteristics such as grip strength, various parameters of the limbs or other body parts, and cardiovascular or cardiopulmonary exercise (Linn et al., 2021; O’Caoimh et al., 2021), neglecting physiological aspects such as age- or muscle-related molecular blood biomarker profiles. Hence, all frailty studies exhibit different strengths and weaknesses, according to a 2021 review by Howlett et al (Howlett et al., 2021). Thus, in practice, the therapies and treatments used to care for frail patients target the symptoms and aim to alleviate the impact on quality of life rather than addressing the underlying causes of frailty (Lally and Crome, 2007). Furthermore, frailty-associated phenotypes including vitamin D deficiency (Shardell et al., 2009; Zhou et al., 2016; Spira et al., 2019; Murad et al., 2011), polypharmacy (Gutiérrez-Valencia et al., 2018; Nwadiugwu, 2020), comorbidities (Espinoza et al., 2018; Tenison and Henderson, 2020), sarcopenia (Patel et al., 2017; Spira et al., 2015), diabetes (Strain et al., 2021), and chronic inflammation (Puts et al., 2005), among others, that are often linked to detrimental effects on the physiological reserve and the individual’s ability to recover from insults, are rarely considered by the existing frailty assessment instruments. In this study, we focus on a dataset of older people aged 60 years and above from the observational Berlin Aging Study II (BASE-II) (Bertram et al., 2014). Frailty in BASE-II was defined according to Fried et al.’s 5-item frailty phenotype (Fried et al., 2001) (Tab. S1) and shown to be associated with low lean mass, physical performance, sex-specific vitamin D deficiency, metabolic syndrome, use of potentially inappropriate medication, and mortality (Buchmann et al., 2019; Spira et al., 2015, 2019; Toepfer et al., 2021; Koenig et al., 2024). Here, we applied machine-learning approaches to identify prognostic biomedical and clinical markers that can best reflect Fried et al.’s frailty phenotype in BASE-II.

Previous studies have harnessed the power of machine-learning algorithms to identify biomarkers and risk factors of frailty development in older people. Gomez-Cabrero et al. identified protective biomarkers as well as a risk factor for frailty in a nested case-control study in four European ageing cohorts (Gomez-Cabrero et al., 2021). The protective factors included, among others, vitamin D and lutein zeaxanthin (carotenoid, and precursor of vitamin A). Troponin T, a protein in the heart muscle which is responsible for binding calcium was found to be main risk factor. Park et al. investigated the least number of digital biomarkers of frailty measurable with sensors during daily activities (Park et al., 2021). Akbari et al. demonstrated that machine-learning modelling can quantify the risk of frailty in older people based on real-time skeletal movements using the Microsoft Kinect-Based Skeleton Pose, where participants performed different physical exercises (sit-and-stand, arm curls, ...) in front of a Kinect sensor (Akbari et al., 2021). In 2023, Da Cunha Leme et al. applied machine-learning on the English Longitudinal Study of Aging to identify the best predictors of frailty in middle-aged and older adults based on features such as age, balance, household wealth, alcohol intake, and depression (Leme et al., 2023).

In this study, we exploited the rich biomedical and clinical information available in BASE-II to narrow down the most important prognostic biomarkers associated with pre-frailty, thereby validating and supplementing the existing body of knowledge with new insights. Our analyses focused primarily on pre-frail individuals (the initial stage on a trajectory that may eventually lead to fully developed frailty), while recognizing that pre-frail and frail represent two distinct clinical stages. With the impending surge in the older population, added to the persisting lack of a gold standard and consensus on frailty, we examined biomedical and clinical parameters ranging from blood-based biomarkers to disease status and functionality. This approach acknowledges the development of frailty as a systemic condition that manifests across domains, necessitating diverse input variables to identify robust and clinically relevant biomarkers. In addition, this study explored factors

relevant to sex-specific pre-frailty trajectories, an under-investigated subject as sex-based biological differences, including hormonal regulation, inflammatory responses, and body composition, may influence frailty development and manifestation. As such, acknowledging sex-specific patterns of pre-frailty patterns could improve risk stratification, early detection, and the development of more effective, personalized interventions.

## 2. Results

The analyses presented here focus on pre-frail participants, that is, individuals at the initial stage of a trajectory that may eventually lead to fully developed frailty. Throughout the text and figures, the label ‘pre-frail/frail’ refers overwhelmingly to pre-frail participants ( $n = 470$ ), with only a very small subset of frail participants ( $n = 14$ ,  $<1\%$ ). Consequently, all findings should be interpreted as reflecting predictors of pre-frailty, no conclusions can be drawn about fully developed frailty from this data.

### 2.1. Descriptive and inferential analysis

#### 2.1.1. Sex-specific differences in the BASE-II description of general frailty-related phenotypes

The BASE-II cohort description of frailty-related phenotypes such as sex, age, body mass index (BMI), waist-to-hip ratio (WHR), appendicular lean mass (ALM), sarcopenia, morbidity index, and polypharmacy revealed interesting differences between non-frail and pre-frail/frail participants when compared across sex (Table 1). Sex itself was not significant in the mixed-sex group ( $p$ -value =  $5.23e-01$ ), but sharp contrasts emerged, for example:

- WHR (significant in men only,  $p$ -value =  $9.48e-03$ )
- ALM (significant in men and mixed-sex,  $p$ -values =  $3.04e-03$  and  $2.84e-02$ , respectively)
- Morbidity index (significant in women and mixed-sex,  $p$ -values =  $1.43e-04$  and  $1.72e-04$ , respectively)
- Polypharmacy (significant in women and mixed-sex,  $p$ -values =  $1.43e-03$  and  $3.39e-04$ , respectively)

Detailed visualizations of the differences in general frailty-related characteristics and their corresponding distributions are depicted in the supplementary section (see Fig. S1 and Fig. S2 for frailty-related features based on data type). As expected, BMI-adjusted ALM, height, ALM, and WHR showed clear sex differences, with men having higher values.

#### 2.1.2. Sex-specificity within Fried et al.’s Frailty phenotype items

Sex-specificity was further investigated across Fried et al.’s Frailty Score, frailty phenotype, as well as the five underlying variables of exhaustion (EX), gait (GA), grip strength (GS), physical activity (PA), and weight loss (WL) (Table 2). No statistical significance could be observed in both the Frailty Score ( $p$ -value =  $7.03e-01$ ) and the frailty phenotype ( $p$ -value =  $5.23e-01$ ), but significant differences manifested within four of the five Fried et al.’s Frailty items, except WL ( $p$ -value =  $5.61e-01$ ). While reported EX ( $p$ -value =  $2.94e-03$ ) and weak GS ( $p$ -value =  $5.77e-04$ ) were more frequent in frail women, GA impairment ( $p$ -value =  $1.34e-02$ ) and lack of PA ( $p$ -value =  $3.88e-02$ ) were more frequent in frail men. The clinical variable of GS in particular shows the largest difference between the two sexes, with a corrected Cramér’s V coefficient of 0.09 (small correlation considering one degree of freedom), and the lowest  $p$ -value of  $5.77e-04$ . These observations suggest that Fried et al.’s frailty phenotype manifests differently in men and women, showing that sex-specific interpretation is strongly recommended in the BASE-II frailty analysis.

**Table 1**

BASE-II cohort characteristics. Context-specific BASE-II cohort characteristics in relation to the frailty phenotype, with the first triplet of columns displaying mixed-sex participants, second men, and third women. P-values obtained with the Cramér's V correlation algorithm corrected for binary and discrete data types. Continuous features underwent Welch's unequal variance T-test after assessing the equality of variances between the non-frail and pre-frail/frail group with the Levene's test. SD standard deviation, BMI body mass index, ALM appendicular lean mass, WHR waist-hip ratio, IQR inter quartile range, ns non-significant, 0.01 < \* < 0.05, 0.001 < \*\* < 0.01, 0.0001 < \*\*\* < 0.001, 0.00001 < \*\*\*\* < 0.0001.

| Cohort characteristics        | Non-frail mixed (N = 1028, 67.99 %) | Pre-frail / frail mixed (N = 484, 32.01 %) | P-value  | Non-frail men (N = 513, 33.93 %) | Pre-frail / frail men (N = 233, 15.41 %) | P-value  | Non-frail women (N = 515, 34.06 %) | Pre-frail / frail women (N = 251, 16.60 %) | P-value  |
|-------------------------------|-------------------------------------|--|----------|----------------------------------|--|----------|------------------------------------|--|----------|
| <b>Sex</b>                    |                                     |  |          |                                  |  |          |                                    |  |          |
| men N (%)                     | 513 (33.93 %)                       | 233 (15.41 %)                              | 5.23e-01 | /                                | /  | /        | /                                  | /  | /        |
| women N (%)                   | 515 (34.06 %)                       | 251 (16.60 %)                              | (ns)     |                                  |  |          |                                    |  |          |
| <b>Age (years)</b>            |                                     |  |          |                                  |  |          |                                    |  |          |
| mean ± SD                     | 68.46 ± 3.44                        | 69.31 ± 4.16                               | 1.05e-04 | 68.68 ± 3.46                     | 69.76 ± 4.33                             | 8.62e-04 | 68.25 ± 3.41                       | 68.89 ± 3.96                               | 2.77e-02 |
| [min, max]                    | [60.16, 83.25]                      | [60.74, 84.63]                             | (***)    | [60.16, 78.12]                   | [60.74, 82.79]                           | (***)    | [61.29, 83.25]                     | [61.46, 84.63]                             | (*)      |
| <b>BMI (kg/m<sup>2</sup>)</b> |                                     |  |          |                                  |  |          |                                    |  |          |
| mean ± SD                     | 26.37 ± 3.79                        | 27.73 ± 4.72                               | 4.73e-08 | 26.93 ± 3.45                     | 27.97 ± 3.77                             | 2.13e-04 | 25.82 ± 4.03                       | 27.50 ± 5.45                               | 1.99e-05 |
| [min, max]                    | [17.03, 44.24]                      | [17.94, 47.68]                             | (****)   | [19.13, 44.24]                   | [19.97, 42.61]                           | (***)    | [17.03, 40.4]                      | [17.94, 47.68]                             | (****)   |
| <b>Waist/Hip ratio</b>        |                                     |  |          |                                  |  |          |                                    |  |          |
| mean ± SD                     | 0.96 ± 0.08                         | 0.96 ± 0.08                                | 3.35e-01 | 1.01 ± 0.05                      | 1.02 ± 0.05                              | 9.36e-03 | 0.90 ± 0.07                        | 0.91 ± 0.06                                | 6.88e-01 |
| [min, max]                    | [0.57, 1.44]                        | [0.74, 1.21]                               | (ns)     | [0.81, 1.25]                     | [0.88, 1.17]                             | (**)     | [0.57, 1.44]                       | [0.74, 1.21]                               | (ns)     |
| <b>Height (cm)</b>            |                                     |  |          |                                  |  |          |                                    |  |          |
| mean ± SD                     | 169.74 ± 8.81                       | 167.84 ± 8.94                              | 1.07e-04 | 176.09                           | 174.53                                   | 1.46e-03 | 163.41                             | 161.63 ± 6.18                              | 1.68e-04 |
| [min, max]                    | [146.0, 194.8]                      | [144.0, 191.0]                             | (***)    | ± 6.17<br>[160.0, 194.8]         | ± 6.21<br>[156.3, 191.0]                 | (**)     | ± 6.06<br>[146.0, 182.5]           | [144.0, 176.0]                             | (***)    |
| <b>ALM (kg)</b>               |                                     |  |          |                                  |  |          |                                    |  |          |
| mean ± SD                     | 21.38 ± 4.95                        | 20.80 ± 4.77                               | 3.05e-02 | 25.49 ± 3.06                     | 24.75 ± 3.17                             | 2.62e-03 | 17.29 ± 2.46                       | 17.13 ± 2.56                               | 3.99e-01 |
| [min, max]                    | [9.28, 35.1]                        | [11.97, 35.82]                             | (*)      | [18.91, 35.1]                    | [17.42, 35.82]                           | (**)     | [9.28, 25.31]                      | [11.97, 26.18]                             | (ns)     |
| <b>ALM/BMI ratio</b>          |                                     |  |          |                                  |  |          |                                    |  |          |
| mean ± SD                     | 0.82 ± 0.18                         | 0.76 ± 0.17                                | 1.54e-08 | 0.96 ± 0.13                      | 0.89 ± 0.11                              | 3.65e-10 | 0.68 ± 0.10                        | 0.64 ± 0.11                                | 3.19e-07 |
| [min, max]                    | [0.42, 1.47]                        | [0.38, 1.31]                               | (****)   | [0.63, 1.47]                     | [0.59, 1.31]                             | (****)   | [0.42, 1.03]                       | [0.38, 0.93]                               | (****)   |
| <b>Heart insufficiency</b>    |                                     |  |          |                                  |  |          |                                    |  |          |
| unaffected                    | 863                                 | 350  | 1.16e-07 | 451                              | 185                                      | 2.37e-03 | 412                                | 165  | 1.73e-05 |
| affected                      | 165                                 | 134  | (****)   | 62                               | 48                                       | (**)     | 103                                | 86   | (****)   |
| median (IQR)                  | 0 (0.0, 0.0)                        | 0 (0.0, 1.0)                               |          | 0 (0.0, 0.0)                     | 0 (0.0, 0.0)                             |          | 0 (0.0, 0.0)                       | 0 (0.0, 1.0)                               |          |
| <b>Vitamin D deficiency</b>   |                                     |  |          |                                  |  |          |                                    |  |          |
| unaffected                    | 537                                 | 194  | 1.02e-05 | 270                              | 97                                       | 5.35e-03 | 267                                | 97   | 5.96e-04 |
| affected                      | 491                                 | 290  | (****)   | 243                              | 136                                      | (**)     | 248                                | 154  | (***)    |
| median (IQR)                  | 0 (0.0, 1.0)                        | 1 (0.0, 1.0)                               |          | 0 (0.0, 1.0)                     | 1 (0.0, 1.0)                             |          | 0 (0.0, 1.0)                       | 1 (0.0, 1.0)                               |          |
| <b>Sarcopenia</b>             |                                     |  |          |                                  |  |          |                                    |  |          |
| unaffected                    | 968                                 | 416  | 8.69e-08 | 468                              | 200                                      | 2.57e-02 | 500                                | 216  | 6.57e-09 |
| affected                      | 60                                  | 68   | (****)   | 45                               | 33                                       | (*)      | 15                                 | 35   | (****)   |
| median (IQR)                  | 0 (0.0, 0.0)                        | 0 (0.0, 0.0)                               |          | 0 (0.0, 0.0)                     | 0 (0.0, 0.0)                             |          | 0 (0.0, 0.0)                       | 0 (0.0, 0.0)                               |          |
| <b>Morbidity Index</b>        |                                     |  |          |                                  |  |          |                                    |  |          |
| unaffected                    | 427                                 | 168  | 1.72e-04 | 205                              | 82                                       | 2.11e-01 | 222                                | 86   | 1.98e-04 |
| only one                      | 295                                 | 128  | (***)    | 133                              | 62                                       | (ns)     | 162                                | 66   | (***)    |
| two - four                    | 294                                 | 168  |          | 169                              | 82                                       |          | 125                                | 86   |          |
| five or more                  | 12                                  | 20   |          | 6                                | 7  |          | 6                                  | 13   |          |
| median (IQR)                  | 1 (0.0, 2.0)                        | 1 (0.0, 2.0)                               |          | 1 (0.0, 2.0)                     | 1 (0.0, 2.0)                             |          | 1 (0.0, 2.0)                       | 1 (0.0, 2.0)                               |          |
| <b>Polypharmacy</b>           |                                     |  |          |                                  |  |          |                                    |  |          |
| unaffected                    | 203                                 | 64   | 3.39e-04 | 116                              | 35                                       | 6.72e-02 | 87                                 | 29   | 1.43e-03 |
| affected                      | 157                                 | 56   | (***)    | 73                               | 31                                       | (ns)     | 84                                 | 25   | (**)     |
| median (IQR)                  | 460                                 | 230  |          | 216                              | 107                                      |          | 244                                | 123  |          |
|                               | 208                                 | 134  |          | 108                              | 60                                       |          | 100                                | 74   |          |
|                               | 2 (1.0, 4.0)                        | 3 (2.0, 5.0)                               |          | 2 (1.0, 4.0)                     | 2 (1.0, 5.0)                             |          | 2 (1.0, 4.0)                       | 3 (2.0, 5.0)                               |          |

**2.1.3. Sex differences within the BASE-II frailty profiles**

Both sexes were balanced in the non-frail and the pre-frail/frail group, with approximately twice as many non-frail participants (Fig. 2a). Most participants (97.1 %) were affected by one or two of the five Fried et al. frailty items, and only 14 participants (3.9 %) affected by three or more items (Fig. 2b). The distribution of the different phenotypes showed that GA and PA were predominantly impaired in men, while EX and GS were predominantly impaired in women (Fig. 2c). Only WL was observed to be balanced, although with the overall lowest count (37 total cases of WL compared to the 115, 133, 137, and 168 cases of GS, PA, EX, and GA, respectively). While most participants (81.2 %) were affected by one single frailty item (Fig. 2d), the intersections revealed that more men are suffering from single GA or PA impairment and combinations thereof, and that single EX or GS affection and combinations thereof are more often observed in women. Although these sex differences in the BASE-II frailty profiles show solid evidence for considering sex-specific modelling of frailty in this cohort, we further analysed the available biomedical data for similar signs using dimensionality reduction. In Fig. 2e, Principal component analysis (PCA) of the continuous data is resulting in two clusters separating both sexes,

showing that these differences not only reside within Fried et al.'s 5-item frailty phenotype, but are also noticeable across the large panel of biomedical information of BASE-II. Furthermore, since frailty is highly associated with age and age-related disorders, we analysed the age differences in non-frail and pre-frail/frail sexes (Fig. 2f), showing a lower average age in non-frail than pre-frail/frail participants, and specifically lower in women (non-frail men 68.68 ± 3.46 years, pre-frail/frail men 69.76 ± 4.33 years (p-value = 8.62e-04); non-frail women 68.25 ± 3.41 years, pre-frail/frail women 68.89 ± 3.96 years (p-value = 2.77e-02)).

**2.2. Pre-frailty biomarker analysis in BASE-II**

**2.2.1. Complete data-driven model architecture and performances**

Using all the available biomedical information as input (indicated by the affix ALL), pre-processing reduced the number of input features to 257 (mixed), 167 (men), and 33 (women) features (see Section 4.4.3 for more details about the low number of input features for the women model, and the summary of feature correlation analysis in Fig. S3a). Among the possible combinations of pipeline architecture and machine-

**Table 2**

BASE-II cohort characteristics of the 5 *Fried et al.* frailty phenotype items. *Fried et al.* frailty score, frailty phenotype, and frailty items characteristics in the mixed-sex, men, and women BASE-II groups. P values obtained with the Cramér's V correlation algorithm corrected for binary and discrete data types. ns non-significant, 0.01 < \* < 0.05, 0.001 < \*\* < 0.01, 0.0001 < \*\*\* < 0.001, 0.00001 < \*\*\*\* < 0.0001.

| BASE-II <i>Fried et al.</i> frailty phenotype description | Mixed (N = 1512, 100 %) | Men (N = 746, 49.34 %) | Women (N = 766, 50.66 %) | P-value        |
|---|-------------------------|------------------------|--------------------------|----------------|
| <b>Fried et al. Frailty Score</b>                         | 1028                    | 513                    | 515                      | 7.03e-01 (ns)  |
| unaffected  | 393                     | 188                    | 205                      |                |
| one   | 77                      | 39                     | 38                       |                |
| two   | 13                      | 51                     | 80                       |                |
| three   | 1                       |                        |                          |                |
| four  |                         |                        |                          |                |
| <b>Fried et al. frailty phenotype</b>                     | 1028                    | 513                    | 515                      | 5.23e-01 (ns)  |
| unaffected  | 484                     | 233                    | 251                      |                |
| affected  |                         |                        |                          |                |
| <b>Exhaustion (poor endurance)</b>                        | 1375                    | 695                    | 680                      | 2.94e-03 (**)  |
|   | 137                     | 51                     | 86                       |                |
| <b>Gait (slowness)</b>                                    | 1344                    | 648                    | 696                      | 1.34e-02 (*)   |
|   | 168                     | 98                     | 70                       |                |
| <b>Grip strength (weakness)</b>                           | 1397                    | 707                    | 690                      | 5.77e-04 (***) |
|   | 115                     | 39                     | 76                       |                |
| <b>Physical activity (low activity)</b>                   | 1379                    | 669                    | 710                      | 3.88e-02 (*)   |
|   | 133                     | 77                     | 56                       |                |
| <b>Weight loss (shrinking)</b>                            | 1475                    | 726                    | 749                      | 5.61e-01 (ns)  |
|   | 37                      | 20                     | 17                       |                |

learning classifier parameters (detailed in [Tab. S3](#) point 3 and [Tab. S4](#); see [Fig. 3e](#) for a summary of the best configurations and parameters), the best performing *ALL*-models each share the use of random under-sampling (RUS) technique to balance pre-frail/frail and non-frail participants, PCA to reduce the input dimensionality, and  $\chi^2$  to select the top discrete features. They differ however by the technique of scaling the continuous input (Min-max scaling for mixed-sex and men, standard scaling for women) and the type of support vector machines (SVM) kernel applied by the classifier (radial basis function for *mixed-ALL*, linear for *men-ALL* and *women-ALL*). Regularization values were 3000 for *mixed-ALL*, 0.1 for *women-ALL*, and 100 for the best *men-ALL* model. The classifier tolerance was the highest for *men-ALL* with 0.01, lowest for *mixed-ALL* with 0.00001, and 0.001 for the best performing *women-ALL* model. In [Fig. 4a](#), the performances are depicted by the receiver operating characteristics (ROC) curves of the 5-times 10-fold cross-validation (CV), the 20 % hold-out test set, and the corresponding hold-out confusion matrix for all three models. The best *mixed-ALL* model reached a CV ROC mean of 0.665 (95 % confidence interval (CI): [0.551 – 0.779]) with a hold-out ROC score of 0.63. In terms of the hold-out confusion matrix, 72.73 % non-frail and 53.85 % pre-frail/frail participants were correctly identified. This mixed-sex model was moderately outperformed by both the *men-ALL* and *women-ALL* models, given their CV ROC mean of 0.705 (95 % CI: [0.567 – 0.843]) and 0.693 (95 % CI: [0.551 – 0.835]), respectively, and both yielded the same hold-out test ROC score of 0.66. The *men-ALL* model correctly identified 64.29 % non-frail and 67.27 % pre-frail/frail participants, whereas the *women-ALL* model identified 69.00 % non-frail and 63.27 % pre-frail/frail participants correctly. Given that sex-specific models outperformed the mixed-sex models, we performed subgroup analysis to gain potentially deeper insights into sex-specific pre-frailty.

### 2.2.2. Subgroup-based models outperform complete models for pre-frailty prediction in men and women

In a second experiment, the interest was focused on four of the ten biomedical subgroups defined in [Section 4.2](#), namely nutrients (NT), physical measurements (PM), body fluids (BF), and cognition (CG), as highlighted in [Fig. 3a](#). The best performing subgroup for each context

was recorded and will be hereafter indicated by their respective affix as *mixed-BF*, *men-PM*, and *women-BF*, which were reduced to 86, 32, and 84 input features, respectively, after pre-processing. (refer to [Section 4.4.3](#) for more details about the low number of input features for the men model, and the summary of feature correlation analysis in [Fig. S3b](#)). Like the complete data-driven models, the subgroup models share some specific characteristics while strongly differing in others. These models' configuration commonly applies the same strategy for balancing out pre-frail/frail participants; however, this time synthetic minority over-sampling technique (SMOTE) was prioritized. Moreover, all three subgroup models performed best using the linear SVM kernel after dimensionality reduction. The *mixed-BF* and *women-BF* models used robust scaling of the continuous input data, PCA to reduce the input dimensionality, and  $\chi^2$  for selecting the top discrete features from the input. The *men-PM* model used standard scaling of the input features and linear discriminant analysis (LDA) to reduce the input dimensionality to one single feature distinguishing non-frail from pre-frail/frail. In [Fig. 4b](#), the performance of the best mixed-sex model (*mixed-BF*) reached a CV ROC mean of  $0.629 \pm 0.047$  (95 % CI: [0.535 – 0.723]) with a hold-out ROC score of 0.61. 61.62 % non-frail and 59.62 % pre-frail/frail participants were correctly identified. This best performing *mixed-BF* model was significantly outperformed by the *men-PM* and moderately outperformed by the *women-BF* model given their CV ROC mean of  $0.721 \pm 0.066$  (95 % CI: [0.619 – 0.853]) and  $0.633 \pm 0.068$  (95 % CI: [0.497 – 0.769]), respectively. The *men-PM* model yielded the highest hold-out test ROC score of 0.70 while the *women-BF* model scored 0.67. The *men-PM* model correctly identified 68.37 % non-frail and 70.91 % pre-frail/frail participants whereas the *women-BF* model identified 63.00 % non-frail and 71.43 % pre-frail/frail participants correctly. With the improvements observed in the women and especially men models based on distinct biomedical subgroups and model architecture, the top contributing features were interpreted context-wise to investigate their underlying associations with the sex-specific pre-frailty profiles observed in BASE-II.

### 2.2.3. Mixed-sex and sex-specific model interpretability

From the best performing *ALL*-models, the 30 most-contributing features based on their permutation score are depicted in [Fig. 4c](#) (n permutation mixed-sex = 1000, men = 500, women = 500). A more detailed view on the feature permutation behaviour in the complete data-driven models can be found in [Fig. S4](#) of the supplementary section. Furthermore, red and green squares shown next to the first ten features in [Fig. 4c](#) indicate the direction of the association (green: positive, red: negative), useful to interpret the model's behaviour and decision from a biological perspective. [Fig. 4c](#) show the performance of the subgroup-based data-driven models using *PM*-, *BF*-, *NT*-, and *CG*-related input features, with values displayed only for the complete and the best performing subgroup models. The most contributing features of the subgroup data-driven models are depicted in [Fig. 4d](#), with the corresponding feature permutation behaviour in [Fig. S5](#). Besides the feature importance and permutation behaviour, an additional layer of model interpretability is given by revealing the predictions in terms of the true *Fried et al.* frailty levels (non-frail, pre-frail, and frail) instead of the combined pre-frail and frail, showing that the models performances do increase with the level of true frailty ([Fig. 6](#)). As a result, the best *mixed-BF* model correctly identified pre-frail and frail participants with sensitivities of 60.0 % and 85.7 % respectively. In *men-PM*, the pre-frail and frail sensitivities are 70.5 % and 83.3 % respectively, while the best *women-BF* model predicted pre-frail and frail participants with sensitivities of 63.8 % and 87.5 % respectively. The false positive rates for the non-frail participants of those three top models are 41.4 %, 35.5 %, and 41.9 %, respectively, with specificities of 58.9 % in *mixed-BF*, 64.5 % in *men-PM*, and 58.1 % in *women-BF*. This stratified analysis shows that the identified predictors remain significant in the small frail subgroup.

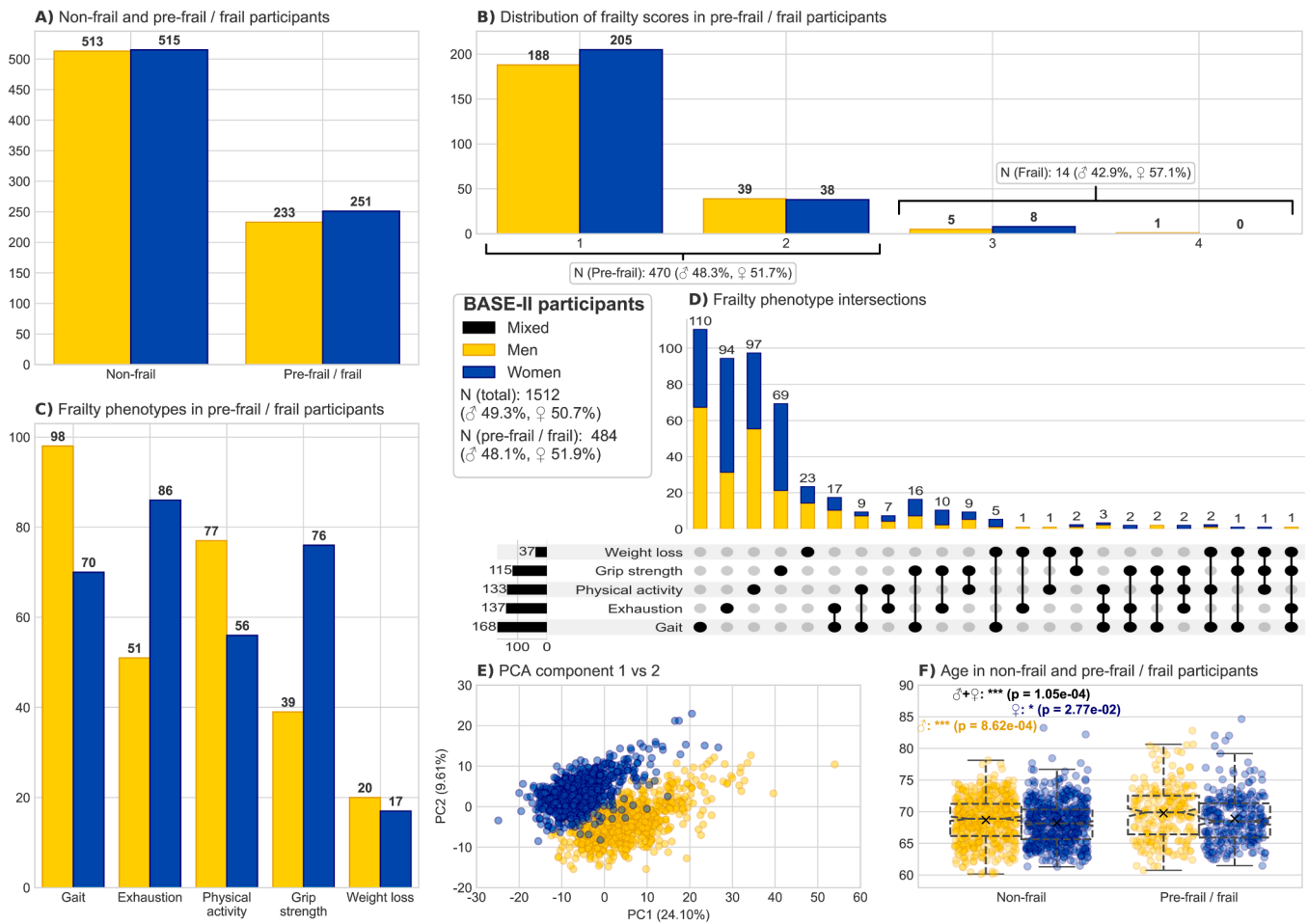


**Fig. 2.** Sex-specific differences in the BASE-II participants' pre-frailty profile call for contextualized modelling. Distribution of the non-frail and pre-frail/frail participants (A), the *Fried et al.* Frailty Score equal or above 1 (B); the *Fried et al.* frailty phenotype items (C) and phenotype intersections (D) show sex-specific frailty profiles. The first and second principal components (E) clearly separate both sex; and the age in non-frail and pre-frail/frail participants do also show significant differences (F). Statistical significance derived from Welch's unequal variance T-test. Showing mixed-sex (black), men (yellow), and women (blue) participants of BASE-II. PCA principal component analysis, 0.01 < \* < 0.05, 0.001 < \*\* < 0.01, 0.0001 < \*\*\* < 0.001, 0.00001 < \*\*\*\* < 0.0001.

**2.2.4. Sex-specific pre-frailty patterns share morbidities but diverge in cognitive and physical traits**

The three most important features driving the *mixed-ALL* model are heart insufficiency, vitamin D deficiency, and sarcopenia, three independent morbidities and deficits linked to cardiovascular, physiologic, and muscular pathologies, respectively. The red marking of those three features in Fig. 4c suggests that the more deficits the participants (men and women alike) have accumulated, the more likely they are to be pre-frail/frail (Fig. S6, training set only). Furthermore, the performance in cognitive tasks, particularly the digit symbol substitution test, was weaker in pre-frail/frail participants. The next most contributing features in the *mixed-ALL* context include multiple body fat composition characteristics, particularly of the head (fat percentage), left arm (fat mass in grams), left leg (fat percentage and mass in grams), and the ALM-to-BMI ratio. Pre-frail/frail participants show higher fat composition in the above-mentioned body parts and lower ALM-to-BMI ratio. The top ten contributing features also included docosanoic (behenic) acid, a non-essential long-chain saturated fatty acid, which appeared to be consumed less by pre-frail/frail participants and may be associated with increased cardiovascular mortality (Tao et al., 2024).

Compared to the mixed-sex model, the top ten contributing features in *men-ALL* include affection by heart insufficiency and larger head fat mass in pre-frail/frail men. Again, heart insufficiency is the most contributing feature and moreover shows a stronger detrimental effect to the model performance after feature permutation as in the mixed-sex

model (comparing their loss in CV score). Although this is also observed for the head fat mass feature, its low z-score indicates lower reliability in this effect. The *men-ALL* model highlights two medication types targeting distinct disease areas: gastroenterology and ophthalmology. Intriguingly, the model behaviour reveals that there is no difference between the non-frail and pre-frail/frail men in terms of the number of medications targeting these two disease areas, and the proportion of pre-frailty is not increasing with the number of medications, even when considering their accumulation (Fig. S7, training set only). This is different in women, as here the proportion of pre-frail participants increases with the number of ophthalmology-related medications and the accumulation with gastroenterology-related medications.

Regarding the *women-ALL* model, two of the top ten contributing features are shared with the *mixed-ALL* model, namely heart insufficiency and sarcopenia. Another indication of the latter deficit is the ALM, which was picked up by the *women-ALL* model, but not in the *mixed-ALL* or *men-ALL* model. Marked as green, the model shows that pre-frail/frail women appear to have lower ALM, or, in other words, lower muscle mass in limbs compared to non-frail women. On the other hand, the *women-ALL* model also shares two common features with the *men-ALL* model, namely again heart insufficiency (which is the only common feature across all three contexts), and the increased time necessary to solve the cognitive trail making test B. The *women-ALL* model is further driven by various drinking habits (increased number of distilled drinks and self-reported drinking frequency), medication intake

Pipeline setup and model configurations

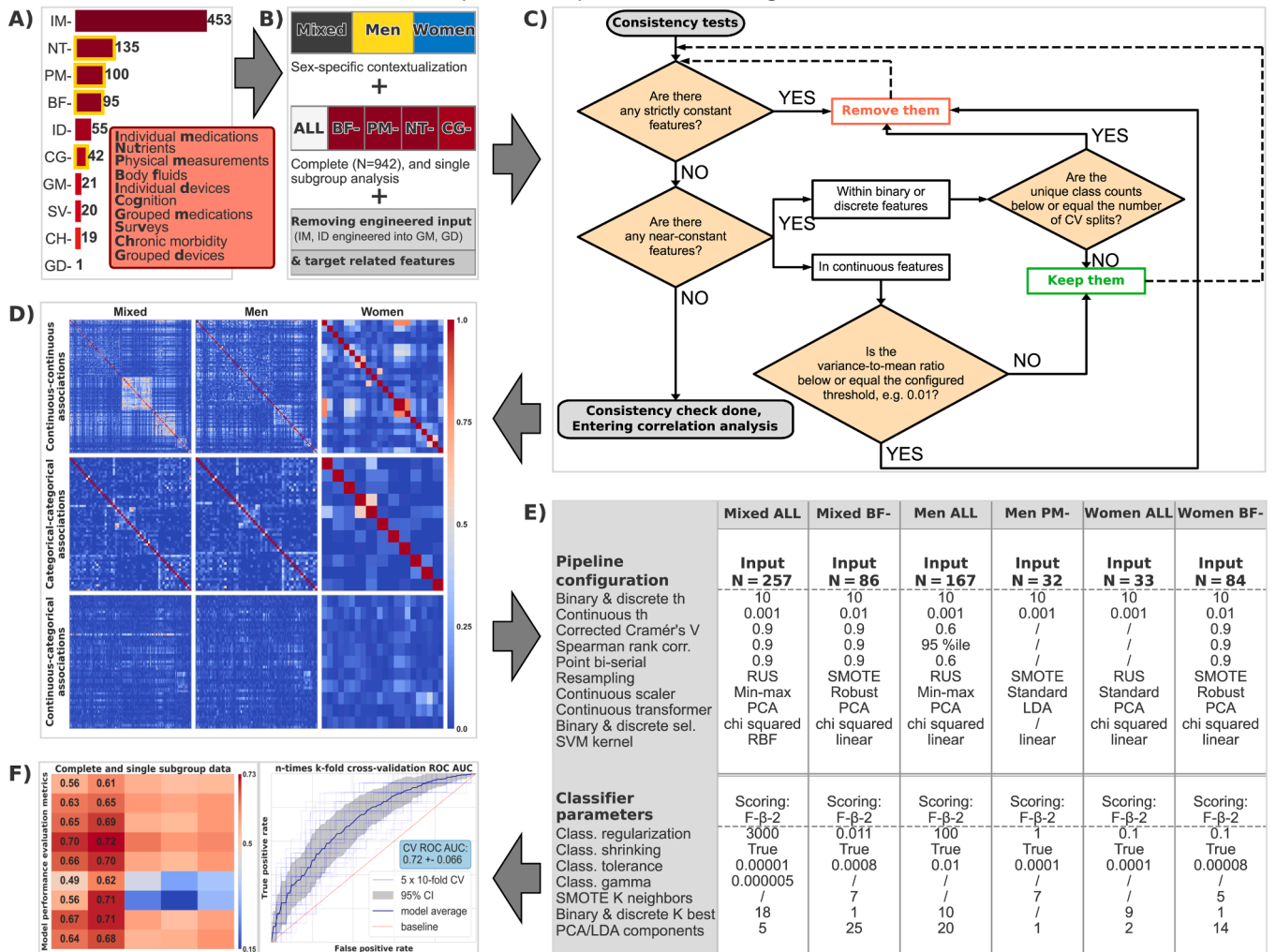


**Fig. 3.** Pipeline setup and context-specific model configurations. The vast amount of biomedical data in BASE-II was divided in 10 subgroups that represent the nature of the biomedical information (A). In a first step, the data is partitioned by sex (mixed-sex, men, women) and either complete or 4 single subgroup analysis (highlighted in A), including the removal of input features that have been used to engineer new ones as well as target related features (B). Next, the filtered data will undergo a consistency test to check for constant and near-constant features according to the configurations (C). The remaining consistent data then undergoes data type-specific correlation analysis to identify and remove mutually correlated features to avoid redundant information according to user-defined parameters (D). The pre-processed data then enters the machine-learning-based classifier pipeline with the predefined configurations and parameter ranges, while showing here only the parameters of the best performing context-specific models (E). Finally, the best performing model selected by exhaustive grid search is evaluated using multiple metrics, and feature importance are measured as loss or gain in CV score during n-times feature permutation (F). IM individual medications, NT nutrients, PM physical measurements, BF body fluids, ID individual devices, CG cognition, GM grouped medications, SV surveys, CH chronic morbidity, GD grouped devices, th threshold, corr correlation, sel selection, SVM Support Vector Machine, SMOTE synthetic minority oversampling technique, PCA principal component analysis, LDA linear discriminant analysis, RUS random under-sampling, RBF radial basis function, CV cross-validation, ROC receiver operating characteristics, DOR diagnostics odds ratio, TP true positive, TN true negative.

targeting dental issues, and decreased cognitive test scores such as the correct wordlist learning total score and the wordlist discriminability z-score. While above observations are revealing first subtle distinctions between mixed-sex, men, and women frailty trajectories in terms of context-specific top contributing features and the interpretation thereof, the subgroup-based data-driven models can offer further insights into the underlying causes and consequences of sex-specific pre-frailty as observed in BASE-II.

**2.2.5. Subgroup-based data-driven models highlight sex-specific physiological and physical traits**

Focusing on the subgroup-based data-driven models, the results hint at intrinsic differences in the pre-frailty profiles in the mixed-sex and sex-specific BASE-II population based on the improved model performance using BF input data for the mixed-sex and women models, and

PM for men (Fig. 4c, heatmaps). Compared to the *mixed-ALL* model, the *mixed-BF* model is foremost attuned to vitamin D deficiency, low vitamin B12 and sodium levels, as well as increased immune markers such as circulating IL-10 and monocytes, suggesting an increased burden of underlying medical conditions or complications in pre-frail/frail participants (Fig. 4d).

Substantial improvements in prediction performance were achieved when restricting the men model to PM data only, with nine of the top ten contributing features causing an average loss of CV score of 5–15 % during the permutation importance. Similar observations were made in the *mixed-ALL* scenario, however, showing much more importance in men. Again, multiple body composition features are increased, especially trunk fat, trunk mass, and left arm fat (percentage and grams), while lean mass-related features such as left arm lean mass (in grams), ALM (in grams), and ALM-BMI ratio are decreased in pre-frail/frail

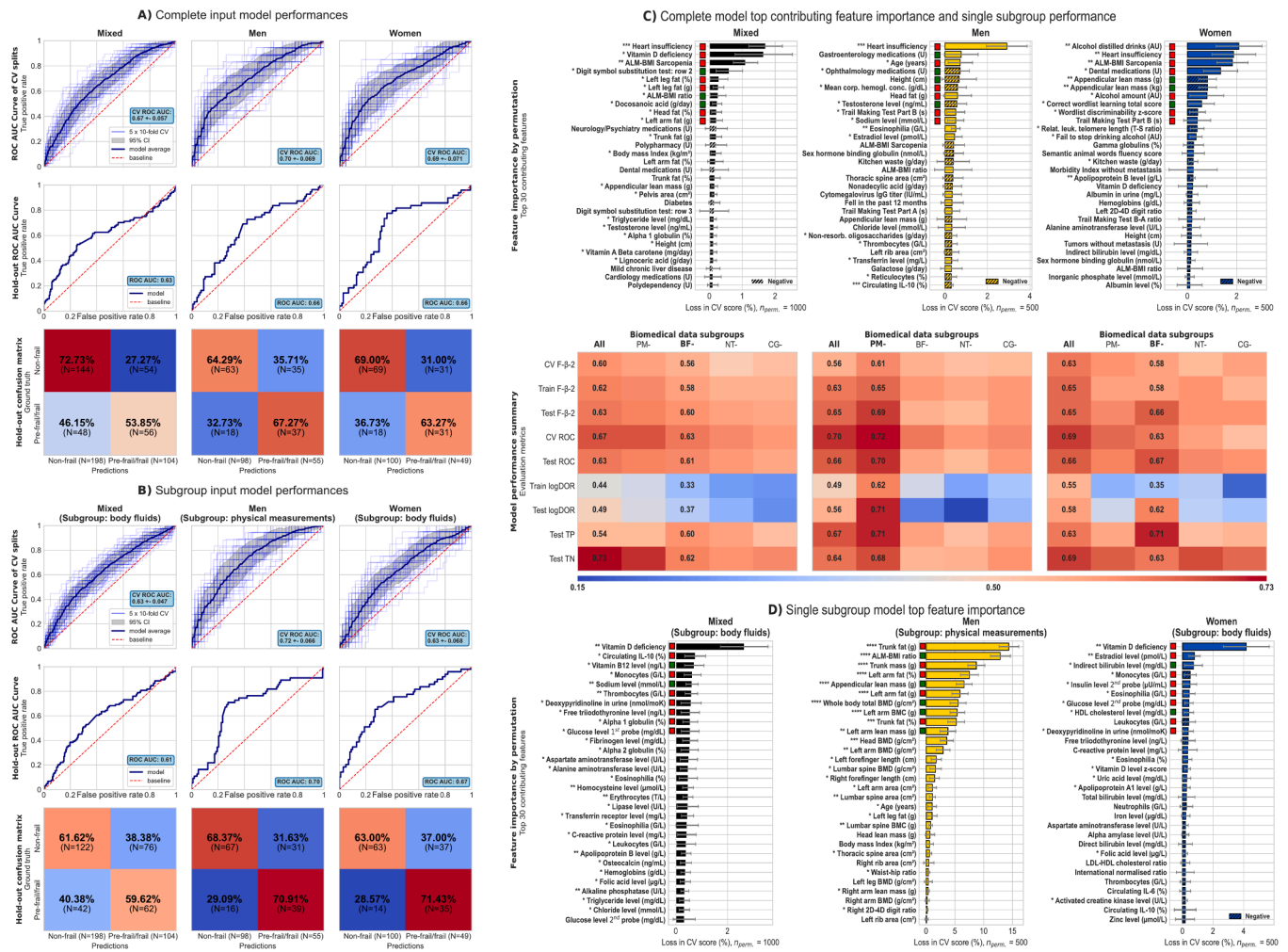


**Fig. 4.** Sex-specific data-driven models outperform mixed-sex models and reveal distinct predictive patterns for pre-frailty in BASE-II. (A) Context-specific model performances in the complete data-driven models, showing the ROC AUC curves from a 5 times 10-fold CV training process [mixed-sex: 0.665 ± 0.057, men: 0.705 ± 0.069, women: 0.693 ± 0.071] and performance on the hold-out test set [mixed-sex: 0.61, men: 0.65, women: 0.68]. (B) Context-specific model performances in the single subgroup data-driven models, showing ROC AUC curves from the 5 times 10-fold CV training process [mixed-sex: 0.629 ± 0.047, men: 0.721 ± 0.066, women: 0.633 ± 0.068] and on the hold-out test set [mixed-sex: 0.60, men: 0.68, women: 0.71]. The CV splits are not identical to the 10-fold splits used in the pipeline (see Fig. 3e). Final row displays the confusion matrix on the hold-out test set for mixed-sex, men, and women models. (C) Sex-specific most predictive features in the complete data-driven models, based on mean and standard deviation of the n-times permuted feature CV score loss. Negative hatched bars indicate gain in CV score. Green and red squares denote the classifier's interpretation of the feature as lower or higher, respectively, in frail-predicted participants compared to non-frail. Asterisks prefixing feature names represent corresponding absolute z-score levels. (D) Sex-specific most predictive features in the single subgroup data-driven models, following the same conventions as in (C). The second row shows the overall heatmap of evaluation scores for the best-performing models in the complete (All) and single subgroup settings. Final row is displaying the confusion matrix on the hold-out test set. The columns represent the mixed-sex, men, and women groups respectively. ROC receiver operating characteristics, AUC area under the curve, ALM appendicular lean mass, BMI body mass index, T-S telomere-single gene ratio, 2D-4D digit 2-to-digit 4 ratio, ROC receiver operating characteristics, DOR diagnostics odds ratio, TP true positive, TN true negative, BMC bone mineral content, BMD bone mineral density, HDL high density lipoprotein, LDL low density lipoprotein.

participants. In addition, whole-body total bone mineral density (BMD, in grams per square centimetre) and the left arm bone mineral content (BMC, in grams) are decreased in pre-frail/frail men. With this, the pre-frail/frail men profile in BASE-II emerges as a participant with higher fat mass in limbs and trunks, and reduced ALM across the body. Furthermore, their low BMD and BMC can be associated to more fragile bone structures, amplifying the risk of serious medical condition, structural instability, and facilitating bone fractures.

In the *women-BF* model, vitamin D deficiency is the leading driving factor, significantly impacting the CV score during permutation measurement compared to other models. This implies that a deficiency in vitamin D ( $\leq 50$  nmol/L of 25-hydroxy-vitamin D in serum) among women goes along with increased likelihood of developing frailty. Furthermore, multiple white blood cell counts are increased in pre-frail/frail women, i.e., monocytes, leukocytes, and eosinophils (immune

functions); but also, indirect bilirubin (clearance function) and high-density lipoprotein (HDL) cholesterol levels (endothelial function) are decreased. These participants show higher levels of oestradiol (hormone and bone health function), insulin (glucose regulation function), and glucose in serum (energy function), as well as higher deoxyypyridinoline in urine (bone resorption function). These imbalances portrait a women pre-frailty profile focussing on internal physiological signals whereas pre-frailty in men is more likely revealed by external physical characteristics.

**2.2.6. Sex-specific aggregated feature associations to pre-frailty**

To better understand the association between frailty and specific features in the different models, statistical analysis was conducted on the top ten and thirty contributing features (Table 3a-b and Tab. S5a-b). This revealed that frailty is associated with aggregated, not always

**Table 3**

BASE-II cohort characteristics of the 10 most predictive features of the complete and single subgroup data-driven models show significant differences in pre-frail/frail and non-frail participants. Cohort characteristics of the top 10 most predictive features in the complete (top 10) and single subgroup (bottom 10) data-driven men (A) and women (B) models respectively. P values obtained with the Cramér's V correlation algorithm corrected for binary and discrete data types. Continuous features underwent Welch's unequal variance T-test after assessing the equality of variances between the non-frail and pre-frail/frail group with the Levene's test. SD standard deviation, BMI body mass index, ALM appendicular lean mass, BMD bone mineral density, BMC bone mineral content, ns non-significant, 0.01 < \* < 0.05, 0.001 < \*\* < 0.01, 0.0001 < \*\*\* < 0.001, 0.00001 < \*\*\*\* < 0.0001.

| A) Most important features (men-ALL)                            | Non-frail men (N = 513, 33.93 %)        | Pre-frail / frail men (N = 233, 15.41 %) | P-value         | B) Most important features (women-ALL)                                   | Non-frail women (N = 515, 34.06 %)                 | Pre-frail / frail women (N = 251, 16.60 %)        | P-value         |
|---|---|--|-----------------|--|--|---|-----------------|
| Heart insufficiency   | 0: 451<br>1: 62                         | 0: 185<br>1: 48                          | 2.37e-03 (**)   | Alcohol distilled drinks (AU)  | 0: 320<br>1: 148<br>2: 27<br>3: 13<br>4: 5<br>5: 2 | 0: 147<br>1: 73<br>2: 14<br>3: 11<br>4: 4<br>5: 2 | 6.46e-01 (ns)   |
| Gastroenterology medications (U)                                | 0: 416<br>1: 83<br>2: 14                | 0: 199<br>1: 32<br>2: 2                  | 1.65e-01 (ns)   | Heart insufficiency  | 0: 412<br>1: 103                                   | 0: 165<br>1: 86                                   | 1.73e-05 (****) |
| Age (years) mean ± SD; [min, max]                               | 68.68 ± 3.46 [60.16, 78.12]             | 69.76 ± 4.33 [60.74, 82.79]              | 8.62e-04 (****) | ALM BMI Sarcopenia   | 0: 500<br>1: 15                                    | 0: 216<br>1: 35                                   | 6.57e-09 (****) |
| Ophthalmology medications (U)                                   | 0: 465<br>1: 36<br>2: 12                | 0: 214<br>1: 17<br>2: 2                  | 3.84e-01 (ns)   | Dental medications (U)   | 0: 431<br>1: 82<br>2: 2                            | 0: 181<br>1: 68<br>2: 2                           | 8.58e-04 (****) |
| Height (cm) mean ± SD; [min, max]                               | 176.09 ± 6.17 [160.0, 194.8]            | 174.53 ± 6.21 [156.3, 191.0]             | 1.46e-03 (**)   | Appendicular lean mass (g) mean ± SD; [min, max]                         | 17290.69 ± 2457.20 [9284.27, 25307.89]             | 17128.66 ± 2564.11 [11970.53, 26183.56]           | 3.99e-01 (ns)   |
| Mean corp. hemogl. conc. (g/dL) mean ± SD; [min, max]           | 34.43 ± 0.99 [31.3, 37.5]               | 34.43 ± 1.00 [31.3, 37.6]                | 9.66e-01 (ns)   | Appendicular lean mass (kg) mean ± SD; [min, max]                        | 17.29 ± 2.46 [9.28, 25.31]                         | 17.13 ± 2.56 [11.97, 26.18]                       | 3.99e-01 (ns)   |
| Head fat (g) mean ± SD; [min, max]                              | 1171.00 ± 147.21 [861.82, 1710.11]      | 1189.52 ± 157.57 [826.91, 1663.2]        | 1.20e-01 (ns)   | Alcohol amount (AU)  | 0: 454<br>1: 58<br>2: 3                            | 0: 211<br>1: 35<br>2: 4                           | 1.53e-01 (ns)   |
| Testosterone level (ng/mL) mean ± SD; [min, max]                | 4.65 ± 1.97 [0.05, 14.19]               | 4.40 ± 1.94 [0.05, 11.69]                | 1.08e-01 (ns)   | Correct wordlist learning total score mean ± SD; [min, max]              | 23.18 ± 2.79 [15.0, 30.0]                          | 22.74 ± 3.18 [9.0, 29.0]                          | 5.20e-02 (ns)   |
| Trail Making Test Part B (s) mean ± SD; [min, max]              | 89.35 ± 34.73 [35.0, 266.0]             | 95.28 ± 37.92 [28.0, 295.0]              | 3.63e-02 (*)    | Wordlist discriminability z score mean ± SD; [min, max]                  | 0.12 ± 0.70 [-3.16, 0.95]                          | 0.11 ± 0.72 [-2.54, 0.87]                         | 8.98e-01 (ns)   |
| Sodium level (mmol/L) mean ± SD; [min, max]                     | 139.35 ± 2.68 [125.0, 147.0]            | 139.51 ± 2.76 [131.0, 148.0]             | 4.57e-01 (ns)   | Trail Making Test Part B (s) mean ± SD; [min, max]                       | 84.84 ± 29.63 [36.0, 238.0]                        | 94.49 ± 33.71 [42.0, 233.0]                       | 5.80e-05 (****) |
| Most important male features (men-PM)                           | Non-frail men (N = 513, 33.93 %)        | Pre-frail / frail men (N = 233, 15.41 %) | P-value         | Most important features (women-BF)                                       | Non-frail women (N = 515, 34.06 %)                 | Pre-frail / frail women (N = 251, 16.60 %)        | P-value         |
| Trunk fat (g) mean ± SD; [min, max]                             | 13812.02 ± 4071.45 [3965.92, 28361.59]  | 15024.44 ± 4742.30 [4878.38, 33258.54]   | 3.72e-04 (****) | Vitamin D deficiency   | 0: 267<br>1: 248                                   | 0: 97<br>1: 154                                   | 5.96e-04 (****) |
| ALM BMI ratio mean ± SD; [min, max]                             | 0.96 ± 0.13 [0.63, 1.47]                | 0.89 ± 0.11 [0.59, 1.31]                 | 3.65e-10 (****) | Estradiol level (pmol/L) mean ± SD; [min, max]                           | 35.73 ± 59.27 [9.2, 817.2]                         | 44.03 ± 60.11 [9.2, 471.4]                        | 7.03e-02 (ns)   |
| Trunk mass (g) mean ± SD; [min, max]                            | 41614.36 ± 6726.38 [24496.4, 72459.25]  | 42853.48 ± 8159.18 [25029.34, 74016.79]  | 4.34e-02 (*)    | Indirect bilirubin level (mg/dL) mean ± SD; [min, max]                   | 0.44 ± 0.15 [0.18, 1.22]                           | 0.42 ± 0.15 [0.11, 1.04]                          | 8.40e-02 (ns)   |
| Left arm fat (%) mean ± SD; [min, max]                          | 31.03 ± 5.85 [13.71, 52.38]             | 33.04 ± 5.82 [16.98, 51.9]               | 1.53e-05 (****) | Monocytes (G/L) mean ± SD; [min, max]                                    | 0.40 ± 0.14 [0.16, 1.1]                            | 0.43 ± 0.16 [0.13, 1.51]                          | 2.41e-02 (*)    |
| Appendicular lean mass (g) mean ± SD; [min, max]                | 25486.42 ± 3064.90 [18910.53, 35100.72] | 24747.02 ± 3173.83 [17423.04, 35815.85]  | 2.62e-03 (**)   | Insulin level 2 <sup>nd</sup> probe (µU/mL) mean ± SD; [min, max]        | 59.35 ± 50.15 [5.45, 460.1]                        | 62.76 ± 52.07 [6.86, 502.5]                       | 3.83e-01 (ns)   |
| Left arm fat (g) mean ± SD; [min, max]                          | 1422.53 ± 405.07 [445.24, 3374.5]       | 1494.40 ± 435.79 [615.73, 3556.75]       | 2.86e-02 (*)    | Eosinophilia (G/L) mean ± SD; [min, max]                                 | 0.15 ± 0.10 [0.01, 0.9]                            | 0.18 ± 0.15 [0.01, 1.46]                          | 4.30e-03 (**)   |
| Whole body total BMD (g/cm <sup>2</sup> ) mean ± SD; [min, max] | 1.24 ± 0.11 [0.94, 1.62]                | 1.23 ± 0.10 [0.96, 1.65]                 | 1.11e-01 (ns)   | Glucose level 2 <sup>nd</sup> probe (mg/dL) mean ± SD; [min, max]        | 109.05 ± 29.00 [38.0, 278.0]                       | 114.24 ± 37.36 [56.0, 333.0]                      | 3.53e-02 (*)    |
| Left arm BMC (g) mean ± SD; [min, max]                          | 206.54 ± 33.64 [115.55, 484.77]         | 199.43 ± 33.22 [121.59, 314.21]          | 7.43e-03 (**)   | High density lipoprotein cholesterol level (mg/dL) mean ± SD; [min, max] | 70.18 ± 16.03 [35.0, 134.0]                        | 67.68 ± 16.98 [32.0, 153.0]                       | 4.81e-02 (*)    |
| Trunk fat (%) mean ± SD; [min, max]                             | 32.62 ± 5.57 [14.66, 47.71]             | 34.39 ± 5.36 [17.46, 51.87]              | 5.02e-05 (****) | Leukocytes (G/L) mean ± SD; [min, max]                                   | 5.56 ± 1.44 [2.7, 11.8]                            | 5.92 ± 2.02 [2.1, 24.4]                           | 4.95e-03 (**)   |

(continued on next page)

Table 3 (continued)

| A) Most important features (men-ALL)            | Non-frail men (N = 513, 33.93 %)             | Pre-frail / frail men (N = 233, 15.41 %)     | P-value           | B) Most important features (women-ALL)                          | Non-frail women (N = 515, 34.06 %) | Pre-frail / frail women (N = 251, 16.60 %) | P-value          |
|---|--|--|-------------------|---|------------------------------------|--|------------------|
| Left arm lean mass (g)<br>mean ± SD; [min, max] | 3123.96<br>± 487.39<br>[1737.97,<br>4738.63] | 2991.33<br>± 504.83<br>[1911.19,<br>4546.69] | 6.95e−04<br>(***) | Deoxyipyridinoline in urine (nmol/moK)<br>mean ± SD; [min, max] | 59.34 ± 24.88<br>[1.0, 191.0]      | 60.55 ± 25.29<br>[3.5, 152.0]              | 5.27e−01<br>(ns) |

individual, features. The top driving sex-specific features (Fig. S9a-b) were also compared within mixed-sex, men, and women using the training dataset only. Some models (e.g., *men-PM*) showed more significant associations compared to the combined training and test set, while other models showed only weaker associations (e.g., *women-BF*). The associations to pre-frailty of the top ten contributing features were then put in perspective with all included features of the BASE-II cohort by comparing the difference in z-score for continuous features (Fig. S10a) and the corrected Cramér's V for binary and categorical features (Fig. S10b) within the training set. Highlighting the top thirty features from the best models (*mixed-ALL*, *men-PM*, *women-BF*) revealed that only a fraction of those individual features is significant, suggesting that these features may show aggregated association to pre-frailty rather than individually.

Multivariate analysis of variance (MANOVA) of all combinations of the top ten features in *men-PM* and *women-BF* revealed increasing statistical significance and increasing “1 - Wilk's lambda” score with the number of features tested (Fig. 5a-b), supporting the idea of sex-specific aggregated feature associations to pre-frailty. Similar behaviour was observed in the complete data-driven and the mixed-sex models (Fig. S11). When comparing the between-cluster distance (BCD), within-cluster distance (WCD), and their ratio in the top combinations of raw, PCA, and LDA transformed values, the clearest separation of non-frail and pre-frail/frail men was seen with the LDA transformation of the top combination of five (BCD-WCD ratio: 1.03) to all ten features (BCD-WCD ratio: 0.94); which has also been the feature reduction technique configured for the *men-PM* model (see Fig. 3e). For raw values and PCA-transformed values, the best separation was observed with the top two features ALM-BMI ratio and whole-body total BMD, achieving a BCD-WCD ratio of 0.94 with raw values, and 0.67 with PCA transformed values. Within the *women-BF* model, the differences between the combinations were less clear, yielding the highest BCD-WCD ratio with all ten features transformed by LDA (BCD-WCD ratio: 0.78). However, the best performing feature reduction technique for this model was PCA, which yielded the largest separation using the top combination of five features (BCD-WCD ratio: 0.54). Overall, this analysis suggests that the machine-learning algorithm indeed identified sex-specific aggregations of clinical features that best characterise physical pre-frailty in older men and women.

### 3. Discussion

#### 3.1. Overview of sex-specific pre-frailty prediction using biomedical profiles

Our results showed that pre-frailty (early stage of frailty), as defined by the *Fried et al.* frailty phenotype, can be characterized by sex-specific factors in people aged  $\geq 60$  years. These observations support our hypothesis of specific men and women frailty profiles, suggesting sex-specific prevention and treatment approaches. The current literature on frailty often addresses multiple subtypes of frailty and mostly within a mixed-sex population; only in recent years have researchers started to look deeper into frailty by revealing sex-specific interventions (Reid et al., 2022), prevalence (Hessey et al., 2020), as well as sex-specific associations of frailty with mortality (Dallmeier et al., 2020; Ver-schoor et al., 2024), CG (Karanth, 2023), and socioeconomic status

(Wang et al., 2024). However, sex-specific prognostic biomarkers for pre-frailty are still largely unexplored. Furthermore, most machine-learning-based approaches to predict frailty have focussed on movement data, self-reported lifestyle habits, or volatile physical characteristics such as GS or chair-sitting exercises (Park et al., 2021; Akbari et al., 2021; Leme et al., 2023), with only a few diving deeper into the biomedical profile of frailty, and then only in mixed-sex populations (Gomez-Cabrero et al., 2021). Here, we analysed machine-learning-based cross-validated prediction performance in the mixed-sex, men, and women population of BASE-II using biomedical data, as well as specific subgroups based on the origin of the biomedical information to predict the *Fried et al.* frailty phenotype (Fried et al., 2001). While frailty was defined using the *Fried et al.* physical frailty phenotype, the included predictors (e.g., inflammatory markers, chronic diseases, medications, or cognitive performance) span domains more aligned with the *Rockwood* frailty index and accumulation of deficit model (Rockwood et al., 1994; Rockwood and Mitnitski, 2007). This conceptual differences between the outcome definition and the feature space provided additional motivation to go beyond a global model and systematically explore frailty prediction within the distinct biomedical subgroups of BF, PM, CG, or NT. By doing so, we aimed to better understand how different physiological systems contribute to pre-frailty in a sex-specific context, and to identify whether certain domains disproportionately drive predictive performance for men versus women. We therefore position our work as exploratory and hypothesis-generating, with the goal of uncovering interpretable biomedical patterns that can inform future mechanistic or intervention studies.

#### 3.2. Sex-specific differences in the expression of pre-frailty

Descriptive analysis revealed first hints of sex-specificity within this cohort. Although sex itself is not significantly associated with the *Fried et al.* frailty phenotype in the mixed-sex population, some of the known frailty-related features such as WHR, ALM, morbidity index or poly-pharmacy manifest non-significant difference in either one of the three populations (Table 1). Even when significant for mixed-sex, men, or women, their effect sizes varied, suggesting that the strength of these associations with pre-frailty is larger in some groups than others. Similar observations have been made regarding the difference of these features across sex alone, or frailty alone (Fhon et al., 2018; Gutiérrez-Valencia et al., 2018; Karanth, 2023; Wang et al., 2024; Gordon et al., 2017; Uchai et al., 2023; Yarnall et al., 2017), but not yet in the combined context of sex-specific physical frailty. This could be because the resulting frailty phenotype, or the underlying frailty score, does not vary between men and women in the BASE-II (Fig. 2a-b). Instead, our results highlight the evidence of sex-specificity among the 5 *Fried et al.* frailty phenotype items (Fig. 2c-d, Table 2) that were used to define the level of frailty. As such, deficits in PA and GA are more prominent in pre-frail/frail men, while pre-frail/frail women more frequently report EX and show lower GS. In contrast, WL is equally represented in men and women, and double interactions of the sex-specific traits with WL do not follow this trend, which is likely due to the low number of self-reported cases of (unintended) WL. Besides the hallmarks of physical frailty, the *Fried et al.* frailty phenotype items, and their interactions, we also note clear variations between men and women in continuous biomedical data, independent of the frailty levels (Fig. 2e). These differences point

to sex-specific clinical manifestations: with men more affected by performance-related deficits (PA and GA), and women more affected by psychological or subjective components (EX), possibly reflecting the role of depression in women's frailty expression (Fhon et al., 2018; Gutiérrez-Valencia et al., 2018; Karanth, 2023; Wang et al., 2024; Gordon et al., 2017; Uchai et al., 2023; Yarnall et al., 2017).

### 3.3. Predictive models reveal divergent pre-frailty profiles in men and women

Our best-performing sex-specific models outperformed the mixed-sex model (Fig. 4a). sex-specific models more accurately predicted pre-frailty, while the mixed-sex model overpredicted non-frailty. Our analysis on the most clearly contributing clinical features of each model and the differences in technical configuration of these models confirms that men and women have different frailty trajectory profiles (Fig. 4c, Table 3). The mixed-sex model composed of these sex-specific profiles struggled to identify predictive features for men and women pre-frailty due to the asymmetric prevalence of most contributing features. Examples of such asymmetric features are vitamin D deficiency, sarcopenia, and alcohol consumption in women, and body fat mass, age, and height in men. While those features were identified in the mixed-sex model, they were only re-identified in one of the sex-specific contexts, aligning with several studies that also attributed distinct sex-specific importance to these features (Patel et al., 2017; Spira et al., 2015; Shardell et al., 2009; Spira et al., 2019). Among the top ten contributing features in all models, only one heart insufficiency showed symmetrical contributions regardless of sex. This feature is known to be highly associated with frailty, and independent of sex (Uchmanowicz et al., 2014; Sze et al., 2019). It is also noticeable that cognitive features, although not identical, ranked among the top ten features in all three models. While the digit symbol substitution test score was identified in the mixed-sex model to be lower in pre-frail/frail participants, both men and women models share the trail-making test as a predictive feature, which takes more time for pre-frail/frail participants to accomplish (coloured squares in Fig. 4c, for values see upper halves of Table 3, Tab. 3a-b). Although several studies have observed associations between poor CG and frailty (Karanth, 2023), the CG measurements included in the current analysis only poorly reflected the Fried et al. physical frailty (Fig. 4c, column 'CG-'). Cognitive frailty itself is a subtype of frailty and focuses explicitly on neurological pathways, markers, and CG decline in susceptible patients (Panza et al., 2015). It is important to emphasize that while these features are ranked by importance within each model, their individual predictive value in isolation is modest. Their utility lies in their combined contribution to model performance, and we avoid over-interpreting such marginal associations, as our findings suggest that the combined feature importance is greater than the sum of each individual feature importance.

### 3.4. Subgroup-based models suggest different biomedical pre-frailty signatures

In our second setup of prediction exercises, we focused on the various origins of biomedical data to identify the best performing subgroup in each context. Although this approach disables the comparability between contexts, it allows us to compare subgroup performance to the complete data-driven models within each context. The single subgroup performances (see heatmap, Fig. 5) tested for PM-, BF-, NT-, and CG-related features show minimal improvement in the mixed-sex population. However, performance for men significantly improved when limited to PM-related biomedical features, whereas the women model moderately improved when limited to BF-related features (Fig. 4b). This observation supports the idea that frailty manifests differently between sexes, suggesting the need for sex-specific subtyping of physical frailty rather than based on deficits such as dementia, sarcopenia, metabolic dysfunction, or a particular insufficiency (Rockwood and Mitnitski,

2007; Fried et al., 2021; Liu et al., 2017; Woo et al., 2015; Church et al., 2020). The top-contributing features measured for the best-performing subgroup data-driven mixed-sex and sex-specific models depicted in Fig. 4d indicate that especially the men model identified a strong frailty signal based on physical characteristics of the body, notably the trunk fat mass (p-value = 3.72e-04), followed by the ALM-BMI ratio (p-value = 3.65e-10). Moreover, the remaining features suggest a high fat and low lean mass profile of men frailty development (coloured squares in Fig. 4d, for values see lower half of Table 3a). This observation of distinct body composition in pre-frail/frail participants aligns with the current literature but has not been specifically shown to be more relevant in men than women (Uchai et al., 2023; Xu et al., 2020). The women model only slightly improved using BF-related features, with vitamin D deficiency contributing by far the most to the model's performance, with over 4 % of CV score loss (p-value = 5.96e-04). Additionally, white blood cell counts such as monocytes (p-value = 2.41e-02), eosinophiles (p-value = 4.30e-03), and leukocytes (p-value = 4.95e-03) appear to be higher in pre-frail/frail women (coloured squares in Fig. 4d, for values see lower half of Table 3b). Vitamin D deficiency and anomalies in blood composition both have recently gained more attention regarding their associations with frailty, although not in the sex-specific context as reported here (Shardell et al., 2009; Zhou et al., 2016; Spira et al., 2019; Mitchell et al., 2022). These results support the hypothesis of sex-specific physical frailty, with men more likely to exhibit an imbalanced physical shape, whereas pre-frail/frail women are more likely to present physiological anomalies or deficits, such as elevated white blood cell counts or vitamin D deficiency. These results suggest a potential sarcopenia-frailty link in men, as low ALM and fat mass-lean mass imbalance are top contributors. In contrast, pre-frailty in women appears more related to exhaustion and physiological factors such as inflammation and hormonal status, pointing to depression and immune dysregulation as possible drivers.

### 3.5. Feature interactions reinforce distinct sex-specific pre-frailty mechanisms

Finally, we investigated the interacting relationships of the top ten contributing features that best describe the dispersion between the non-frail and pre-frail/frail participants in *men-PM* and *women-BF* models using the MANOVA additive formulation of the single features in relation to the Fried et al. frailty phenotype (Fig. 5). Both the men (Fig. 5a) and women (Fig. 5b) model show increasing separation of non-frail and pre-frail/frail participants with every added feature up to all ten. The p-values for the various combinations of features peak for the *men-PM* model using the five following features: ALM-BMI ratio, ALM, whole body total BMD, left arm BMC, and left arm lean mass (MANOVA p-value = 2.36e-16). Noticeably, the single feature of ALM-BMI ratio shows a significant dispersion already (MANOVA p-value = 9.40e-15), and consequently this feature is included in all top combination of features (see table below Fig. 5a). Regarding the *women-BF* model, the best combination of features consists of vitamin D deficiency, oestradiol level, eosinophil count, HDL cholesterol level, and deoxyypyridinoline in urine (MANOVA p-value = 9.21e-11). The best performing single feature remains vitamin D deficiency (MANOVA p-value = 1.40e-07), which is also included in all top combination of features (see table below Fig. 5b). With this approach, we substantiated the hypothesis that physical pre-frailty involves an accumulation of measurable deficits (Rockwood and Mitnitski, 2007; Lachmann et al., 2019), and that the nature of these deficits differs between sexes: in men, frailty aligns with traits of sarcopenia (ALM-BMI ratio, BMC, BMD), while in women, frailty aligns with hormonal insufficiency, immune activation, and exhaustion-related variables (white blood cell count, vitamin-D deficiency). Further analysis of the features' combinatory effect shows increasing separation of the pre-frail/frail from non-frail participants by the raw, PCA-, and LDA-transformed values with the one, two, five, and ten top features (Fig. 5), with the LDA version yielding overall the

highest BCD-WCD ratio. Although this simplified approach of combining and transforming features does not mimic the processing of our prediction pipeline (see Tab. S4 for details), it still reveals important insights into the sex-specific differences of the physical frailty profiles.

### 3.6. Sex-specific patterns in medication use and other frailty-associated features

In conclusion, we were able to identify sex-specific pre-frailty profiles in a cohort of individuals aged  $\geq 60$  years at the level of the Fried et al. 5-item frailty phenotype (Fig. 2), as well as at the level of currently known physical frailty-associated phenotypes (Fig. S1, Fig. S2, Table 1). Further analysis of this sex-specific divergence identified common, and more importantly, sex-specific frailty factors and patterns that subsequently improved the machine-learning-based prediction performance. Post-hoc analysis of the top-contributing features additionally revealed that pre-frail/frail participants are more likely to suffer from accumulated organ deficits and alcohol consumption behaviour as well as medication intake (Fig. S6, Fig. S7, Fig. S8). Concerning the latter, this suggests that pre-frail/frail women could require more medication due to possible higher disease burden or health-seeking behaviour. The

opposite effect in men indicates that men who are less frail are taking more medications, potentially due to effective management, proactive healthcare, or a mere survivor effect. These contrasting patterns in medication use between men and women may also reflect sex-specific differences in comorbidity burden or treatment adherence, which have already been reported in literature showing such disparities in older adults' care and outcomes (Reid et al., 2022; Hessey et al., 2020; Dallmeier et al., 2020; Verschoor et al., 2024; Karanth, 2023; Wang et al., 2024). However, the individual features show only very minor differences between the healthy and pre-frail/frail participants (Fig. S10). This suggests that the machine-learning-based trained profile of pre-frail/frail participants is rather based on the interplay between the top contributing features. As such, our final exercise on the simple additive feature combinations was able to highlight the differences in men and women pre-frailty given their physical body shape and BF-based physiological profile, respectively (Fig. 5, Fig. S11).

### 3.7. Study limitations and conceptual framework considerations

There are several limitations to this study. During data cleaning, a substantial number of features with available data for at least 80 % of

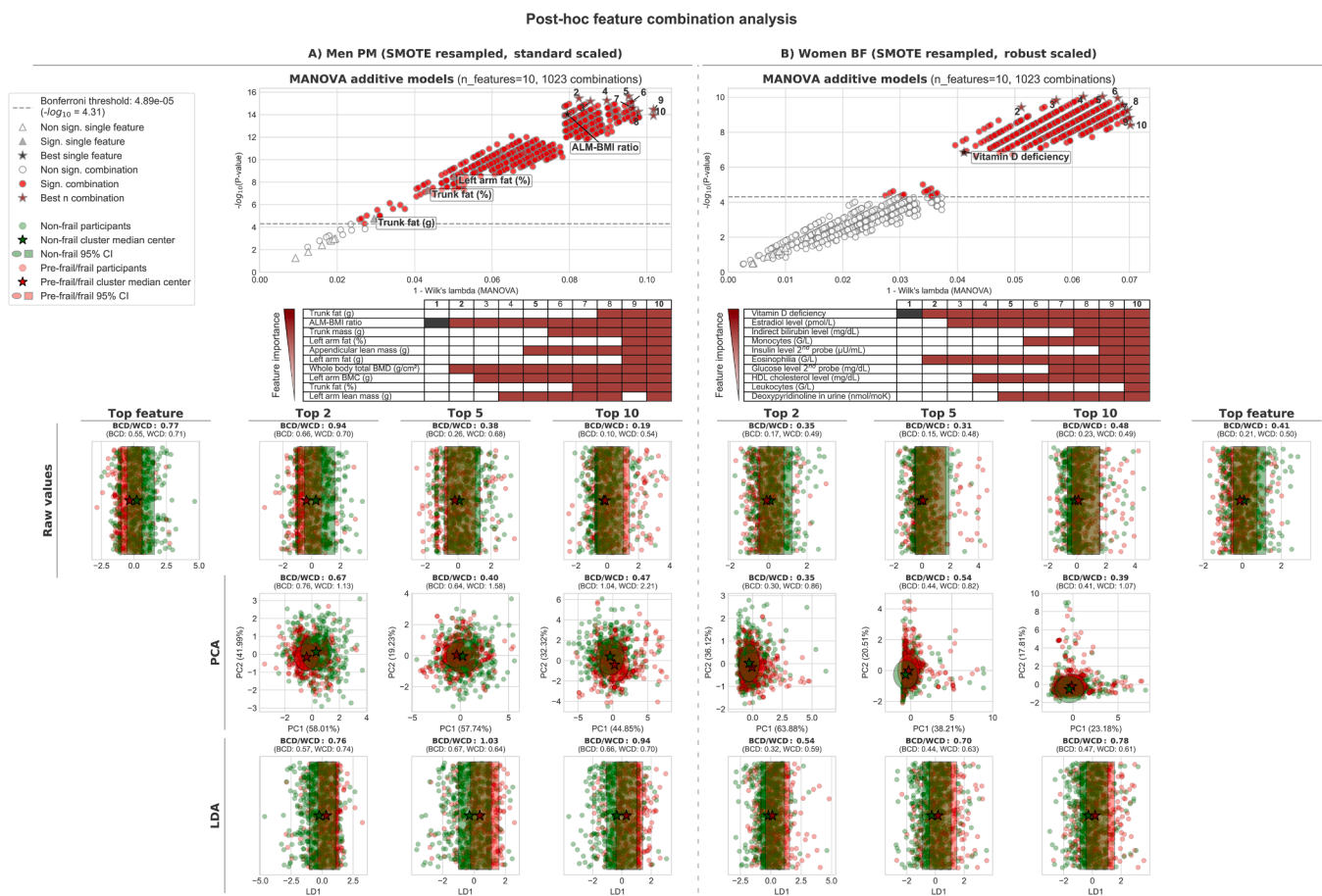


**Fig. 5.** Post hoc analysis of the best feature combinations shows increasing separation of the clusters between the best performing top single feature and the best combinations. The men (A) and women (B) subgroup data-driven models applied the respective sampling and scaling technique before undergoing MANOVA. Combinations from single to all ten features (1023 combinations in total) were tested and the performance was measured by the Wilk's lambda coefficient and represented as "1-Wilk's lambda". The resulting p-value was log base-10 transformed. Significant combinations are marked in red while the best performing set of n features are marked in dark red star shapes and annotated with the respective n. Single features are represented by triangles, with significant single features coloured in black. The table underneath the figure shows the top ten features in decreasing performance order and the components of the n best combinations are highlighted in dark red (black in case of single top significant feature). The p-value threshold of 0.05 was adjusted by the Bonferroni method and is visualized by the horizontal dashed line. Below the tables are the raw values, principal component analysis and linear discriminant analysis of the best single feature and the best combinations of two, five, and all ten features. The various representations are annotated with cluster distance characteristics to describe the separation and tightness of the non-frail (green) and frail (red) clusters. A 95 % CI is applied, and the cluster median centres are depicted in star shapes. BF body fluids, PM physical measurements, RUS random under-sampling, SMOTE synthetic minority over-sampling technique, sign. Significant, BCD between-cluster distance, WCD within-cluster distance.

participants needed imputation to retain as many participants as possible for the subsequent prediction analysis. We limited data leakage by imputing the train and test sets separately based on the statistical characteristics of the train set. Furthermore, the low number of participants affected by three or more *Fried et al.* frailty items (14 participants in total, 0.9 %) is a critical limitation to the statistical power and interpretation of findings related to full frailty. They have been merged with the pre-frail participants, potentially masking biomedical and pathophysiological constituents that could be able to describe not only the axis between non-frail and pre-frail/frail, but also the transition from pre-frail to frail in more detail. However, to mitigate the complete loss of these ‘true’ frail participants and their values, and to avoid resampling for this very small subset, pre-frail and frail participants were merged in one single category. Despite this, we were still able to investigate the performance of our binary-targeted models on the three original *Fried et al.* labels and showed that in fact the models were able to predict nearly all frail and most pre-frail participants correctly (Fig. 6). Here, the identified predictors in the combined pre-frail/frail models remain significantly predictive in the much smaller frail subgroup with increased sensitivities compared to the pre-frail subgroup. However, as the merged category is dominated by pre-frail participants, the present results reflect biomarkers of pre-frailty, not frailty. Pre-frail and frail are distinct clinical stages, and future studies with larger frail cohorts will be required to extend these findings to fully developed frailty. Another machine-learning-based limitation is the cross-validated scoring system in the case of imbalanced datasets, as after merging pre-frail and frail, there are still twice as many non-frail participants in the cleaned dataset. We addressed these limitations by selecting a validation score that prioritizes recall over precision, namely the F-β-2 score (see Eq. 2) and considered under- and over-sampling techniques during the training process to mitigate the data imbalance in BASE-II. Still, since the available biomedical feature space spans predictors that can be linked to Rockwood’s frailty index and accumulation of deficit model (Rockwood et al., 1994; Rockwood and Mitnitski, 2007), we acknowledge this conceptual discrepancy as potential source of overfitting or model bias, particularly when interpreting biomedical contributors to the *Fried et al.* frailty phenotype. We therefore framed our findings as exploratory and hypothesis-generating. Another major limitation of this study is the cross-sectional nature of the biomedical data used in the current analysis, meaning that they only reflect a snapshot of the participants. Having access to multiple cross-sections at different timepoints would be important and interesting, e.g., it could help to investigate whether the false-positive participants would later develop frailty or not. Moreover importantly, our models were only validated using cross-validation techniques within the BASE-II cohort, and external validation in an

independent dataset is needed to confirm generalizability of the presented predictors. Finally, the analysis of the top feature combinations as shown with MANOVA is not exactly representing the model behaviour as it did during the training process. Instead, it is a simpler, linear, and independent representation of the combined features’ power to separate healthy from pre-frail/frail participants by simple addition of their scaled values, PCA-driven, and LDA-driven data transformation (Fig. 5). Altogether, further research is required to better understand the sex-specific differences in pre-frailty that we have thoroughly observed and analysed in BASE-II.

#### 4. Materials and methods

##### 4.1. BASE-II participants and frailty phenotype

BASE-II is an observational study including 2200 participants from age 20–35 and 60–85, recruited between 2009 and 2015 in the greater Berlin area, Germany (see <https://www.base2.mpg.de/en>, and references (Bertram et al., 2014; Baltes and Mayer, 1998; Demuth et al., 2021)). All BASE-II participants provided written informed consent before participation, and the study was conducted in accordance with the Declaration of Helsinki and approved by the Ethics Committee of the Charité – Universitätsmedizin Berlin (approval number EA2/029/09; date of approval: 19 March 2009). Participants attended a wide range of examinations resulting in the rich collection of psychological, genetic, medical, socioeconomic, and immunological data. Frailty in BASE-II was measured by the 5-item *Fried et al.* frailty phenotype (Fried et al., 2001), composed of the clinical variables WL, PA, EX, GS, and GA, with adjustments described in Spira et al (Spira et al., 2015). (see Tab. S1). The presence of frailty was determined with the below Eq. (1) as the sum of positive frailty-related phenotypes to give a frailty score ( $FR_{score}$ ).

$$FR_{score} = WL + PA + EX + GS + GA \tag{1}$$

The *Fried et al.* frailty phenotype is derived from the resulting  $FR_{score}$  and participants are labelled as either non-frail (level 0,  $FR_{score} = 0$ ), pre-frail (level 1,  $FR_{score} \in \{1; 2\}$ ), or frail (level 2,  $FR_{score} \geq 3$ ).

##### 4.2. Data cleaning

In this study, a cross-section of the BASE-II cohort was analysed with a focus on the clinical and socioeconomic characteristics of the older study population. Data cleaning included the removal of features with low data coverage and participants missing the information to determine the frailty phenotype, engineering of features for clinically relevant characteristics linked to frailty risk factors (i.e., vitamin D

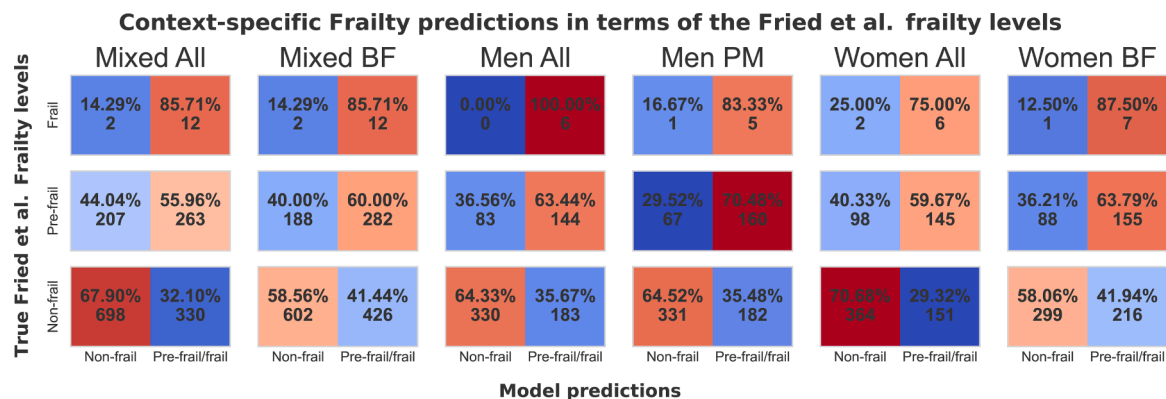


Fig. 6. Context-specific frailty predictions in terms of the *Fried et al.* frailty phenotype levels. Each model’s prediction performance of true frail, pre-frail, and non-frail are shown as number and percentage of the total context-specific BASE-II population, combining the training and test set participants. The best *mixed-BF* model yields sensitivities of 60.0 % in the pre-frail and 85.7 % in the frail subgroup, with a false positive rate (FPR) of 41.4 % and specificity of 58.9 %. The best *men-PM* model yields sensitivities of 70.5 % in the pre-frail and 83.3 % in the frail subgroup, with a FPR of 35.5 %, and specificity of 64.5 %. The best *women-BF* model yields sensitivities of 63.8 % in the pre-frail and 87.5 % in the frail subgroup, with a FPR of 41.9 %, and specificity of 58.1 %.

deficiency (Shardell et al., 2009; Zhou et al., 2016; Spira et al., 2019), polypharmacy including reported drug side-effects, allergies, and drug-specific disease area (Gutiérrez-Valencia et al., 2018; Nwadiugwu, 2020; König et al., 2018), and poly-dependency (Abreu et al., 2019)); the labelling of feature subgroups (10 subgroups: individual medications (IM), individual devices (ID), grouped medications (GM), surveys (SV), chronic morbidity (CH), grouped devices (GD), NT, PM, BF, and CG (Fig. 3a); splitting into training and test set; and imputation of the remaining missing values. With the scope of this study being the prediction of pre-frailty in older people, and the literature especially showing phenotypic relationships between older age groups and frailty (Lally and Crome, 2007; Clegg et al., 2013; Fulop et al., 2010; Rockwood et al., 1994; Abizanda et al., 2016; Holliday, 1995; Fedarko, 2011; Fhon et al., 2018), participants of age 60 or above were retained. Of the initial 2171 participants with baseline data assessed in the medical part of BASE-II, 1671 satisfy this criterion.

#### 4.2.1. Handling missing values and redundancies

In general, features with more than 20 % of missing values are considered not informative enough to describe the entire dataset for the task of training a prediction model (Broeck et al., 2005; Eekhout et al., 2012). Of the initial 975 raw BASE-II features, 555 features had more than 20 % of missing values. Among those features, 506 binary variables are related to specific medication intake or using a specific helping device (1 = yes, 0 = no). Due to the large number of such features and their sparsity (most participants reported using only a few), we later aggregated them into counts of total helping devices and total medication per target disease (see Section 4.2.3). For these features, missing values were likely the result of non-response rather than actual usage, and we therefore treated missing values as negative response. In contrast, 40 other features related to clinical walking assessments were missing for most participants. The disruption in these features due to changes in the methodology, leaving them unusable for classification. The remaining 9 features with low coverage were redundant and thus discarded. With 919 remaining features having missing value coverage of less than 20 %, one additional feature related to sex was removed due to redundancy, being available both in Boolean (0 = men, 1 = women) and discrete form (1 = men, 2 = women). Furthermore, 159 participants were missing one or multiple frailty-related phenotypes necessary for Eq. (1) and were therefore removed. After handling the features with missing values and redundancies in BASE-II, the size of the dataset was reduced to 1512 participants and 918 features.

#### 4.2.2. Feature engineering

Feature engineering was performed to reduce the sparsity within the IM and ID features, and to combine the available measurements for two different methodologies of measuring 25-hydroxy-vitamin D levels in serum conducted in BASE-II. The IM subgroup constituted 452 features in total, reflecting various information on 124 drugs, including name, administered dose, active substance, and experienced side-effects. Like the approach of König et al. (König et al., 2018), we engineered the raw medication intake counts as a new feature called polypharmacy (ranging from 0 to 15) and summed up the number of experienced side-effects and allergies for each participant as cumulative side-effects (ranging from 0 to 3) and cumulative allergies (ranging from 0 to 2).

Furthermore, the drug-related disease area of the 124 drugs described in BASE-II was determined using the Drug Repurposing Hub of the Broad Institute (version of 24th May 2021, see <https://clue.io/repurposing-app>, and reference (Corsello et al., 2017)), a curated collection of more than 6700 drugs, either FDA-approved or in clinical trial, as well as the Drug Information Database Drugs.com (see <https://www.drugs.com/drug-information.html>, and reference (Leah Plumb, 2004)). With all correct FDA-approved names at hand, we extracted 93 unique drug interactions, 77 unique modes of action, and 18 disease areas. To effectively reduce the number of features related to IM, only the targeted disease area was retained (cardiology, dental, dermatology,

endocrinology, gastroenterology, haematology, infectious disease, metabolism, nephrology, neurology/psychiatry, obstetrics/gynaecology, oncology, ophthalmology, orthopaedics, otolaryngology, pulmonary, rheumatology, and urology). The number of drugs targeting the same disease area was computed for each participant, ranging up to a maximum of 7 drugs (cardiology). Besides IM-derived polypharmacy, an identical approach was used to transform the ID information of the BASE-II participants (including 55 distinct assistive or helping devices) into the single feature poly-dependency, shown previously to be linked with medication intake, overcoming physical disabilities, moderate or severe frailty, and dementia (Abreu et al., 2019; Tomita et al., 2004).

Then, two low-coverage features related to 25-hydroxy-vitamin D levels in blood were identified in BASE-II with complementary missing values, representing two distinct measuring methods conducted during the study. As both features showed similar distributions, they were merged before computing the standard z-score, creating a new normally distributed feature of vitamin D levels. In addition to the merged z-score values, another binary feature representing vitamin D deficiency was engineered based on 25-hydroxy-vitamin D levels according to the recommendations of the Institute of Medicine (Spira et al., 2019; Ross et al., 2011), reporting 50 nmol/L or less as a threshold for vitamin D deficiency.

Lastly, the feature of interest, frailty phenotype, was scaled down from the three initial levels non-frail ( $FR_{score} = 0$ ;  $N = 1028$ ), pre-frail ( $2 \geq FR_{score} \geq 1$ ;  $N = 470$ ), and frail ( $FR_{score} \geq 3$ ;  $N = 14$ ) to only two levels, the non-frail and pre-frail/frail group. Latter combines both pre-frail and frail, totalling 484 participants. This combination was necessary due to a pronounced imbalance between the three groups, a circumstance that could potentially exert a detrimental influence on the performance of machine-learning-based classification. Importantly, since this merged category consists almost entirely of pre-frail individuals, results of this study should be interpreted as predictors of pre-frailty. No reliable inference about fully developed frailty is possible from this data.

Following feature engineering, the BASE-II dataset dimensions increased from 918 to 942 by 21 GM (side-effects, allergies, multiple disease areas and polypharmacy), one GD (poly-dependency), and two vitamin D-related engineered features (vitamin D level z-score and vitamin D deficiency status).

#### 4.2.3. Stratified data splitting and imputation

Stratified splitting of the reshaped dataset was performed generating a training and hold-out test set with an 80-to-20 ratio using MATLAB's Statistics and Machine-learning Toolbox *cvpartition* function with the hold-out method. This method ensures to preserve the same class distribution in both sets and prevents bias in the model due to imbalanced class proportions (non-frail to pre-frail/frail ratio in complete BASE-II: 2.12, training: 2.18, test: 1.90). Of the 1512 participants (746 men, 766 women), 1210 composed the training set (593 men, 617 women), and 302 the test set (153 men, 149 women). Imputation was then performed in both training and test sets based on the information from the training set only. Discrete and binary features in the training and test set were imputed using the mode, while continuous features were imputed using the mean of the training set given their non-skewed distributions (Amballa, 2020).

#### 4.3. Data processing

After the data has been cleaned and imputed, cohort characteristics were first computed for the most important frailty-related variables according to the literature, including sex (Spira et al., 2019; Gordon et al., 2017), age (Fulop et al., 2010; Fedarko, 2011), ALM, ALM-to-BMI ratio and sarcopenia (Spira et al., 2015; Fhon et al., 2018; Uchai et al., 2023); as well as heart insufficiency (Uchmanowicz et al., 2014; Sze et al., 2019), vitamin D deficiency (Shardell et al., 2009; Zhou et al., 2016; Spira et al., 2019), morbidity index (Espinoza et al., 2018; Tenison

and Henderson, 2020; Yarnall et al., 2017), and polypharmacy (Gutiérrez-Valencia et al., 2018; Nwadiugwu, 2020; König et al., 2018). Subsequently, the dataset was cleared from features used for feature engineering then split by sex and partitioned by the subgroups that have the most available information (PM, NT, CG, BF). Furthermore, we removed constant and highly correlated features within each sex- and context-specific combination. This data processing part is the first main step of the pipeline we have created for this study (see [https://github.com/sysbiolux/Clinical\\_Biomarker\\_Detection](https://github.com/sysbiolux/Clinical_Biomarker_Detection)) and is an indispensable step before applying machine-learning-based strategies for classification in the second step. Data processing and machine-learning were performed using the python programming language and the High-Performance Computing (HPC) facilities of the University of Luxembourg (see <https://hpc.uni.lu/>, and reference (Varrette et al., 2022)).

#### 4.3.1. BASE-II cohort characteristics

In Table 1, we conducted comparative analysis of the cohort characteristics between the non-frail and pre-frail/frail participants in mixed-sex, men, and women. The statistical significance between each group was computed using the Welch's unequal variance T-test (WELCH, 1947) (with the equality of variance determined by the Levene's test) for continuous features, and the Cramér's V correlation algorithm (Cramér, 1946) corrected for binary and discrete feature data types (Bergsma, 2013). The characteristics are either presented in mean and standard deviation (continuous features), or the counts of the categories (binary and discrete), and their interquartile range (discrete).

#### 4.3.2. Data filtering and partitioning

Of the 942 cleaned and imputed cohort features, the two sparse subgroups IM ( $N = 453$ ) and ID ( $N = 55$ ) were taken care of during the feature engineering and thus were removed from the dataset. Additionally, seven features related to the Fried et al. frailty phenotype were removed as they directly or indirectly represent the five frailty characteristics WL, PA, GS, GA, and EX, as well as the resulting  $FR_{score}$ . The reduced dataset is further separated by sex, resulting in three distinct datasets: mixed-sex, men, and women. While each dataset underwent a classification exercise using all remaining subgroups, denoted 'ALL', we additionally conducted context-specific experiments for the largest subgroup datasets, namely BF, PM, NT, and CG ( $N \geq 40$ ), resulting in 15 distinct models (Fig. 3a-b).

#### 4.3.3. Removing constant and near-constant features

A first round of quality checks of the partitioned datasets consisted of the identification of strictly constant (identical) features or near-constant (extremely low variance-to-mean ratio or positive cases) features (see Fig. 3c). For each analytical context (mixed-sex, men, women), only a very few strictly constant features were identified and thus removed. Considering near-constant features, two distinctions were made to identify them either within the continuous features or the binary and categorical features. In the realm of continuous features, two arbitrary thresholds were considered to define near-constancy by using the variance-to-mean ratio of 0.01 and 0.001 as cut-off. With this, only features were kept that, considering their mean, show at least a 1 % or 0.1 % variance to it within the population. All datasets and partitions thereof were assessed for both suggested thresholds, and the best performing thresholds were retained. Near-constant binary or categorical features were removed if the lowest class count is below the number of CV splits applied in the machine-learning part, which was set to 10 splits. A more detailed summary of the number of constant and near-constant features that have been removed in each model can be reviewed in the supplementary files (Tab. S2).

#### 4.3.4. Removing highly correlated features

A subsequent round of quality check of the datasets and partitions thereof aimed to identify and remove features that are highly correlated

to each other based on predefined correlation coefficient thresholds for every possible data-type association. Not only was the dimensionality of each dataset further reduced by this step, but it was also cleaned of redundant features that would not necessarily bring additional information to the models but rather make it more complex and more prone for the risk of errors. Three different data-type associations were considered, and their correlations computed appropriately: the continuous-continuous associations using the Spearman rank coefficient (Spearman, 1904), the categorical-categorical associations using the Cramér's V correlation coefficient corrected for binary and discrete feature, and the continuous-categorical associations using the point bi-serial correlation coefficient (Glass and Hopkins, 1996). For each of the three associations, multiple thresholds were tested and the thresholds leading to the best performing downstream classifications were retained (see Fig. 3d-e, and supplementary figures Fig. S3a-b). For continuous-categorical associations, the features removed were always selected from the group of continuous features. The number of features removed in each category can be reviewed in the supplementary files (Tab. S2).

#### 4.4. Machine-learning

The second main part of the pipeline is dedicated to the machine-learning-based classification. Due to the imbalance of frailty in BASE-II, the datasets were resampled based on two distinct approaches: RUS and SMOTE (Chawla et al., 2002). Then, feature scaling and dimensionality reduction were applied. We assessed three scaling strategies (min-max, standard, and robust scaler) and retained for each dataset the strategy that contributed to the best prediction performance of frailty. Reducing the dimensionality was performed using the two linear approaches of PCA and LDA, as well as the non-linear kernel PCA for continuous features, whereas discrete features were directly selected using the  $k$  best features correlated to the frailty phenotype target. Therefore, we assessed two different correlation statistics, namely chi-squared ( $\chi^2$ ) and Cramér's V correlation coefficient corrected for binary and discrete data types. As the order of manipulations (resampling and feature transformation) can affect the prediction performance and no preferred order is given for the scenario of imbalance classification (Zhang et al., 2017), we assessed both possibilities and observed that first resampling followed by feature transformation was always the more performant strategy to predict frailty.

The resampled and transformed datasets were then passed to a SVM classifier (Boser et al., 1992) using linear and non-linear kernels. The best-fitting model parameters in each scenario were identified using the exhaustive CV grid search method for large ranges of hyper-parameter values (Fig. 3e). Model selection was based on the best CV F- $\beta$ -2 score during training, which emphasizes recall twice as much as precision (see Eq. 2), making it particularly suitable for tasks where minimizing false negatives is a high priority in imbalanced datasets.

$$F_{\beta} = (1 + \beta^2) * \frac{\text{precision} * \text{recall}}{(\beta^2 * \text{precision}) + \text{recall}} \quad (2)$$

Each model was evaluated using multiple metrics during the CV, the training process, and within the hold-out validation test set (Fig. 3f). These metrics include the ROC, diagnostics odds ratio (DOR), true positives (TP), and true negatives (TN). From the best models, feature contributions were assessed using feature permutation, which measures the difference in model CV training score when single feature values are randomly permuted to mimic a perturbation in the machine-learning based prediction system (Breiman, 2001). A detailed summary of the minimum information for medical artificial intelligence reporting (see (Hernandez-Boussard et al., 2020)) can be found in Tab. S3.

#### 4.4.1. Hyper-parameter optimization and stratified k-fold cross-validation

Hyper-parameter optimization and stratified k-fold CV were

performed using exhaustive grid search of preselected parameter ranges (see Tab. S4) using stratified 10-fold CV while training, and the F- $\beta$ -2 scorer (see Eq. 2). For each partition of the data (by sex and by feature subgroups), we documented the most suitable models and restricted their optimal parameters to a more limited range. This process of constraint iteration was repeated up to four times, depending on whether it could lead to enhanced performance of the model. For the combined subgroups model, the best performance was achieved after one single iteration in the case of the mixed-sex and men model, after the third one in the women model, and the fourth one in the other subgroup-specific models.

#### 4.4.2. Measuring feature importance

For each optimized model, feature importance was assessed using systematic feature permutation, in which features were randomized individually at least 500 times, and the resulting CV score are compared to the original ones. The contribution of each feature is represented by the mean and standard deviation of change of the optimized CV score after shuffling. Feature robustness was determined via z-score. We limited the analysis of the best contributing features to only the top thirty features with the largest change in CV score. Importantly, permutation scores reflect the relative significance of individual feature in the model, not their standalone predictive power.

#### 4.4.3. Subsequent feature extractions that improved sex-specific models

Next, we further investigated the top features for each model. The top thirty features were reused as input features, and two to three context-specific hallmarks were further added if they were not already within these thirty features. This approach improved the prediction performance in specific contexts: subgroup-driven men model using PM, and all-driven women models using all clinical subgroups combined. In the PM subgroup-driven men model, the raw ALM in grams and kilograms were added to the thirty most contributing features and showed a higher performance using the same information in two different units. For the all-driven women model, raw ALM in kilograms, vitamin D deficiency and vitamin D levels z-score were added. These models also underwent hyper-parameter optimization to constraint the parameters and further enhance the performance, which was observed after two iterations in both cases.

#### 4.4.4. Multi-variate model evaluation

All hyper-parameterisation exercises used the F- $\beta$ -2 scorer to evaluate the stratified 10-fold CV and select the best fitting model. Although this scorer prioritizes recall over precision, it does not guarantee that the model with the highest F- $\beta$ -2 score has a better recall than precision. As this was observed in early experiments. To address this, we supplemented the CV evaluation with independent five times 10-fold CV ROC and precision-recall (PR) curves to better assess the training performance. In addition to CV, F- $\beta$ -2, ROC, and PR were measured for the overall training performance and the hold-out validation test set. DOR, F- $\beta$ -1, and accuracy were also measured in the overall training and test set. TP and TN were recorded from the hold-out test set as well.

#### 4.4.5. Post-hoc feature contribution analysis

The ten most contributing features for each model were analysed for their individual and combined influence on the distinction between non-frail and pre-frail/frail participants in the training set. This included deficits (vitamin D deficiency, heart insufficiency, and sarcopenia) in the mixed-sex model, medication intake (ophthalmology and gastroenterology) in the men model, and alcohol intake in the women model. In each case, the proportion of pre-frail/frail participants is represented in the respective figures. Associations between the individual top continuous features and the frailty phenotype were analysed in a combined error bar and letter-value plot for the non-frail and pre-frail/frail mixed-sex, men, and women. The mean z-score difference between pre-frail/frail and non-frail participants of all available continuous features was

plotted and significant top ten features were highlighted. For the non-continuous features, the Cramér's V correlation coefficient corrected for binary and discrete data types was plotted with a significance threshold of 0.10. In both exercises the p-value thresholds were adjusted using the Bonferroni method. Feature combinations were then analysed using the linear MANOVA method (formula: " $feature_1 + feature_2 + \dots + feature_n \sim target$ "), reporting Wilk's lambda coefficient as well as the best combinations ( $1 \leq n \leq 10$ ). Given the multifactorial nature of frailty, this post-hoc analysis allowed us to evaluate the collective contribution of selected features, aiming to identify combinations with enhanced discriminatory power beyond what univariate analyses could capture (Beam et al., 2015). In the examples of the *men-PM* and *women-BF* models, the resulting combinations of the best two, five, and all ten features were plotted as raw values and in the form of reduced dimensions using PCA and LDA to showcase how well they separate non-frail from pre-frail/frail participants.

#### CRedit authorship contribution statement

**Schneider Jochen G:** Writing – review & editing, Formal analysis, Conceptualization. **Ali Kishk:** Writing – review & editing, Conceptualization. **Maria Pires Pacheco:** Writing – review & editing, Conceptualization. **Sébastien De Landtsheer:** Writing – review & editing, Formal analysis, Conceptualization. **Ilja Demuth:** Writing – review & editing, Data curation, Conceptualization. **Dominik Spira:** Writing – review & editing, Data curation, Conceptualization. **Graham Pawelec:** Writing – review & editing, Data curation, Conceptualization. **David Goldeck:** Writing – review & editing, Data curation, Conceptualization. **Jeff Didier:** Writing – review & editing, Writing – original draft, Visualization, Validation, Software, Resources, Methodology, Investigation, Formal analysis, Data curation, Conceptualization. **Thomas Sauter:** Writing – review & editing, Supervision, Funding acquisition, Formal analysis, Conceptualization.

#### Author contributions

All authors have contributed to the study conception and design. Material preparation was done by JD, data contribution by DG, GP, DS, and ID, and analysis by JD, SDL, JGS, and TS. The first draft of the manuscript was written by JD with contributions from SDL, AK, and MPP. All authors read and approved the final manuscript for submission.

#### Declaration of Competing Interest

No financial or non-financial conflicts of interest have been identified for disclosure purposes.

#### Acknowledgments

The experiments presented in this paper were carried out using the High-Performance Computing (HPC) facilities of the University of Luxembourg (see <https://hpc.uni.lu/>, and reference (Varrette et al., 2022)). The authors would like to thank the steering committee of BASE-II and the BASE-II participants.

The Doctoral Training Unit Data-driven computational modelling and applications (DRIVEN) is funded by the Luxembourg National Research Fund under the PRIDE program (PRIDE17/12252781). This article uses data from the Berlin Aging Study II (BASE-II) which was supported by the German Federal Ministry of Education and Research under grant numbers #01UW0808; #16SV5536K, #16SV5537, #16SV5538, #16SV5837, #01GL1716A and #01GL1716B.

#### Appendix A. Supporting information

Supplementary data associated with this article can be found in the online version at [doi:10.1016/j.mad.2025.112114](https://doi.org/10.1016/j.mad.2025.112114).

## Data availability

The authors do not have permission to share data.

## References

- Abizanda, P., Romero, L., Sánchez-Jurado, P.M., Ruano, T.F., Ríos, S.S., Sánchez, M.F., 2016. Energetics of aging and frailty: the FRADEA study. *J. Gerontol. Ser. A* 71 (6), 787–796.
- Abreu, W., Tolson, D., Jackson, G.A., Staines, H., Costa, N., 2019. The relationship between frailty, functional dependence, and healthcare needs among community-dwelling people with moderate to severe dementia. *Health Soc. Care Commun.* 27 (3), 642–653.
- Akbari, G., Nikkhou, M., Wang, L., Chen, C.P.C., Han, D.S., Lin, Y.H., et al., 2021. Frailty level classification of the community elderly using microsoft Kinect-Based skeleton pose: a machine learning approach. *Sensors* 21 (12), 4017.
- Amballa, A., 2020. Feature engineering Part-1 mean/ median imputation. *Analytics Vidhya*. (<https://medium.com/analytics-vidhya/feature-engineering-part-1-mean-median-imputation-761043b95379>).
- Baltes, P.B., Mayer, K.U. (Eds.), 1998. *The Berlin Aging Study: Aging from 70 to 100* [Internet]. Cambridge University Press, Cambridge. (<https://www.cambridge.org/core/books/berlin-aging-study/B1641E71F86F59A1A20BBE8824CB2EE5>).
- Beam, A.L., Motsinger-Reif, A.A., Doyle, J., 2015. An investigation of gene-gene interactions in dose-response studies with Bayesian nonparametrics. *BioData Min.* 6.
- Bergsma, W., 2013. A bias-correction for Cramér's V and Tschuprow's T. *J. Korean Stat. Soc.* 42 (3), 323–328.
- Bertram, L., Böckenhoff, A., Demuth, I., Düzel, S., Eckardt, R., Li, S.C., et al., 2014. Cohort profile: the Berlin aging study II (BASE-II). *Int. J. Epidemiol.* 43 (3), 703–712.
- Boser, B.E., Guyon, I.M., Vapnik, V.N., 1992. A training algorithm for optimal margin classifiers. *Proceedings of the fifth annual workshop on Computational learning theory* [Internet]. Association for Computing Machinery, New York, NY, USA, pp. 144–152 (COLT '92). Available from: <https://dl.acm.org/doi/10.1145/130385.130401>.
- Breiman, L., 2001. Random forests. *Mach. Learn.* 45 (1), 5–32.
- Broeck, J.V., den, Cunningham, S.A., Eeckels, R., Herbst, K., 2005. Data cleaning: detecting, diagnosing, and editing data abnormalities. *PLOS Med.* 2 (10), e267.
- Buchmann, N., Spira, D., König, M., Demuth, I., Steinhagen-Thiessen, E., 2019. Frailty and the metabolic syndrome — results of the Berlin aging study II (BASE-II). *J. Frailty Aging* 8 (4), 169–175.
- Chawla, N.V., Bowyer, K.W., Hall, L.O., Kegelmeyer, W.P., 2002. SMOTE: synthetic minority over-sampling technique. *J. Artif. Int. Res.* 16 (1), 321–357.
- Chen, X., Mao, G., Leng, S.X., 2014. Frailty syndrome: an overview. *Clin. Interv. Aging* 9, 433–441.
- Church, S., Rogers, E., Rockwood, K., Theou, O., 2020. A scoping review of the clinical frailty scale. *BMC Geriatr.* 20 (1), 393.
- Clegg, A., Young, J., Iliffe, S., Rikkert, M.O., Rockwood, K., 2013. Frailty in elderly people. *Lancet* 381 (9868), 752–762.
- Collard, R.M., Boter, H., Schoevers, R.A., Oude Voshaar, R.C., 2012. Prevalence of frailty in community-dwelling older persons: a systematic review. *J. Am. Geriatr. Soc.* 60 (8), 1487–1492.
- Corsello, S.M., Bittker, J.A., Liu, Z., Gould, J., McCarren, P., Hirschman, J.E., et al., 2017. The drug repurposing hub: a next-generation drug library and information resource. *Nat. Med.* 23 (4), 405–408.
- Cramér, H., 1946. *Mathematical methods of statistics*. Princeton University Press, p. 598.
- Dallmeier, D., Braisch, U., Rapp, K., Klenk, J., Rothenbacher, D., Denking, M., et al., 2020. Frailty index and sex-specific 6-year mortality in community-dwelling older people: the ActiFE study. *J. Gerontol. A Biol. Sci. Med. Sci.* 75 (2), 366–373.
- Demuth, I., Banzarus, V., Drexelies, J., Düzel, S., Seeland, U., Spira, D., et al., 2021. Cohort profile: follow-up of a Berlin aging study II (BASE-II) subsample as part of the GendAge study. *BMJ Open* 11 (6), e045576.
- Di Sabatino, A., Lenti, M.V., Cammalleri, L., Corazza, G.R., Pilotto, A., 2018. Frailty and the gut. *Dig. Liver Dis.* 50 (6), 533–541.
- Dibello, V., Zupo, R., Sardone, R., Lozupone, M., Castellana, F., Dibello, A., et al., 2021. Oral frailty and its determinants in older age: a systematic review. *Lancet Healthy Longev.* 2 (8), e507–e520.
- Eekhout, I., de Boer, R.M., Twisk, J.W.R., de Vet, H.C.W., Heymans, M.W., 2012. Missing data: a systematic review of how they are reported and handled. *Epidemiology* 23 (5), 729.
- Espinoza, S.E., Quiben, M., Hazuda, H.P., 2018. Distinguishing comorbidity, disability, and frailty. *Curr. Geriatr. Rep.* 7 (4), 201–209.
- Fedarko, N.S., 2011. The biology of aging and frailty. *Clin. Geriatr. Med.* 27 (1), 27–37.
- Fhon, J.R.S., Rodrigues, R.A.P., Santos, J.L.F., Diniz, M.A., dos Santos, E.B., Almeida, V.C., et al., 2018. Factors associated with frailty in older adults: a longitudinal study. *Rev. Saúde Pública* 52, 74.
- Fried, L.P., Tangen, C.M., Walston, J., Newman, A.B., Hirsch, C., Gottdiener, J., et al., 2001. Frailty in older adults: evidence for a phenotype. *J. Gerontol. Ser. A* 56 (3), M146–M157.
- Fried, L.P., Cohen, A.A., Xue, Q.L., Walston, J., Bandeen-Roche, K., Varadhan, R., 2021. The physical frailty syndrome as a transition from homeostatic symphony to cacophony. *Nat. Aging* 1 (1), 36–46.
- Fulop, T., Larbi, A., Witkowski, J.M., McElhane, J., Loeb, M., Mitnitski, A., et al., 2010. Aging, frailty and age-related diseases. *Biogerontology* 11 (5), 547–563.
- Glass, G.V., Hopkins, K.D., 1996. *Statistical methods in education and psychology* [Internet]. Allyn and Bacon, Boston, p. 698. (<http://archive.org/details/statisticalmeth00glas>) (Available from).
- Gomez-Cabrero, D., Walter, S., Abugessaisa, I., Miñambres-Herraiz, R., Palomares, L.B., Butcher, L., et al., 2021. A robust machine learning framework to identify signatures for frailty: a nested case-control study in four aging european cohorts. *GeroScience* 43 (3), 1317–1329.
- Gordon, E.H., Peel, N.M., Samanta, M., Theou, O., Howlett, S.E., Hubbard, R.E., 2017. Sex differences in frailty: a systematic review and meta-analysis. *Exp. Gerontol.* 89, 30–40.
- Gutiérrez-Valencia, M., Izquierdo, M., Cesari, M., Casas-Herrero, Á., Inzitari, M., Martínez-Velilla, N., 2018. The relationship between frailty and polypharmacy in older people: a systematic review. *Br. J. Clin. Pharmacol.* 84 (7), 1432–1444.
- Hernandez-Boussard, T., Bozkurt, S., Ioannidis, J.P.A., Shah, N.H., 2020. MINIMAR (MINimum Information for Medical AI Reporting): developing reporting standards for artificial intelligence in health care. *J. Am. Med. Inf. Assoc.* 27 (12), 2011–2015.
- Hessey, E., Montgomery, C., Zuege, D.J., Rolfsen, D., Stelfox, H.T., Fiest, K.M., et al., 2020. Sex-specific prevalence and outcomes of frailty in critically ill patients. *J. Intensive Care* 8 (1), 75.
- Holliday, R., 1995. *Understanding ageing* [Internet]. Developmental and Cell Biology Series. Cambridge University Press, Cambridge. (<https://www.cambridge.org/core/books/understanding-ageing/7C795DA1F52124A30E0F6A6278A4C8E8>).
- Howlett, S.E., Rutenberg, A.D., Rockwood, K., 2021. The degree of frailty as a translational measure of health in aging. *Nat. Aging* 1 (8), 651–665.
- Idris S., Badruddin N. Classification of Cognitive Frailty in Elderly People from Blood Samples using Machine Learning. In: 2021 IEEE EMBS International Conference on Biomedical and Health Informatics (BHI). 2021. p. 1–4.
- Karanth, S.D., 2023. Sex-specific association of physical frailty and cognitive function in a population-based cross-sectional study of American older adults. *Alzheimers Dement* 19 (S6), e068336.
- Koenig M., Malsch C., Marino J., Vetter V.M., Komleva Y., Demuth I., et al. Nocturia as a Risk Factor for Developing Frailty in Older Adults: Results of the Berlin Aging Study II [Internet]. medRxiv; 2024 [cited 2024 Sep 24]. p. 2024.09.20.24313292. Available from: (<https://www.medrxiv.org/content/10.1101/2024.09.20.24313292v1>).
- König, M., Spira, D., Demuth, I., Steinhagen-Thiessen, E., Norman, K., 2018. Polypharmacy as a risk factor for clinically relevant sarcopenia: results from the Berlin aging study II. *J. Gerontol. Ser. A* 73 (1), 117–122.
- Lachmann, R., Stelmach-Mardas, M., Bergmann, M.M., Bernigau, W., Weber, D., Pischon, T., et al., 2019. The accumulation of deficits approach to describe frailty. *PLOS ONE* 14 (10), e0223449.
- Lally, P., Cromie, P., 2007. Understanding frailty. *Post. Med. J.* 83 (975), 16–20.
- Laur, C.V., McNicholl, T., Valaitis, R., Keller, H.H., 2017. Malnutrition or frailty? Overlap and evidence gaps in the diagnosis and treatment of frailty and malnutrition. *Appl. Physiol. Nutr. Metab.* 42 (5), 449–458.
- Leah Plumb, A., 2004. *Drugs.com: drug information online 2004*. Ref. Rev. 18 (6), 41–41.
- Leme, D.E., da, C., de Oliveira, C., 2023. Machine learning models to predict future frailty in community-dwelling middle-aged and older adults: the ELSA cohort study. *J. Gerontol. A Biol. Sci. Med. Sci.* 78 (11), 2176–2184.
- Linn, N., Goetzinger, C., Regnaud, J.P., Schmitz, S., Desseigne, C., Fagherazzi, G., et al., 2021. Digital health interventions among people living with frailty: a scoping review. *J. Am. Med. Dir. Assoc.* 22 (9), 1802–1812 e21.
- Liu, L.K., Guo, C.Y., Lee, W.J., Chen, L.Y., Hwang, A.C., Lin, M.H., et al., 2017. Subtypes of physical frailty: latent class analysis and associations with clinical characteristics and outcomes. *Sci. Rep.* 7 (1), 46417.
- Mitchell, E., Spencer Chapman, M., Williams, N., Dawson, K.J., Mende, N., Calderbank, E.F., et al., 2022. Clonal dynamics of haematopoiesis across the human lifespan. *Nature* 606 (7913), 343–350.
- Morley, J.E., Vellas, B., van Kan, G.A., Anker, S.D., Bauer, J.M., Bernabei, R., et al., 2013. Frailty consensus: a call to action. *J. Am. Med. Dir. Assoc.* 14 (6), 392–397.
- Murad, M.H., Elamin, K.B., Abu Elnour, N.O., Elamin, M.B., Alkhatib, A.A., Fatourechi, M., et al., 2011. The effect of vitamin D on falls: a systematic review and meta-analysis. *J. Clin. Endocrinol. Metab.* 96 (10), 2997–3006.
- Nwadiugwu, M.C., 2020. Frailty and the risk of polypharmacy in the older person: enabling and preventative approaches. *J. Aging Res.* 2020, e6759521.
- O'Caioimh, R., Sezgin, D., O'Donovan, M.R., Molloy, D.W., Clegg, A., Rockwood, K., et al., 2021. Prevalence of frailty in 62 countries across the world: a systematic review and meta-analysis of population-level studies. *Age Ageing* 50 (1), 96–104.
- Ofori-Asenso, R., Chin, K.L., Mazidi, M., Zomer, E., Ilomaki, J., Zullo, A.R., et al., 2019. Global incidence of frailty and prefrailty among community-dwelling older adults: a systematic review and Meta-analysis. *JAMA Netw. Open* 2 (8), e198398.
- Panza, F., Seripa, D., Solfrizzi, V., Tortelli, R., Greco, A., Pilotto, A., et al., 2015. Targeting cognitive frailty: clinical and neurobiological roadmap for a single complex phenotype. *J. Alzheimers Dis.* 47 (4), 793–813.
- Park, C., Mishra, R., Golledge, J., Najafi, B., 2021. Digital biomarkers of physical frailty and frailty phenotypes using Sensor-based physical activity and machine learning. *Sensors* 21 (16), 5289.
- Patel, H.P., Clift, E., Lewis, L., Cooper, C., Patel, H.P., Clift, E., et al., 2017. *Epidemiology of sarcopenia and frailty. Frailty and Sarcopenia - Onset, Development and Clinical Challenges*. IntechOpen. (<https://www.intechopen.com/chapters/56116>).
- Puts, M.T.E., Visser, M., Twisk, J.W.R., Deeg, D.J.H., Lips, P., 2005. Endocrine and inflammatory markers as predictors of frailty. *Clin. Endocrinol. (Oxf.)* 63 (4), 403–411.
- Reid, N., Young, A., Hanjani, L.S., Hubbard, R.E., Gordon, E.H., 2022. Sex-specific interventions to prevent and manage frailty. *Maturitas* 164, 23–30.

- Rockwood, K., Mitnitski, A., 2007. Frailty in relation to the accumulation of deficits. *J. Gerontol. Ser. A* 62 (7), 722–727.
- Rockwood, K., Fox, R.A., Stolee, P., Robertson, D., Beattie, B.L., 1994. Frailty in elderly people: an evolving concept. *CMAJ Can. Med. Assoc. J.* 150 (4), 489–495.
- Ross, A.C., Manson, J.E., Abrams, S.A., Aloia, J.F., Brannon, P.M., Clinton, S.K., et al., 2011. The 2011 report on dietary reference intakes for calcium and vitamin d from the institute of medicine: what clinicians need to know. *J. Clin. Endocrinol. Metab.* 96 (1), 53–58.
- Shardell, M., Hicks, G.E., Miller, R.R., Kritchevsky, S., Andersen, D., Bandinelli, S., et al., 2009. Association of low vitamin D levels with the frailty syndrome in men and women. *J. Gerontol. Ser. A* 64A (1), 69–75.
- Spearman, C., 1904. The proof and measurement of association between two things. *Am. J. Psychol.* 15 (1), 72–101.
- Spira, D., Buchmann, N., Nikolov, J., Demuth, I., Steinhagen-Thiessen, E., Eckardt, R., et al., 2015. Association of low lean mass with frailty and physical performance: a comparison between two operational definitions of Sarcopenia—Data from the Berlin aging study II (BASE-II). *J. Gerontol. Ser. A* 70 (6), 779–784.
- Spira, D., Buchmann, N., König, M., Rosada, A., Steinhagen-Thiessen, E., Demuth, I., et al., 2019. Sex-specific differences in the association of vitamin d with low lean mass and frailty: results from the Berlin aging study II. *Nutrition* 62, 1–6.
- Strain, W.D., Down, S., Brown, P., Puttanna, A., Sinclair, A., 2021. Diabetes and frailty: an expert consensus statement on the management of older adults with type 2 diabetes. *Diabetes Ther.* 12 (5), 1227–1247.
- Sze, S., Pellicori, P., Zhang, J., Weston, J., Clark, A.L., 2019. Identification of frailty in chronic heart failure. *JACC Heart Fail* 7 (4), 291–302.
- Tao, X., Liu, L., Ma, P., Hu, J., Ming, Z., Dang, K., et al., 2024. Association of circulating very long-chain saturated fatty acids with cardiovascular mortality in NHANES 2003–2004, 2011–2012. *J. Clin. Endocrinol. Metab.* 109 (2), e633–e645.
- Tenison, E., Henderson, E.J., 2020. Multimorbidity and frailty: tackling complexity in Parkinson's disease. *J. Park Dis.* 10 (s1), S85–S91.
- Toepfer, S., König, M., Spira, D., Drewelies, J., Kreutz, R., Bolbrinker, J., et al., 2021. Sex differences in characteristics associated with potentially inappropriate medication use and associations with functional capacity in older participants of the Berlin aging study II. *Gerontology* 68 (6), 664–672.
- Tomita, M.R., Mann, W.C., Fraas, L.F., Stanton, K.M., 2004. Predictors of the use of assistive devices that address physical impairments among community-based frail elders. *J. Appl. Gerontol.* 23 (2), 141–155.
- Uchai, S., Andersen, L.F., Hopstock, L.A., Hjartåker, A., 2023. Body mass index, waist circumference and pre-frailty/frailty: the Tromsø study 1994–2016. *BMJ Open* 13 (2), e065707.
- Uchmanowicz, I., Lobo-Rudnicka, M., Szelag, P., Jankowska-Polańska, B., Lobo-Grudzień, K., 2014. Frailty in heart failure. *Curr. Heart Fail Rep.* 11 (3), 266–273.
- Varrette, S., Cartiaux, H., Peter, S., Kieffer, E., Valette, T., Olloh, A., 2022. Management of an academic HPC & research computing facility: the ULHPC experience 2.0. Proceedings of the 2022 6th High Performance Computing and Cluster Technologies Conference [Internet]. Association for Computing Machinery, New York, NY, USA, pp. 14–24. <https://doi.org/10.1145/3560442.3560445>.
- Vaz Fragoso, C.A., Enright, P.L., McAvay, G., Van Ness, P.H., Gill, T.M., FRAILTY, A.N.D., 2012. Respiratory impairment in older persons. *Am. J. Med.* 125 (1), 79–86.
- Verschoor, C.P., Theou, O., Ma, J., Montgomery, P., Mossey, S., Nangia, P., et al., 2024. Age- and sex-specific associations of frailty with mortality and healthcare utilization in community-dwelling adults from Ontario, Canada. *BMC Geriatr.* 24 (1), 223.
- Wang, C.W., Lebsack, A., Chau, S., Lai, J.C., 2019. The range and reproducibility of the liver frailty index. *Liver Transpl.* 25 (6), 841–847.
- Wang, H. yu, Zhang, M., Sun, X., 2024. Sex-specific association between socioeconomic status, lifestyle, and the risk of frailty among the elderly in China. *Front. Med.* (<http://www.frontiersin.org/articles/10.3389/fmed.2021.775518>).
- Welch, B.L., 1947. The generalization of 'student's' problem when several different population variances are involved. *Biometrika* 34 (1–2), 28–35.
- Woo, J., Yu, R., Wong, M., Yeung, F., Wong, M., Lum, C., 2015. Frailty screening in the community using the FRAIL scale. *J. Am. Med. Dir. Assoc.* 16 (5), 412–419.
- Xu, L., Zhang, J., Shen, S., Hong, X., Zeng, X., Yang, Y., et al., 2020. Association between body composition and frailty in elder inpatients. *Clin. Interv. Aging* 15, 313–320.
- Xue, Q.L., 2011. The frailty syndrome: definition and natural history. *Clin. Geriatr. Med.* 27 (1), 1–15.
- Yarnall, A.J., Sayer, A.A., Clegg, A., Rockwood, K., Parker, S., Hindle, J.V., 2017. New horizons in multimorbidity in older adults. *Age Ageing* 46 (6), 882–888.
- Zhang, C., Bi, J., Soda, P., 2017. Feature selection and resampling in class imbalance learning: which comes first? An empirical study in the biological domain. International Conference on Bioinformatics and Biomedicine (BIBM) [Internet]. IEEE, pp. 933–938. (<https://ieeexplore.ieee.org/abstract/document/8217782>).
- Zhou, J., Huang, P., Liu, P., Hao, Q., Chen, S., Dong, B., et al., 2016. Association of vitamin d deficiency and frailty: a systematic review and meta-analysis. *Maturitas* 94, 70–76.

## **Appendix A2: TOD**

Article title: **Time-of-day effects of cancer drugs revealed by high-throughput deep phenotyping**

Contributions: Data analysis

Discussion and interpretation of results

Method section writing (concerning techniques we applied)

Figure 6; S6; S7

DOI link: <https://doi.org/10.1038/s41467-024-51611-3>

Published in: Nature Communications

# Time-of-day effects of cancer drugs revealed by high-throughput deep phenotyping

Received: 7 November 2023

Accepted: 13 August 2024

Published online: 22 August 2024

 Check for updates

Carolin Ector<sup>1,2</sup>, Christoph Schmal<sup>3</sup>, Jeff Didier<sup>4</sup>, Sébastien De Landtsheer<sup>4</sup>, Anna-Marie Finger<sup>5,9</sup>, Francesca Müller-Marquardt<sup>1,10</sup>, Johannes H. Schulte<sup>6,11</sup>, Thomas Sauter<sup>4</sup>, Ulrich Keilholz<sup>1,7</sup>, Hanspeter Herzel<sup>3,8</sup>, Achim Kramer<sup>5</sup> & Adrián E. Granada<sup>1,7</sup> ✉

The circadian clock, a fundamental biological regulator, governs essential cellular processes in health and disease. Circadian-based therapeutic strategies are increasingly gaining recognition as promising avenues. Aligning drug administration with the circadian rhythm can enhance treatment efficacy and minimize side effects. Yet, uncovering the optimal treatment timings remains challenging, limiting their widespread adoption. In this work, we introduce a high-throughput approach integrating live-imaging and data analysis techniques to deep-phenotype cancer cell models, evaluating their circadian rhythms, growth, and drug responses. We devise a streamlined process for profiling drug sensitivities across different times of the day, identifying optimal treatment windows and responsive cell types and drug combinations. Finally, we implement multiple computational tools to uncover cellular and genetic factors shaping time-of-day drug sensitivity. Our versatile approach is adaptable to various biological models, facilitating its broad application and relevance. Ultimately, this research leverages circadian rhythms to optimize anti-cancer drug treatments, promising improved outcomes and transformative treatment strategies.

The circadian clock is a central regulator of multiple physiological and behavioral processes found in cyanobacteria, plants, fungi, and animals. In mammals, the hierarchical organization of the circadian system ensures coordinated biological rhythms from the level of the individual cell to the whole organism level<sup>1</sup>. Primate and mouse studies showed that protein-coding genes are rhythmically expressed in a tissue-specific by up to 80% and 40%, respectively<sup>2,3</sup>. These clock-controlled genes regulate key biological processes such as metabolism<sup>4,5</sup>, cell proliferation<sup>6</sup>, immune response<sup>7</sup>, DNA repair, and apoptosis<sup>8</sup>.

Disruption of the circadian system is classified as a carcinogen and is associated with multiple cancer subtypes<sup>9–12</sup>. Cancer hallmarks such as sustained proliferation and metastasis<sup>13,14</sup> have been linked to the circadian clock<sup>15,16</sup> and patients with mutations in circadian clock genes exhibit lower survival rates<sup>17–19</sup>. Beyond its role in cancer development, the circadian clock directly interacts with therapeutic targets that affect drug responses<sup>19–21</sup>. Consistent with these observations, recent works have shown that administration of chemotherapeutic agents aligned with the circadian rhythm changes their degree of efficacy

<sup>1</sup>Charité Comprehensive Cancer Center, Charité – Universitätsmedizin Berlin, Berlin, Germany. <sup>2</sup>Faculty of Life Sciences, Humboldt-Universität zu Berlin, Berlin, Germany. <sup>3</sup>Institute for Theoretical Biology, Humboldt-Universität zu Berlin, Berlin, Germany. <sup>4</sup>Department of Life Sciences and Medicine, University of Luxembourg, Esch-sur-Alzette, Luxembourg. <sup>5</sup>Institute for Medical Immunology, Charité – Universitätsmedizin Berlin, Berlin, Germany. <sup>6</sup>Department of Pediatric Oncology, Hematology and Stem Cell Transplantation, Charité – Universitätsmedizin Berlin, Berlin, Germany. <sup>7</sup>German Cancer Consortium (DKTK), Berlin, Germany. <sup>8</sup>Charité – Universitätsmedizin Berlin, Berlin, Germany. <sup>9</sup>Present address: Department of Anatomy, University of California, San Francisco, San Francisco, CA, USA. <sup>10</sup>Present address: Institute of Research for Development, University of Montpellier, Montpellier, France. <sup>11</sup>Present address: Clinic for Pediatrics and Adolescent Medicine, Universitätsklinikum Tübingen, Tübingen, Germany. ✉ e-mail: [adrian.granada@charite.de](mailto:adrian.granada@charite.de)

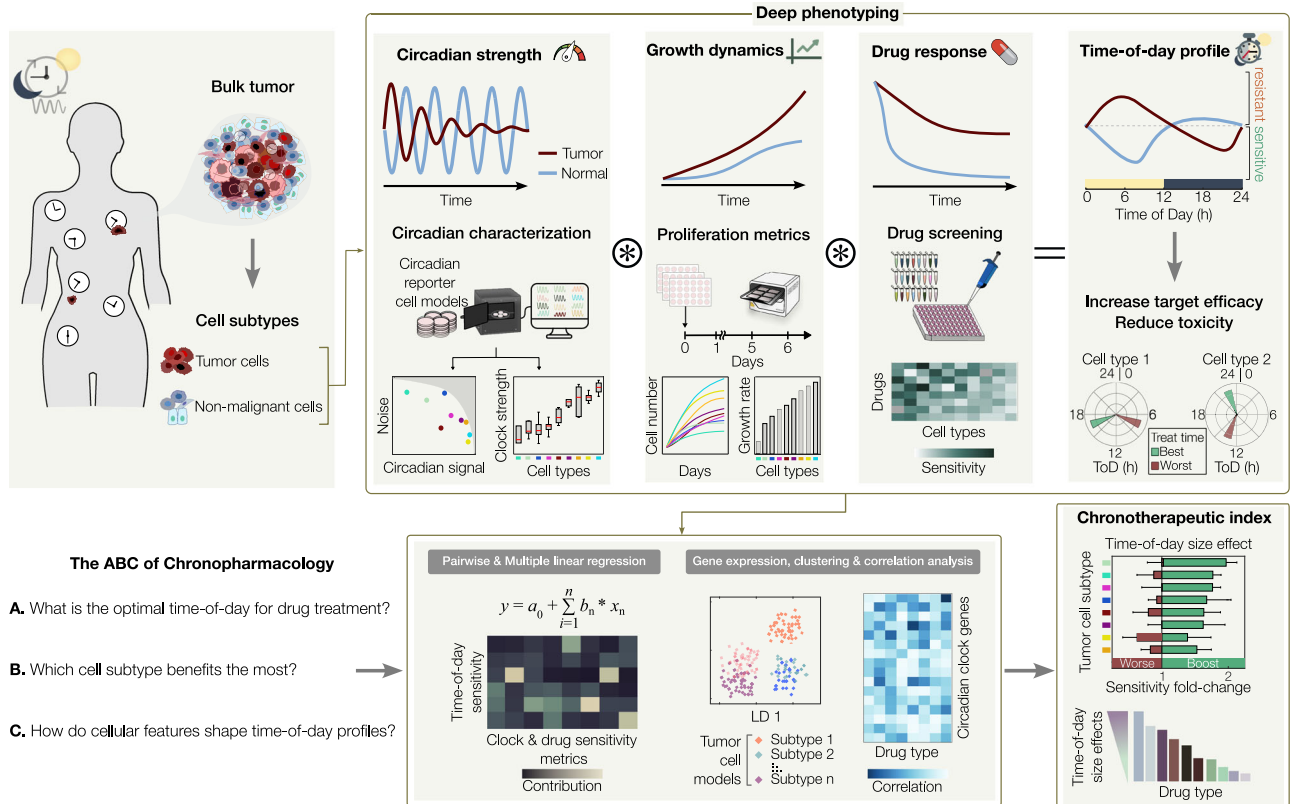


**Fig. 1 | Framework for identifying optimal treatment times in cancer and healthy tissue models.** Schematic of the experimental and computational framework to thoroughly characterize time-of-day drug responses in a variety of cell subtypes, such as cancer and non-malignant cell models. A combination of live recordings is implemented for the deep phenotyping of circadian strength, growth dynamics, and drug responses that shape time-of-day profiles. Using a novel streamlined experimental approach, time-of-day sensitivity profiles are obtained in

tumor and non-malignant cell models, providing best and worst timings for increased efficacy and reduced toxicity (top panel). A tandem computational pipeline integrates the deep phenotyping metrics as well as gene expression data of circadian clock genes to quantitatively address three fundamental questions in chronopharmacology (bottom panel). Combining multiple signatures, we define a chronotherapeutic index, ranking cellular models and drug agents by their size-effect gains from drug treatments aligned with the circadian clock (bottom right panel).

throughout the day<sup>20,22–24</sup>. Despite the broad recognition of the benefits of circadian-based drug treatments<sup>22,25,26</sup>, an efficient strategy to identify optimal treatment times remains elusive, creating a bottleneck in the implementation. In addition, the mechanisms shaping time-of-day (ToD) sensitivity profiles remain widely unknown.

Here, we introduce a method for the thorough characterization of time-of-day responses in tumor and healthy tissue cell models (Fig. 1). Using an array of experimental and data analysis methods we perform a deep-phenotyping of the critical cellular factors underlying time-of-day responses, i.e., the circadian clock strength, growth dynamics and drug response features. We then deploy a high-throughput strategy to obtain ToD profiles in a panel of drugs and cell line models. Comparing tumor versus non-tumor ToD profiles provides candidate treatment timings to increase efficacy and reduce toxicity. We subsequently integrate our dataset with publicly available gene-expression databases to rigorously address three fundamental questions in the field of circadian pharmacology, known as chronopharmacology. These questions are: (A) What is the optimal time of day for drug treatment? (B) Which cell subtype benefits the most from circadian-aligned drug treatment? and (C) How do cellular features shape time-of-day profiles? Finally, we define a chronotherapeutic index, ranking cellular models and drug agents that stand to gain the most benefit from circadian-based treatments.

## Results

### Deep circadian phenotyping in cancer cell models

Despite the increasing recognition of the role of the circadian clock in cancer progression and treatment response, the extent to which different cancer subtypes maintain circadian rhythmicity remains poorly

understood. To address this and quantitatively characterize the degree of rhythmicity of cancer cell models, we implement an approach that integrates recordings of circadian clock activity with comprehensive time-series analysis techniques, as depicted in Fig. 2a. To robustly characterize the circadian clock molecular network, we monitored the positive and negative feedback arms of the molecular clock using a combination of two circadian luciferase reporters for *Bmal1* and *Per2* (Fig. 2b). In Fig. 2c we show representative raw luciferase signals from the breast cancer cell line MDAMB468 and the corresponding detrended and normalized signals<sup>27</sup>. As expected for a robust functional clock network, *Bmal1* and *Per2* signals show stable anti-phasic expression patterns throughout the recording (Fig. 2c and Supplementary Fig. 1a, b).

### Circadian clock strength varies in cancer and healthy cell models

Following the acquisition of *Bmal1* and *Per2* expression dynamics, we conducted a comprehensive circadian phenotyping of the signals. To accurately capture different aspects of the circadian clock dynamics, we implemented a strategy that integrates three complementary time-series analysis techniques, i.e., autocorrelation (AC), continuous wavelet transform (CWT), and multiresolution analysis (MRA). The rationale behind using this complementary analysis is to harness the strengths of each technique; AC for identifying stable temporal features, CWT for revealing time-dependent amplitude and period changes, and MRA for extracting multi-scale features, ensuring a comprehensive understanding of the signal dynamics. Using this approach we screened a broad panel of cell models, including non-malignant breast epithelial MCF10A, cancer cell models of various

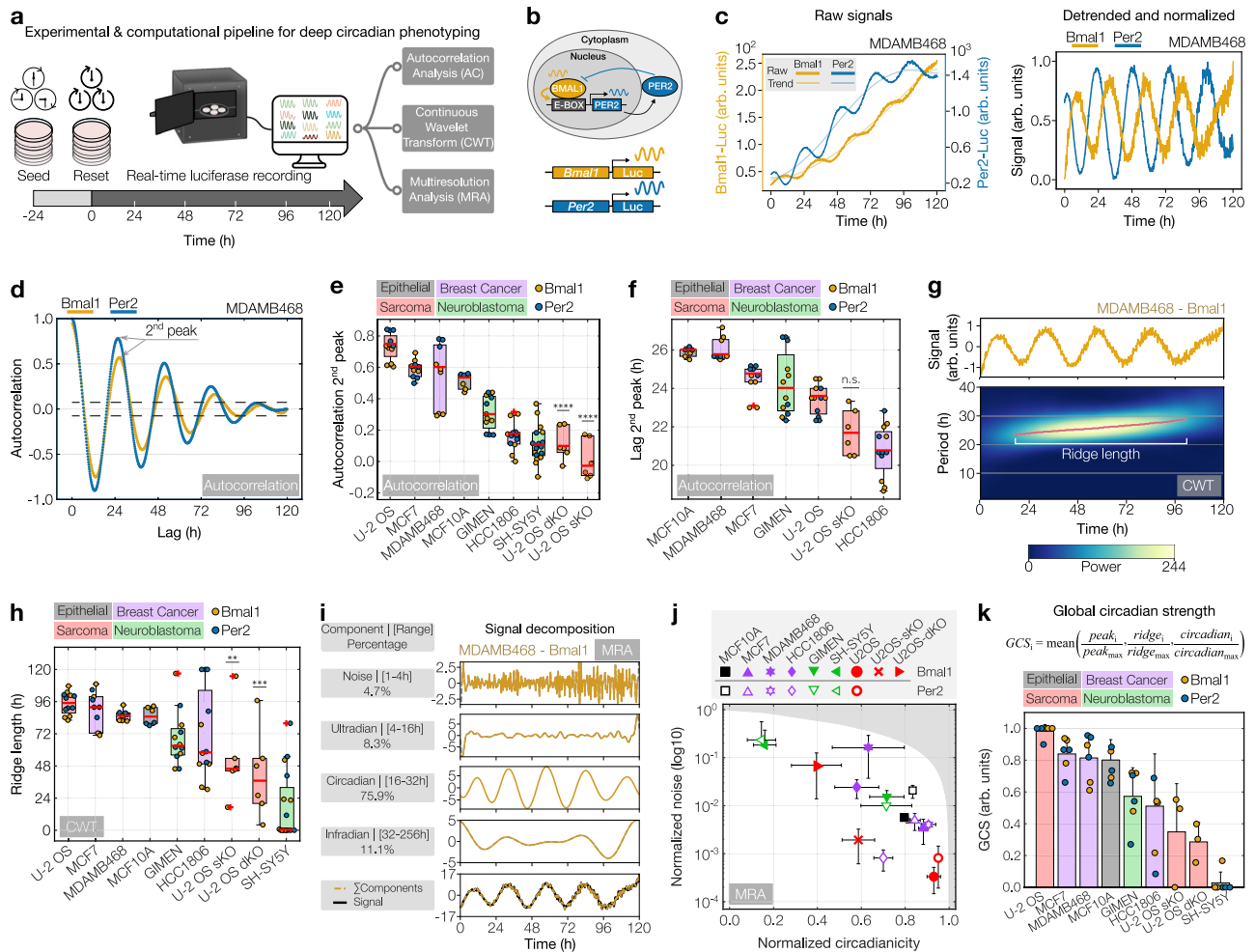


**Fig. 2 | Determining circadian clock strength in cancer and healthy tissue cell models.** **a** Schematic of the deep circadian phenotyping approach. **b** Simplified circadian feedback loops involving *Bmal1* and *Per2*. **c** Raw and processed signals from MDAMB468-*Bmal1/Per2*-Luc cells. **d** Example of autocorrelation (AC) analysis. The arrow indicates 2<sup>nd</sup> peak and abscissa (lag). Dashed lines = 95% CI. **e** Boxplot of AC values and **(f)** lags of signals from various cell models. **g** Wavelet power spectrum (bottom) from continuous wavelet transform (CWT) showing time-resolved periods of detrended-amplitude-normalized signals from MDAMB468-*Bmal1*-Luc cells (top). Red line = main oscillatory component (ridge). **h** Boxplot of CWT ridge lengths from various cell models. Box bounds in **(e, f, h)** are defined by the 25<sup>th</sup> and 75<sup>th</sup> percentiles. Extending whiskers represent data points within 1.5 times the interquartile range from lower and upper quartiles. Red lines and crosses denote the median and outliers, respectively.  $n = 12$  samples, collected from *Bmal1*-/*Per2*-reporters, with 6 samples per reporter ( $n = 2$  biological replicates  $\hat{a}$  technical triplicates or duplicates [HCC1806 *Per2*-Luc]).  $n = 6$  for U-2 OS KO-lines (*Bmal1*-Luc-only) and MCF10A (single experiment).  $n = 9$  for MDAMB468 (*Per2*-Luc: single

experiment).  $n = 17$  for SH-SY5Y (biological triplicates with technical triplicates or duplicates). **i** Multiresolution analysis (MRA) of detrended MDAMB468-*Bmal1*-Luc signal. % = fraction to signal. **j** Scatterplot of normalized MRA noise versus circadianicity components from the indicated cell models. The shaded area covers an unattainable range. Data represents the mean  $\pm$  s.d. of multiple samples per reporter cell line (see above). **k** Bar diagram ranking cell models by global circadian strength, integrating min-max scaled parameters from AC (peak), CWT (ridge), and MRA (circadianicity) for *Bmal1*-Luc and, where applicable, *Per2*-Luc signals. Data represents mean  $\pm$  s.d. of scaled parameters ( $n = 6$ , except U-2 OS knockouts where  $n = 3$  parameters). Only the positive s.d. is shown. Color coding in **(b–l, k)** corresponds to *Bmal1* (yellow) and *Per2* (blue) reporters. Color coding of cell models in **(e, f, h, j, k)** corresponds to tissue origin. One-way ANOVA and Tukey's post-hoc test compared U-2 OS WT and KO cell lines, where \*\*, \*\*\*, and \*\*\*\* indicate  $p$ -values of  $5.7 \times 10^{-3}$ ,  $4.8 \times 10^{-4}$  and  $\leq 0.0001$ , respectively. n.s. = non-significant. Source data for **(c–k)** are provided as a Source Data file.

entities (breast cancer, neuroblastoma, and sarcoma) as well as two knockout variants of osteosarcoma U-2 OS cells with a single deletion in the circadian clock gene *Cry1* (U-2 OS sKO) or paired with a deletion in the *Cry2* locus<sup>28</sup> (U-2 OS dKO).

Autocorrelation is a robust method for estimating the periodic quality of a signal, particularly for time series whose properties remain stable over time, known as stationary signals. Calculating the autocorrelation function from each recording provides the strength and period values, obtained from the second peak ordinate and abscissa (lag), respectively (Fig. 2d). This analysis showed a wide range of circadian strengths across models with the U-2 OS wild-type ranking highest with a median autocorrelation value of 0.74, whereas U-2 OS sKO and U-2 OS dKO variants ranked lowest with median correlation

values of  $-0.04$  ( $p = 7.7 \times 10^{-12}$ ) and  $0.09$  ( $p = 1.4 \times 10^{-10}$ ), respectively (Fig. 2e). Heterogeneity between and within cancer types was further observed for the oscillation period ranging from short periods of  $\sim 21$  h in HCC1806 and U-2 OS sKO cells ( $p = 0.83$ ) to longer periods of  $\sim 26$  h in MDAMB468 and MCF10A cells. U-2 OS dKO ( $34.8$  h,  $p = 8.2 \times 10^{-5}$ ) and the neuroblastoma cell line SH-SY5Y ( $39.2$  h) showed periods well above the circadian range and were excluded from this analysis (Fig. 2f). Consistent with these results, detrended signal traces of the different cell models and additional breast cancer cell lines indicate high variability in circadian clock signals across the models tested (Supplementary Fig. 1c).

To capture non-stationary features of circadian signals, such as unstable periods and fluctuating amplitudes, we implemented

continuous wavelet transform, a prevalent technique for analyzing dynamic temporal signals<sup>29</sup>. Figure 2g shows a CWT power spectrum heatmap of the *Bmal1* signal from the MDAMB468 example. The heatmap displays signal components (0–40 h period) over the 120-h recording, color-coded by relative power (see “Methods”). Time-connected regions of high relative power mark the signal’s main oscillatory component, referred to as the ridge. Strong signals exhibit continuous long ridges whereas weaker signals have short and discontinuous ridges. As a complementary measure of clock strength, we quantified the ridge length from all our recordings. Our analysis shows that U-2 OS cells have a well-maintained clock with a median ridge length of 4.1 days, closely followed by MCF7, MDAMB468, and MCF10A cells (3.4–3.8 days). U-2 OS skO and dKO cells showed ridges shorter than two days (1.9 days [ $p = 5.7 \times 10^{-3}$ ] and 1.5 days [ $p = 4.8 \times 10^{-4}$ ], respectively) (Fig. 2h).

While both autocorrelation and continuous wavelet transform, provide insights into the most significant signal component, they do not quantify how the signal is distributed among non-circadian frequencies. To obtain more comprehensive signal information and an analogous signal-to-noise metric, we next implemented multi-resolution analysis. MRA involves decomposing the detrended signal into four distinct component bands, namely the noise (1–4 h), ultradian (4–16 h), circadian (16–32 h), and infradian (32–48 h) components (see “Methods”). In Fig. 2i, we present an example of MDAMB468 *Bmal1*-Luc where 75.9% of the signal is in the circadian range, 4.7% in the noise and the remaining 19.4% in the ultradian or infradian range. To obtain an analogous signal-to-noise measure of all recorded cell models, we plotted the circadian component (“circadianicity”) versus the noise component and observed a broad range of ratios (Fig. 2j). Consistent with our previous analysis, U-2 OS cells show strong circadian signal with the lowest noise levels (<1%) and the highest proportion of circadian components (~93%) for both reporters. Knockout of *Cry1* or *Cry1/Cry2* reduced the circadian component to 59% ( $p = 5.8 \times 10^{-6}$ ) and 40% ( $p = 2.0 \times 10^{-8}$ ), respectively, while increasing the noise component by 5.8-fold in the single knockout and by 209-fold in the double knockout. This signal-to-noise analysis map indicates that signals from the *Per2*-reporter were slightly more circadian and less noisy than those from the *Bmal1*-reporter (Fig. 2j and Supplementary Fig. 1d). *Bmal1* and *Per2* exhibit unique oscillatory patterns, reflecting distinct biological pathways within the circadian clock system. Their individual behaviors might offer valuable insights into the functionality of the circadian rhythm. To streamline our analysis and facilitate comparison, we averaged the values of *Bmal1* and *Per2* in Fig. 2e, f, h, and k. However, for a more detailed examination, separate analyses for each can be found in Supplementary Fig. 1e, f.

Finally, to obtain a global strength metric, we normalized each circadian parameter to its respective maximum value across all tested cell line models and computed the mean, facilitating a gradual ranking of cell models from low to high circadian strength (Fig. 2k, see “Methods”).

In summary, by using a multi-faceted approach to characterize circadian rhythms in the different models tested, we identified heterogeneous circadian clock phenotypes, suggesting a strong clock in U-2 OS, MCF7, MDAMB468, and MCF10A cells and an impaired but present clock in GIMEN and HCC1806 cells. These results challenge the common expectation that most cancer cells have a weak clock and underscore the significance of defining gradual metrics of circadian strength in a model-specific manner.

### Growth and drug response dynamics in cancer cell models

Together with circadian potency, cell growth dynamics and how cells respond to drug treatment in time are expected to influence responses throughout the day. Thus, we next evaluated growth characteristics and drug sensitivities across a spectrum of drug and cell line models. To showcase our approach’s ability to detect within-subtype

differences, we examined nine cell lines of the triple-negative breast cancer (TNBC) subtype alongside the non-malignant MCF10A breast cell model. The TNBC cell lines were analyzed across several molecular subtypes as classified by Lehmann et al., specifically the basal-like 1 (BL1), basal-like 2 (BL2), and mesenchymal-like (MES) TNBC subtypes. Growth and drug sensitivity assays in cancer models often rely on single time point measurements (e.g., ATP-based viability and replating assays) that provide a time-averaged snapshot. However, cancer cells respond dynamically to drugs, with temporally evolving effects, so conclusions drawn from single time point data can potentially mask the true effects of drugs. To accurately capture the dynamics of growth and drug response, we implemented a time-resolved live-cell imaging setup, directly counting cell nuclei in a fluorescence channel, while simultaneously evaluating confluency in the complementary bright-field channel (Fig. 3a). Figure 3b shows representative snapshots of both imaging channels from MDAMB468 cells under untreated conditions. Frame-by-frame quantification provides growth trajectories for each cell model tested (Supplementary Fig. 2a), with MDAMB468 cells showing a 5.3-fold increase in growth and reaching a ~100% confluency after 4 days (Fig. 3c). Quantification of doubling times (DTs) calculated from confluency and cell numbers correlated well across the 10 cell line models tested ( $R^2 = 0.69$ ) (Supplementary Fig. 2b). Upon examining the normalized cell number trajectories, we observed substantial variability in growth across the cell line models, ranging from approximately 2- to 16-fold over the 4-day recordings (Fig. 3d). To capture growth signatures from the entire recording, we fitted an exponential function to each time series and obtained the growth rate  $k$  for each trajectory (Fig. 3e). As expected, cell number growth rates and doubling times exhibit a strong anticorrelation ( $R^2 = 0.83$ ) (Fig. 3f and Supplementary Fig. 2c).

Next, we studied the response of the cancer cell models upon treatment with a panel of seven drugs targeting a broad range of mechanisms and pathways, i.e., the DNA synthesis inhibitors 5-FU and doxorubicin, mitosis-inhibiting alisertib and paclitaxel, the PI3K/AKT/mTOR inhibitor torin2, as well as cisplatin and olaparib which target the DNA damage response (DDR) pathway (Fig. 3g). We then tracked responses to a broad range of drug concentrations, as exemplified in Fig. 3h by MDAMB468’s olaparib treatment. Here, doses up to 1.5  $\mu\text{M}$  resulted in slightly slower growth relative to the control, while 6.3  $\mu\text{M}$  of olaparib significantly hindered growth, and  $\geq 25 \mu\text{M}$  led to total inhibition and cell death. Fitting an exponential function to growth curves yielded positive growth rate values for weak doses while higher doses resulted in negative growth rates, indicating population decline. Using this approach, we next quantified the response and stratified all tested cell lines and drugs.

### Multi-parametric evaluation of drug sensitivity reveals heterogeneity between and within models

Accurate assessment of drug effects is essential for identifying exploitable weaknesses in cancer treatments. Traditional drug sensitivity metrics, like the  $\text{IC}_{50}$  (the drug concentration that reduces cell counts by 50% relative to the control), can be greatly influenced by factors such as the assay duration and the number of cell divisions between drug administration and the final evaluation of drug sensitivity. These factors can inadvertently introduce artefactual correlations and lead to misinterpretations of drug sensitivity results. To obtain robust drug sensitivity metrics, we employed the normalized growth rate inhibition ( $GR$ ) approach as described by Hafner et al.<sup>30</sup>. Here, growth rates under-treated and untreated conditions are compared and normalized to a single cell division. Fitting a dose-response equation to  $GR$ -values yields five drug sensitivity parameters, namely, the concentrations at half-maximal effect ( $GEC_{50}$ ) and at which  $GR = 0.5$  ( $GR_{50}$ ), the drug effect at the infinite concentration ( $GR_{inf}$ ), the steepness of the sigmoidal fit (*Hill coefficient*), and the area over the curve ( $GR_{AOC}$ ) (Fig. 3i). Moreover, the  $GR$  value directly reflects cellular response phenotypes, indicating

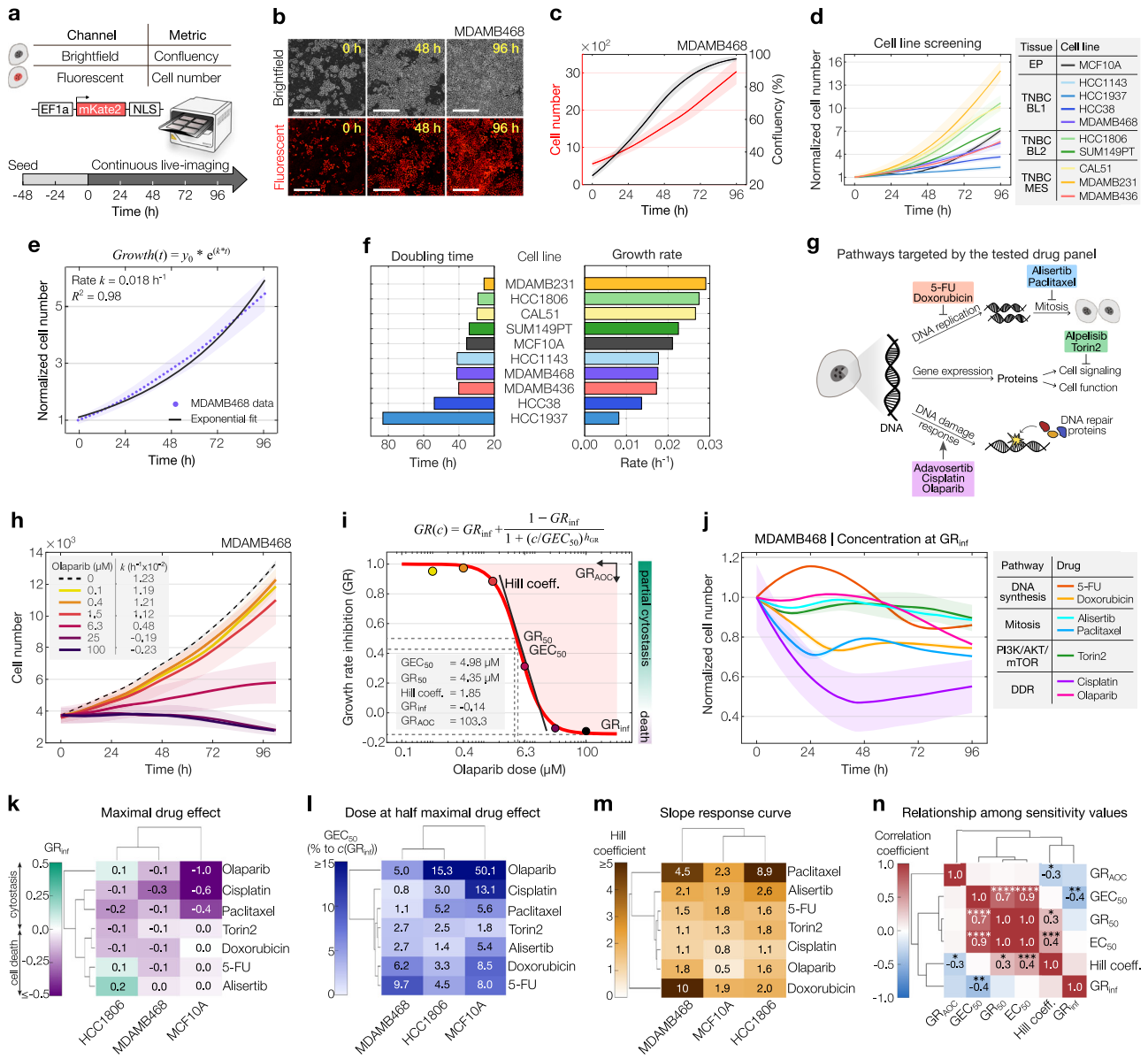


**Fig. 3 | Unraveling growth and drug response dynamics through long-term live-cell imaging.** **a** Schematic of the experimental setup. NLS = nuclear localization sequence. **b** Snapshots of MDAMB468 growth in brightfield (top) and red-fluorescent channel (bottom). Ruler = 400  $\mu\text{m}$ . **c** MDAMB468 confluency (black) and cell numbers (red) over time. **d** Normalized growth curves of indicated cell models. BL1, BL2, and MES refer to TNBC subtypes basal-like-1/-2, and mesenchymal-like, respectively. EP = epithelial. **e** Exponential fit (solid line) for MDAMB468 growth curves, yielding growth rate ( $k$ ), and fit accuracy ( $R^2$ ). Dots represent normalized cell numbers averaged across 9 images taken per well. The shaded area represents the standard deviation. **f** Bar diagrams of doubling times and growth rates, sorted in descending order from highest to lowest growth rates. Parameters calculated from growth curves, averaged across 9 images taken per well (CAL51, HCC38, HCC1806, HCC1937, MDAMB231, MDAMB468), or across six control wells from later described time-of-day experiments. **g** Schematic of pathways targeted by drugs used in this study. **h** Cell numbers and growth rates of MDAMB468 cells treated with varying olaparib doses (color-coded) or solvent (dashed line). Data

represents the mean  $\pm$  s.d. of two plates. **i** Dose-response curve of  $GR$ -values, highlighting various drug sensitivity metrics. The underlying data corresponds to the example shown in **(h)**. Error bars = 95% CI. **j** Normalized cell numbers of MDAMB468 treated with approximate  $GR_{inf}$  doses of the indicated drugs. Data represents the mean  $\pm$  s.d. of two plates or mean  $\pm$  s.e.m of 9 images taken on a single plate (cisplatin). **k-m** Hierarchical clustering of drug sensitivity parameters across cell-drug combinations.  $GEC_{50}$ -values are shown relative to the approximate  $GR_{inf}$  dose. **n** Pearson's correlation coefficients of sensitivity parameters shown in **(k-m)** and additional combinations (Supplementary Data 1;  $n = 50$  cell-drug combinations per parameter, except for  $EC_{50}$ -values where  $n = 49$  due to fitting constraints). Denoted are significant pairwise correlation coefficients (two-sided test with no adjustments made), where \* indicate  $p$ -values of 0.03 (Hill coeff. vs.  $GR_{AOC}$ ) or 0.018 (Hill coeff. vs.  $GR_{50}$ ), \*\* $p$ -value of 0.0016, \*\*\* $p$ -value of 0.0015, and \*\*\*\* $p$ -values  $\leq 0.0001$ . Data in **(k-n)** is based on the mean of two plates, or 9 images taken per well on a single plate (cisplatin). Source data for **(b-f, h-n)** are provided as a Source Data file.

partial growth inhibition for values between 0 and 1, complete cytotoxicity for a value of 0, and signifying cell death in the range from 0 to -1. Interestingly, when the same cell line was treated with different cancer drugs at their respective concentration evoking a saturating  $GR_{inf}$  response, distinct drug-dependent trajectories emerged (Fig. 3j). This underscores the importance of a time-resolved approach for

characterizing drug sensitivity across different drugs and, accordingly, across distinct cell line models.

We next compared a subset of drug-sensitivity metrics and cell line models for the different drugs tested (Fig. 3k-m). While most drugs were able to induce death in the subset of cell lines to varying degrees, we identified three drugs that resulted in partial growth

inhibition of HCC1806, namely olaparib, 5-FU and alisertib (Fig. 3k). Hierarchical clustering of  $GR_{inf}$ -values revealed a grouping of the two TNBC cell lines and while this clustering was maintained for the  $GEC_{50}$ -values (Fig. 3l), the Hill coefficient resulted in a different clustering of the cell lines (Fig. 3m). To explore the potential relationships between various sensitivity metrics, we combined data from multiple drugs and cell models and computed cross-correlations, revealing significant associations among  $GEC_{50}$ ,  $GR_{50}$ , and  $EC_{50}$ -values ( $p \leq 0.0001$ ) (Fig. 3n). In addition, significant yet less pronounced correlations emerged between the Hill coefficient and different drug sensitivity parameters, whereas the  $GR_{inf}$  and  $GR_{AOC}$ -values showed minimal correlation with other metrics. For complete  $GR$  curves and information on additionally tested cell lines and drugs, see Supplementary Fig. 3 and Supplementary Data 1.

### Variability throughout the day depends on the drug and cell model

The presence of a robust circadian clock combined with drugs that efficiently affect growth in a tumor model are promising prerequisites for identifying drug variability throughout the day. However, these prerequisites do not provide a priori insights into the specific time-of-day response profile. To systematically screen ToD drug sensitivities, we developed an experimental strategy designed to significantly reduce the investigator's workload and number of consecutive drug perturbations, thereby increasing throughput, reproducibility and accuracy (Fig. 4a). In this approach, cell populations are seeded 24 h prior to the start of continuous live-cell imaging followed by performing a 3-step circadian clock resetting protocol in which separate cell populations receive a dexamethasone pulse at three different times (0, 4, 8 h). To test cells in later stages of the circadian cycle, drugs are administered at their estimated half-effective dose 32 and 48 h after the first resetting step, creating a range of time differences between reset and treatment of 0, 4, 8, 16, 20 and 24 h in relative circadian time (Fig. 4a, right panel). The effects of the different treatment times on cell growth were monitored by live-cell imaging up to day 6, enabling the evaluation of drug responses for 4 days in both treatment groups, as shown for the alisertib-treated TNBC cell line HCC1937 in Fig. 4b. In typical ToD assays, cells are constantly proliferating during the 24 h of ToD treatments, resulting in varying cellular densities at the time of the drug treatments. These varying cell densities have the potential to influence drug responses in vitro, possibly concealing or introducing bias when determining ToD-specific drug effects. To account for different cell densities at the time of treatment, drug responses are determined as the ratio of the number of cells at the time of each treatment to the number of cells 96 h after each treatment, keeping the time window from treatment to evaluation identical across conditions (Fig. 4c, left panel). To highlight relative response differences within a day, results are presented relative to the circadian time of 0 h. Values  $> 1$  indicate increased resistance, while values  $< 1$  indicate higher sensitivity compared to treatment at time 0 h (Fig. 4c, right panel). We quantify the maximum variability in relative responses as the ToD Maximum Range ( $ToD_{MR}$ ).

Our next objective was to explore the variability of ToD profiles of different drugs within a subset of TNBC cells. To accomplish this, we screened ten cell line models shown in Fig. 3 treated with eight different drugs, generating approximately 80 ToD profiles (Fig. 4d, e and Supplementary Fig. 4a, b). Comparing examples from individual cell lines, namely HCC1937 and MCF10A, revealed that HCC1937 exhibited relatively conserved ToD profiles, whereas the non-malignant cell line showed greater ToD variability for the different drugs (Fig. 4d). Furthermore, ToD sensitivity profiles varied significantly from drug to drug (Fig. 4e and Supplementary Fig. 4b),

suggesting that ToD profiles may be highly dependent on the cancer cell model and drug mechanism of action.

To assess varying time-of-day sensitivities across all tested cell line models and drugs, we calculated the corresponding  $ToD_{MR}$  value for each drug-cell combination (Fig. 4f). Averaging the  $ToD_{MR}$ -values per drug and cell line revealed a gradual ranking of ToD variability for each drug and cell model tested (Fig. 4g). Within the drug panel, the highest and lowest ToD variability was observed for cisplatin and alisertib, respectively, with a ~2-fold difference in the average  $ToD_{MR}$  value (Fig. 4g, top panel). Similarly, the ToD variability of the tested cell lines varied by ~2-fold, with MCF10A showing the highest and HCC38 the lowest average variability. Considering only cancer cell lines, SUM149PT ranked highest and showed a similar degree of ToD sensitivity variability as the non-malignant cell line (Fig. 4g, bottom panel).

To assess the impact of circadian clock disruptions on ToD-dependent drug sensitivity, we evaluated circadian-perturbed U-2 OS *Cry1/2*-dKO cells, alongside wild-type cells that demonstrated the strongest circadian rhythms in our assessments (see Fig. 2). Using our ToD treatment approach (see Fig. 4a), we tested three drugs which elicited high ToD response variations in our breast cancer panel (see Fig. 4g), and which target distinct molecular pathways. Our results demonstrate substantial ToD-dependent drug sensitivity in WT cells and markedly reduced responses in *Cry1/2*-dKO cells (Supplementary Fig. 4c). Specifically,  $ToD_{MR}$ -values decreased by 62% for cisplatin, 58% for paclitaxel, and 40% for 5-FU in *Cry1/2*-dKO compared to WT cells (Supplementary Fig. 4d), highlighting a critical role of the circadian clock in influencing drug sensitivity throughout the day.

Together, our findings reveal distinct ToD profiles across most tested drugs and models, highlighting individualized ToD sensitivity within distinct drugs and cell models despite the common TNBC categorization and shared drug-target pathways.

### Determining treatment times for maximum drug effect

The critical factor in the design of future chronotherapeutic treatments may be not only the sensitivity of cancer cells but rather the differential time-of-day sensitivity between cancer and non-malignant tissues<sup>26</sup>. To illustrate this, we compared the ToD response profiles of TNBC cancer cell models with the profile of MCF10A, as shown for HCC1937 and alisertib in Fig. 4h. In this case, the cancer and non-malignant cell models show an antiphasic ToD response profile, with an almost inverted profile. By calculating the greatest response differences between the two cell models, we determined the treatment times of maximum and minimum benefit (Fig. 4h-j). Analyzing the entire panel of tested drugs per cell line model and plotting polar density histograms of the times of maximum and minimum benefit, we found that the highest overall benefit is achieved at 10–12 h and 18–20 h in the treatment of HCC1937, while earlier treatment times of the day yield minimum benefit. In contrast, SUM149PT and MDAMB231 show a single prominent time window throughout the day that provides maximum treatment benefit (Fig. 4i). In addition to cell model-to-model variability in the benefit times, we explored the drug-to-drug variability by calculating the polar density histogram for the individual drugs tested across all cell line models (Fig. 4j). 5-FU showed a clear preference for administration between 8 and 10 h, while torin2 and paclitaxel showed more variability in maximum and minimum benefit times, indicating different response relationships to the non-malignant cell model across the cancer cell lines tested.

Finally, we quantified the extent of maximum and minimum treatment benefit by calculating the corresponding fold changes in ToD responses between the cancer and non-malignant cell model (Fig. 4k). By averaging these fold changes across cell lines and drugs, we established a ranking referred to here as the “chronotherapeutic index”. While the average ToD variability highlights the benefits of a single model (Fig. 4g), the chronotherapeutic index reveals distinctions between the cancer models and the non-malignant MCF10A cell

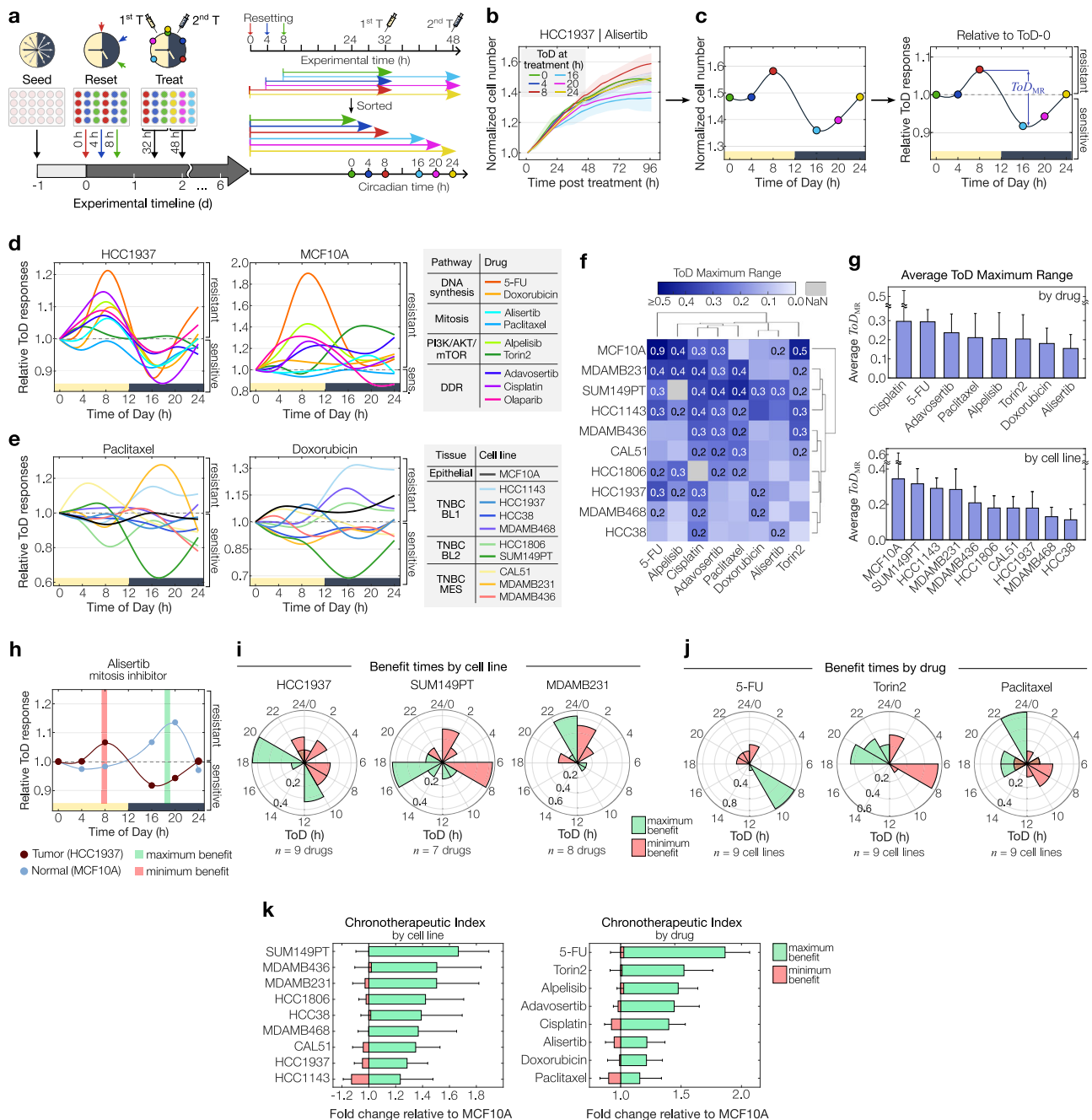


**Fig. 4 | Time-of-day drug sensitivity is drug and tissue model dependent.**

**a** Schematic of the experimental setup to screen for time-of-day (ToD) responses. Three clock-resetting steps are performed in 4-h intervals. Drugs are administered 32 or 48 hours post initial reset, resulting in six circadian times (0, 4, 8, 16, 20, 24 h). Growth is monitored by long-term live-cell imaging. Timelines on the right depict experimental (top) and relative circadian times (bottom), color-coded by each ToD tested. **b** Cell counts of HCC1937 treated with alisertib at different times of the day. Normalization to the respective time of treatment. **c** Cell numbers 4 days post-treatment versus treatment times, corresponding to **(b)** (left). ToD response curve (ToD-RC) depicting relative responses to ToD 0 h. Blue arrows mark the maximum ToD response range ( $ToD_{MR}$ ) (right). **d** ToD-RCs for HCC1937 (left) or MCF10A (right) cells treated with different drugs (color-coded). **e** ToD-RCs for 10 cell models treated with paclitaxel (left) or doxorubicin (right). Color coding of cell models according to tissue origin. **f** Hierarchical clustering of  $ToD_{MR}$ -values across drug-cell

combinations. Values above 0.2 are shown. Data clustering with the UPGMA method and Euclidian distance. **g** Bar diagrams ranking  $ToD_{MR}$ -values per drug (top) and cell model (bottom). **h** ToD-RCs for alisertib-treated HCC1937 tumor and MCF10A non-tumor cells overlaid, yielding maximum and minimum benefit times. Data shown in **(b-h)** represents the mean ( $\pm$  s.d.) of two plates. **i** Polar histograms for benefit times across cell models ( $n = 7-9$  drugs, as indicated in the figure) and **j**, drugs ( $n = 9$  cell models). **k** Butterfly charts depicting fold changes relative to MCF10A at benefit times, averaged per cancer cell model (left) and drug (right). Color-coding of maximum and minimum benefit times is shown in **(h-k)** in green and red, respectively. Data are shown in **(g** and **k** represents mean  $\pm$  s.d. of tested cell models per drug ( $n = 9$  cell models; alpelisib and cisplatin:  $n = 8$ ) and vice versa ( $n = 8$  drugs; HCC1806 and SUM149PT:  $n = 7$ ). For clarity, one-sided error bars are shown. Source data for **(b-k)** are provided as a Source Data file.

model, thereby offering valuable insights into the potential advantages of adopting a chronotherapeutic-based schedule. It's worth noting that the rankings based solely on average ToD variability within a single model or drug didn't align completely with the ranking of the chronotherapeutic index. This emphasizes the importance of evaluating effects in relation to healthy tissues when considering chronotherapy applications (Fig. 4g, k).

To sum up, our findings emphasize distinct chronotherapeutic response dynamics in vitro between cancer and healthy cell models, underscoring two key objectives of chronotherapy: pinpointing optimal treatment times to maximize cancer toxicity while minimizing impacts on healthy tissues.

### The relationship between time-of-day profiles and clock, growth, and drug sensitivity metrics

The time-of-day sensitivity in cancer models results from complex interactions involving the circadian clock, cancer cell growth, and drug responses. However, the specific mechanisms governing these interactions remain largely unknown. To address this, we employ statistical tools, including linear regression, dominance analysis, and determinant ranking, to uncover the main parameters influencing a key aspect of ToD sensitivity curves, namely the maximum range in responses ( $ToD_{MR}$ ) (Fig. 5a). To explore how individual metrics relate to  $ToD_{MR}$ -values, we first performed pairwise linear regression analysis (Fig. 5b–f). We considered each circadian channel individually or combined and found the strongest and most significant correlations for clock metrics from the *Bmal1* channel (Fig. 5d and Supplementary Fig. 5a, see Supplementary Data 2 for a complete set of circadian metrics across the cell models tested).  $ToD_{MR}$ -values of 5-FU were significantly correlated with amplitudes ( $r = 0.8$ ,  $R^2 = 0.6$ ) and the prominence of the circadian component (circadianicity) of the *Bmal1* signal ( $r = 0.7$ ,  $R^2 = 0.43$ ), whereas other circadian clock metrics were poorly associated (Fig. 5b, d). On the other hand, we observed no significant and rather low associations for  $ToD_{MR}$ -values and growth metrics as well as for  $ToD_{MR}$ -values and drug sensitivity metrics (Fig. 5c, e, f). To identify the best associated individual metric and drug, we integrated all correlations and generated a ranking as shown in Fig. 5g. For the different metrics, we observed the highest correlation for the amplitude ( $r = 0.43 \pm 0.02$ , mean  $\pm$  s.e.m.). Among the individual drugs, adavosertib ranked highest in overall correlation ( $r = 0.39 \pm 0.03$ , mean  $\pm$  s.e.m.) between  $ToD_{MR}$ -values and the different metrics. Relative average associations between all metrics and  $ToD_{MR}$ -values were predominantly positive, with only five metrics demonstrating inverse relationships (Supplementary Fig. 5b). Notably, only one drug, paclitaxel, displayed average negative associations across all metrics. To further test the associations between individual cellular parameters and  $ToD_{MR}$ -values, we applied a linear regression model and compared calculated versus actual  $ToD_{MR}$ -values of up to five new cell line models in Bland-Altman plots (Supplementary Fig. 5c, see Supplementary Data 3 for the complete new dataset). This revealed mean biases of  $-0.04$ ,  $-0.05$ , and  $0.06$  between calculated and actual  $ToD_{MR}$ -values for the clock, growth, and drug sensitivity metrics, respectively. As also shown in Supplementary Fig. 5c, mean biases are near zero and most predicted data points lie within the limits of agreement, which indicates minimal overall bias and good agreement between the predicted and observed data points.

While linear regression approaches are robust for examining individual metrics, they do not provide relative information about which metrics have the most significant impact on  $ToD_{MR}$ -values. To address this, we used dominance analysis and systematically tested all possible combinations of metrics. By measuring how much each metric improved the accuracy of the model when added or removed, we identified the highest contributing ones to the  $ToD_{MR}$ -values of the different drugs. For alpelisib, our analysis identified the amplitude of *Bmal1* signals as the most important factor, accounting for 42% of the

observed ToD sensitivity variability (Fig. 5h). In contrast, paclitaxel and adavosertib showed the most homogeneous distribution of individual contributions, with no single metric appearing especially important. Considering the shares of each determinant combined for all drugs led to a ranking of determinants as shown in Fig. 5i. Here, we observed the largest contributions for the *Bmal1* amplitude (mean = 21.9%) and smallest for the Hill coefficient of drug response curves (mean = 9.9%).

In summary, we were able to identify systematic dependencies of the maximal time-of-day drug sensitivities and different circadian clock, growth, and drug sensitivity parameters. We have further shown that the relative importance of the different determinants varies substantially depending on the specific drug, highlighting the importance of considering multiple factors in understanding the time-of-day dependent variability of drug response in a cell model.

### Differential impact of core clock genes in shaping time-of-day sensitivity of cancer models

Beyond a cancer model's circadian clock, growth, and drug features, the expression levels of core circadian clock genes are likely to contribute to the time-of-day sensitivity profiles. Thus, we explored the connection between the expression patterns of 16 essential clock genes and the maximum range in ToD sensitivity profiles ( $ToD_{MR}$ ). We defined core clock genes as those that directly control the transcriptional-translational feedback loops of the molecular clock network and whose dysregulation or mutations result in disrupted circadian rhythms<sup>31,32</sup>. The selected gene panel displayed distinct expression patterns across the TNBC cell lines tested (Supplementary Fig. 6a). To examine potential relationships between core clock genes and  $ToD_{MR}$ -values, we used three different methods, namely linear correlation analysis, dimensionality reduction by linear discriminant analysis (LDA) and principal component analysis (PCA) (Fig. 6a).

Linear correlation analysis revealed significant correlations between  $ToD_{MR}$ -values of five tested compounds from our drug panel and selected core clock genes (Fig. 6b). Focusing on the mitosis inhibitor paclitaxel, we identified particularly strong anticorrelations with the expression levels of *Per3* ( $r = -0.88$ ,  $R^2 = 0.78$ ) and *Dbp* ( $r = -0.72$ ,  $R^2 = 0.51$ ) (Fig. 6b, c). Yet, the overall correlation between circadian clock genes and  $ToD_{MR}$ -values was relatively weak, which was also apparent when accumulating absolute correlations per drug or per metric (Supplementary Fig. 6b). Here, the highest overall correlation of  $ToD_{MR}$ -values were found for cisplatin ( $r = 0.40 \pm 0.21$ , mean  $\pm$  s.d.), while *Per2* was most associated with  $ToD_{MR}$ -values among the circadian clock gene panel ( $r = 0.48 \pm 0.20$ , mean  $\pm$  s.d.) (Supplementary Fig. 6b).

To assess the cumulative impact of circadian gene expression on the strength of time-of-day effects as indicated by the  $ToD_{MR}$ -values, aiming to uncover more complex patterns that might not be explainable through linear correlations alone, we proceeded to apply LDA on a drug-by-drug basis. To do so, we first categorized cell models into two groups based on the median  $ToD_{MR}$ -value for each drug. Figure 6d provides an example using paclitaxel, effectively separating the data into groups of high and low  $ToD_{MR}$ -values. Implementing LDA to examine the individual linear discriminant components of each circadian clock gene revealed a clear ranking of genes in terms of their importance in discriminating the cell lines into the two  $ToD_{MR}$  groups. For paclitaxel, the core clock genes *Cry2*, *Dbp*, and *Per3* were the most important contributors to the specific discrimination, collectively accounting for approximately 46% of the discriminative information (Fig. 6d, right panel). Importantly, the contribution of each gene in discriminating between  $ToD_{MR}$ -response groups varied for the tested drugs, suggesting that either the drug or the drug targets may interact differently with the molecular components of the circadian clock (Supplementary Fig. 6c–i). To explore the circadian clock's impact on ToD sensitivity across various drug treatments, we assessed the overall contribution of each gene by cumulating their effects across all drugs. This revealed modest overall contributions, with the highest ranking

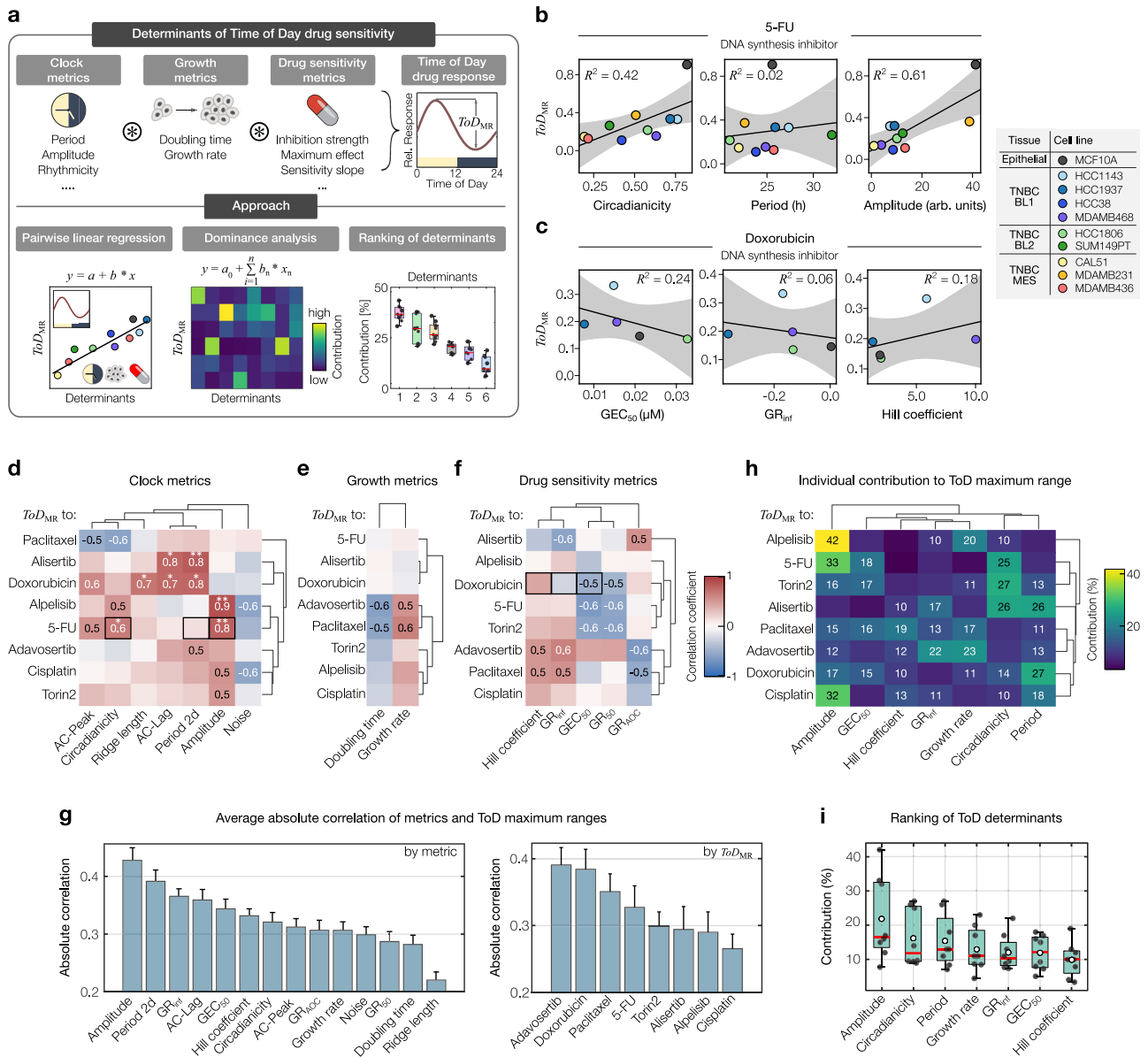


**Fig. 5 | Clock and drug sensitivity metrics shape ToD curves.** **a** Computational approach to investigate how circadian rhythms, cell growth dynamics, and drug sensitivity factors influence the time-of-day (ToD) drug efficacy. **b** and **c** Example of linear correlations between  $ToD_{MR}$  and circadian (**b**) or drug sensitivity parameters (**c**), for 5-FU ( $n = 10$  cell models) and cisplatin ( $n = 5$  cell models), respectively. Color coding of cell models according to tissue origin. The central black line represents the regression line. Gray-shaded area = 95% CI of the linear regression fit. Model accuracy is indicated by  $R^2$ -values. **d–f** Hierarchical clustering of Pearson correlation coefficients ( $r$ ) between  $ToD_{MR}$ -values of different drugs (rows) and the respective metric (columns) for clock strength (**d**,  $n = 10$  cell models), growth (**e**,  $n = 10$  cell models) or drug sensitivity (**f**,  $n = 5$  cell models).  $r$ -values  $\geq 0.5$  and  $\leq -0.5$  are shown. Black rectangles indicate examples shown in (**b** and **c**). Significant pairwise correlations (two-sided test with no adjustments made) are indicated by stars, where \*, and \*\*, denote  $p$ -values  $\leq 0.05$  and  $0.01$ , respectively. Exact  $p$ -values: Alisertib-AC-Lag = 0.011; Alisertib-Period-2d = 0.004; Doxorubicin-Ridgelen =

0.030; Doxorubicin-AC-Lag = 0.014; Doxorubicin-Period-2d = 0.012; Alpelisib-Amplitude = 0.002; 5-FU-Circadianicity = 0.044; 5-FU-Amplitude = 0.007. Note: sample size in (**d–f**) for alpelisib =  $n-1$ ; and for cisplatin = 9. **g** Bar diagrams ranking the absolute correlation between  $ToD_{MR}$ -values, and each metric depicted in (**d–f**), ranked by metric ( $n = 8$  drugs) or by drug ( $n = 14$  metrics). Data represents the mean  $\pm$  s.e.m. For clarity, one-sided error bars are shown. **h** Hierarchical clustering of the dominance analysis matrix showing the individual contribution of the circadian clock, growth, and drug sensitivity parameters (columns) in predicting drug-dependent  $ToD_{MR}$ -values (rows). Colors indicate the percentage contribution, as detailed in the color bar. See key for **d–f** for sample sizes ( $n$ ). **i** Boxplot of the overall contribution of cellular metrics to predict  $ToD_{MR}$ -values, corresponding to (**h**). Box bounds are defined by the 25<sup>th</sup> and 75<sup>th</sup> percentiles. Extending whiskers represent data points within 1.5 times the interquartile range from lower and upper quartiles. Red lines denote the data's median, and white circles the mean. Source data for **b–i** are provided as a Source Data file.

*Rorb* accounting for  $10.5\% \pm 9.6\%$  (mean  $\pm$  s.d.) of the discriminative information (Fig. 6e).

While LDA is a powerful method to determine the discriminatory contribution of the individual core clock genes, PCA allows for identifying underlying patterns and relationships among the different genes. For paclitaxel, PCA distributed the cell models well along the first two principal components which combined explained 73.7% of the

variability among the different ToD sensitivity profiles (Supplementary Fig. 6j, left panel). Ranking of the PC loadings showed that the degree of contribution of each circadian clock gene in shaping the PCA outcome was highly individual. For paclitaxel, *Csnk1d* was the major contributor to the ToD sensitivity variability within the first principal component, while along the second principal component, *Clock* ranked as the main contributor (Supplementary Fig. 6j, right panels).

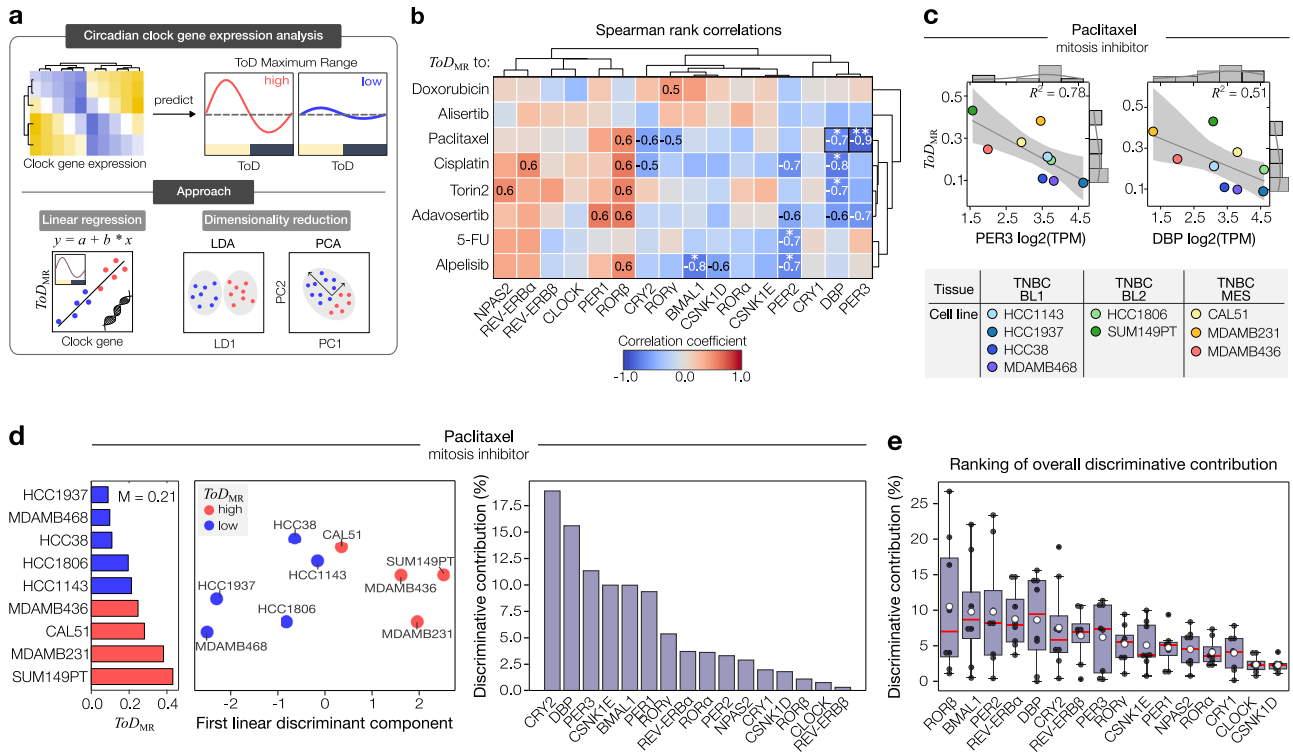


**Fig. 6 | Gene expression analysis unveils diverse roles of circadian genes in determining time-of-day patterns.** **a** Approach to identify the role of core clock genes in determining the strength of time-of-day (ToD) drug sensitivity. **b** Hierarchical clustering of Spearman rank correlation coefficients between drug-dependent  $ToD_{MR}$ -values (rows) and core clock genes (columns). Black boxes indicate examples shown in (c). Statistical significance of the correlations are indicated as stars, where \* and \*\*, denote  $p$ -values  $\leq 0.05$  and  $0.01$ , respectively. Exact  $p$ -values: Paclitaxel-*Per3* = 0.002; Paclitaxel-*Dbp* = 0.030; Cisplatin-*Dbp* = 0.021; Torin2-*Dbp* = 0.036; 5-FU-*Per2* = 0.050; Alpelisib-*Bmal1* = 0.021; Alpelisib-*Per2* = 0.047. Cisplatin and alpelisib:  $n = 8$  cell lines, else  $n = 9$  cell lines. **c** Example of linear correlation analysis between paclitaxel  $ToD_{MR}$ -values and *Per3* or *Dbp* expression levels measured as log<sub>2</sub>(TPM). Color-coded data points indicate different cancer cell models. The gray continuous line indicates the normal distribution fit of the samples. Gray

shaded area = 95% CI of the linear regression fit. Model accuracy is indicated by  $R^2$ -values. Top and lateral histograms indicate the count of samples along the range of gene expression, and  $ToD_{MR}$ -values, respectively.  $n = 9$  cell lines. **d** Linear discriminant analysis (LDA) on median-based binarized  $ToD_{MR}$ -values for paclitaxel. Cell models with  $ToD_{MR}$ -values below or above the median ( $M$ ) are colored in blue and red, respectively (middle and left panel). The contribution to the obtained discriminative information is shown in percentage for each of the circadian clock genes (right panel). **e** Boxplot showing the mean-based ranking of overall discriminative contributions of each circadian clock gene across all tested drugs.  $n = 8$  drugs. Box bounds are defined by the 25<sup>th</sup> and 75<sup>th</sup> percentiles. Extending whiskers represent data points within 1.5 times the interquartile range from lower and upper quartiles. Red lines denote the data's median, and white circles the mean. Source data for b–e are provided as a Source Data file.

Collectively, our findings suggest limited associations between individual expression levels of core clock genes and the observed ToD maximum ranges within the examined cell lines. However, we found interesting relationships when considering the circadian clock gene panel as a collective, indicating potential connections between the molecular circadian clock and drug-dependent time-of-day sensitivity.

## Discussion

While the fundamental role of the circadian clock in influencing disease progression and treatment response is widely recognized<sup>22,33,34</sup>, our understanding of the underlying biological mechanisms remains fragmented. Approaches that enable the precise study of drug perturbations and treatment responses within controlled circadian-timed environments play a pivotal role in advancing our understanding of the effects regulated by the circadian clock. To date, there has been a notable absence of standardized methodologies for the comprehensive exploration of the chronotherapeutic potential of drugs and cancer models. In this work, we present an integrative approach for the high-throughput quantification of time-of-day response profiles and the elucidation of circadian, growth, and drug sensitivity factors that shape these profiles (Fig. 1). This innovative method holds significant promise for advancing biological discovery, offering a robust platform

to explore the intricate interplay between circadian rhythms, cellular growth, and drug timing efficacy.

Despite the general expectation that the circadian clock is likely dysregulated in highly transformed cancers<sup>19,33</sup>, our approach reveals robust rhythms in numerous cancer cell models (Fig. 2). Furthermore, our assessment of circadian rhythms in non-malignant epithelial cells, luminal breast cancer cells, and osteosarcoma cells aligns with prior research<sup>28,35–37</sup>, underscoring the versatility of our approach in elucidating circadian clock properties across various cancer and tissue types.

Among these, we focused on triple-negative breast cancer, a highly aggressive and heterogeneous subtype, representing about 15% of diagnosed breast tumors. Current therapies are ineffective, with cytotoxic chemotherapy still being an integral part of treatment despite limited efficacy and severe side effects<sup>38</sup>. Our investigation into the growth dynamics and drug responses of multiple TNBC cell models has generated a diverse array of metrics. Notably, our results indicate that our set of drug sensitivity metrics, namely the  $GR_{50}$ ,  $GEC_{50}$ ,  $GR_{AOC}$ ,  $GR_{inf}$ , and the Hill coefficient, exhibit milder correlations to each other, which is in agreement with recent studies<sup>39</sup>. This challenges the conventional binary classification of sensitive versus resistant models and suggests that drug sensitivity rankings are rather drug-dependent and sensitivity metric-specific (Fig. 3).

By implementing our screening approach for the profiling of drug sensitivities across different times of the day, we generated approximately 80 distinct time-of-day sensitivity profiles, unveiling a wide range of sensitivity variations across drugs and cell line models (Fig. 4 and Supplementary Fig. 4). We then ranked models by their time-of-day sensitivity and observed up to 30% response differences throughout the day for the top scoring models. We further detected substantial variation in time-of-day sensitivity among the panel of drugs tested, revealing time-of-day dependent drug effects. Consistent with previous findings, we show time-of-day dependent variability in responses to the DNA synthesis inhibitors 5-FU<sup>22,23,40</sup> and doxorubicin<sup>22,41</sup> as well as to the DNA intercalator cisplatin<sup>22,41</sup>. Furthermore, we have introduced a chronotherapeutic index, which gauges the relative advantages of adopting a circadian-based drug schedule. Various non-malignant cell models may be employed for calculating this index, tailored to the particular disease model under investigation. For example, fibroblast models, whose strong circadian rhythms have been described in several works<sup>42–44</sup>, are expected to show unique relationships with cancer models in terms of sensitivity patterns at different times of the day.

Delving into the molecular mechanisms that potentially govern time-of-day sensitivity, our method has unraveled key relationships between circadian clock dynamics, growth patterns, and drug sensitivities, all of which significantly impact time-of-day drug responses. It is noteworthy that the specific contribution of these parameters varies depending on the drug under consideration, underscoring the multifactorial nature of time-of-day dependent variability in drug reactions (Fig. 5). Aiming to simplify the circadian analysis and to provide an overarching view of circadian clock dynamics, we initially combined *Bmal1*- and *Per2*-signals in Fig. 2. However, separate evaluations of the circadian genes, as presented in Supplementary Fig. 1e and f, proved crucial to elucidate the significant impact of oscillatory *Bmal1* dynamics on  $ToD_{MR}$ -values.

In an exploratory approach, we identified limited associations between expression levels of core circadian clock genes and  $ToD$  sensitivities (Fig. 6). This may hint at a more complex role of the molecular circadian clock network in this context, where distinct associations might be masked by high redundancy and interconnection between core clock genes. In addition, our results could indicate a discrete role of the cell cycle in shaping our observed  $ToD$  sensitivity profiles<sup>45–47</sup>, which also invites for further research in that context.

Assessing the cumulative impact of circadian gene expression on  $ToD_{MR}$ -values, we found differential contributions of each circadian gene in discriminating between high and low  $ToD$ -dependent sensitivity based on the drug tested. To investigate whether this observation underlies variations in the expression levels of the drug targets, follow-up explorations involving e.g., mRNA or protein quantification techniques performed at different times of the day could be conducted in future studies focusing on the molecular mechanisms of  $ToD$  sensitivity.

Given their recognized influence on pharmacodynamics<sup>22,33,34</sup>, our study primarily focused on circadian rhythms. Nevertheless, our multi-resolution analysis of *Bmal1* and *Per2* oscillatory signals uncovered distinct alternate rhythms of shorter and longer periods, as illustrated in Fig. 2i, j. The significant impact of independent 12-h ultradian rhythms on stress responses has been previously documented for mammalian cells<sup>48</sup> and constitutes an interesting field for future research in the scope of our time-of-day drug sensitivity profiles.

Despite employing a robust method to introduce luciferase reporters and validating several circadian results, as well as using population-based recordings of non-clonal cell lines, our approach does not rule out the potential impact of random reporter insertions on circadian clock estimation. Moreover, while our findings are primarily based on in vitro models and are not directly applicable to treatment recommendations, our framework can be directly applied to

model organisms of higher complexity, such as 3D patient-derived organoids and animal models where the circadian clock can be tracked.

Altogether, we provide a comprehensive method to determine optimal drug treatment times for complex diseases and to identify the cell subtypes that will most benefit from a time-of-day based treatment. Leveraging innovative experimental and computational techniques our approach further elucidates the specific biological features that shape time-of-day response profiles, thereby advancing our understanding of the cellular mechanisms that drive time-of-day sensitivity. As a result, our method provides tools to uncover the cellular mechanisms that govern time-of-day sensitivity, paving the way for new biological discoveries.

## Methods

### Experimental methods

**Cell culture.** HCC1143, HCC1806, HCC1937, HCC38, and MDAMB468 cells were obtained from the American Type Culture Collection. BT549, CAL51, MDAMB231, MDAMB436, and SUMI49PT cells were kindly provided by the Sorger lab (Harvard Medical School, Ludwig Cancer Center, Boston, USA). MCF10A and MCF7 cells were kindly gifted by the Brugge lab (Harvard Medical School, Ludwig Cancer Center, Boston, USA). GIMEN and SH-SY5Y cells were provided by the Schulte lab (Universitätsklinikum Tübingen, Clinic for Pediatrics and Adolescent Medicine, Tübingen, Germany) and the U-2 OS reporter cell lines by the Kramer lab (Charité, Institute for Medical Immunology, Berlin, Germany). MCF10A cells were maintained according to the Brugge lab's media recipe based on DMEM/F12 media (Gibco, I1320033) supplemented with 5% horse serum (Gibco, 26050088), 20 ng/ml EGF (Peprotech, AF-100-15), 0.5 mg/ml Hydrocortisone (Sigma, 50-23-7), 100 ng/ml Cholera Toxin (Sigma, 9012-63-9), 10 µg/ml Insulin (Sigma, I1882) and 1% penicillin-streptomycin (Pen-Strep, Gibco, 15140122). All other cell lines were maintained in RPMI 1640 (Gibco, I1875-093) supplemented with 10% fetal bovine serum (FBS) (Gibco, A5256701) and 1% Pen-Strep. For bioluminescence recordings and long-term imaging, cells were cultured in FluoroBrite DMEM medium (Gibco, A1896701) supplemented with 10% FBS, 300 mg L-Glutamine (Gibco, 25030024) and 1% Pen-Strep. Cells were kept at 37 °C in a humidified 5% CO<sub>2</sub> environment and regularly tested for mycoplasma.

**Generation of reporter cell lines.** To produce lentivirus carrying constitutive red-fluorescent nuclear reporters, HEK293T cells at 80% confluence were transfected with a mix of 1.8 µg gag/pol packaging plasmid (Addgene #14887), 0.7 µg pRev packaging plasmid (Addgene #12253), 0.3 µg VSV-G envelope plasmid (Addgene #14888) and 3.2 µg of a plasmid with a EF1 $\alpha$ -mKate2-NLS sequence. Lentivirus expressing either *Bmal1*- or *Per2*-promoter driven luciferase reporter was produced by transfecting HEK293T cells with 6 µg psPAX2 (Addgene #12260), 3.6 µg pMD2G (Addgene #12259) and 8.4 µg lentiviral expression plasmid (pAB-mBmal1:Luc-Puro or plenti6-mPer2:Luc-Blast, respectively). Transfections were conducted using Lipofectamine 3000 (Invitrogen, L3000015) according to the manufacturer's instructions, and media was replaced by RPMI 1640 medium supplemented with 10 mM HEPES (Gibco, 15630080) before adding the transfection mixture. Lentiviral supernatant was collected after 48 h and 72 h and passed through a 0.45 µm filter (Millipore, HAWPO4700). For lentiviral transduction, receiver cells at 70% confluence were incubated with a mix of 1 ml lentivirus-containing supernatant, 8 µg/ml protamine sulfate (Sigma, P4020), and 10 µM HEPES for 6 h. Ensuing, cells were washed with PBS (Gibco, 10010-015) and cultured in their regular culture medium for 2 days before starting antibiotic selection of transduced cells. To select for transduced cells, cells were grown in a medium containing 5 µg/ml blasticidin (Adooq, A21608) or 2 µg/ml puromycin (Gibco, A1113803) according to the resistance cassette on the lentiviral expression plasmid until non-transduced control cells died. Details about the generation of

the U-2 OS *Cry1*-sKO, U-2 OS *Cry2*-sKO, and U-2 OS *Cry1/Cry2*-dKO cell lines can be found in the original publication by Börding et al.<sup>28</sup>.

**Bioluminescence recordings.** Cells expressing *Bmal1*- or *Per2*-promoter driven luciferase reporters were seeded in 35-mm dishes (Nunc) to reach approximate confluence on the following day. To account for potentially different phases of single-cell circadian clocks in cell populations, we collectively reset the circadian clocks by administering a standard dose of 1  $\mu$ M dexamethasone<sup>49,50</sup> (Sigma, D4902, dissolved in EtOH). After 30 min incubation, cells were washed once with PBS, and an imaging medium supplemented with 250  $\mu$ M D-Luciferin (Abmole, M9053) was added. To avoid evaporation of the media throughout the bioluminescence recordings, the dishes were sealed with parafilm as described in Finger et al.<sup>49</sup>. Luminescence intensity was monitored at 10-min intervals for 5 days in an incubator-embedded luminometer (LumiCycle, Actimetrics). Bioluminescence recordings were conducted using two biological replicates. For each individual experiment, three, in some cases only two, technical replicates were assessed. MCF10A cells have been tested on a single day using three technical replicates.

**Long-term live-cell imaging.** All live-cell imaging experiments were performed with cells expressing the fluorescent mKate2-NLS nuclear reporter, seeded in 48-well plates (Falcon) at a density that saturates at unperturbed growth conditions towards the end of each experiment. Long-term live-cell imaging was conducted using an incubator-embedded Incucyte live-cell widefield microscope (Essen BioScience). Cells were imaged in the brightfield and for nuclei segmentation and cell counting in the red channel (excitation: 567–607 nm, emission: 622–704 nm). Images were analyzed by frame-by-frame nuclei counting with the in-built Incucyte software and results were further processed in MATLAB. For experiments that involved drug treatments, cells were seeded 1 day before starting the live recordings, and images were taken using a 4x magnification lens in 2 fields-of-views per well every 1–2 h for a total duration of 4–6 days. Two independent plates per condition were assayed in a single experiment. For drug response experiments with cisplatin, a single plate per condition was assayed in a single experiment, imaged in 9 fields-of-views per well using a 10x magnification lens. For experiments capturing unperturbed growth dynamics, 300–1000 cells, corresponding to ~10% confluency, were seeded 2 days before starting the live recordings. Using a 10x magnification lens, 9 images per well were acquired in 1–2 h intervals for a total duration of 4 days.

**Dose-response curves.** Drug stock solutions (100–10 mM) were prepared in DMSO and preserved at –20 °C. Cisplatin (Sigma, 232120) stock solution of 3.33 mM was prepared in 0.9% NaCl and stored at room temperature. For dose-response assays, a serial 5–6 point log<sub>4</sub> dilution of each drug was freshly prepared in its solvent prior to treatment. Following concentration ranges were tested: 100–0.1  $\mu$ M for 5-fluorouracil (5-FU, Sigma, 03738-100MG), alpelisib (Biozol, TGM-T1921-10MG) and olaparib (Adooq, A10111); 10–0.01  $\mu$ M for torin2 (Sigma, SML1224-5MG) and alisertib (Hözlzel, S1133-5); 10–0.04  $\mu$ M for adavosertib (Biocat, T2077-5mg-TM); 1–0.004  $\mu$ M for doxorubicin (Hözlzel, A14403-100); and 0.4–0.0004  $\mu$ M for paclitaxel (Hözlzel, M1970-50mg). Cisplatin was tested in a serial 10-point log<sub>2</sub> dilution with doses ranging from 70–0.14  $\mu$ M. Compounds were added to the cells one day after cell seeding in a drug-media mixture of 9% of the total well volume. Solvent-only treated control cells were assayed along the treated conditions. Each tested condition contained equal amounts of the solvent. Cell growth was monitored by live-cell imaging for at least 4 days as described above.

**Time-of-day treatments.** Cells were seeded and allowed to attach overnight. The next day, live recordings commenced as described

earlier. We performed independent resetting steps every 4 h over an 8-h period, creating distinct cell populations at 0, 4, or 8 h of circadian time. Subsequently, we administered the same drug concentration, which corresponded to the estimated half-maximal effective concentration, at either 32 or 48 hours after the initial resetting step. This allowed us to simultaneously test six different circadian stages (0, 4, 8, 16, 20, and 24 h). Drug concentrations were determined separately for each cell line and drug combination. For cisplatin, the treatments we performed were slightly different, using 4 independent resetting steps every 3 h over a 9-h period followed by drug treatments 32 or 48 h post initial resetting. In all cases, cell growth was continuously monitored through long-term live-cell imaging for a total of 6 days.

## Computational methods

### Time-series analysis of circadian signals

**Detrending.** Raw time-series data were detrended by applying a sinc filter with a 48-h cut-off period using the open-source software package pyBOAT<sup>27</sup> (v0.9.1) within the Anaconda Navigator (v1.10.0).

**Amplitude envelope and normalization.** Continuous amplitude envelope calculation was obtained using continuous wavelet transform implemented in pyBOAT with a time window of 48 h. The amplitude normalization was done by taking the inverse of the envelope of the detrended signal as described in Mönke G, et al.<sup>27</sup>.

**Autocorrelation analysis.** Periodicity data was assessed by calculating its autocorrelation and abscissa at the second peak using the ‘autocorr’ and ‘findpeaks’ MATLAB functions<sup>51</sup> from the detrended time series.

**Continuous wavelet transform.** The main oscillatory component, known as the ridge component, was obtained using a wavelet-based spectral analysis from amplitude-normalized and detrended signals. For the ridge detection, we used both an adaptable threshold and a fixed threshold. The adaptable threshold was based on each signal’s half-maximal spectral power and was implemented for the “period” and “phase difference” metrics shown in Fig. 2 and Fig. S1. The instantaneous phase difference between the *Bmal1* and *Per2* signals was calculated using the MATLAB ‘atan2’ function (Supplementary Fig. 1a) and for the polar histogram representation, we deployed the ‘polarhistogram’ function and the ‘Circular Statistics Toolbox’ (v1.21.9.0. by Philipp Behrens) from MATLAB (Supplementary Fig. 1b). For the analysis of “amplitudes” and “ridge lengths” shown in Fig. 2 and the determinants for time-of-day sensitivity shown in Fig. 5, the metrics of the main oscillatory component were derived using a fixed-ridge threshold of 40. This ridge threshold value was chosen as it offered a well-balanced threshold suitable for comparing signals of varying strengths.

**Multiresolution analysis.** Detrended time-series data were decomposed into a set of different wavelet details  $D_j$  representing distinct disjoint frequency bands and a final smooth using a discrete wavelet transform-based multiresolution analysis<sup>52</sup>. The algorithm has been implemented using the ‘PyWavelets’ python package<sup>53</sup>, with a *db20* wavelet of the Daubechies wavelet family as previously described in Myung, Schmal and Hong et al.<sup>54</sup>. Since each wavelet detail  $D_j$  represents a period range between  $2^j\Delta t$  and  $2^{j+1}\Delta t$  (for  $j = 1, 2, 3, \dots$ ) we down-sampled the time series from a  $\Delta t = 10$  min to a  $\Delta t = 30$  min sampling frequency to obtain a circadian period band between 16–32 h for further analysis. Since the MRA decomposes the variance of the detrended signal with respect to the different disjoint period bands, it can be used to determine the rhythmicity of the signal in the circadian period range<sup>55</sup>.

**Global circadian strength.** To calculate the global circadian strength (GCS) of a cell line model  $i$ , the autocorrelation peak value

(peak), the wavelet-based continuous ridge length (ridge), and the discrete circadianity component (circadianity) were normalized to the respective maximum (max) value measured among all tested cell line models and averaged according to the following equation:

$$GCS_i = \text{mean} \left( \frac{\text{peak}_i}{\text{peak}_{\max}}, \frac{\text{ridge}_i}{\text{ridge}_{\max}}, \frac{\text{circadianity}_i}{\text{circadianity}_{\max}} \right) \quad (1)$$

**Statistical analysis.** Linear regression model fitting of *Bmal1* and *Per2* circadianity components obtained by MRA was done with the ‘fitlm’ MATLAB function. Significant variances in circadian parameters between wild-type U-2 OS cells and both *Cry1*-sKO and *Cry1/2*-dKO cells were calculated with a one-way ANOVA and Tukey’s post-hoc test using the ‘anova1’ and ‘multcompare’ MATLAB functions.

### Multi-parametric analysis of growth dynamics

Growth data obtained from long-term live-cell imaging was smoothed using a robust local regression approach of weighted linear least squares and a 2<sup>nd</sup> degree polynomial model (‘rloess’ MATLAB function). Doubling times of smoothed cell numbers or confluency were calculated according to the following equation:

$$\text{Doubling time}(t) = t * \frac{\log(2)}{\log(y_0/y_t)} \quad (2)$$

where  $t$  refers to the time of assessment, in our case 96 h, and  $y_0$  refers to the cell number at timepoint 0. To calculate the exponential growth rate  $k$  per unit of time  $t$ , we normalized cell numbers to the initial timepoint 0 ( $y_0$ ) and fitted an exponential function to the growth curves:

$$\text{Growth}(t) = y_0 * e^{(k*t)} \quad (3)$$

Exponential function fitting was done with the MATLAB ‘fit’ function<sup>51</sup>. Linear regression model fitting to different combinations of growth parameters was done with the ‘fitlm’ MATLAB function.

### Estimation of drug sensitivity parameters

Drug response data obtained from long-term live-cell imaging was smoothed using a robust local regression approach of weighted linear least squares and a 2<sup>nd</sup> degree polynomial model (‘rloess’ MATLAB function). Following the method established by Hafner et al.<sup>30</sup>, we computed the growth rate inhibition ( $GR$ ) at time  $t$  and for each dose  $c$  as follows:

$$GR(c, t) = 2^{k(c,t)/k(0)} - 1 \quad (4)$$

where  $k(c, t)$  is the growth rate under drug treatment and  $k(0)$  is the growth rate of untreated cells. Drug response parameters were retrieved by fitting the dose-dependent  $GR$ -values to a sigmoid curve using the following equation:

$$GR(c) = GR_{\text{inf}} + \frac{1 - GR_{\text{inf}}}{1 + (c/EC_{50})^{h_{\text{GR}}}} \quad (5)$$

where the fitted parameters are as described in Hafner et al.<sup>30</sup>. Standard  $EC_{50}$ -values were calculated by fitting final nucleus counts, normalized to the respective count of the control, to the following sigmoidal function:

$$f(c) = E_{\text{min}} + \frac{1 - E_{\text{min}}}{1 + (c/EC_{50})^h} \quad (6)$$

where  $E_{\text{min}}$  corresponds to the minimum response, restricted to values between 0 and 1, and  $h$  is the hill slope of the response curve, constrained to 0.5–10. Sigmoidal function fitting steps were done with the MATLAB functions ‘fit’ ( $GR$  metrics) or ‘lsqnonlin’ ( $EC_{50}$  value)<sup>51</sup>. Hierarchical clustering analysis was implemented with the MATLAB ‘clustergram’ function using an Euclidian distance and average linkage method<sup>51</sup>. To account for the different tested dose ranges across drugs for clustering,  $GEC_{50}$ -values were normalized to the dose at  $GR_{\text{inf}}$ . Pearson’s linear correlation coefficients across drug sensitivity metrics were computed using the MATLAB ‘corr’ function. For the comparison of cellular growth dynamics to drug doses evoking the maximum tested effect, we chose growth curves corresponding to the doses closest to the determined  $GR_{\text{inf}}$ -values.

### Time-of-day sensitivity evaluation

Drug response data of time-of-day treatment experiments was smoothed using a moving average (‘smoothdata’ MATLAB function). Final nucleus counts were normalized to the nucleus count at the respective time of treatment. ToD response data from U-2 OS WT and *Cry1/2*-dKO cell lines were obtained from confluency readouts in the brightfield channel. Time-of-day response curves were generated from the relative final responses of each treatment timepoint to the final response at timepoint 0 and interpolated using the ‘smoothing spline’ function in MATLAB. The smoothing parameter was set to 0.7. The maximum range across smoothed time-of-day responses ( $ToD_{\text{MR}}$ ) was calculated by subtraction of the minimum from the maximum relative response. To assess whether the smoothing of response data introduces artifacts into  $ToD_{\text{MR}}$  estimates, we performed linear regression analysis between  $ToD_{\text{MR}}$ -values from raw and spline smoothed data using the ‘fitlm’ MATLAB function and confirmed a high positive correlation (Supplementary Fig. 7a).  $ToD_{\text{MR}}$ -values were clustered as described for the drug sensitivity parameters, with missing data points substituted by values from the closest relevant column, adhering to the ‘nearest-neighbor’ principle. Polar histograms of the treatment times with maximum and minimum benefit were generated using the ‘polarhistogram’ MATLAB function with ‘probability’ normalization to depict each bar’s height as the fraction of observations within its bin relative to the total observations.

### Correlation and shapley value regression analysis

Linear regressions of cell-intrinsic features and drug-dependent ToD sensitivity have been obtained using the ‘stats’ and ‘optimize’ modules of the ‘SciPy’ and the ‘uncertainties’ package of the Python programming language. Predictions of  $ToD_{\text{MR}}$ -values from new data was based on fitting a linear regression model to the original data that was associated with Pearson correlation coefficients  $\geq 0.5$ , utilizing the ‘fitlm’ MATLAB function. Bland-Altman plots comparing predicted and actual  $ToD_{\text{MR}}$ -values were generated using the ‘Bland-Altman and Correlation Plot’ package (v1.12.0.0) from MATLAB Central File Exchange (2017, Ran Klein). Live-imaging data yielding growth, drug sensitivity, and ToD sensitivity metrics from the new cell lines utilized for the predictions were based on the confluency readout due to the unviability of nuclear reporter cell lines for most models. Only the drug sensitivity metrics for MCF7 were based on nuclear counts. The relative importance of the different parameters in a multiple linear regression model is obtained by Shapley value regression via the Python ‘dominance-analysis’ package.

### Circadian clock gene expression analysis

Gene expression data of circadian clock genes were obtained from the Cancer Cell Line Encyclopedia Dependency Map (CCLE DepMap, <https://sites.broadinstitute.org/ccle/datasets>, Q4 of 2022)<sup>56</sup>. Circadian clock genes of the individual breast cancer cell lines were clustered using the ‘clustermap’ plotting function of ‘seaborn’ with the euclidian distance metric and complete linkage method. Spearman rank

correlation coefficients of circadian clock genes and drug-specific ToD sensitivity values were computed using the Spearman rank correlation algorithm of the 'SciPy stats' Python language module and hierarchically clustered with the correlation distance metric and single linkage method. Regression plots were obtained using the 'jointplot' plotting function from 'seaborn', showing drug-specific correlation between the ToD sensitivities and gene expression of each cell line, including their distribution, squared spearman rank correlation coefficient,  $p$ -value, and a confidence interval of 95%.

### Supervised and unsupervised dimensionality reduction

Supervised dimensionality reduction by linear discriminant analysis was performed with the 'LinearDiscriminantAnalysis' function of the 'sklearn discriminant\_analysis' Python language module. The default parameters were retained, using the exact full singular value decomposition solver and 1 component. Median-based binarization of the drug-dependent ToD sensitivity values was used as a target, and the resulting linear discriminant vector was plotted using random y-axis units to avoid overlapping of the data points. The robustness of the discriminative information from the LDA was tested using a leave-one-out cross-validation (LOOCV) strategy (Supplementary Fig. 7b). LOOCV was conducted using the 'model\_selection' module from 'sklearn' in Python (v3.9.7) and implemented via the PyCharm Community Edition IDE (v2021.2.2). The contribution to the obtained discriminative information is shown in percentage for each of the circadian clock genes. Unsupervised dimensionality reduction by principal component analysis (PCA) was performed with the 'PCA' function of the 'sklearn decomposition' Python language module using the exact full singular value decomposition solver and number of components equivalent to the sample size of the corresponding drug. Further analysis of the most informative PCA components was done by drawing the biplots of the first two principal components and showing the loadings of each circadian clock gene for both components.

### Reporting summary

Further information on research design is available in the Nature Portfolio Reporting Summary linked to this article.

### Data availability

The experimental raw data and data tables generated in this study have been deposited in the Figshare database under the identifier <https://figshare.com/projects/Time-of-Day-Drug-Response/180916>. Source data are provided in this paper.

### Code availability

All code used for the data analysis in this work (in MATLAB and Python) is publicly available through the dataset repository Zenodo under the identifier <https://zenodo.org/doi/10.5281/zenodo.11656060>.

### References

- Chaix, A., Zarrinpar, A. & Panda, S. The circadian coordination of cell biology. *J. Cell Biol.* **215**, 15–25 (2016).
- Zhang, R., Lahens, N. F., Ballance, H. I., Hughes, M. E. & Hogenesch, J. B. A circadian gene expression atlas in mammals: implications for biology and medicine. *Proc. Natl. Acad. Sci. USA* **111**, 16219–16224 (2014).
- Mure, L. S. et al. Diurnal transcriptome atlas of a primate across major neural and peripheral tissues. *Science* **359**, <https://doi.org/10.1126/science.aao0318> (2018).
- Saini, C. et al. A functional circadian clock is required for proper insulin secretion by human pancreatic islet cells. *Diabetes Obes. Metab.* **18**, 355–365 (2016).
- Neufeld-Cohen, A. et al. Circadian control of oscillations in mitochondrial rate-limiting enzymes and nutrient utilization by PERIOD proteins. *Proc. Natl. Acad. Sci. USA* **113**, E1673–E1682 (2016).
- Chakrabarti, S. & Michor, F. Circadian clock effects on cellular proliferation: Insights from theory and experiments. *Curr. Opin. Cell Biol.* **67**, 17–26 (2020).
- Scheiermann, C., Kunisaki, Y. & Frenette, P. S. Circadian control of the immune system. *Nat. Rev. Immunol.* **13**, 190–198 (2013).
- Sancar, A. et al. Circadian clock control of the cellular response to DNA damage. *FEBS Lett.* **584**, 2618–2625 (2010).
- Schernhammer, E. S. et al. Rotating night shifts and risk of breast cancer in women participating in the nurses' health study. *J. Natl. Cancer Inst.* **93**, 1563–1568 (2001).
- Puram et al. Core circadian clock genes regulate leukemia stem cells in AML. *Cell* **165**, 303–316 (2016).
- Papagiannakopoulos, T. et al. Circadian rhythm disruption promotes lung tumorigenesis. *Cell Metab.* **24**, 324–331 (2016).
- Chun, S. K. et al. Disruption of the circadian clock drives Apc loss of heterozygosity to accelerate colorectal cancer. *Sci. Adv.* **8**, eabo2389 (2022).
- Diamantopoulou, Z. et al. The metastatic spread of breast cancer accelerates during sleep. *Nature* **607**, 156–162 (2022).
- Wang, J. et al. Circadian protein BMAL1 promotes breast cancer cell invasion and metastasis by up-regulating matrix metalloproteinase9 expression. *Cancer Cell Int.* **19**, 182 (2019).
- Lee, Y. et al. G1/S cell cycle regulators mediate effects of circadian dysregulation on tumor growth and provide targets for timed anticancer treatment. *PLOS Biol.* **17**, e3000228 (2019).
- Chen, W.-D. et al. The circadian rhythm controls telomeres and telomerase activity. *Biochem. Biophys. Res. Commun.* **451**, 408–414 (2014).
- Rida, P., Syed, M. I. & Aneja, R. Time will tell: Circadian clock dysregulation in triple negative breast cancer. *Front Biosci. Schol. Ed.* **11**, 178–192 (2019).
- Innominato, P. F. et al. Prediction of overall survival through circadian rest-activity monitoring during chemotherapy for metastatic colorectal cancer. *Int. J. Cancer* **131**, 2684–2692 (2012).
- Ye, Y. et al. The genomic landscape and pharmacogenomic interactions of clock genes in cancer chronotherapy. *Cell Syst.* **6**, 314–328.e312 (2018).
- Lee, Y. et al. Time-of-day specificity of anticancer drugs may be mediated by circadian regulation of the cell cycle. *Sci. Adv.* **7**, eabd2645 (2021).
- Dallmann, R., Brown, S. A. & Gachon, F. Chronopharmacology: New insights and therapeutic implications. *Annu. Rev. Pharmacol. Toxicol.* **54**, 339–361 (2014).
- Lévi, F., Okyar, A., Dulong, S., Innominato, P. F. & Clairambault, J. Circadian timing in cancer treatments. *Annu. Rev. Pharmacol. Toxicol.* **50**, 377–421 (2010).
- Wood, P. A., Du-Quiton, J., You, S. & Hrushesky, W. J. M. Circadian clock coordinates cancer cell cycle progression, thymidylate synthase, and 5-fluorouracil therapeutic index. *Mol. Cancer Ther.* **5**, 2023–2033 (2006).
- Damato, A. R. et al. A randomized feasibility study evaluating temozolomide circadian medicine in patients with glioma. *Neuro Oncol. Pract.* **9**, 193–200 (2022).
- Ruben, M. D., Smith, D. F., FitzGerald, G. A. & Hogenesch, J. B. Dosing time matters. *Science* **365**, 547–549 (2019).
- Kramer, A. et al. Foundations of circadian medicine. *PLOS Biol.* **20**, e3001567 (2022).
- Mönke, G., Sorgenfrei, F. A., Schmal, C. & Granada, A. E. Optimal time frequency analysis for biological data - pyBOAT. Preprint at *bioRxiv* <https://doi.org/10.1101/2020.04.29.067744> (2020).
- Börding, T., Abdo, A. N., Maier, B., Gabriel, C. & Kramer, A. Generation of human CRY1 and CRY2 knockout cells using duplex CRISPR/Cas9 technology. *Front. Physiol.* **10**, 577 (2019).
- Leise, T. L. Analysis of nonstationary time series for biological Rhythms research. *J. Biol. Rhythms* **32**, 187–194 (2017).

30. Hafner, M., Niepel, M., Chung, M. & Sorger, P. K. Growth rate inhibition metrics correct for confounders in measuring sensitivity to cancer drugs. *Nat. Methods* **13**, 521–527 (2016).
31. Ko, C. H. & Takahashi, J. S. Molecular components of the mammalian circadian clock. *Hum. Mol. Genet.* **15**, R271–R277 (2006).
32. Takahashi, J. S. Transcriptional architecture of the mammalian circadian clock. *Nat. Rev. Genet.* **18**, 164–179 (2017).
33. Mormont, M.-C. & Levi, F. Cancer chronotherapy: Principles, applications, and perspectives. *Cancer* **97**, 155–169 (2003).
34. Sulli, G., Lam, M. T. Y. & Panda, S. Interplay between circadian clock and cancer: New frontiers for cancer treatment. *Trends Cancer* **5**, 475–494 (2019).
35. Lin, H.-H., Qraitem, M., Lian, Y., Taylor, S. R. & Farkas, M. E. Analyses of BMAL1 and PER2 oscillations in a model of breast cancer progression reveal changes with malignancy. *Integr. Cancer Ther.* (2019).
36. Lellupitiyage Don, S. S. et al. Circadian oscillations persist in low malignancy breast cancer cells. *Cell Cycle* **18**, 2447–2453 (2019).
37. Baggs, J. E. et al. Network features of the mammalian circadian clock. *PLOS Biol.* **7**, e1000052 (2009).
38. Gupta, G. K. et al. Perspectives on triple-negative breast cancer: Current treatment strategies, unmet needs, and potential targets for future therapies. *Cancers* **12**, 2392 (2020).
39. Fallahi-Sichani, M., Honarnejad, S., Heiser, L. M., Gray, J. W. & Sorger, P. K. Metrics other than potency reveal systematic variation in responses to cancer drugs. *Nat. Chem. Biol.* **9**, 708–714 (2013).
40. Lévi, F. A. et al. Chronomodulated versus fixed-infusion—rate delivery of ambulatory chemotherapy with oxaliplatin, fluorouracil, and folinic acid (Leucovorin) in patients with colorectal cancer metastases: a randomized multi-institutional trial. *J. Natl. Cancer Inst.* **86**, 1608–1617 (1994).
41. Sothorn, R. B., Lévi, F., Haus, E., Halberg, F. & Hrushesky, W. J. Control of a murine plasmacytoma with doxorubicin-cisplatin: dependence on circadian stage of treatment. *J. Natl. Cancer Inst.* **81**, 135–145 (1989).
42. Nagoshi, E. et al. Circadian gene expression in individual fibroblasts: cell-autonomous and self-sustained oscillators pass time to daughter cells. *Cell* **119**, 693–705 (2004).
43. Izumo, M., Johnson, C. H. & Yamazaki, S. Circadian gene expression in mammalian fibroblasts revealed by real-time luminescence reporting: Temperature compensation and damping. *Proc. Natl. Acad. Sci. USA* **100**, 16089–16094 (2003).
44. Balsalobre, A., Damiola, F. & Schibler, U. A serum shock induces circadian gene expression in mammalian tissue culture cells. *Cell* **93**, 929–937 (1998).
45. Bieler, J. et al. Robust synchronization of coupled circadian and cell cycle oscillators in single mammalian cells. *Mol. Syst. Biol.* **10**, 739 (2014).
46. Gérard, C. & Goldbeter, A. Entrainment of the mammalian cell cycle by the circadian clock: Modeling two coupled cellular rhythms. *PLOS Comput. Biol.* **8**, e1002516 (2012).
47. Bernard, S., Čajavec Bernard, B., Lévi, F. & Herzog, H. Tumor growth rate determines the timing of optimal chronomodulated treatment schedules. *PLOS Comput. Biol.* **6**, e1000712 (2010).
48. Zhu, B. et al. A cell-autonomous mammalian 12 hr clock coordinates metabolic and stress rhythms. *Cell Metab.* **25**, 1305–1319 (2017).
49. Finger, A.-M. et al. Intercellular coupling between peripheral circadian oscillators by TGF- $\beta$  signaling. *Sci. Adv.* **7**, eabg5174 (2021).
50. Balsalobre, A. et al. Resetting of circadian time in peripheral tissues by glucocorticoid signaling. *Science* **289**, 2344–2347 (2000).
51. version 9.11.0.1769968 (R2021b) (The MathWorks Inc., 2021).
52. Leise, T. L. & Harrington, M. E. Wavelet-based time series analysis of circadian rhythms. *J. Biol. Rhythms* **26**, 454–463 (2011).
53. Lee, G. R., Gommers, R., Waselewski, F., Wohlfahrt, K. & O’Leary, A. PyWavelets: A Python package for wavelet analysis. *J. Open Source Softw.* **4**, 1237 (2019).
54. Myung, J. et al. The choroid plexus is an important circadian clock component. *Nat. Commun.* **9**, 1062 (2018).
55. Leise, T. L. Wavelet analysis of circadian and ultradian behavioral rhythms. *J. Circadian Rhythms* <https://doi.org/10.1186/1740-3391-11-5> (2013).
56. Barretina, J. et al. The Cancer Cell Line Encyclopedia enables predictive modelling of anticancer drug sensitivity. *Nature* **483**, 603–607 (2012).

## Acknowledgements

We thank Malthe Skytte Nordentoft Nielsen, as well as the laboratories of Michela Di Virgilio and Ingeborg Tinhofer-Keilholz, for their valuable feedback on our project. We are grateful to Annika Winkler and Marie Möser for their assistance with sample preparation, as well as to Sofía Peso-García and Franziska Reiher for their experimental support. Lastly, we thank Christian Gabriel and Valentina Alejandra Balde Araya for valuable feedback during the review of this manuscript. The results are part of a project funded by the German Federal Ministry of Education and Research (BMBF) through the e:Med Juniorverbund DeepLTNBC TP3-01ZX1917C. C.E. was partially supported by the Deutsche Forschungsgemeinschaft (DFG, German Research Foundation)—RTG2424/CompCancer – project number: 377984878 and is enrolled in the doctoral program of the Berlin School of Integrative Oncology (BSIO). C.S. acknowledges support from the DFG—SCHM 3362/4–1 project number: 511886499.

## Author contributions

C.E., A.K., and A.E.G. conceived and planned the experiments. C.E. performed the experiments. F.M.M. performed bioluminescence recordings of three cell lines. C.E., C.S., J.D., and S.D.L. analyzed the data. A.M.F. and A.K. supported the planning and implementation of the bioluminescence recordings. C.E., C.S., A.M.F., J.D., S.D.L., J.S., T.S., U.K., H.H., A.K., and A.E.G. contributed to the interpretation of the results. C.E. and A.E.G. wrote the manuscript. All authors provided critical feedback and helped shape the research and manuscript.

## Funding

Open Access funding enabled and organized by Projekt DEAL.

## Competing interests

The authors declare no competing interests.

## Additional information

**Supplementary information** The online version contains supplementary material available at <https://doi.org/10.1038/s41467-024-51611-3>.

**Correspondence** and requests for materials should be addressed to Adrián E. Granada.

**Peer review information** *Nature Communications* thanks the anonymous reviewers for their contribution to the peer review of this work. A peer review file is available.

**Reprints and permissions information** is available at <http://www.nature.com/reprints>

**Publisher’s note** Springer Nature remains neutral with regard to jurisdictional claims in published maps and institutional affiliations.

**Open Access** This article is licensed under a Creative Commons Attribution 4.0 International License, which permits use, sharing, adaptation, distribution and reproduction in any medium or format, as long as you give appropriate credit to the original author(s) and the source, provide a link to the Creative Commons licence, and indicate if changes were made. The images or other third party material in this article are included in the article's Creative Commons licence, unless indicated otherwise in a credit line to the material. If material is not included in the article's Creative Commons licence and your intended use is not permitted by statutory regulation or exceeds the permitted use, you will need to obtain permission directly from the copyright holder. To view a copy of this licence, visit <http://creativecommons.org/licenses/by/4.0/>.

© The Author(s) 2024

## **Appendix A3: TNBC**

Article title: **Circadian clock features define novel subtypes among breast cancer cells and shape drug sensitivity**

Contributions: Data analysis

Discussion and interpretation of results

Method section writing (concerning techniques we applied)

Figure 3; 4; S2

DOI link: <https://doi.org/10.1038/s44320-025-00092-7>

Published in: Molecular Systems Biology



# Circadian clock features define novel subtypes among breast cancer cells and shape drug sensitivity

Carolin Ector <sup>1,2,3</sup>, Jeff Didier <sup>4</sup>, Sébastien De Landtsheer<sup>4</sup>, Malthe S Nordentoft<sup>5</sup>, Christoph Schmal<sup>6</sup>, Ulrich Keilholz<sup>1,7</sup>, Hanspeter Herzel <sup>6,8</sup>, Achim Kramer <sup>9</sup>, Thomas Sauter <sup>4</sup> & Adrián E Granada <sup>1,7</sup>✉

## Abstract

The circadian clock regulates key physiological processes, including cellular responses to DNA damage. Circadian-based therapeutic strategies optimize treatment timing to enhance drug efficacy and minimize side effects, offering potential for precision cancer treatment. However, applying these strategies in cancer remains limited due to a lack of understanding of the clock's function across cancer types and incomplete insights into how the circadian clock affects drug responses. To address this, we conducted deep circadian phenotyping across a panel of breast cancer cell lines. Observing diverse circadian dynamics, we characterized metrics to assess circadian rhythm strength and stability *in vitro*. This led to the identification of four distinct circadian-based phenotypes among 14 breast cancer cell models: functional, weak, unstable, and dysfunctional clocks. Furthermore, we demonstrate that the circadian clock plays a critical role in shaping pharmacological responses to various anti-cancer drugs and we identify circadian features descriptive of drug sensitivity. Collectively, our findings establish a foundation for implementing circadian-based treatment strategies in breast cancer, leveraging clock phenotypes and drug sensitivity patterns to optimize therapeutic outcomes.

**Keywords** Circadian Clock; Circadian Medicine; Systems Biology; Breast Cancer

**Subject Category** Cancer

<https://doi.org/10.1038/s44320-025-00092-7>

Received 16 August 2024; Revised 11 February 2025;

Accepted 12 February 2025

Published online: 24 February 2025

## Introduction

In alignment with the solar 24-h day–night cycle, the circadian clock regulates essential physiological and behavioral processes in almost all organisms. In mammals, a hierarchical structure coordinates rhythmic activities across both whole-organism and cellular levels (Chaix et al, 2016; Golombek et al, 2014), with the master clock residing in the suprachiasmatic nucleus (SCN) and

individual peripheral clocks oscillating across tissue types (Chaix et al, 2016). Remarkably, about 40% of all genes are rhythmically expressed in a tissue-specific manner (Zhang et al, 2014), influencing various biological functions such as metabolism (Neufeld-Cohen et al, 2016), cell growth (Chakrabarti and Michor, 2020), immune responses (Scheiermann et al, 2013), and DNA repair (Sancar et al, 2010), thereby maintaining cellular balance.

At its core, the circadian mechanism is composed of transcriptional-translational feedback loops (TTFLs) (Takahashi, 2017). These TTFLs consist of the CLOCK and BMAL1 transcription factors, which induce the transcription of *Per1/2/3* and *Cry1/2* genes through the binding to the respective promoter regions. In turn, PER and CRY proteins inhibit the binding of CLOCK/BMAL1, and consequently their own transcription. In a complementary second feedback loop the transcription of *Bmal1* is rhythmically regulated by REV-ERBa/β repressor and RORa/β/γ activator proteins, whose transcription is likewise dependent on the CLOCK/BMAL1 transactivation complex (Chaix et al, 2016; Takahashi, 2017).

Environmental factors are crucial in maintaining the synchronization of circadian rhythms in our body. Misalignments of this synchronization, for example through prolonged exposure to shift work, are associated with various diseases, including cancer (Sulli et al, 2019)—the second-leading cause of death worldwide (<https://www.who.int/health-topics/cancer>, 2022). In-depth studies have further shown how the disturbance of the circadian clock, through either genetic mutations or the suppression of core clock genes is directly linked to the progression of cancer and poorer survival rates (Ye et al, 2018). The clock's influence extends to cancer therapy, affecting the efficacy and toxicity of treatments in a time-of-day-dependent manner (Lee et al, 2021; Ye et al, 2018). Despite its high medical importance, the distinct role of the circadian clock in cancer remains poorly understood, highlighting the need for further research to optimize treatment strategies by circadian rhythms.

To illuminate the circadian clock's role in cancer, our study focuses on breast cancer, the most prevalent cancer among women and the second most common overall (Bray et al, 2024). Breast cancer is categorized into four main subtypes, distinguished by the cell phenotype (basal or luminal) and specific biomarkers,

<sup>1</sup>Charité Comprehensive Cancer Center, Charité – Universitätsmedizin Berlin, 10117 Berlin, Germany. <sup>2</sup>Berlin School of Integrative Oncology, Charité – Universitätsmedizin Berlin, 10117 Berlin, Germany. <sup>3</sup>Faculty of Life Sciences, Humboldt-Universität zu Berlin, 10115 Berlin, Germany. <sup>4</sup>Department of Life Sciences and Medicine, University of Luxembourg, L-4365 Esch-sur-Alzette, Luxembourg. <sup>5</sup>Niels Bohr Institute, University of Copenhagen, 2100 Copenhagen, Denmark. <sup>6</sup>Institute for Theoretical Biology, Humboldt-Universität zu Berlin, 10115 Berlin, Germany. <sup>7</sup>German Cancer Consortium (DKTK), Berlin, Germany. <sup>8</sup>Charité – Universitätsmedizin Berlin, 10117 Berlin, Germany. <sup>9</sup>Laboratory of Chronobiology, Charité – Universitätsmedizin Berlin, 10117 Berlin, Germany. ✉E-mail: [adrian.granada@charite.de](mailto:adrian.granada@charite.de)

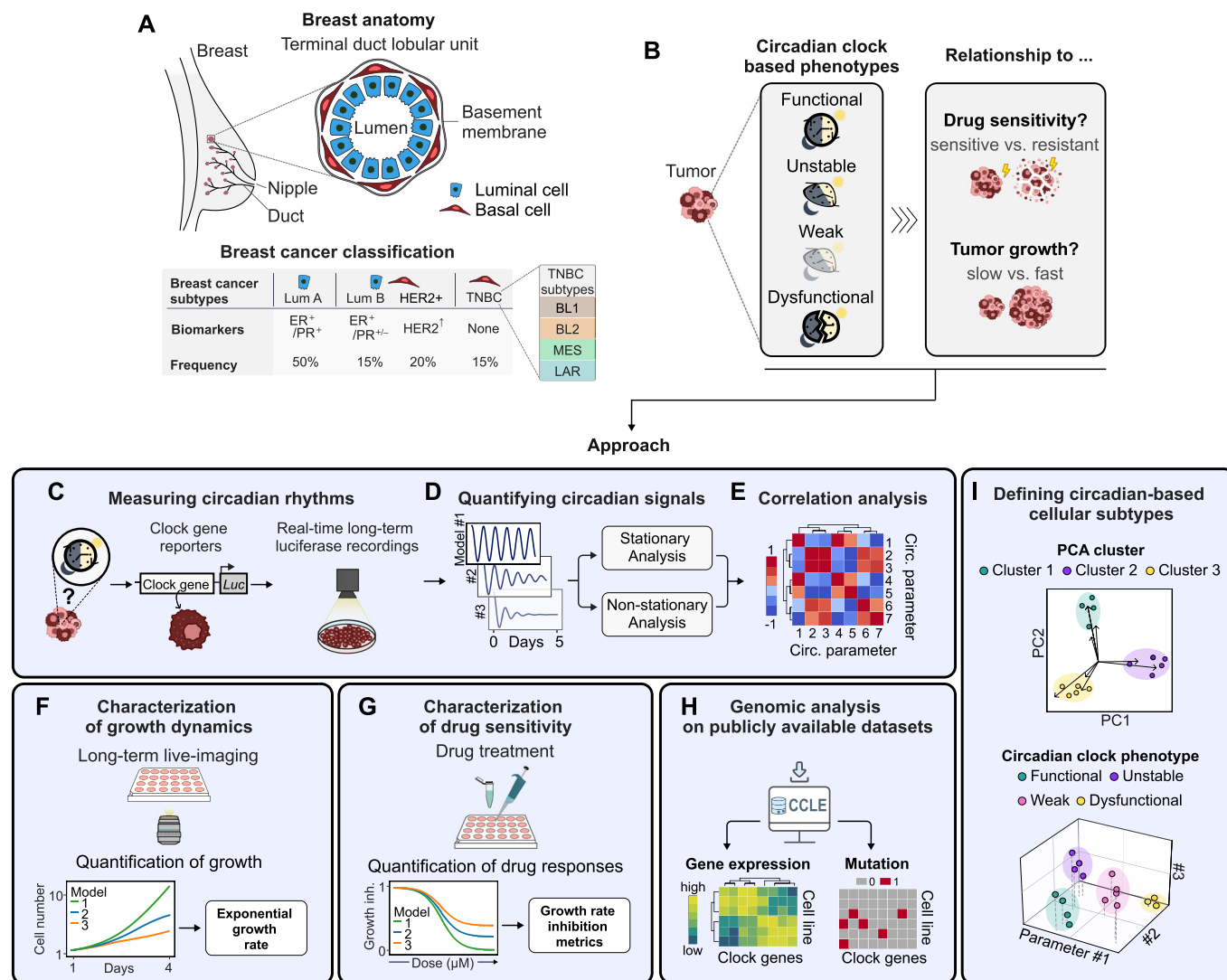


**Figure 1. Definition of circadian-based breast cancer subtypes by deep phenotyping.**

(A) Classification of breast cancer based on cancer cell phenotype and biomarker expression status. Approximate frequency among all breast cancer cases indicated in percentage. –, negative; +, positive; ER, estrogen receptor; PR, progesterone receptor; HER, human epidermal growth factor receptor 2; LumA/B, Luminal A/B; TNBC, triple-negative breast cancer, BL1/2, basal-like 1/2; MES, mesenchymal-like; LAR, luminal androgen receptor positive (LAR) (Lehmann et al, 2011; Lehmann et al 2016). While the presence of circadian rhythms have been shown for selected breast cancer models (Lellupitiyage Don et al, 2019; Li et al, 2024), the general assumption is that more aggressive breast cancer subtypes including TNBC exhibit disrupted circadian rhythms (Lellupitiyage Don et al, 2019; Li et al, 2024; Rida et al, 2019). In this study, we aim to define novel circadian clock-based phenotypes within breast cancer and to uncover how circadian properties relate to drug sensitivity and tumor growth (Fig. 1B). For this, we employ a comprehensive set of data analysis methods to deep-phenotype the circadian clock (Fig. 1C–E), and to collect information on cellular growth dynamics (Fig. 1F), drug responses (Fig. 1G), and genomic properties of circadian clock genes (Fig. 1H). Subsequently, we integrate our acquired cellular parameters to identify cell clusters and establish novel circadian-based subtypes within breast cancer (Fig. 1I).

including progesterone and estrogen receptors, as well as HER2-receptor overexpression (Sotiriou et al, 2003) (Fig. 1A). Within the highly heterogeneous and aggressive triple-negative breast cancer (TNBC) subtype lacking all three biomarkers, Lehmann et al, identified four molecular TNBC subtypes: basal-like 1 (BL1) and 2 (BL2), mesenchymal-like (MES) and immunomodulatory (IM) and luminal androgen receptor positive (LAR) (Lehmann et al, 2011; Lehmann et al 2016). While the presence of circadian rhythms have been shown for selected breast cancer models (Lellupitiyage Don et al, 2019; Li et al, 2024), the general assumption is that more aggressive breast cancer subtypes including TNBC exhibit

disrupted circadian rhythms (Lellupitiyage Don et al, 2019; Li et al, 2024; Rida et al, 2019). In this study, we aim to define novel circadian clock-based phenotypes within breast cancer and to uncover how circadian properties relate to drug sensitivity and tumor growth (Fig. 1B). For this, we employ a comprehensive set of data analysis methods to deep-phenotype the circadian clock (Fig. 1C–E), and to collect information on cellular growth dynamics (Fig. 1F), drug responses (Fig. 1G), and genomic properties of circadian clock genes (Fig. 1H). Subsequently, we integrate our acquired cellular parameters to identify cell clusters and establish novel circadian-based subtypes within breast cancer (Fig. 1I).

Finally, we investigate how drug responses depend on the circadian clock, identifying several drugs that could be further explored for their potential in chronotherapeutic approaches. Altogether, our approach sets the stage for a deeper understanding of distinct tumor-specific circadian clocks and how they shape cancer therapy outcomes.

## Results

### Deep circadian phenotyping reveals variability in clock strength across breast cancer models

The role of the circadian clock in cancer progression and treatment is gaining increasing interest, yet the degree of circadian rhythmicity and intrinsic timing profiles for various cancer subtypes remains largely unclear. To address this, we utilized high-resolution circadian clock recordings alongside a range of time-series analysis techniques to effectively measure and characterize circadian rhythms in cancer models. Building on our previously described deep-circadian phenotyping approach (Ector et al, 2024), which is comprehensively detailed in Box 1, we expanded our dataset by incorporating additional cell line models and novel analysis methods.

To obtain an initial estimate of the periodic quality of the time-series, we commenced our deep circadian phenotyping approach with autocorrelation (AC) analysis. Screening of 19 different cancer and non-cancer cell lines with the majority classifying as the highly heterogeneous and aggressive TNBC, we identified a broad spectrum of rhythmicity indices and period lengths, mostly centered around the 24-h human circadian cycle. Interestingly, rhythmicity indices below 0.3, indicative for weaker rhythms, often deviated from 24 h, whereas higher indices aligned with the circadian cycle (Fig. 2A). These results indicate a considerable variability of circadian phenotypes within the cell lines tested, highlighting the need to further dissect the circadian characteristics.

To quantify the proportion of distinct frequency components, present in each signal, we employed multiresolution analysis (MRA). This process segmented the detrended signal into four frequency bands: noise (1–4 h), ultradian (4–16 h), circadian (16–32 h), and infradian (32–256 h) (see Methods). Relating the circadian to the noise component revealed a spectrum of signal-to-noise ratios across cell lines, where higher circadian signals corresponded to lower noise, indicating circadian signal robustness, and vice versa. Alongside the osteosarcoma cell line U-2 OS, which is well-studied for its functional circadian clock (Baggs et al, 2009), high signal-to-noise ratios were found for the epithelial MCF10A, the LumA-MCF7 and the TNBC-MDAMB468 cell line (Fig. 2B). Interestingly, a knockout of *Cry2* in the U-2 OS cell line alone did not essentially alter the signal-to-noise ratio. In contrast, the knockout of *Cry1* or both, *Cry1* and *Cry2*, decreased the circadian component substantially by 34.9% ( $p = 5.3 \times 10^{-6}$ ) and 59.8% ( $p = 8.9 \times 10^{-8}$ ), while significantly enhancing the noise component by 3.3-fold ( $p = 9.0 \times 10^{-5}$ ) and 120.1-fold ( $p = 1.2 \times 10^{-5}$ ), respectively.

### Clock dynamics vary within subtypes of breast cancer

After evaluating the strength and composition of rhythmic structures within our signals, we analyzed their dynamic nature

through continuous wavelet transform (CWT). This approach visualizes the signal in a CWT power spectrum heatmap, showcasing the range and relative power of signal components over time within a specified period range. By tracking the main oscillatory component (“ridge”), CWT effectively reveals non-stationary and time-dependent features, such as dynamic periods and amplitudes (see Appendix Fig. S1A and Methods).

Aggregating the distribution of weighted mean periods and amplitudes per subtype, we noted variability of these parameters over time, particularly for the three TNBC subtypes (Fig. 2C; see Appendix Fig. S1B and Methods for weighting approach). Furthermore, we revealed varying prevailing periods and amplitudes for each subtype where only the osteosarcoma subtype showed a distinct period peak at approximately 24 h, combined with the highest amplitudes, while the prevailing periods for the other subtypes were mainly prolonged (Fig. 2C). Focusing on the breast cancer subtypes, a clear differentiation in circadian properties was visible, where the more aggressive TNBC subtypes exhibited longer periods and lower amplitudes than the LumA subtype (Fig. 2C). Though, when considering median CWT periods and amplitudes of each cell model, we found considerable within-subtype diversity, indicating that individual cancer tissue types exhibit a spectrum of circadian clock phenotypes (Appendix Fig. S1C). This within-subtype diversity extends to the ridge lengths, a measure of circadian clock strength, where longer and continuous ridges denote robust signals and shorter, discontinuous ridges indicate weaker ones (Fig. 2D). Here, only TNBC-M cell models ranked alongside of each other, whereas cell models of the LumA and basal-like TNBC subtypes displayed considerable variability in ridge lengths.

Building on the identified temporal circadian dynamics within and across cancer subtypes, we next assessed *Bmal1-Per2* phase differences over time. Consistent with the previously discussed circadian parameters, we observed a spectrum of phase differences across and within tissue types (Fig. 2E,F). Despite this variability, a notable pattern emerged in which non-cancerous and osteosarcoma tissues consistently showed phase differences around  $2\pi/3$ , an 8-h lag in a 24-h cycle, in contrast to breast cancer subtypes, which tended to have no phase difference ( $2\pi$ ) (Fig. 2F).

Circadian clocks in breast cancer cell lines may exhibit either self-sustained or damped oscillatory behaviors, a distinction that depends on the degree of intercellular coupling. Aiming to infer intercellular circadian coupling strength, we next analyzed signal amplitudes and corresponding exponential decay rates. Inspired by previous studies (Del Olmo et al, 2024; Finger et al, 2021; Guenther et al, 2014), we used a network of identical Poincaré oscillators to model individual cells within a tissue, featuring a constant coupling strength ( $\kappa$ ) and periods averaging a 24-h cycle. By varying the coupling strength, we observed distinct signal patterns, with strong coupling leading to amplified and self-sustained oscillations, while weak coupling results in a damped oscillation pattern (Fig. EV1).

We then fitted our experimental data to an exponentially decaying sinusoidal function (Fig. 2G and Methods) to determine initial amplitudes ( $A_0$ ) and amplitude decay rates ( $\gamma$ ). A comparative analysis unveiled an L-shaped trend in both, the simulated and experimental datasets, facilitating the approximation of coupling strengths in experimental data (Fig. 2H). Here, stronger intercellular coupling was identified for signals with high

### Box 1 Methods and techniques for deep circadian phenotyping

(A) Schematic of the experimental and computational approach to deep phenotype circadian rhythms. Stable circadian reporter cell lines expressing Luciferase reporters for either *Bmal1* or *Per2*, two core clock genes of the circadian clock network, were generated by lentiviral transduction. The circadian clocks of individual cells in a cell population were reset, and signals from the reporters were monitored in real-time by bioluminescence recordings spanning multiple days.

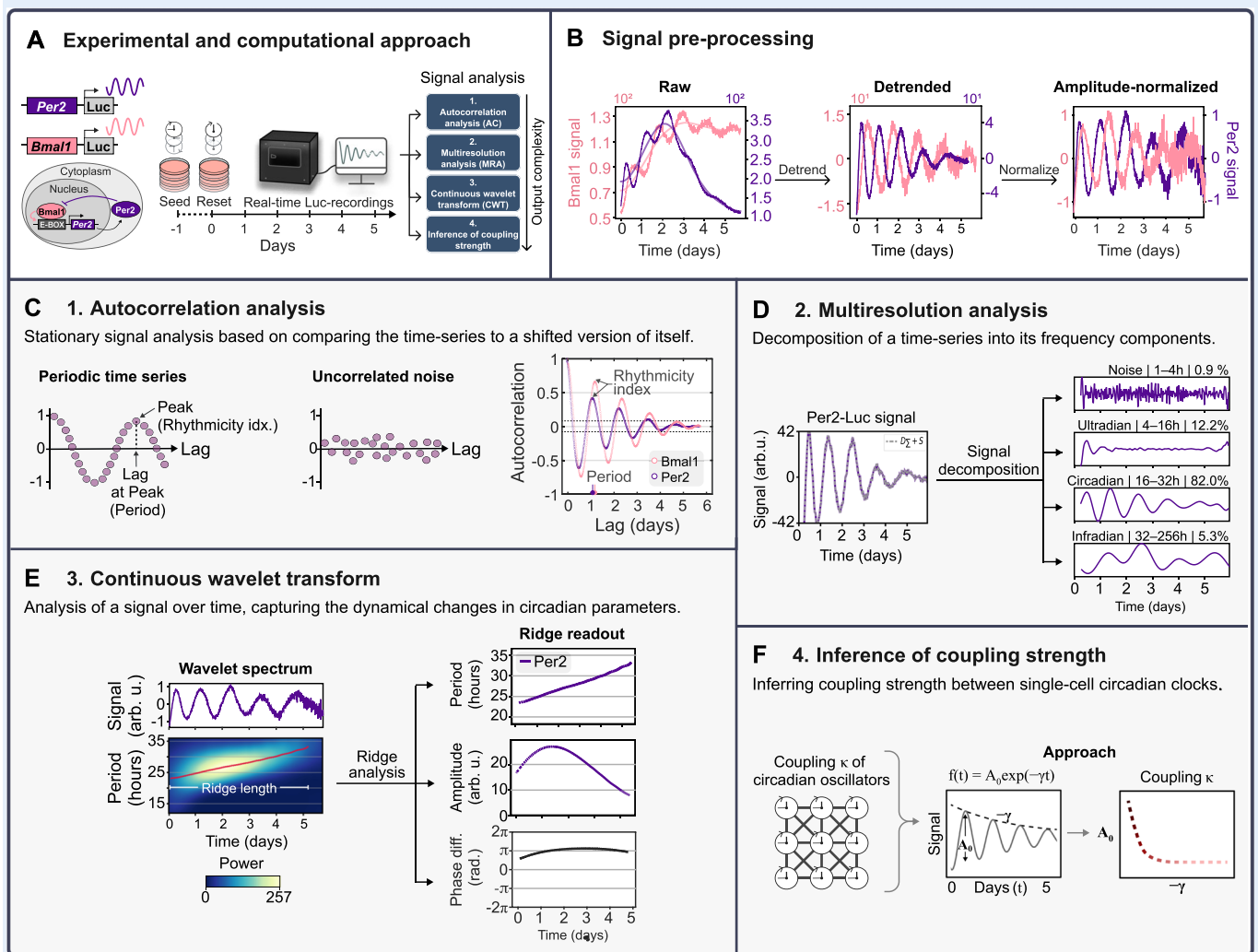
(B) Raw signal (left plot) and pre-processed signal traces (middle and right plots) of the TNBC cell line HCC1143 *Bmal1*- and *Per2*-Luc. Pre-processing of raw signals involved detrending (middle plot) and, for parts of the analysis, amplitude-normalization (left plot).

(C) Autocorrelation analysis of detrended HCC1143 *Bmal1*- and *Per2*-Luc signals. The arrow indicates the rhythmicity index and corresponding period of the time-series (lag). Dashed lines = 95.4% CI.

(D) Multiresolution analysis of detrended HCC1143 *Per2*-signal to decompose the signal into four frequency components, % = fraction of each component to the total signal.

(E) Continuous wavelet transform analysis on detrended and amplitude-normalized HCC1143 *Per2*-signal (top left plot), showing time-resolved signal periods in a wavelet spectrum (bottom left plot). The red line marks the main oscillatory component (ridge). The right panel shows the corresponding ridge readout for the period (top), amplitude (middle), and phase difference (difference to HCC1143 *Bmal1*-signal (bottom)).

(F) Approach to calculate the coupling strength ( $\kappa$ ) of circadian oscillators within a population of cells from the signal's amplitude ( $A_0$ ) and exponential decay rate ( $\gamma$ ).

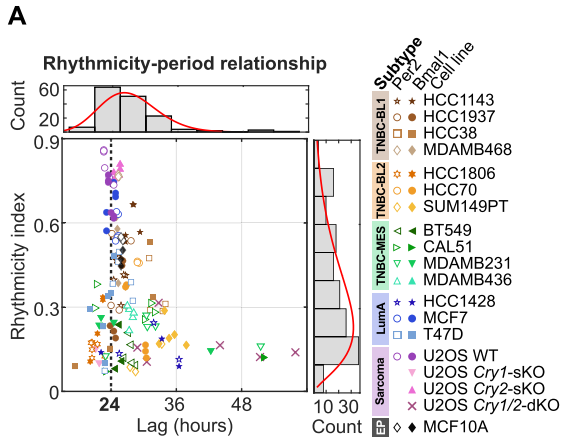


amplitudes and slow decay rates and vice versa. These findings align with previous studies, which demonstrated that a reduction in coupling strength results in increased variance, disrupting both the summed amplitude and period (Del Olmo et al, 2024; Guenther et al, 2014). Furthermore, focusing on U-2 OS cells, we observed a

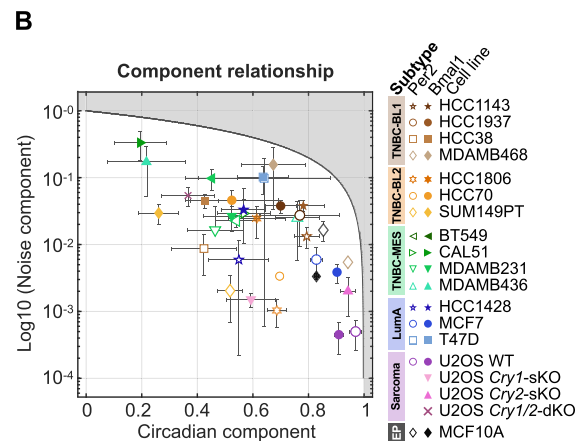
significant decrease in coupling strength in the circadian knockout cell lines compared to the wild-type (Fig. 2H), which is consistent with predictions from earlier research (Del Olmo et al, 2024).

These insights into the dynamics of circadian clock features, together with the broad range of circadian rhythm strengths

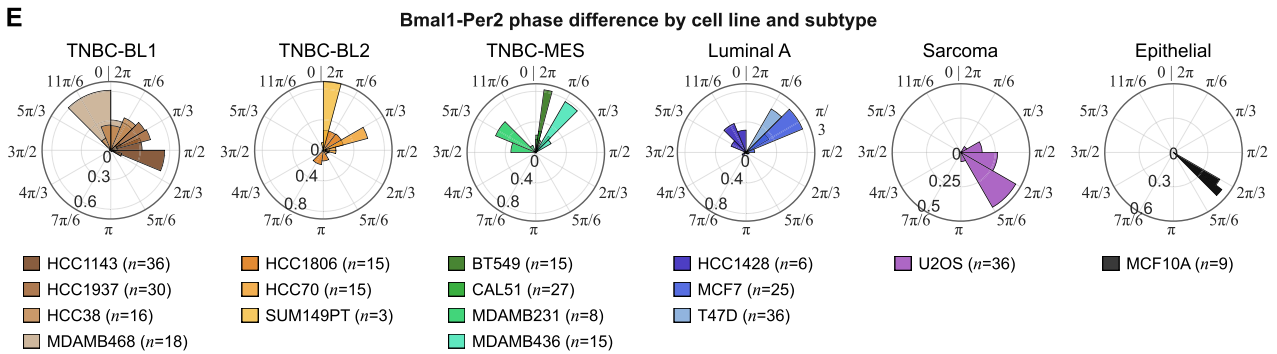
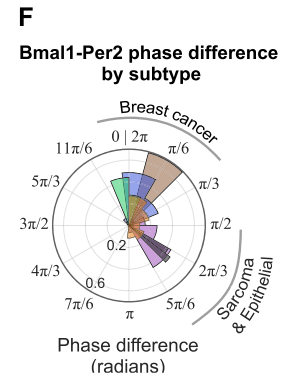
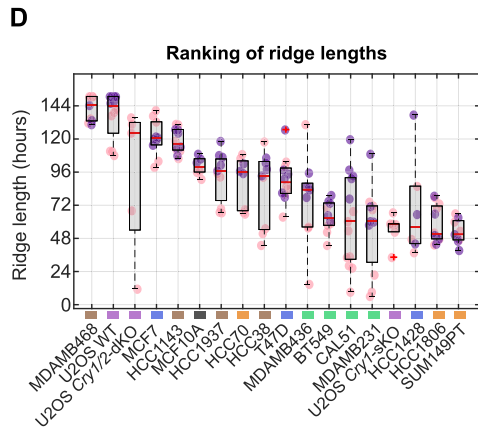
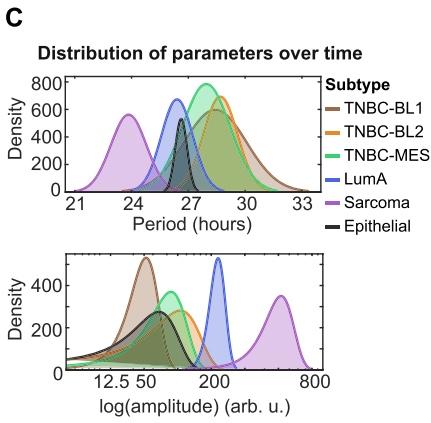
1. Autocorrelation analysis



2. Multiresolution analysis



3. Continuous Wavelet Transform



4. Inference of cell-to-cell circadian coupling strength

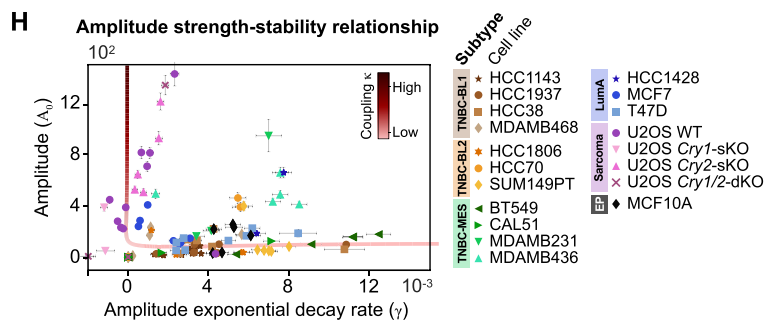
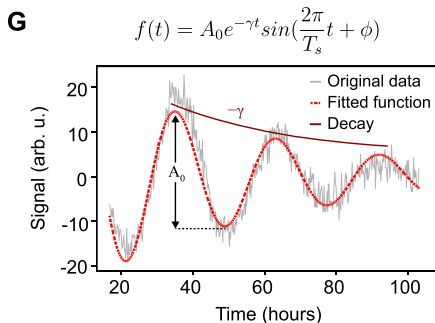


**Figure 2. Deep phenotyping of circadian rhythms in breast cancer cell line models.**

(A) Relationship between rhythmicity indices and periods for various cell line models, distinguished by markers and colored by subtype ( $n = 141$  samples represented as individual measurements). Dashed line at period = 24 h. Gamma distribution of periods and rhythmicity indices shown in histograms in the top and left panel, respectively. (B) Relationship between normalized noise and circadian components across cell line models, determined by multiresolution analysis. Cell models are color-coded by subtype and distinguished by markers. Shaded area covers unattainable range. Data represents the mean  $\pm$  s.d. of 6 samples per reporter ( $n = 2$  biological replicates  $\times$  technical triplicates or duplicates [HCC1806 Per2-Luc,  $n = 5$ ]).  $n = 3$  for MCF10A and MDAMB468-Per2-Luc (single experiment). (C) Normal distribution of subtype-averaged and time-resolved periods (top panel) and amplitudes (bottom panel) ( $n = 1-4$  cell line models per subtype, see legends of (A) and (B) for exact numbers). Before calculating subtype averages, all available replicates per cell model were averaged ( $n = 3-6$ , see (B) for exact numbers) and used as input. (D) Boxplot of CWT ridge lengths from *Bmal1*- and *Per2*-signals of specified cell models, with the bottom and top edges of the boxes representing the 25th and 75th percentiles, respectively. Extending whiskers represent data points within 1.5 times the interquartile range from lower and upper quartile. Median values are marked by red horizontal lines, and outliers by red crosses.  $n = 4-12$  samples per cell line (see (B) for exact numbers). (E) Subtype-specific polar histograms of *Bmal1*-*Per2* phase differences over time, averaged across multiple replicates and color-coded by cell line. The number  $n$  of *Bmal1*-*Per2*-combinations per cell line is indicated next to the cell line name. Polar histograms were normalized by probability. (F) Polar histogram of *Bmal1*-*Per2* phase differences over time, averaged and colored by subtype ( $n = 1-4$  cell line models, see (E) for exact numbers). In the polar histograms in (E) and (F)  $2\pi$  corresponds to one full circadian cycle. (G) Example of fitting signals to an exponentially decaying sinusoidal model with constant periods to deduce initial amplitudes ( $A_0$ ) and amplitude decay rates ( $\gamma$ ). Dark red amplitude decay trace is sketched for illustration purposes. (H) Relationship between initial signal amplitudes and amplitude decay rates across samples of different cell line models ( $n = 117$  samples). Cell models are color-coded by subtype and distinguished by markers. Error bars represent the standard deviation of the fitted parameters, reflecting their uncertainty as determined by the fitting process. The L-shaped line represents the simulated coupling strength ( $\kappa$ ). Source data are available online for this figure.

previously described, underscore the heterogeneity of circadian regulation within cancer tissues. Such within subtype-diversity motivated us to establish a novel circadian-based classification that could potentially inform chronotherapeutic strategies.

### Establishing a novel circadian-based subtyping in breast cancer

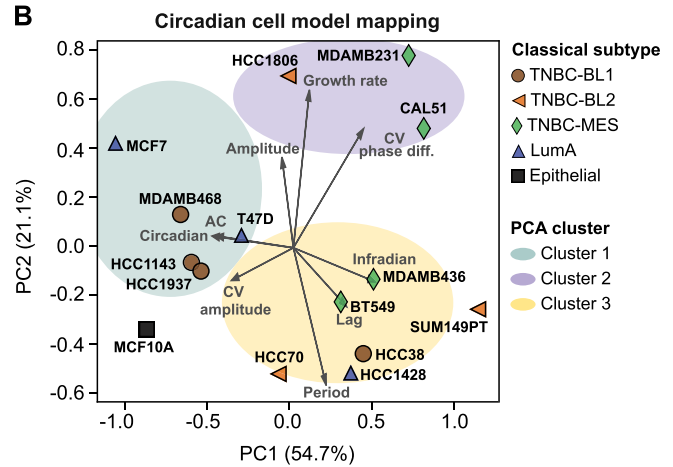
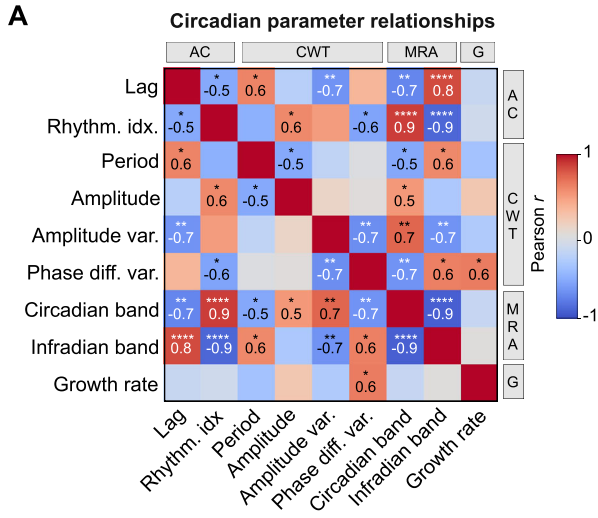
After extracting various circadian clock parameters from the different cell lines, we next investigated whether circadian clock-based clusters are present among these lines and how this clustering relates to their classical subtypes. Considering the established molecular connections between the circadian clock and cell cycle (Feillet et al, 2015; Gonze, 2024; Gutu et al, 2024), we integrated cellular growth rates into our analysis, which we determined by exponential curve fitting of long-term growth data (Appendix Fig. S2). To streamline our extensive dataset, we initially assessed the relationships between the parameters by calculating pairwise Pearson correlation coefficients, aggregating data from all replicates per cell line and from both circadian reporters. In line with our expectations, we discovered several strong correlations as well as redundancies across the dataset (Fig. EV2), allowing us to narrow down the circadian dataset to key parameters shown in Fig. 3A. We observed significant positive correlations between the different clock strength metrics, highlighting consistency across the different signal analysis approaches. In contrast, clock-strength parameters were mostly negatively, yet weaker, correlated with the growth rate, demonstrating accelerated growth in cell models with weaker circadian rhythms, whereas parameters representative of clock instability such as period and phase difference variations over time were positively correlated with growth (Fig. 3A and Fig. EV2A).

Upon refinement of our dataset, we employed principal component analysis (PCA) to investigate the presence of circadian-based clusters within the breast cancer and epithelial cell line panel. PCA showed the formation of three distinct circadian-based clusters where the respective cell models share characteristics of circadian clock or growth dynamics (Fig. 3B). Notably, most of the variability in the dataset was captured by the first two principal components alone, which accounted for 54.7% and 21.1% of the

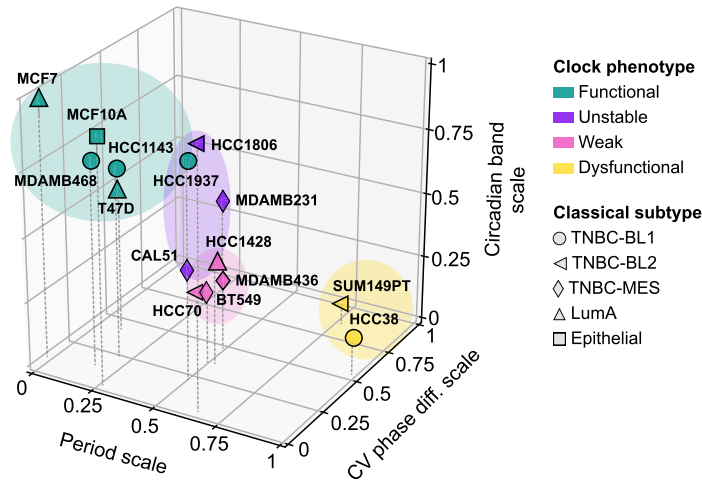
variance, respectively. Ranking of parameters by their corresponding PC loading, revealed that the highest influence on the observed clustering for the first principal component comes from the infradian and circadian components, underlining their potential as key markers in the circadian characterization of the cell models (Fig. EV2B). Interestingly, the circadian-based grouping deviated from the classical subtyping, providing a novel perspective on the subtyping of these cell models.

Since the identified PCA clusters do not directly translate into circadian phenotypes, we selected one key circadian parameter of each of the identified PCA clusters and performed k-means cluster analysis (Fig. 3C). In detail, we focused on the oscillation period, the *Bmal1*-*Per2* phase difference variability over time for clock stability, and the circadian component as a measure of clock strength. K-means clustering classified the cell models into four circadian phenotypes based on their circadian clock functionality: functional, unstable, weak, or dysfunctional (Fig. 3C). The functional phenotype, marked by a high circadian component and stable phase difference, suggests a strong and consistent circadian rhythm, and is composed of the epithelial MCF10A, two LumA, and two TNBC-BL1 cell line models. In contrast, the dysfunctional phenotype, comprising of two cell models only, is characterized by instable phase differences over time, long periods and low circadian bands. The intermediate phenotypes, weak and unstable, display decreased rhythm strength and stability, respectively (Fig. 3C). The decision to use four clusters was guided by the elbow method, analyzing the relationship between the within-cluster sum of squares (WCSS) and the number of clusters ( $k$ ). The point of diminishing returns was observed at  $k = 4$ , suggesting it as the optimal number of clusters, which was further reflected by the greatest silhouette score of 0.445 (Appendix Fig. S3). Consistent with k-means clustering, cell models sharing similar circadian clock phenotypes were mapped in proximity using Uniform Manifold Approximation and Projection (UMAP) with varying dimensions ( $n = 2, 3, \text{ and } 4$ ) (Fig. EV2C).

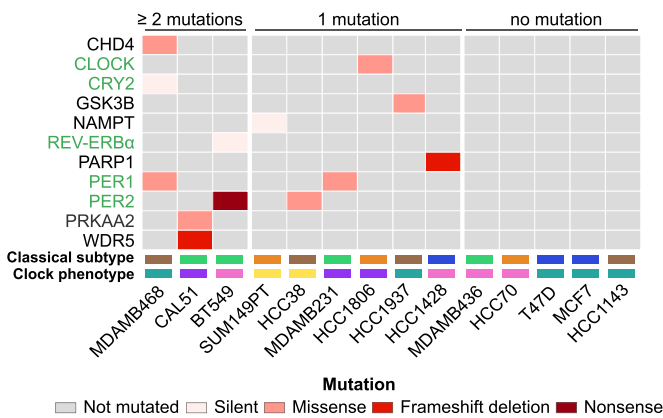
In summary, we introduced a new phenotypic framework that categorizes breast cancer cell lines according to their circadian phenotypes. This approach provides a complement to traditional subtyping methods, potentially enhancing the evaluation of cancer models for circadian-based therapeutic strategies.



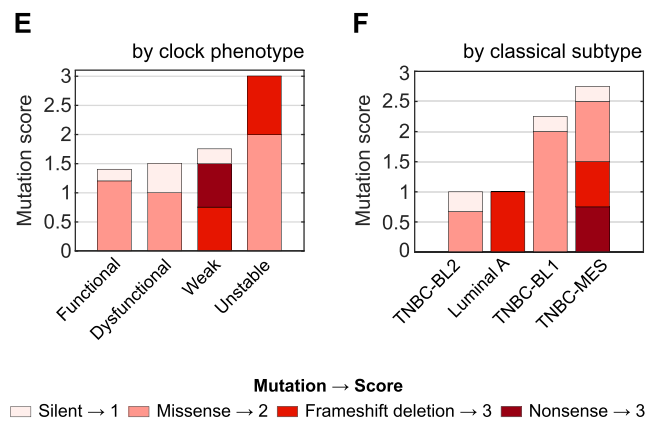
**C** Defining circadian-based phenotypes



**D** Mutations of circadian clock genes across cell models



**E** Mutation scores



**Genetic profiles of circadian-based phenotypes**

To evaluate the role of circadian genetic profiles in the newly identified circadian-based phenotypes, we extracted the mutation

and gene expression profiles of 16 core clock genes and 44 circadian clock-related genes from the cancer cell line encyclopedia (Barretina et al, 2012) (Dataset EV1). We specified core clock genes as those essential for regulating the circadian TTFLs and for

**Figure 3. Circadian clock features define circadian-based subtypes in breast cancer cell line models.**

(A) Pearson correlation coefficients between selected *Bmal1-Per2*-averaged circadian features and growth rates across all breast cancer cell line models and the epithelial MCF10A cell line ( $n = 15$  cell lines). Parameters are categorized by their approach of calculation: AC, autocorrelation; CWT, continuous wavelet transform; MRA, multiresolution analysis; G = growth. Displayed are statistically significant correlation values, where \*, \*\*, \*\*\*, and \*\*\*\* indicate  $p$ -values  $< 0.05$ , 0.01, 0.001, and 0.0001, respectively. Exact  $p$ -values: Rhythm. idx.-Lag and Amplitude-Period =  $3.2 \times 10^{-2}$ ; Period-Lag =  $1.4 \times 10^{-2}$ ; Amplitude-Rhythm. idx. and Phase diff. var.-Rhythm. idx. =  $2.1 \times 10^{-2}$ ; Amplitude var.-Lag =  $6 \times 10^{-3}$ ; Circadian band-Lag and Circadian band-Amplitude var. =  $2 \times 10^{-3}$ ; Circadian band-Rhythm. idx. and Infradian band-Rhythm. idx. =  $1.1 \times 10^{-5}$ ; Circadian band-Period =  $2.9 \times 10^{-2}$ ; Circadian band-Amplitude =  $4.6 \times 10^{-2}$ ; Circadian band-Phase diff. var. and Infradian band-Amplitude var. =  $6 \times 10^{-3}$ ; Infradian band-Lag =  $1 \times 10^{-4}$ ; Infradian band-Period =  $2 \times 10^{-2}$ ; Infradian band-Phase diff. var. and Growth rate-Phase diff. var. =  $1.2 \times 10^{-2}$ ; Infradian band-Circadian band =  $1 \times 10^{-6}$ . (B) Principal component analysis (PCA) biplot of the indicated circadian and growth parameters, displaying the distribution of 15 cell line models across the first two principal component scores. Cell models are depicted by different markers and colors indicating their classical subtype. Color-coded clusters are outlined around closely positioned cell models, based on visual inspection. The variance (PC loadings) explained by each component is expressed in percentage. CV = coefficient of variation. (C) Three-dimensional k-means clustering ( $k = 4$ ) of the indicated cell line models. Discretization was based on three min-max-scaled circadian parameters from each PCA-cluster defined in subplot (B). Novel clock phenotypes (distinct clusters) are color-coded. Classical subtypes are denoted with different markers (refer to subplot (B) for key). Within cluster sum of squares = 0.79, cluster silhouette score = 0.445. CV, coefficient of variation. (D) Cell line-specific mutation map, color-coded by type, of core circadian clock (green) and circadian clock associated genes (black). Color-coded rectangles above the cell line names indicate the classical subtype and clock phenotype (refer to subplot (B) and (C) for color-coding). See Dataset EV1 for full list of investigated circadian genes. (E) Ranking of mutation scores, normalized by cell line model per clock phenotype. (F) Ranking of mutation scores, normalized by cell line model per classical subtype. In (E) and (F), stacked bars show the proportion of each mutation type contributing to the final score,  $n = 2-4$  cell models per category; for exact numbers of cell line models per group refer to (C). Source data are available online for this figure.

which any dysregulation or mutation can lead to disrupted circadian rhythms (Ko and Takahashi, 2006; Takahashi, 2017).

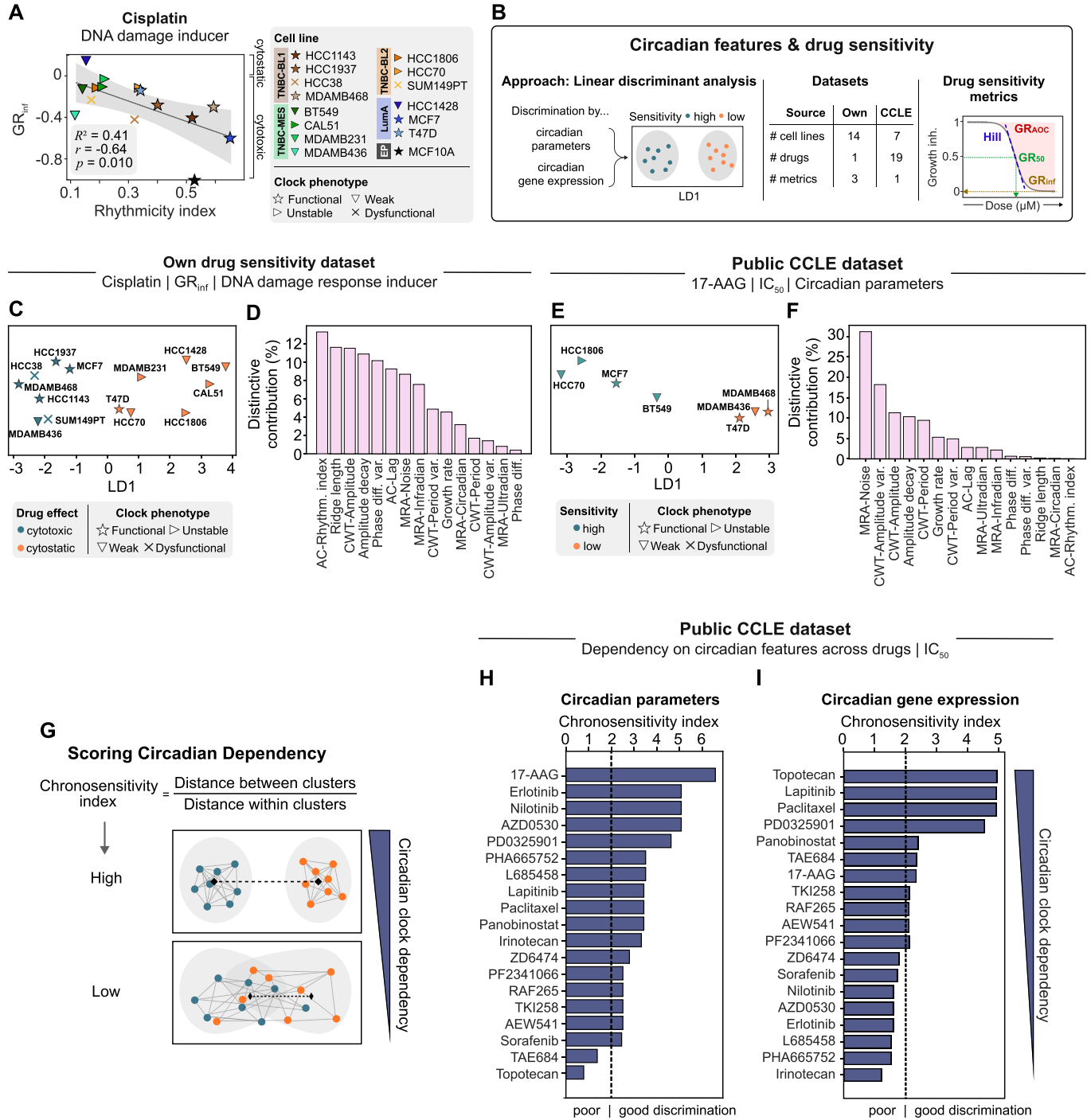
We noted varying mutation profiles of the circadian genes across the 14 tested breast cancer cell lines, with the majority of cell models exhibiting at least one mutation, whereas five cell lines showed no mutations in their circadian clock network (Fig. 3D). We then categorized mutations based on their impact on the protein sequence, assigning scores from 1 for silent mutations to 3 for highly damaging mutations like nonsense and frameshift mutations. Thereby we could compare the clock phenotypes by their circadian mutation burden, revealing that the unstable clock phenotype exhibits the highest mutation score while the functional phenotype had the lowest one (Fig. 3E). Notably, damaging mutations appeared exclusively in the unstable and weak clock phenotypes, suggesting a dysregulation of the circadian clock mechanism. Contrary to our expectations, the dysfunctional clock phenotype shared a similar low mutation burden with the functional phenotype, indicating that the number and severity of mutations alone may not fully explain clock functionality, and that additional factors might play a role for defining the underlying clock phenotypes (Fig. 3E). When analyzing the mutation scores across classical cancer subtypes, we found that the TNBC-mesenchymal subtype had the highest mutation burden, while TNBC basal-like 2 had the lowest one (Fig. 3F). We also identified a tendency for less damaging mutations in basal-like subtypes, whereas Luminal A and TNBC-mesenchymal subtypes exhibited more damaging mutations in the circadian gene panel.

We next sought to identify whether expression patterns of core circadian clock genes align with the identified clock phenotypes. To do so, we clustered the cell models based on their circadian gene expression dynamics and exposed three overarching clusters (Fig. EV2D). However, these clusters did not reflect the clock phenotypes but rather showed a distinction between the LumA and the TNBC subtypes. This distinction also emerged when mapping the cell models in a dimensionality-reduced UMAP-space (Fig. EV2E), indicating that the difference in circadian gene expression dynamics is associated with underlying breast cancer subtypes rather than the intrinsic circadian phenotype. It is important to note that overall transcriptional activities vary significantly between breast cancer subtypes (Perou et al, 2000; Rida et al, 2019). These differences in general transcriptional activity may influence the expression levels of

core clock genes independently of their circadian functionality, reinforcing our observed gene expression variations reflecting subtype-specific transcriptional programs rather circadian phenotypes.

### Circadian features drive sensitivity profiles to numerous drugs

Due to several interactions between circadian clock genes and therapeutic drug targets, circadian clock-aligned treatments have proved to increase drug effects based on the optimal time-of-day at their administration (Dallmann et al, 2014; Lee et al, 2021; Ye et al, 2018). To unravel the crucial link between circadian features and drug sensitivity, we employed linear regression and Pearson correlation analysis on a set of sensitivity parameters to various drugs and circadian oscillation features. To account for cell division events during drug perturbation assays and to obtain robust sensitivity metrics, we assessed drug sensitivity using the normalized growth rate inhibition (GR) approach (Hafner et al, 2016). For this, we expanded the analysis of our drug-response dataset published in Ector et al, (Ector et al, 2024). We analyzed a broad spectrum of drugs including DNA synthesis inhibitors (5-FU, doxorubicin), mitosis inhibitors (alisertib, paclitaxel), inhibitors for PI3K (alpelisib), or mTOR (torin2), and DNA damage response (DDR) targeting agents (adavosertib, cisplatin, olaparib). Through pairwise linear correlation analysis, we discovered a significant anti-correlation between the maximal effect of the DDR-inducer cisplatin and the autocorrelation rhythmicity index ( $r = -0.64$ ,  $R^2 = 0.41$ ) (Fig. 4A). Here, higher rhythmicity was associated with more cytotoxic responses to cisplatin, whereas lower rhythmicity was linked to cytostatic or less toxic responses. This anti-correlation extended to other circadian strength-related parameters such as the amplitude, ridge length and circadian component (Fig. EV3A). Aligning with these observations, weaker responses to cisplatin were positively correlated with clock instability parameters, such as the variability in periods and phase differences. Across all drugs tested, we identified additional significant relationships between circadian metrics and  $GR_{inf}$  values. Notably,  $GR_{inf}$  values from alpelisib showed the strongest correlation with circadian parameters (median  $r = 0.82$ ), hinting to a role of the



circadian clock in driving response phenotypes to the PI3K inhibitor (Fig. EV3B). Vice versa, we found the highest overall correlation for the circadian amplitude parameter (median  $r=0.74$ ), suggesting a predictive role for maximal drug responses (Fig. EV3C). This was supported by significant correlations between circadian parameters and other drug sensitivity metrics, like the drug concentration at half-maximal effect ( $GR_{50}$ ) (Fig. EV3D-F), and the slope of the dose-response curve (Hill coefficient) (Fig. EV3G-I).

Despite identifying selected significant correlations between individual clock or growth parameters and drug responses, overall correlations were modest. Given the multilayered nature of the circadian clock, drug sensitivity is likely influenced not by a single circadian factor, but by the collective impact of various circadian features. To investigate this, we utilized linear discriminant analysis (LDA) on both our own and publicly available drug sensitivity datasets, enabling the screening of various drug classes (Fig. 4B; information about drugs listed in Dataset EV2). LDA not only

**Figure 4. Investigating the role of circadian features in driving drug sensitivity.**

(A) Linear regression analysis between cisplatin  $GR_{inf}$  values (absolute drug effect; annotated on the right side of the plot) and the rhythmicity indices assessed by autocorrelation analysis (averaged *Bmal1-Per2* data, see Fig. 2B for exact samples size). Cell models are color-coded and illustrated with their circadian phenotype by distinct markers. Gray-shaded area = 95% CI. Model accuracy indicated by  $R^2$ -values.  $r$ , Pearson correlation coefficient,  $p$ , Pearson correlation  $p$ -value. (B) LDA-based approach and analyzed datasets to study the role of circadian features in shaping drug sensitivity profiles. Sketch on the right illustrates a dose-response curve and corresponding drug sensitivity parameters that were analyzed. (C) LDA on median-binarized  $GR_{inf}$  values to cisplatin, using *Bmal1-Per2* circadian and growth parameters as predictors ( $n = 15$  parameters). Cell models exhibiting drug sensitivity values below or above the cell panel's median are colored in blue-green and orange, respectively. The x-axis represents the first linear discriminant (LD1), capturing the maximum variance between groups. (D) Bar plot ranking circadian and growth parameters by their respective contribution to the obtained discriminative information shown in (C). (E) LDA on median-binarized  $IC_{50}$  values to 17-AAG. (F) Bar plot ranking the contribution of each parameter to the obtained discriminative information shown in (E). (G) Approach to identify circadian dependencies of drugs (termed as “chronosensitivity index”), calculated from the between-cluster-distance (BCD) to within-cluster-distance (WCD) ratio. The higher the chronosensitivity index, the more accurate the distinction into drug sensitivity groups, hence the higher the dependency on the circadian clock. (H) Ranking of chronosensitivity indices of multiple drugs, based on their dependency on circadian oscillation parameters. (I) Ranking of chronosensitivity indices of multiple drugs, based on their dependency on circadian gene expression values. The dashed line ( $y = 2$ ) denotes the cut-off for good and poor discrimination within the LDA space. Source data are available online for this figure.

assesses the individual contributions of the parameters to the classification into drug sensitivity groups but also facilitates the identification of drugs whose effects are likely driven by circadian rhythms (see Methods).

In our dataset, LDA successfully differentiated cell models based on their cytostatic or cytotoxic responses to cisplatin (Fig. 4C). The circadian parameters contributed to varying degrees to this discrimination, with the rhythmicity index and ridge length collectively explaining ~25% of the separation between the classes, emerging as the most influential discriminative features (Fig. 4D). To deepen our understanding of the molecular mechanisms by which the circadian clock modulates cellular responses to drug perturbations, we next investigated the influence of circadian clock gene expression on drug responses. In line with our findings for the circadian parameters obtained from our deep circadian phenotyping approach, the circadian gene set was able to broadly categorize cell models by their responses to cisplatin (Fig. EV4A, left panel). Examining the individual linear discriminant components of each circadian clock gene revealed a clear ranking of genes in terms of their discriminative importance, with the core clock genes *Rora* and *Cry2* being the most important contributors, collectively accounting for approximately 34% of the discriminative information (Fig. EV4A, right panel). The potential of circadian parameters, growth rates and circadian genes to reliably group cell models according to their sensitivity to cisplatin was further identified for  $GR_{50}$  values and Hill coefficients of the response curves (Fig. EV4B–E).

Given the sample size constraints in our study, we primarily used LDA for sensitivity classification. To explore alternative methods for assessing the cumulative impact of circadian features on drug sensitivity, we also evaluated ridge and lasso regression models, preserving continuous drug sensitivity values, and logistic regression as an additional classification method. Accuracy of each method was measured as relative between true and predicted values for ridge and lasso regression, and by leave-one-out cross-validation for the classification methods, using multiple sensitivity metrics, including  $GR_{AOC}$  and  $GEC_{50}$  (Hafner et al, 2016). This revealed moderate to low mean accuracies for all methods, likely reflecting limited sample size and varying dependencies on cell line models and sensitivity metrics (Appendix Fig. S4). Classification-based approaches (LDA and logistic regression) achieved mean accuracies of 0.42–0.51, outperforming regression methods, which showed up to two-fold lower accuracies (Appendix Fig. S4A–D).

This validation analysis reinforces confidence in our LDA-based approach while highlighting significant variability across cell lines and drug sensitivity parameters in their predictability.

To broaden the scope of our analysis, we incorporated publicly available drug sensitivity data from a subset of our circadian-phenotyped cell models. Our analysis revealed that sensitivity to the HSP90 inhibitor 17-AAG was particularly well discerned by circadian parameters (Fig. 4E). Among these, factors related to clock stability contributed most to the classification of cell models into high and low sensitivity groups, based on their respective  $IC_{50}$  values (Fig. 4F). To quantitatively evaluate LDA performances and the discriminative power of circadian features on drug responses, we calculated the ratio of between-cluster-distances (BCD) to within-cluster-distances (WCD), a standard metric for assessing clustering separation (Tibshirani et al, 2002). We termed this ratio the “chronosensitivity index” of a drug (Fig. 4G), to highlight the context of our analysis and make the ratio more interpretable. Strikingly, the circadian parameters provided a well separation of cell models into sensitivity groups for almost all 19 drugs analyzed (Fig. 4H), as indicated by chronosensitivity indices greater than 2, which we defined as a threshold for effective separation (see Fig. EV4F for a direct comparison of LDA profiles with different chronosensitivity indices). Consistent with its high chronosensitivity index, 17-AAG demonstrated the highest accuracy in LOOCV analysis, correctly classifying 71% of cell lines, while the lowest-ranking drug, topotecan, showed the poorest performance with only 14% accuracy (Appendix Fig. S5A). Although the LDA accuracy for other top-ranked drugs, including erlotinib, nilotinib, and AZD0530, was lower, complementary LOOCV using logistic regression revealed an accuracy of 71% for these drugs, which supports their elevated chronosensitivity rankings (Appendix Fig. S5A,B).

Expanding on these findings, circadian clock gene expression also demonstrated a strong association with sensitivity patterns for several drugs based on their chronosensitivity index (Fig. 4I). However, for approximately half of the drugs, the chronosensitivity index fell below the threshold, indicating poor separation into sensitivity groups. Notably, while circadian parameters alone did not effectively classify cell models by their sensitivity to the topoisomerase inhibitor topotecan, its chronosensitivity index and classification performance were substantially improved when using the circadian gene expression panel (Fig. 4I; Appendix Fig. S5C). Interestingly, the top three scoring drugs in the chronosensitivity

index derived from circadian gene expression data, namely topotecan, lapatinib, and paclitaxel, were with 71% to 86% accuracy in LOOCV for LDA also the most robustly classified drugs (Fig. 4I; Appendix Fig. S5C), although such accuracy was not observed in logistic regression analysis (Appendix Fig. S5D,D).

In summary, our analysis underscores the circadian clock's critical role in determining drug sensitivity across a wide range of drugs. We demonstrate that a combination of circadian features, rather than a single factor, discriminates between high and low drug responses. Through the "chronosensitivity index", we introduce a metric for quantifying the circadian clock's impact on differentiating between high and low drug sensitivity groups, thereby identifying potential drugs that act in a circadian-dependent manner.

## Discussion

Despite the wide acknowledgement of the fundamental role that the circadian clock has in the progression of diseases and in the modulation of treatment responses (Lévi et al, 2010; Mormont and Levi, 2003; Sulli et al, 2019), our understanding of the underlying molecular mechanisms remains fragmented. Using a high-resolution circadian phenotyping approach to thoroughly characterize circadian rhythms in cancer models, we discovered strong circadian rhythms in numerous breast cancer cell models. Among these, models of the most aggressive TNBC subtype showed distinct circadian rhythms, challenging the general expectations that the circadian clock is rather dysregulated in highly transformed cancer (Mormont and Levi, 2003; Ye et al, 2018) (Fig. 2). Our measurements of the circadian clock in the non-malignant epithelial cell line MCF10A, luminal A (LumA) breast cancer cell line MCF7, and the osteosarcoma U-2 OS cells aligns with prior research (Baggs et al, 2009; Börding et al, 2019; Lellupitiyage Don et al, 2019; Lin et al, 2019), proving the applicability and flexibility of our approach for deep circadian phenotyping across tissue and cancer types.

In our study, we identified a range of *Bmal1-Per2* phase differences across and within various tissue types, where non-cancerous and osteosarcoma tissues exhibited consistent phase differences around  $2\pi/3$  (an 8-h lag in a 24-h cycle), whereas breast cancer subtypes generally showed minimal phase differences ( $2\pi$ ), though with considerable variability (Fig. 2E,F). These observations contrast with the findings of other studies, which identified conserved circadian phase relationships in vivo across different tissues in baboon, mice, and human samples (Mure et al, 2018; Talamanca et al, 2023; Zhang et al, 2014). Those studies utilized intact biological systems, allowing for the influence of systemic cues and the coordination of circadian rhythms across the organism. In contrast, our analysis was conducted on isolated cell lines in vitro, which lack these systemic signals. This methodological difference, along with our examination of various disease subtype models, likely contributes to the broader spectrum of phase differences we observed, particularly among breast cancer subtypes.

Recent work revealed subtype-dependent clock functionality in breast cancer and that breast cancer clocks are critically regulated by estrogen responsiveness (Li et al, 2024). Our analysis of multiple cell models per breast cancer subtype and our broad set of circadian parameters confirms variations in clock strength across breast

cancer subtypes, however, we also revealed substantial variability within the individual subtypes of breast cancer. This variety of distinct clock features motivated us to define circadian clock-based subtypes within the panel of cell lines tested. In detail, we systematically categorized cell models into groups with functional, weak, unstable, or dysfunctional clocks, based on representative parameters indicative of circadian strength, stability, and periodicity (Fig. 3C). This classification diverged from traditional subtyping, exposing functional clocks in only two of the three tested estrogen-positive LumA cell models, alongside three out of four estrogen-negative TNBC models. Together, the defined clock subtypes offer a complementary viewpoint on the subtyping of breast cancer which could refine the assessment of cancer models for circadian-aligned therapeutic strategies and improve the prediction of their outcomes. The previously mentioned study on assessing global rhythm strength in breast cancer patient samples following an informatic approach emphasizes the importance of tumor subtype-specific analysis of circadian rhythms (Li et al, 2024). Our findings further support this need and highlight the importance of assessments that consider the distinct characteristics of each tumor individually.

On the molecular level, circadian clocks ensure coordinated rhythmicity from the individual cell to whole organism level by organized TFFLs, regulated through the interaction of multiple circadian clock genes (Chaix et al, 2016; Takahashi, 2017). The functionality of the circadian clock is highly dependent on genomic integrity, as proved by animal studies revealing distinct phenotypic effects for mutations of mammalian clock genes (Ko and Takahashi, 2006). When exploring the potential to infer our established circadian-based subtypes from publicly available genetic profiles of the cell models, we found high mutation burdens in circadian genes and compromised clock functionality within the unstable and weak circadian subtypes, which suggests a genetic basis for circadian disruption in these groups. However, for dysfunctional clocks, the mutation burden was not significantly higher compared to functional clocks, indicating that factors beyond mutation burden may influence clock dysfunction (Fig. 3E). Here, clock dysfunction may be driven by non-genetic factors, including epigenetic modifications or post-translational modifications of clock proteins, which do not necessarily correlate with increased mutation burdens (Liu et al, 2024).

Illuminating the link between the circadian clock and drug sensitivity, we found strong correlations between selected circadian features and drug sensitivity metrics (Fig. EV3). Analyzing absolute correlation values for each circadian metric, we identified circadian amplitude as the most correlated metric with both maximal drug responses ( $GR_{inf}$ ) and the concentration at half-maximal drug growth inhibition ( $GR_{50}$ ) across nine distinct drugs. However, despite these significant correlations, overall pairwise correlation strength was fairly moderate. This suggests that drug sensitivity is not shaped by a single circadian factor, but rather by the collective influence of multiple circadian features which we confirmed by linear discriminant analysis. Furthermore, we found that the most distinctive circadian features vary depending on the specific drug or sensitivity parameter in question. For example, while strength-related circadian parameters such as the rhythmicity index and circadian amplitude were strong predictors for the drug sensitivity to the DDR-inducer cisplatin (Fig. 4D), parameters indicative for clock stability were mostly contributing to the discrimination into sensitivity groups to the HSP90 inhibitor 17-AAG (Fig. 4F). These results suggest a complex

relationship between circadian rhythms and drug responses that needs to be evaluated on a drug-by-drug basis.

With the “chronosensitivity index” we systematically quantified the dependency of drug responses on the circadian clock, based on the ability of circadian parameters or circadian gene expression levels to effectively classify cell models into distinct sensitivity groups. By that we identified circadian clock-sensitivity relationships for most drugs studied, highlighting a global influence of the circadian system on pharmacodynamics (Fig. 4H,I). Importantly, 17-AAG ranked highest in the chronosensitivity index and predictive accuracy for separating the cell line panel into high- and low-response groups based on circadian clock parameters. High-throughput screenings of time-of-day effects on anticancer drug activity by Lee et al, revealed high time-of-day-specific action for the HSP90 inhibitor 17-AAG, mediated by the circadian regulation of the cell cycle (Lee et al, 2021). Our time-of-day-independent drug sensitivity results complement these findings, underscoring a critical impact of circadian rhythms on drug efficacy and highlighting the necessity of incorporating circadian biology into pharmacological research and treatment strategies. Though, while circadian parameters and gene expression profiles proved to offer insights into drug responses, differences in their predictive power for certain drugs, such as topotecan, suggest areas for future research.

It is important to note that variations in growth rate among cell lines could potentially influence bioluminescence reporter readings, independently affecting perceived circadian rhythms. To ensure that observed effects are specifically attributable to circadian regulation rather than confounding factors like cell cycle dynamics (Bieler et al, 2014; Gutu et al, 2024), future studies could employ single-cell imaging techniques where both the circadian clock and the proliferation behavior of individual cells is measured. This approach would enable more precise measurements of circadian rhythms, reducing potential interference from high proliferation rates during bioluminescence recordings. Moreover, the drugs identified in this study to likely depend on circadian clock properties could be tested in single-cell time-of-day treatment settings, which could also help identify potential bidirectional drug effects on the circadian clock (Manella et al, 2021).

While our study provides valuable insights into circadian rhythm variations in breast cancer cell models, it is crucial to acknowledge the limitations in transferring these findings directly to a clinical setting. Recent work by the Anafi/Meng groups utilizing patient-derived models suggests alternative approaches that may bridge this gap by more closely mimicking the in vivo environment (Anafi et al, 2017). Therefore, while our results contribute to a deeper understanding of circadian dynamics in breast cancer cell lines, extrapolation to patient tumors requires cautious interpretation and further validation using patient-derived models.

In summary, the proposed methodological refinements and follow-up studies offer promising opportunities to deepen our understanding of circadian rhythms in breast cancer. By illuminating the role of the circadian clock across various breast cancer cell models, our research establishes a foundational framework for exploring chronotherapeutic strategies. These insights potentially pave the way for more personalized and circadian-based therapeutic interventions, which could transform our approach to breast cancer treatment.

## Methods

### Reagents and tools table

| Reagent/Resource                 | Reference or Source                  | Identifier or Catalog Number |
|----------------------------------|--------------------------------------|------------------------------|
| <b>Experimental models</b>       |                                      |                              |
| HCC1143                          | ATCC                                 | CRL-2321                     |
| HCC1806                          | ATCC                                 | CRL-2335                     |
| HCC1937                          | ATCC                                 | CRL-2336                     |
| HCC38                            | ATCC                                 | CRL-2314                     |
| HCC70                            | ATCC                                 | CRL-2315                     |
| MDAMB468                         | ATCC                                 | HTB-132                      |
| BT549                            | Gift of Prof. Peter Sorger (Harvard) |                              |
| CAL51                            | Gift of Prof. Peter Sorger (Harvard) |                              |
| HCC1428                          | Gift of Prof. Peter Sorger (Harvard) |                              |
| MDAMB231                         | Gift of Prof. Peter Sorger (Harvard) |                              |
| MDAMB436                         | Gift of Prof. Peter Sorger (Harvard) |                              |
| SUM149PT                         | Gift of Prof. Peter Sorger (Harvard) |                              |
| MCF10A                           | Gift of Prof. Joan Brugge (Harvard)  |                              |
| MCF7                             | Gift of Prof. Joan Brugge (Harvard)  |                              |
| T47D                             | Gift of Prof. Joan Brugge (Harvard)  |                              |
| U-2 OS                           | Gift of Prof. Achim Kramer (Charité) |                              |
| U-2 OS Cry1-sKO                  | Börding et al, 2019                  |                              |
| U-2 OS Cry2-sKO                  | Börding et al, 2019                  |                              |
| U-2 OS Cry1/2-dKO                | Börding et al, 2019                  |                              |
| HEK293T                          | Gift of Prof. Galit Lahav (Harvard)  |                              |
| <b>Recombinant DNA</b>           |                                      |                              |
| pAB-mBmal1:Luc-Puro              | Gift of Prof. Achim Kramer (Charité) |                              |
| plenti6-mPer2:Luc-Blas           | Gift of Prof. Achim Kramer (Charité) |                              |
| psPAX2                           | Addgene                              | Cat #12260                   |
| pMD2G                            | Addgene                              | Cat #12259                   |
| gag/pol packaging plasmid        | Addgene                              | Cat #14887                   |
| pRev packaging plasmid           | Addgene                              | Cat #12253                   |
| VSV-G envelope plasmid           | Addgene                              | Cat #14888                   |
| EF1 $\alpha$ -mKate2-NLS plasmid | Gift of Prof. Galit Lahav (Harvard)  |                              |

| Reagent/Resource  | Reference or Source   | Identifier or Catalog Number |
|---|---|------------------------------|
| <b>Antibodies</b>   |   |                              |
| Not applicable  |   |                              |
| <b>Oligonucleotides and other sequence-based reagents</b> |   |                              |
| Not applicable  |   |                              |
| <b>Chemicals, Enzymes and other reagents</b>              |   |                              |
| DMEM/F12  | Gibco   | Cat #11320033                |
| RPMI-1640   | Gibco   | Cat #21875091                |
| FluoroBrite DMEM  | Gibco   | Cat #A1896701                |
| Horse serum   | Gibco   | Cat #26050088                |
| Fetal bovine serum  | Gibco   | Cat #10270106                |
| EGF Peptide   | Gibco   | Cat #AF-100-15-500UG         |
| Hydrocortisone  | Sigma   | Cat #H-0888-1g               |
| Cholera Toxin   | Sigma   | Cat #C-8052-2mg              |
| Insulin   | Sigma   | Cat #I-1882                  |
| Penicillin-Streptomycin                                   | Gibco   | Cat #15140122                |
| L-Glutamine   | Gibco   | Cat #25030-024               |
| HEPES   | Gibco   | Cat #15630056                |
| Lipofectamine 3000  | Invitrogen  | Cat #L3000001                |
| Protamine sulfate   | Sigma   | Cat #P3369                   |
| PBS   | Gibco   | Cat #10010056                |
| Blasticidin   | Adooq   | Cat #A14212                  |
| Puromycin   | Gibco   | Cat #A1113803                |
| Dexamethasone   | Sigma   | Cat #D4902                   |
| D-Luciferin   | Abmole  | Cat #M9053                   |
| 5-Fluorouracil  | Sigma   | Cat #O3738-100MG             |
| Torin2  | Sigma   | Cat #SML1224-5MG             |
| Alpelisib   | Biozol  | Cat #TGM-T1921-10MG          |
| Adavosertib   | Biocat  | Cat #T2077-5mg-TM            |
| Doxorubicin   | Hölzel  | Cat #A14403-100              |
| Paclitaxel  | Hölzel  | Cat #M1970-50mg              |
| Alisertib   | Hölzel  | Cat #S1133-5                 |
| Olaparib  | Adooq   | Cat #A10111                  |
| Cisplatin   | Sigma   | Cat #232120                  |
| <b>Software</b>   |   |                              |
| MATLAB v2021b   | <a href="https://mathworks.com">https://mathworks.com</a>                               |                              |
| Python Spyder v5.4.5                                      | <a href="https://github.com/spyder-ide/">https://github.com/spyder-ide/</a>             |                              |
| pyBOAT v0.9.12  | Mönke et al, 2020   |                              |
| Anaconda Navigator v2.5.0                                 | <a href="https://docs.anaconda.com/navigator/">https://docs.anaconda.com/navigator/</a> |                              |
| <b>Other</b>  |   |                              |
| LumiCycle   | Actimetrics   |                              |
| Incucyte  | Essen BioScience  |                              |

## Experimental methods

### Cell lines and cell culture

MCF10A cells were cultured following the Brugge lab's media recipe including a DMEM/F12 medium base (Gibco) supplemented with 5% horse serum (Gibco), 20 ng/ml EGF (Peprotech), 0.5 mg/ml Hydrocortisone (Sigma), 100 ng/ml Cholera Toxin (Sigma), 10 µg/ml Insulin (Sigma) and 1% penicillin-streptomycin (Pen-Strep, Gibco). All other cell lines were maintained in RPMI-1640 medium (Gibco) supplemented with 10% fetal bovine serum (FBS) (Gibco) and 1% Pen-Strep. Bioluminescence recordings and live imaging required phenol red-free FluoroBrite DMEM medium, supplemented with 10% FBS, 300 mg L-Glutamine (Gibco) and 1% Pen-Strep. Cells were cultured in a controlled 37 °C and 5% CO<sub>2</sub> environment.

### Cell line quality control

All cell lines were monitored for morphology, growth characteristics and health, mostly by long-term live-cell imaging, confirming that cell line-specific features did not vary throughout the study. No commonly misidentified cell line, according to the ICLAC register, was used in this study. Cells were routinely tested for mycoplasma for quality assurance.

### Generation of luciferase and fluorescence reporter cell lines

HEK293T cells at 80% confluency were retained in RPMI-1640 medium supplemented with 10 mM HEPES and transfected with a mix of 8.4 µg lentiviral expression plasmid (pAB-mBmal1:Luc-Puro or plenti6-mPer2:Luc-Blas), 6 µg psPAX2 (Addgene #12260) and 3.6 µg pMD2G (Addgene #12259) to produce lentivirus carrying circadian luciferase reporters. Similarly, lentivirus for the red-fluorescent nuclear reporters were produced using a mix of 1.8 µg gag/pol packaging plasmid (Addgene #14887), 0.7 µg pRev packaging plasmid (Addgene #12253), 0.3 µg VSV-G envelope plasmid (Addgene #14888) and 3.2 µg of EF1α-mKate2-NLS plasmid. The transfections were performed using Lipofectamine 3000 (Invitrogen) according to the manufacturer's instructions. Virus was harvested and filtered through a 0.45 µm filters (Millipore) 48 h and 72 h post-transfection. For transduction, target cells at 70% confluence underwent a 6-h incubation with a mix of 1 ml lentivirus-containing supernatant, 8 µg/ml protamine sulfate (Sigma) and 10 µM HEPES (Gibco). Post-incubation, cells were washed with PBS (Gibco) and maintained in standard culture medium. After 2 days, antibiotic selection of transduced cells was initiated using either 5 µg/ml of blasticidin (Adooq) or 2 µg/ml of puromycin (Gibco), depending on the resistance marker present in the lentiviral expression vector. Details on how the different U-2 OS knockout cell lines were developed are described in the original publication (Börding et al, 2019).

### Circadian bioluminescence recordings

Cells expressing luciferase reporters under the control of the *Bmal1* or *Per2* promoters were plated in 35-mm dishes (Nunc) to reach approximate confluence by the next day. To synchronize single-cell circadian clocks in cell populations, a standard dose of 1 µM dexamethasone (Balsalobre et al, 2000; Finger et al, 2021) (Sigma, dissolved in EtOH) was applied. Following a 30-min incubation period, cells were rinsed once with PBS before adding imaging medium containing 250 µM D-Luciferin (Abmole). To prevent the imaging medium from evaporating during the duration of the

bioluminescence measurements, the dishes were sealed with parafilm (Finger et al, 2021). Bioluminescence was then recorded every 10 min for a span of 5.7 days, utilizing an incubator-embedded luminometer (LumiCycle, Actimetrics).

### Live-cell imaging

Continuous live-cell monitoring was performed utilizing an incubator-embedded live-cell widefield microscope (Incucyte, Essen BioScience). Cells expressing the fluorescent nuclear marker EF1 $\alpha$ -mKate2-NLS were plated in 48-well plates (Falcon) at a seeding density where cell growth saturated under normal growth conditions by the conclusion of each experiment. Growth was measured in both brightfield and red-fluorescent channels with an excitation between 567 and 607 nm and emission between 622 and 704 nm. The acquired images were subjected to per-frame analysis for nuclei counting using the integrated software of the Incucyte system, followed by data processing in MATLAB. In experiments involving pharmacological treatments, cell seeding was done 1 day prior to the initiation of imaging. We employed a 4 $\times$  objective to take images across two fields of view for each well, at intervals of 1–2 h, over a period of 4 days. These experiments were replicated across two separate plates for each condition. In the case of cisplatin treatment studies, we conducted the experiment in a single plate per condition, capturing images across nine fields of view with a 10 $\times$  objective. For the assessment of unperturbed growth dynamics, we seeded cells at approximately 10% confluency, two days before initiating the live imaging. Using a 10 $\times$  lens, we obtained nine snapshots per well at 1 to 2-h intervals, for 4 days.

### Drug perturbations

Stock solutions for drugs were prepared in DMSO and stored at  $-20^{\circ}\text{C}$ , except for cisplatin (Sigma) that was prepared in 0.9% NaCl and kept at room temperature. For dose-response experiments, drugs were freshly diluted in a logarithmic series (5–6 points, log<sub>4</sub>) using their respective solvents just before application. The following concentration ranges were evaluated: 5-fluorouracil (5-FU, Sigma), alpelisib (Biozol), and olaparib (Adooq) were tested from 100 to 0.1  $\mu\text{M}$ ; torin2 (Sigma) and alisertib (Hözel) from 10 to 0.01  $\mu\text{M}$ ; adavosertib (Biacat) from 10 to 0.04  $\mu\text{M}$ ; doxorubicin (Hözel) from 1 to 0.004  $\mu\text{M}$ ; and paclitaxel (Hözel) from 0.4 to 0.0004  $\mu\text{M}$ . Cisplatin underwent a 10-point log<sub>2</sub> dilution series, spanning 70 to 0.14  $\mu\text{M}$ . The compounds were mixed media to achieve a final volume of 9% of the well and administered to the cells 24 h post-seeding. Cisplatin doses were given 48 h post-seeding. Control groups received the respective solvent to account for potential solvent-based effects on growth. Growth of the cells was tracked by long-term live-cell imaging over a minimum period of 4 days, as previously detailed.

### Experimental study design and statistics

The sample size for this study was based on standard field practices. We conducted two independent bioluminescence experiments, each with two to three technical replicates. While MCF10A *Bmal1*- and *Per2*-Luc and MDAMB468-*Per2*-Luc studies lacked biological replication, the technical replicates demonstrated high consistency. Given the extensive data generated, live-imaging experiments were performed once, with nine images analyzed per cell line for growth and cisplatin sensitivity analysis, and four images per condition from two separate plates for sensitivity analysis involving other drugs. Due to the study design not involving large treatment and

control cohorts, we did not employ randomization procedures for sample allocation, nor did we implement blinding during experiments or data analysis. Data points were included in the analysis unless identified as outliers using box plot methods, with pre-established exclusion criteria of 1.5 times the interquartile range above the 75th or below the 25th percentile. Statistical analyses were tailored to the nature of the data in each figure. For cluster analysis, we used k-means clustering and determined optimal cluster numbers through elbow plots, validating our approach with Within-Cluster Sum of Squares (WCSS) and silhouette scores. We assessed statistical parameter relationships using Pearson correlation coefficients and their corresponding *p*-values. The LDA model's performance was evaluated using the BCD to WCD ratio and cross-validated through LOOCV. Throughout the analysis, group variability was estimated and reported as standard deviation.

## Computational methods

### Time-series analysis of circadian signals

#### Signal pre-processing

An initial dexamethasone-related signal peak within the first 5 h was uniformly removed from all raw time-series. To standardize the duration of recordings, time-series exceeding 137.7 h (~5.7 days) were shortened accordingly. In the case of the MDAMB468 *Per2*-Luc reporter cell line, one replicate required a further adjustment by shortening the dataset by 8 h (129.7 h). This was due to an anomalous, intense, and brief peak during the last recording hours that skewed the analysis of circadian parameters, and that was not present in other replicates. The signals were detrended with a 48-h cut-off period using a sinc filter. Signal normalization was achieved by inverting the continuous amplitude envelope of the detrended signal (Mönke et al, 2020). The amplitude envelope was calculated by continuous wavelet transform with a time window of 48 h. The signal pre-processing steps were performed in the open-source software package pyBOAT (Mönke et al, 2020) (version 0.9.12), accessed via the Anaconda Navigator (version 2.5.0).

#### Autocorrelation analysis

Autocorrelation of detrended signals was calculated using the 'autocorr' MATLAB function. Rhythmicity strength was determined from autocorrelation values at the second peak in the correlogram using the 'findpeaks' MATLAB function, with the corresponding abscissa (lag) reflecting the main period. To facilitate peak detection and to filter out non-periodic samples from further analysis, autocorrelation values were smoothed using a Gaussian filter and peaks outside the 95.5% confidence intervals or below 0 were not considered for further analysis.

#### Multiresolution analysis

Decomposition of detrended signals into the underlying frequency bands, referred to as wavelet details  $D_j$ , was done by a discrete wavelet transform-based multiresolution analysis (Leise and Harrington, 2011), ensued by a final smooth. The analysis was carried out in accordance with the method outlined by Myung, Schmal and Hong et al (Myung et al, 2018), employing the 'PyWavelets' Python library and utilizing a *db20* wavelet from the Daubechies family for the transformation. For each wavelet detail

$D_j$ , which encapsulates a frequency span from  $2^j\Delta t$  and  $2^{j+1}\Delta t$  (where  $j = 1, 2, 3, \dots$ ), the time series was resampled by reducing the sampling interval from  $\Delta t = 10$  min to  $\Delta t = 30$  to capture a circadian frequency range between 16 and 32 h (Leise, 2013).

### Continuous wavelet transform

Continuous wavelet transform (CWT) was employed for the identification of a time-series signal's main oscillatory feature, referred to as ridge, across the entire recording time. The application of this wavelet-based spectral analysis varied with the specific readout parameter being examined. To increase the detectability of oscillatory patterns associated with the "period" and "phase" readout parameters, the CWT was applied to detrended amplitude-normalized signals. Furthermore, an adaptive ridge detection threshold was set according to the quarter-maximal spectral power of each signal (Appendix Fig. S1A, right panel). Conversely, for the readout parameters "amplitude" and "ridge length", indicative of circadian strength and robustness, the analysis was conducted on detrended, unnormalized signals with a global ridge detection threshold that results in a broad distribution of ridge lengths across all samples tested and which we set to a quarter of the median half-maximal wavelet power from the aggregate of samples (Appendix Fig. S1A, left panel). Except for the "ridge length" parameter, we focused on analyzing ridges detectable for a minimum duration of 48 h, thereby ensuring the tracking of at least two full circadian cycles for our subsequent analysis. The CWT was performed with pyBOAT using the Python programming language in the Spyder environment (version 5.4.5). The instantaneous phase differences between *Bmal1* and *Per2* was determined using the 'atan2' function, and for visual representation in polar histograms, the 'polarhistogram' function from MATLAB.

### Weighting of CWT parameters

To account for variations in ridge lengths from which CWT period, amplitude, and phase parameters were derived, we weighted the importance of each sample through a sigmoidal fitting method applied to the lengths of the respective ridges (Appendix Fig. S1B), based on the formula:

$$Relative\ weight = \frac{1}{1 + e^{(-0.1(ridge\ length - x_0))}} \quad (1)$$

Here, the steepness of the curve was uniformly set to  $-0.1$ , while the reflection point of the curve,  $x_0$ , lied between the highest and lowest ridge length. This method ensured that parameters from longer ridge lengths had a higher relative weight for median and mean calculations, as opposed to lower-weighted parameters from shorter ridge lengths.

### Amplitude envelope decay rate calculation

Decay rates of amplitude envelopes used for later correlation analyses were derived by applying an exponential decay model to detrended signal amplitudes:

$$f(t) = A_0 e^{-\gamma t} \quad (2)$$

where  $A_0$  denotes the initial amplitude,  $t$  the time, and  $\gamma$  the decay rate. Only decay rates from fits where  $R^2 \geq 0.6$  were considered for further analysis. For the analysis of circadian coupling strengths, the

model was extended to fit signals to an exponentially decaying sinusoidal oscillation.

$$f(t) = A_0 e^{-\gamma t} \sin\left(\frac{2\pi}{T_s} t + \phi\right) \quad (3)$$

where  $T_s$  is the oscillation period, and  $\phi$  adjusts for phase shifts. Again, values obtained from fits where  $R^2 \geq 0.6$  were used for further analysis.

### Simulating circadian population signals

The intercellular coupling was modeled assuming cells as mean-field coupled Poincaré oscillators. These dynamics were described in Cartesian coordinates  $X$  and  $Y$  as:

$$X_{i,n+1} = X_{i,n} + \lambda \left( \sqrt{X_{i,n}^2 + Y_{i,n}^2} - R_0 \right) X_{i,n} - \frac{2\pi}{T_i} Y_{i,n} + \frac{\kappa}{2N} \sum_{i=0}^N X_{i,n} \quad (4)$$

$$Y_{i,n+1} = Y_{i,n} + \lambda \left( \sqrt{X_{i,n}^2 + Y_{i,n}^2} - R_0 \right) Y_{i,n} + \frac{2\pi}{T_i} X_{i,n} + \frac{\kappa}{2N} \sum_{i=0}^N Y_{i,n} \quad (5)$$

Here,  $N$  represents the number of identical oscillators,  $\kappa$  the circadian coupling strength,  $T_i$  the inherent period,  $R_0$  the natural limit-cycle radius,  $\lambda$  the correction strength toward the oscillator's natural radius,  $n$  the time step, and  $i$  the individual oscillator. To simulate the model, we used the Euler's method with a time step of  $\Delta t = 0.1$ . For simplicity we set  $R_0 = \lambda = 1$ , as these parameters had no significant impact on the outcome of the experiment. To reenact the in vivo resetting, all oscillators were given similar initial phases by Uniform(0,  $\pi/5$ ), and periods with a normal distribution Norm(24, 3). Further, we set  $N$  to 300 to simulate enough oscillators and to avoid edge case results while keeping the simulation relatively small. Identical oscillators and uniform coupling in the simulations were justified by our assumption of absent spatial correlations in the experiment. The cumulative cell signal was modeled by summing individual oscillator outputs ( $\frac{\kappa}{2N} \sum_{i=0}^N Y_{i,n}$ ), varying  $\kappa \in [0.00001: 0.1]$ , with amplitudes scaled by 0.5 for compatibility, while keeping a constant seed to ensure similar distribution of periods for all simulations.

### Statistical analysis

Significance in variations in circadian parameters between knock-out and wild-type U-2 OS cells were assessed using a two-sample  $t$ -test through the M ATLAB 'ttest2' function, assuming normal distributions and equal variances between groups. Variations were considered significant with corresponding  $p$ -values  $\leq 0.05$ .

### Analysis of growth dynamics

Growth data acquired by long-term live-cell imaging was smoothed by robust local regression of weighted linear least squares combined with a 2nd-degree polynomial model, as implemented by the

'rloess' function MATLAB. The exponential growth rate, denoted as  $k$ , for each time unit  $t$  was determined by normalizing the cell counts to their initial values at timepoint zero ( $y_0$ ) and applying an exponential model to the 4-day growth trajectories:

$$\text{Growth}(t) = y_0 e^{(k \cdot t)} \quad (6)$$

For the BT549 and MDAMB436 cell lines fluorescent reporter lines were not available, which is why growth was quantified based on confluency levels. For all other cell models, nuclear counting was employed to calculate growth rates. Fitting of the exponential model was employed by the 'fit' function in MATLAB.

### Circadian parameter-based phenotype analysis

The relationships between different circadian parameters and growth rates were analyzed by first averaging the circadian parameter values from both Luc-reporters, *Bmal1* and *Per2*, across breast cancer cell lines. Pearson correlation coefficients and corresponding  $p$ -values were then calculated between these averaged circadian and growth parameters to reduce redundancy within the dataset. From the reduced set of eight circadian parameters and the growth rate, unsupervised dimensionality reduction by principal component analysis (PCA) was executed using the 'PCA' function of the 'sklearn decomposition' Python language module with the exact full singular value decomposition solver and two output components. Min-max scaling of the circadian parameters was applied prior to processing to preserve the distribution of the data while ensuring that all features are bound between 0 and 1, regardless of their different units and ranges. The reduced 2-dimensional space of *Bmal1-Per2* circadian features of each cell line was plotted in a biplot together with each feature's loading by annotated arrows, revealing three distinct clusters. The resulting component loadings were plotted separately in bars to facilitate the interpretation of each circadian feature's contribution. Based on the feature contributions, one representative parameter was selected from each of the three PCA clusters (period, phase difference variability, circadian component) and their min-max scaled values were plotted in a three-dimensional space. Elbow plots were generated to determine the optimal number of clusters for subsequent k-means clustering, based on the trade-off between cluster coherence and model complexity. We used the KneeLocator python library to locate the most adequate number of clusters ( $k=4$ ) with the sensitivity parameter set to 1. The analysis evaluated the average intra-cluster distances across a range of number of clusters ( $2 \leq n \leq 7$ ).

### Circadian gene expression and mutation analysis

Gene expression data and somatic mutation information of circadian clock genes were sourced from the Cancer Cell Line Encyclopedia Dependency Map (CCLE DepMap, available at <https://sites.broadinstitute.org/ccle/datasets>, gene expression: 2022-Q2, mutation profiles: 2023-Q2) (Barretina et al, 2012). Cell models were grouped together based on their expression values of core circadian clock genes using the 'seaborn' library's 'clustermap' function, utilizing Euclidean distance for measurement and the complete linkage approach for clustering. We extended our mutation analysis from the set of 16 core clock genes to additional 44 circadian clock associated genes (see Dataset EV1 for gene lists). Cell lines were hierarchically clustered by their mutational burden ranging from zero to greater or equal two, using the hamming

distance metric and single linkage method. Depending on the severity of the mutation, each mutation was assigned a value between 1 to 3 (with 3 reflecting damaging mutations), and final mutation scores per clock phenotype or classical subtype were calculated from averaging individual mutation scores across cell line models.

### Circadian feature and gene expression mapping

Min-max scaled gene expression values of sixteen core clock genes across TNBC cell line models were clustered using the 'clustermap' function of the 'seaborn' Python language module with the Euclidean distance metric and complete linkage method. The Uniform Manifold Approximation and Projection (UMAP) algorithm of the same Python language module was applied on both, the circadian parameters, and circadian gene expression values, to project TNBC cancer cell lines in a two-dimensional space. The number of nearest neighbors selected to construct the initial high-dimensional graph was set to three.

### Estimation of growth rate inhibition values

Drug-response data acquired by long-term live-cell imaging was smoothed using the same approach as described for the growth analysis. Following the method outlined by Hafner et al (2016), the growth rate inhibition ( $GR$ ) at a given time  $t$  and for each concentration  $c$  was calculated using:

$$GR(c, t) = 2^{k(c,t)/k(0)} - 1 \quad (7)$$

where  $k(c, t)$  represents the growth rate with drug treatment, and  $k(0)$  signifies the growth rate of untreated control cells. To obtain final drug sensitivity values, dose-dependent  $GR$  values were modeled against a sigmoidal curve, expressed as:

$$GR(c) = GR_{\text{inf}} + \frac{1 - GR_{\text{inf}}}{1 + (c/GE_{50})^{h_{GR}}} \quad (8)$$

with the parameters defined as described in the original publication (Hafner et al, 2016). Fitting of the sigmoidal curve was executed with the MATLAB 'fit' function.

### Pairwise correlation and linear regression analysis

Pearson's linear correlation coefficients between drug sensitivity metrics and circadian parameters were calculated and clustered using the 'corr' and 'clustergram' functions in MATLAB, respectively. For clustering, the 'correlation' distance metric was applied. Corresponding linear regression analysis was employed by the MATLAB 'fitlm' function.

### Predicting drug sensitivity from circadian clock features

Drug sensitivity prediction analysis was performed using the supervised linear discriminant analysis algorithm by the 'sklearn discriminant\_analysis' Python language module. The default parameters were retained, using the exact full singular value decomposition solver and a single component (LD1). We applied a median-based binary approach to categorize cell models into high and low drug sensitivity groups for cisplatin (own dataset) and 24

additional drugs that we obtained from the CCLE pharmacological profiling dataset archive (2015-Q1) (Barretina et al, 2012). These sensitivity groups served as target variable for the discrimination analysis using either the circadian parameter set (combined *Bmal1-Per2* data), or the CCLE core clock gene expression values. The resulting linear discriminant vector was jittered along the y-axis to avoid overlapping of the data points in the 1-dimensional space. Individual contributions to the obtained discriminative information of the parameters were plotted alongside each linear discriminant plot, and combined sum up to 100%. The discrimination performance (“chronosensitivity index”) was calculated from the BCD-WCD ratio, where the between-cluster-distance (BCD) is the Euclidean distance between the mean LD1 values of each class, and the within-cluster-distance (WCD) is the average Euclidean distance of class members to their respective class mean. The minimum BCD-WCD ratio to deem effective discrimination in a single dimension is equal to two, with  $BCD = 2 * WCD$ . This ensures that the centers of both clusters are at least twice as far away as the distance of each member to its respective class mean.

### Multi-dimensional lasso and ridge regressions

Regression analysis was conducted to identify circadian features associated with drug sensitivity in breast cancer cells. L1 (Lasso) and L2 (Ridge) regularization were applied to reduce overfitting and improve model interpretability by shrinking the coefficients of less significant features to zero (Tibshirani, 1996) (Hoerl and Kennard, 1970). The regularization strengths were set to 0.1 for L1 and 1.0 for L2. All analyses were performed using the scikit-learn library, with default parameters unless otherwise specified.

### Leave-one-out cross-validation

Leave-one-out cross-validation (LOOCV) was employed to evaluate model performance, leveraging the entire dataset by iteratively using one observation as the test set while the remainder constituted the training set. This method provides an unbiased estimate of model performance, particularly for smaller datasets. LOOCV was executed using custom functions with the different types of estimators.

### Data availability

The raw experimental data and generated data tables from this study are available in the Figshare database under the identifier <https://figshare.com/projects/Circadian-Subtypes-Breast-Cancer-Cells/234353>. The computer code produced in this study is available through the dataset repository Zenodo under the identifier <https://doi.org/10.5281/zenodo.14657750>.

The source data of this paper are collected in the following database record: [biostudies:S-SCDT-10\\_1038-S44320-025-00092-7](https://biostudies.org/studies/S-SCDT-10_1038-S44320-025-00092-7).

Expanded view data, supplementary information, appendices are available for this paper at <https://doi.org/10.1038/s44320-025-00092-7>.

### Peer review information

A peer review file is available at <https://doi.org/10.1038/s44320-025-00092-7>

## References

- Anafi RC, Francey LJ, Hogenesch JB, Kim J (2017) CYCLOPS reveals human transcriptional rhythms in health and disease. *Proc Natl Acad Sci USA* 114:5312–5317
- Baggs JE, Price TS, DiTacchio L, Panda S, FitzGerald GA, Hogenesch JB (2009) Network features of the mammalian circadian clock. *PLoS Biol* 7:e1000052
- Balsalobre A, Brown Steven A, Marcacci L, Tronche F, Kellendonk C, Reichardt Holger M, Schütz G, Schibler U (2000) Resetting of circadian time in peripheral tissues by glucocorticoid signaling. *Science* 289:2344–2347
- Barretina J, Caponigro G, Stransky N, Venkatesan K, Margolin AA, Kim S, Wilson CJ, Lehár J, Kryukov GV, Sonkin D et al (2012) The Cancer Cell Line Encyclopedia enables predictive modelling of anticancer drug sensitivity. *Nature* 483:603–607
- Bieler J, Cannavo R, Gustafson K, Gobet C, Gatfield D, Naef F (2014) Robust synchronization of coupled circadian and cell cycle oscillators in single mammalian cells. *Mol Syst Biol* 10:739
- Börding T, Abdo AN, Maier B, Gabriel C, Kramer A (2019) Generation of human CRY1 and CRY2 knockout cells using duplex CRISPR/Cas9 technology. *Front Physiol* 10:577
- Bray F, Laversanne M, Sung H, Ferlay J, Siegel RL, Soerjomataram I, Jemal A (2024) Global cancer statistics 2022: GLOBOCAN estimates of incidence and mortality worldwide for 36 cancers in 185 countries. *CA Cancer J Clin* 74:229–263
- Chaix A, Zarrinpar A, Panda S (2016) The circadian coordination of cell biology. *J Cell Biol* 215:15–25
- Chakrabarti S, Michor F (2020) Circadian clock effects on cellular proliferation: insights from theory and experiments. *Curr Opin Cell Biol* 67:17–26
- World Health Organization (2022) Cancer. <https://www.who.int/health-topics/cancer>
- Dallmann R, Brown SA, Gachon F (2014) Chronopharmacology: new insights and therapeutic implications. *Annu Rev Pharmacol Toxicol* 54:339–361
- Del Olmo M, Kalashnikov A, Schmal C, Kramer A, Herzog H (2024) Coupling allows robust mammalian redox circadian rhythms despite heterogeneity and noise. *Heliyon* 10:e24773
- Ector C, Schmal C, Didier J, De Landtsheer S, Finger A-M, Müller-Marquardt F, Schulte J, Sauter T, Keilholz U, Herzog H et al (2024) Time-of-day effects of cancer drugs revealed by high-throughput deep phenotyping. *Nat Commun* 15:7205
- Feillet C, van der Horst GTJ, Levi F, Rand DA, Delaunay F (2015) Coupling between the circadian clock and cell cycle oscillators: implication for healthy cells and malignant growth. *Front Neurol* 6:96–96
- Finger A-M, Jäschke S, del Olmo M, Hurwitz R, Granada AE, Herzog H, Kramer A (2021) Intercellular coupling between peripheral circadian oscillators by TGF- $\beta$  signaling. *Sci Adv* 7:eabg5174
- Golombek DA, Bussil IL, Agostino PV (2014) Minutes, days and years: molecular interactions among different scales of biological timing. *Philos Trans R Soc B: Biol Sci* 369:20120465
- Gonze D (2024) Coupling between the cell cycle and the circadian clock: lessons from computational modelling and consequences for cancer chronotherapy. *Curr Opin Syst Biol* 37:100507
- Guenther CJ, Luitje ME, Pyle LA, Molyneux PC, Yu JK, Li AS, Leise TL, Harrington ME (2014) Circadian rhythms of *Per2::Luc* in individual primary mouse hepatocytes and cultures. *PLoS One* 9:e87573
- Gutu N, Nordentoft MS, Kuhn M, Ector C, Finger A-M, Heltberg MS, Jensen MH, Keilholz U, Kramer A, Herzog H et al (2024) Circadian coupling orchestrates cell growth. Preprint at <https://doi.org/10.1101/2024.05.18.594797>

- Hafner M, Niepel M, Chung M, Sorger PK (2016) Growth rate inhibition metrics correct for confounders in measuring sensitivity to cancer drugs. *Nat Methods* 13:521–527
- Hoerl AE, Kennard RW (1970) Ridge regression: biased estimation for nonorthogonal problems. *Technometrics* 12:55–67
- Ko CH, Takahashi JS (2006) Molecular components of the mammalian circadian clock. *Hum Mol Genet* 15:R271–R277
- Lee Y, Fong SY, Shon J, Zhang SL, Brooks R, Lahens NF, Chen D, Dang CV, Field JM, Sehgal A (2021) Time-of-day specificity of anticancer drugs may be mediated by circadian regulation of the cell cycle. *Sci Adv* 7:eabd2645
- Lehmann BD, Bauer JA, Chen X, Sanders ME, Chakravarthy AB, Shyr Y, Pietenpol JA (2011) Identification of human triple-negative breast cancer subtypes and preclinical models for selection of targeted therapies. *J Clin Invest* 121:2750–2767
- Lehmann BD, Jovanović B, Chen, X, Estrada MV, Johnson KN, Shyr Y, Moses HL, Sanders ME, Pietenpol JA (2016) Refinement of Triple-Negative Breast Cancer Molecular Subtypes: Implications for Neoadjuvant Chemotherapy Selection. *PLOS ONE*, 11:e0157368
- Leise TL (2013) Wavelet analysis of circadian and ultradian behavioral rhythms. *J Circ Rhythms* 11:5
- Leise TL, Harrington ME (2011) Wavelet-based time series analysis of circadian rhythms. *J Biol Rhythms* 26:454–463
- Lellupitiyage Don SS, Lin HH, Furtado JJ, Qraitem M, Taylor SR, Farkas ME (2019) Circadian oscillations persist in low malignancy breast cancer cells. *Cell Cycle* 18:2447–2453
- Lévi F, Okyar A, Dulong S, Innominato PF, Clairambault J (2010) Circadian timing in cancer treatments. *Annu Rev Pharmacol Toxicol* 50:377–421
- Li S-Y, Hammarlund JA, Wu G, Lian J-W, Howell SJ, Clarke RB, Adamson AD, Gonçalves CF, Hogenesch JB, Anafi RC et al (2024) Tumor circadian clock strength influences metastatic potential and predicts patient prognosis in luminal A breast cancer. *Proc Natl Acad Sci USA* 121:e2311854121
- Lin H-H, Qraitem M, Lian Y, Taylor SR, Farkas ME (2019) Analyses of BMAL1 and PER2 oscillations in a model of breast cancer progression reveal changes with malignancy. *Integr Cancer Ther* 18:1534735419836494–1534735419836494
- Liu X-L, Duan Z, Yu M, Liu X (2024) Epigenetic control of circadian clocks by environmental signals. *Trends Cell Biol* 34:992–1006
- Manella G, Aizik D, Aviram R, Golik M, Asher G (2021) Circa-SCOPE: high-throughput live single-cell imaging method for analysis of circadian clock resetting. *Nat Commun* 12:5903
- Mönke G, Sorgenfrei FA, Schmal C, Granada AE (2020) Optimal time frequency analysis for biological data - pyBOAT. Preprint at <https://doi.org/10.1101/2020.04.29.067744>
- Mormont M-C, Levi F (2003) Cancer chronotherapy: principles, applications, and perspectives. *Cancer* 97:155–169
- Mure LS, Le HD, Benegiamo G, Chang MW, Rios L, Jillani N, Ngotho M, Kariuki T, Dkhissi-Benyahya O, Cooper HM et al (2018) Diurnal transcriptome atlas of a primate across major neural and peripheral tissues. *Science* 359:eaao0318
- Myung J, Schmal C, Hong S, Tsukizawa Y, Rose P, Zhang Y, Holtzman MJ, De Schutter E, Herzog H, Boryugov G et al (2018) The choroid plexus is an important circadian clock component. *Nat Commun* 9:1062
- Neufeld-Cohen A, Robles MS, Aviram R, Manella G, Adamovich Y, Ladeux B, Nir D, Rousso-Noori L, Kuperman Y, Golik M et al (2016) Circadian control of oscillations in mitochondrial rate-limiting enzymes and nutrient utilization by PERIOD proteins. *Proc Natl Acad Sci USA* 113:E1673–E1682
- Perou CM, Sørlie T, Eisen MB, van de Rijn M, Jeffrey SS, Rees CA, Pollack JR, Ross DT, Johnsen H, Akslen LA et al (2000) Molecular portraits of human breast tumours. *Nature* 406:747–752
- Rida P, Syed MI, Aneja R (2019) Time will tell: circadian clock dysregulation in triple negative breast cancer. *Front Biosci* 11:178–192
- Sancar A, Lindsey-Boltz LA, Kang TH, Reardon JT, Lee JH, Ozturk N (2010) Circadian clock control of the cellular response to DNA damage. *FEBS Lett* 584:2618–2625
- Scheiermann C, Kunisaki Y, Frenette PS (2013) Circadian control of the immune system. *Nat Rev Immunol* 13:190–198
- Sotiriou C, Neo S-Y, McShane LM, Korn EL, Long PM, Jazaeri A, Martiat P, Fox SB, Harris AL, Liu ET (2003) Breast cancer classification and prognosis based on gene expression profiles from a population-based study. *Proc Natl Acad Sci USA* 100:10393–10398
- Sulli G, Lam MTY, Panda S (2019) Interplay between circadian clock and cancer: new frontiers for cancer treatment. *Trends Cancer* 5:475–494
- Takahashi JS (2017) Transcriptional architecture of the mammalian circadian clock. *Nat Rev Genet* 18:164–179
- Talamanca L, Gobet C, Naef F (2023) Sex-dimorphic and age-dependent organization of 24-hour gene expression rhythms in humans. *Science* 379:478–483
- Tibshirani R (1996) Regression shrinkage and selection via the lasso. *J R Stat Soc Ser B-Methodol* 58:267–288
- Tibshirani R, Walther G, Hastie T (2002) Estimating the number of clusters in a data set via the gap statistic. *J R Stat Soc Ser B: Stat Methodol* 63:411–423
- Ye Y, Xiang Y, Ozguc FM, Kim Y, Liu C-J, Park PK, Hu Q, Diao L, Lou Y, Lin C et al (2018) The genomic landscape and pharmacogenomic interactions of clock genes in cancer chronotherapy. *Cell Syst* 6:314–328.e312
- Zhang R, Lahens NF, Ballance HI, Hughes ME, Hogenesch JB (2014) A circadian gene expression atlas in mammals: implications for biology and medicine. *Proc Natl Acad Sci USA* 111:16219–16224

## Acknowledgements

We would like to express our thankfulness to Nica Gutu for kickstarting the modeling ideas. We also thank Anna-Marie Finger and Astrid Grudziecki for their guidance in the bioluminescence recordings as well as Francesca Müller-Marquardt for her assistance in the recordings. Lastly, we thank the laboratories of Ingeborg Tinhofer-Keilholz and Ulrich Keilholz for their continuous feedback on the project. The results are part of a project funded by the German Federal Ministry of Education and Research (BMBF) through the e:Med Juniorverbund DeepLTNBC TP3-01ZX1917C. CE was partially supported by the Deutsche Forschungsgemeinschaft (DFG, German Research Foundation)–RTG2424/CompCancer – project number: 377984878. JD was supported by the Luxembourg National Research Fund (FNR) under the PRIDE programme (PRIDE17/12252781). MSN acknowledges support from the Novo Nordisk Foundation (NNF20OC0064978). CS acknowledges support from the DFG–SCHM 3362/4–1 project number: 511886499.

## Author contributions

**Carolin Ector:** Conceptualization; Data curation; Software; Formal analysis; Validation; Investigation; Visualization; Writing—original draft; Writing—review and editing. **Jeff Didier:** Data curation; Software; Formal analysis; Validation; Methodology; Writing—review and editing. **Sébastien De Landtsheer:** Data curation; Software; Formal analysis; Validation; Methodology; Writing—review and editing. **Malthe S Nordentoft:** Data curation; Software; Formal analysis; Methodology. **Christoph Schmal:** Software; Methodology; Writing—review and editing. **Ulrich Keilholz:** Resources; Writing—review and editing. **Hanspeter Herzog:** Conceptualization; Writing—review and editing. **Achim Kramer:** Conceptualization; Writing—review and editing. **Thomas Sauter:** Resources; Supervision; Writing—review and editing. **Adrián E Granada:** Conceptualization; Resources; Supervision; Funding acquisition; Visualization; Writing—original draft; Project administration; Writing—review and editing.

Source data underlying figure panels in this paper may have individual authorship assigned. Where available, figure panel/source data authorship is

listed in the following database record: [biostudies:S-SCDT-10\\_1038-S44320-025-00092-7](https://www.ebi.ac.uk/biostudies/studies/S-SCDT-10_1038-S44320-025-00092-7).

### Funding

Open Access funding enabled and organized by Projekt DEAL.

### Disclosure and competing interests statement

The authors declare no competing interests.

**Open Access** This article is licensed under a Creative Commons Attribution 4.0 International License, which permits use, sharing, adaptation, distribution and reproduction in any medium or format, as long as you give appropriate credit to the original author(s) and the source, provide a link to the Creative Commons licence, and indicate if changes were made. The images or other third party material in this article are included in the article's Creative Commons licence,

unless indicated otherwise in a credit line to the material. If material is not included in the article's Creative Commons licence and your intended use is not permitted by statutory regulation or exceeds the permitted use, you will need to obtain permission directly from the copyright holder. To view a copy of this licence, visit <http://creativecommons.org/licenses/by/4.0/>. Creative Commons Public Domain Dedication waiver <http://creativecommons.org/public-domain/zero/1.0/> applies to the data associated with this article, unless otherwise stated in a credit line to the data, but does not extend to the graphical or creative elements of illustrations, charts, or figures. This waiver removes legal barriers to the re-use and mining of research data. According to standard scholarly practice, it is recommended to provide appropriate citation and attribution whenever technically possible.

© The Author(s) 2025

## Expanded View Figures

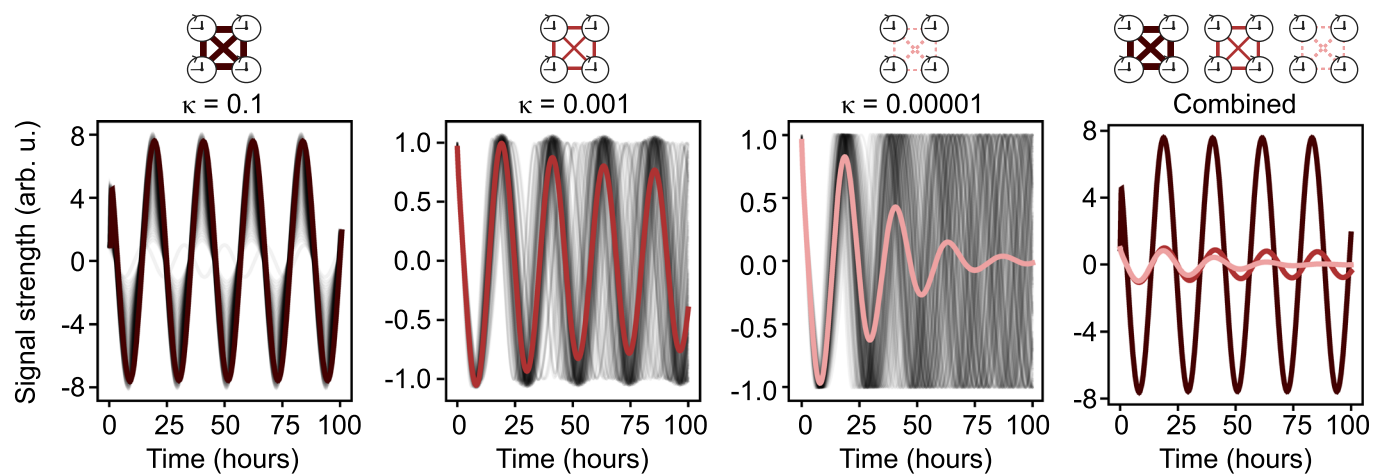
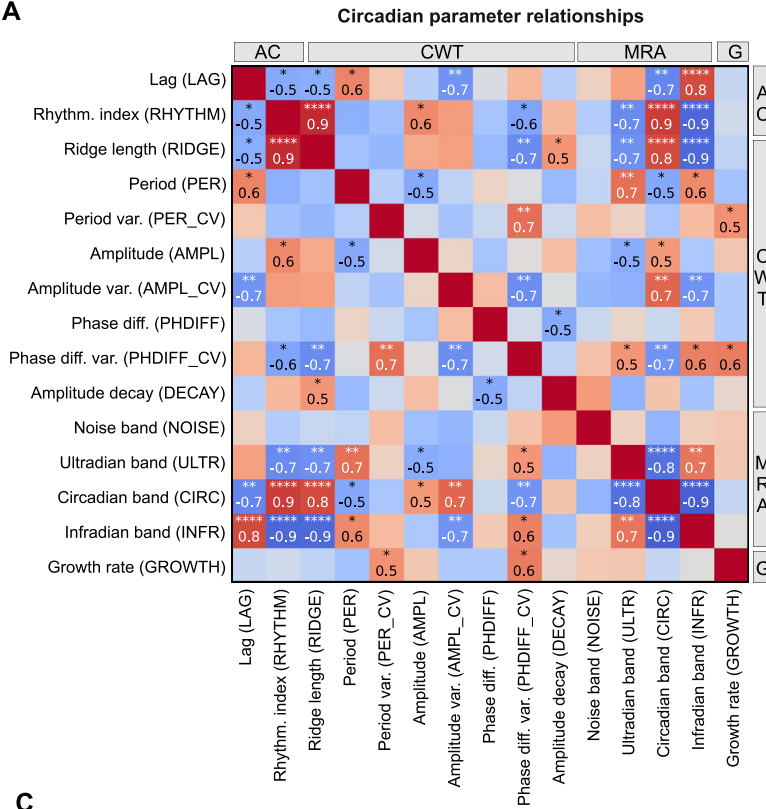


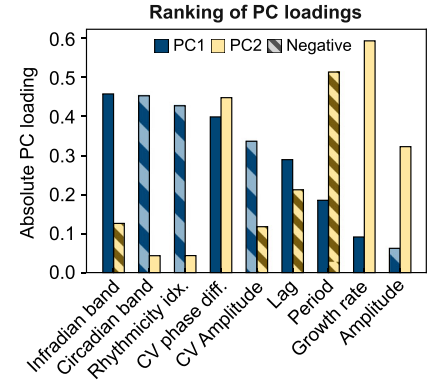
**Figure EV1. Expanded view for Fig. 2.**

Simulated oscillators of varying coupling strengths  $\kappa$ . Individual traces of each oscillator are shown in black, collective signals are shown as thick lines with gradients of red, based on their coupling strength, where dark red denotes high coupling strength, and pink refers to low coupling. The right panel is a composite of all collective signals.

**A**

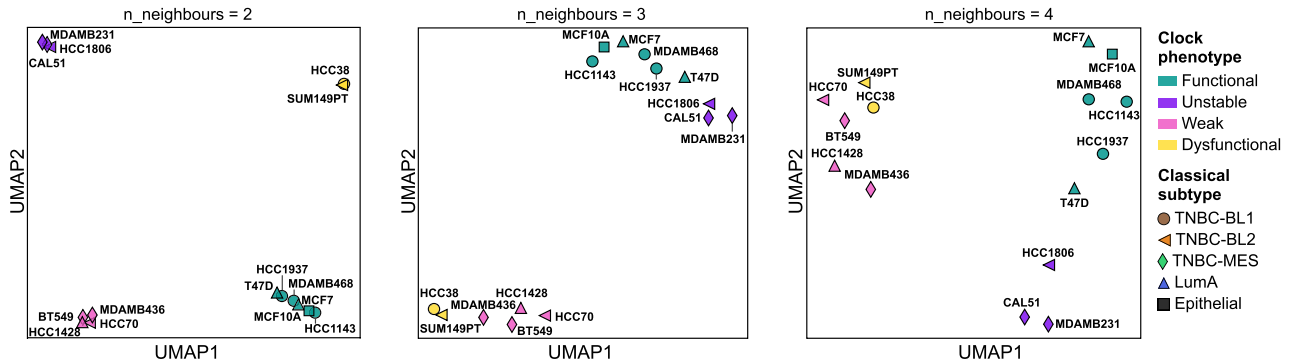


**B**

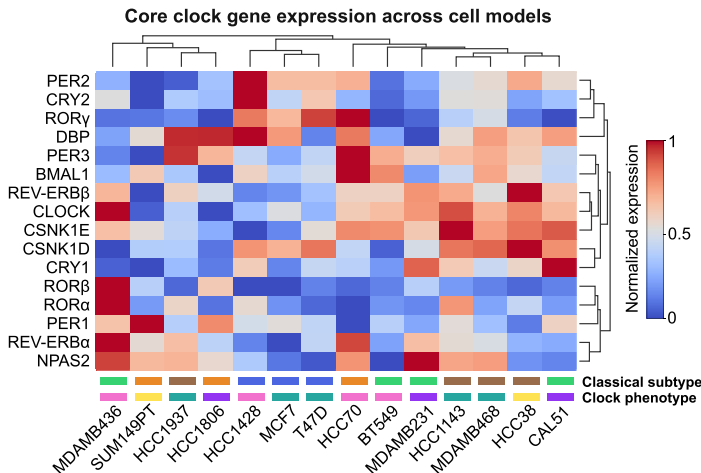


**C**

**Mapping of selected circadian clock features**



**D**



**E**

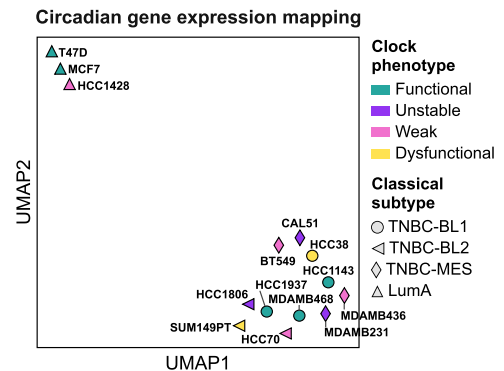
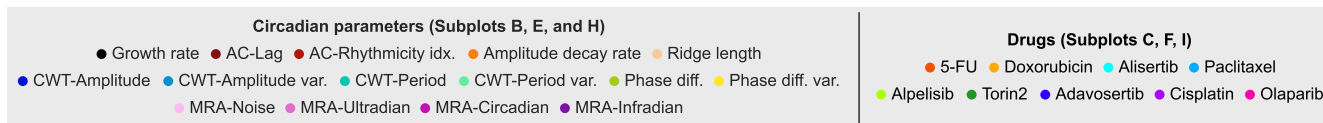
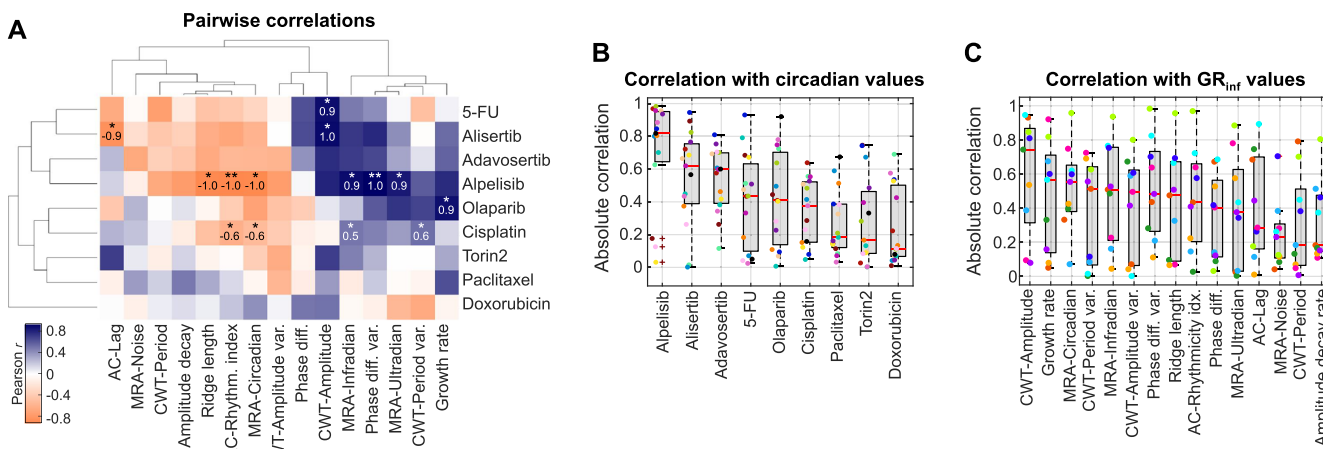


**Figure EV2. Expanded view for Fig. 3.**

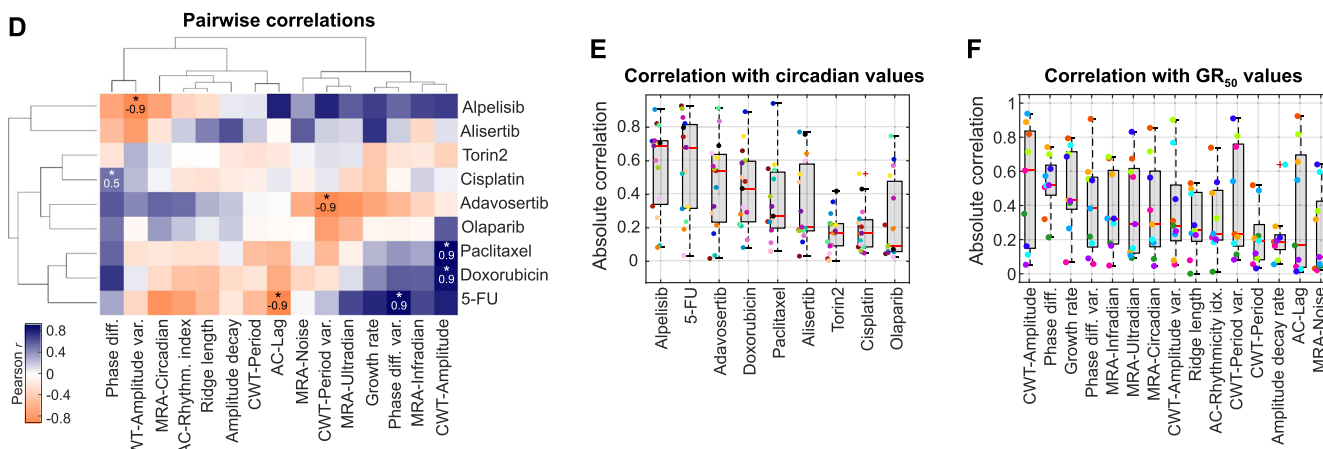
(A) Pearson correlation coefficients between the complete set of *Bmal1-Per2*-averaged circadian features and growth rates across all breast cancer cell models and the epithelial MCF10A cell line ( $n = 15$  cell lines). Parameters are categorized by their approach of calculation (refer to Fig. 3A legend). Displayed are statistically significant correlation values, where \*, \*\*, and \*\*\*\* indicate  $p$ -values  $< 0.05$ ,  $0.01$ , and  $0.0001$ , respectively. Exact  $p$ -values: RIDGE-LAG =  $4.2 \times 10^{-2}$ ; RIDGE-RHYTHM =  $2.8 \times 10^{-7}$ ; PHDIFF\_RIDGE =  $2 \times 10^{-3}$ ; PHDIFF\_CV-PER\_CV =  $3 \times 10^{-3}$ ; DECAY-RIDGE =  $4.3 \times 10^{-2}$ ; DECAY-PHDIFF =  $3.3 \times 10^{-2}$ ; ULTR-RHYTHM =  $3 \times 10^{-3}$ ; ULTR-RIDGE =  $4 \times 10^{-3}$ ; ULTR-PER =  $3 \times 10^{-3}$ ; ULTR-AMPL =  $3.8 \times 10^{-2}$ ; ULTR-PHDIFF\_CV =  $4.1 \times 10^{-2}$ ; ULTR-INFR =  $5.5 \times 10^{-3}$ ; CIRC-RIDGE =  $8 \times 10^{-5}$ ; CIRC-ULTR =  $8.8 \times 10^{-5}$ ; INFR-RIDGE =  $1.8 \times 10^{-5}$ ; INFR-ULTR =  $5.5 \times 10^{-3}$ ; INFR-CIRC =  $1 \times 10^{-6}$ ; GROWTH-PER\_CV =  $3.7 \times 10^{-2}$ . Refer to Fig. 3A for all other significant  $p$ -values. (B) Ranking of absolute PC loadings for each circadian and growth parameter, corresponding to the PCA biplot shown in Fig. 3B. Parameters are sorted in descending order based on their absolute contribution in the first principal component. Negative values are shaded. (C) Uniform Manifold Approximation and Projection (UMAP) of cell models complementary to the k-means clustering analysis in Fig. 3C. The classical subtype and clock phenotype of each model is illustrated by different markers and colors, respectively. Nearest neighbors = 2-4. (D) Cluster map of core clock gene expression values across breast cancer cell models, using the Euclidian distance method. Color-coded rectangles above the cell line names indicate the classical subtype and clock phenotype. Refer to (C) for color-coding. (E) UMAP of cell models based on core circadian gene expression values shown in (D). The classical subtype and clock phenotype of each model is illustrated by different markers and colors, respectively. Nearest neighbors = 3.



$GR_{inf}$   
Maximal drug effect at infinite concentration

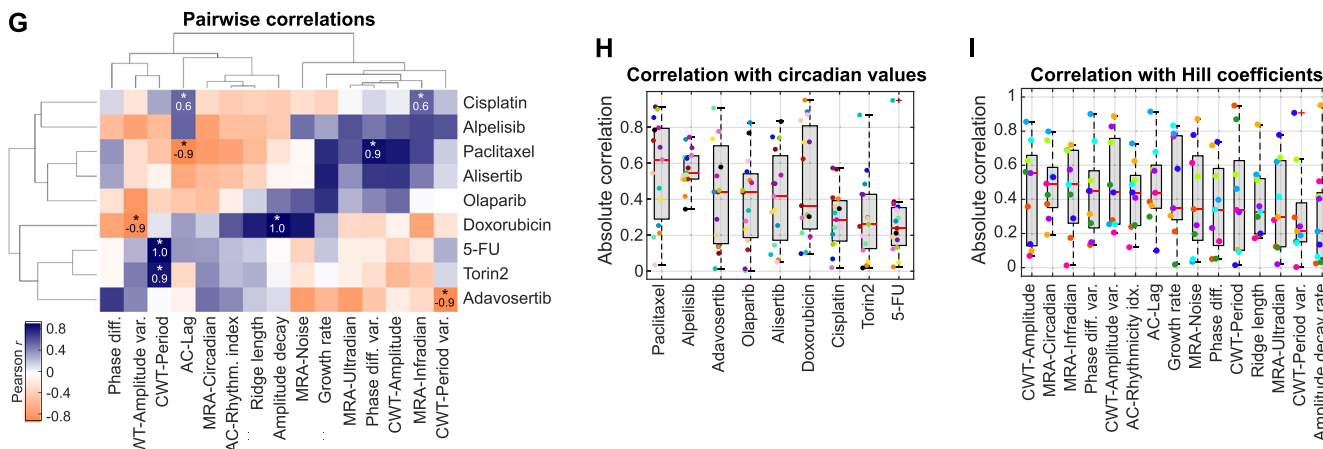


$GR_{50}$   
Drug concentration reducing growth by half



**Hill coefficient**

Steepness of the dose-response curve

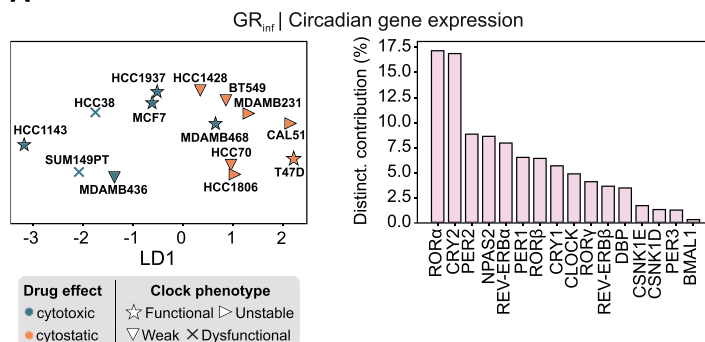


◀ **Figure EV3. Expanded view for Fig. 4.**

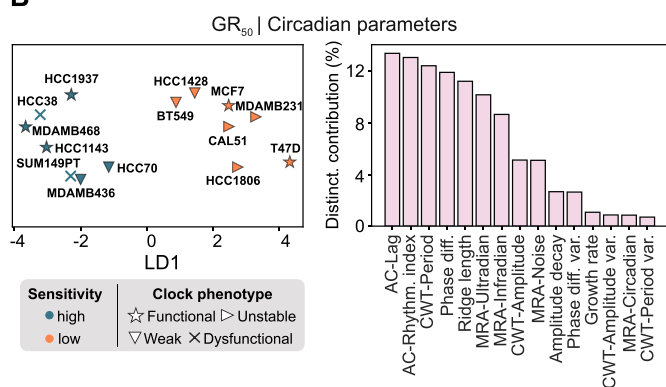
(A) Hierarchical clustering of Pearson correlation coefficients between  $GR_{inf}$  values for 9 drugs (rows) and 15 circadian clock and growth parameters (columns, averaged *Bmal1-Per2* data). Shown are statistically significant correlation values, where \*, and \*\*, indicate  $p$ -values 0.05, and 0.01, respectively. exact  $p$ -values: 5-FU-Amplitude =  $2.2 \times 10^{-2}$ ; Alisertib-Lag =  $4.1 \times 10^{-2}$ ; Alisertib-Amplitude =  $1.5 \times 10^{-2}$ ; Alpelisib-Ridge =  $1 \times 10^{-2}$ ; Alpelisib-Rhythmicity =  $6.6 \times 10^{-3}$ ; Alpelisib-Circadian =  $1 \times 10^{-2}$ ; Alpelisib-Infradian =  $1.9 \times 10^{-2}$ ; Alpelisib-Phase diff. var =  $2.7 \times 10^{-3}$ ; Alpelisib-Ultradian =  $4.6 \times 10^{-2}$ ; Olaparib-Growth =  $2.7 \times 10^{-2}$ ; Cisplatin-Rhythmicity =  $1 \times 10^{-2}$ ; Cisplatin-Circadian =  $3.2 \times 10^{-2}$ ; Cisplatin-Infradian =  $4.4 \times 10^{-2}$ ; Cisplatin-Period var. =  $3.1 \times 10^{-2}$ .  $n = 5$  cell lines per drug, except for cisplatin, where  $n = 15$  cell lines. (B) Ranking of absolute correlation values between cellular  $GR_{inf}$  values and circadian clock/growth parameters, accumulated by individual drugs ( $n = 15$  parameters). Bottom and top edges of the boxes represent the 25th and 75th percentiles, respectively. Extending whiskers represent data points within 1.5 times the interquartile range from lower and upper quartile. Red horizontal lines denote median values, red crosses mark outliers. (C) Ranking of absolute correlation values between cellular  $GR_{inf}$  values and circadian clock/growth parameters, accumulated by individual parameter ( $n = 9$  drugs). See (B) for definition of boxes. (D) See (A), but shown for  $GR_{50}$  values.  $p$ -values: Alpelisib-Amplitude var. =  $3.6 \times 10^{-2}$ ; Cisplatin-Phase diff =  $4.8 \times 10^{-2}$ ; Adavosertib-Period var. =  $3.2 \times 10^{-2}$ ; Paclitaxel-Amplitude =  $1.8 \times 10^{-2}$ ; Doxorubicin-Amplitude =  $4.4 \times 10^{-2}$ ; 5-FU-Lag =  $2.5 \times 10^{-2}$ ; 5-FU=Phase diff. var. =  $3.3 \times 10^{-2}$ . (E) See (B), but shown for  $GR_{50}$  values. (F) See (C), but shown for  $GR_{50}$  values. (G) See (A), but shown for Hill coefficient values.  $p$ -values: Cisplatin-Lag =  $2.7 \times 10^{-2}$ ; Cisplatin-Infradian =  $2.5 \times 10^{-2}$ ; Paclitaxel-Lag =  $3 \times 10^{-2}$ ; Paclitaxel-Phase diff. var. =  $3.7 \times 10^{-2}$ ; Doxorubicin-Amplitude var. =  $4.5 \times 10^{-2}$ ; Doxorubicin-Amplitude decay =  $1.2 \times 10^{-2}$ ; 5-FU-Period =  $1.3 \times 10^{-2}$ ; Torin2-Period =  $2.4 \times 10^{-2}$ ; Adavosertib-Period var. =  $3.4 \times 10^{-2}$ ; (H) See (B), but shown for Hill coefficient values. (I) See (C), but shown for Hill coefficient values.

**Own drug sensitivity dataset**  
Cisplatin | DNA damage response inducer

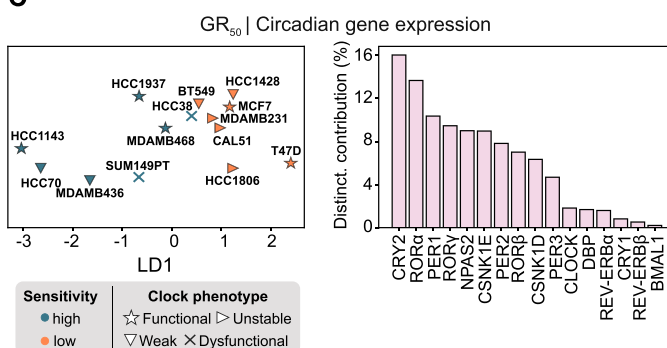
**A**



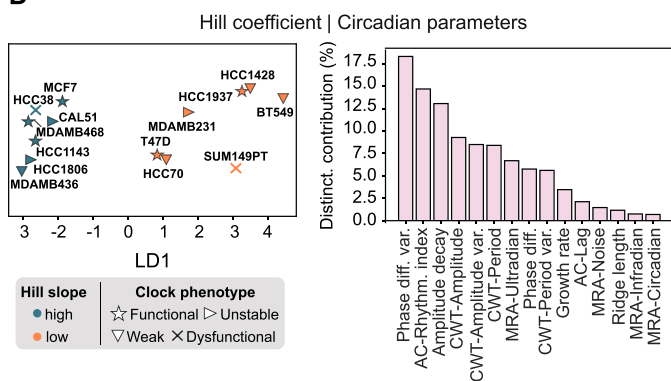
**B**



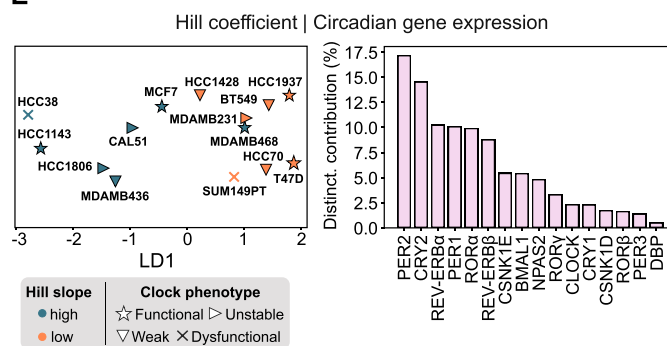
**C**



**D**

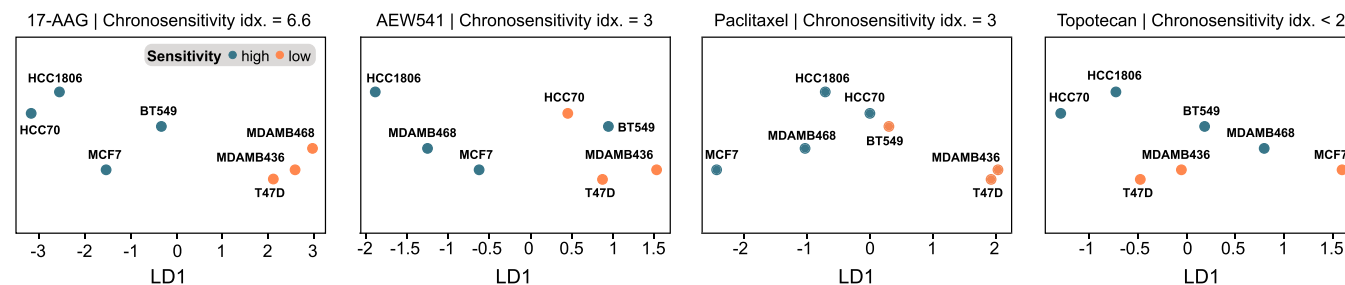


**E**



**F**

**Public CCLE dataset**  
Circadian parameters | IC<sub>50</sub>



**◀ Figure EV4. Expanded view for Fig. 4.**

(A) Linear discriminant analysis (LDA) on median-binarized cisplatin  $GR_{inf}$  values using circadian gene expression data as input. Cell models shown in with  $GR_{inf}$  values below or above the median are colored in blue-green and orange, respectively. The right bar plots rank the individual contribution of each input parameter to the obtained discriminative information. (B) See (A), but shown for  $GR_{50}$  values and *Bmal1-Per2* oscillation and growth parameters as input. (C) See (A), but shown for  $GR_{50}$  values. (D) See (B), but shown for Hill coefficient values and *Bmal1-Per2* oscillation and growth parameters as input. (E) See (A), but shown for Hill coefficient values. (F) LDA profiles of different drugs, exemplifying cell model distributions along LD1 for varying chronosensitivity indices, sorted from highest index (left panel) to lowest (right panel).

## **Appendix A4: Neuroblastoma**

Article title: **Circadian rhythm heterogeneity modulates drug response variations in neuroblastoma models**

Contributions: Data analysis

Discussion and interpretation of results

Method section writing (concerning techniques we applied)

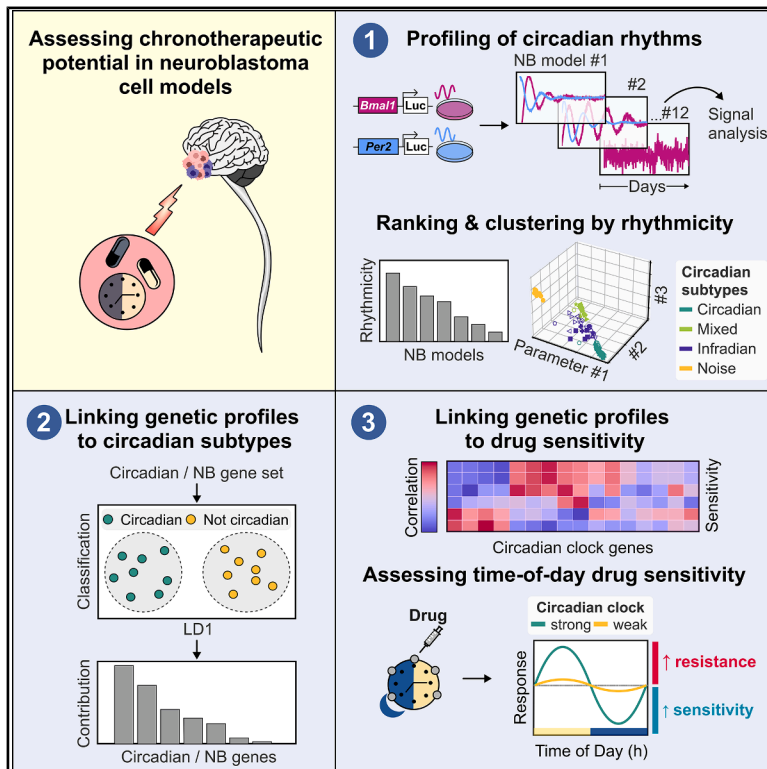
Figures 3; 4; S3; S5; S6

DOI link: <https://doi.org/10.1016/j.celrep.2026.116975>

Published in: Cell Reports

# Circadian rhythm heterogeneity modulates drug response variations in neuroblastoma models

## Graphical abstract



## Authors

Carolin Ector, Christoph Schmal, Jeff Didier, ..., Achim Kramer, Hanspeter Herzog, Adrián E. Granada

## Correspondence

adrian@granadalab.org

## In brief

Ector et al. uncover circadian heterogeneity across neuroblastoma cell models and link rhythmic strength to drug sensitivity. Their findings suggest that circadian competence may influence treatment outcomes, pointing to chronotherapy as a potential avenue for improving pediatric cancer care.

## Highlights

- Long-term live-cell imaging reveals circadian oscillations in neuroblastoma cells
- Deep circadian phenotyping shows diverse clock dynamics in neuroblastoma cell models
- Genetic profiles associate with circadian rhythm strength and drug sensitivity patterns
- Circadian-competent neuroblastoma cells vary in drug sensitivity by time of day



## Resource

# Circadian rhythm heterogeneity modulates drug response variations in neuroblastoma models

Carolin Ector,<sup>1,2,9</sup> Christoph Schmal,<sup>2</sup> Jeff Didier,<sup>3</sup> Sébastien De Landtsheer,<sup>3</sup> Johannes H. Schulte,<sup>4,10</sup> Ulrich Keilholz,<sup>1,5</sup> Thomas Sauter,<sup>3</sup> Achim Kramer,<sup>7</sup> Hanspeter Herzel,<sup>2,6</sup> and Adrián E. Granada<sup>8,11,\*</sup>

<sup>1</sup>Charité Comprehensive Cancer Center, Charité – Universitätsmedizin Berlin, 10117 Berlin, Germany

<sup>2</sup>Institute for Theoretical Biology, Humboldt-Universität zu Berlin, 10115 Berlin, Germany

<sup>3</sup>Department of Life Sciences and Medicine, University of Luxembourg, 4365 Esch-sur-Alzette, Luxembourg

<sup>4</sup>Department of Pediatric Oncology, Hematology and Stem Cell Transplantation, Charité – Universitätsmedizin Berlin, Charitéplatz 1, 10117 Berlin, Germany

<sup>5</sup>German Cancer Consortium (DKTK), Berlin, Germany

<sup>6</sup>Charité – Universitätsmedizin Berlin, 10117 Berlin, Germany

<sup>7</sup>Laboratory of Chronobiology, Charité – Universitätsmedizin Berlin, 10117 Berlin, Germany

<sup>8</sup>Work Conducted While Affiliated with Charité – Universitätsmedizin Berlin, 10117 Berlin, Germany

<sup>9</sup>Present address: The Francis Crick Institute, London NW1 1AT, UK

<sup>10</sup>Present address: Clinic for Pediatrics and Adolescent Medicine, Universitätsklinikum Tübingen, Hoppe-Seyler-Str. 1, 72076 Tübingen, Germany

<sup>11</sup>Lead contact

\*Correspondence: [adrian@granadalab.org](mailto:adrian@granadalab.org)

<https://doi.org/10.1016/j.celrep.2026.116975>

## SUMMARY

Circadian clocks regulate essential cellular functions and influence cancer development and treatment outcomes. Aligning therapy with circadian rhythms can improve efficacy and reduce toxicity, yet whether neuroblastoma, a heterogeneous pediatric tumor, maintains circadian function remains unclear. Here, we systematically profiled circadian dynamics across 12 neuroblastoma cell models using long-term bioluminescence assays and computational analysis. Our findings reveal heterogeneous circadian patterns ranging from robust to arrhythmic, which we linked to distinct neuroblastoma genetic features. By integrating drug sensitivity data, we identified candidate compounds whose effectiveness correlates with circadian expression profiles. Moreover, time-of-day treatment assays with the ALK inhibitor lorlatinib and frontline chemotherapeutics revealed distinct temporal drug responses that were more pronounced in circadian-competent than weakly rhythmic cell lines. Together, these findings establish circadian heterogeneity as a previously unrecognized dimension of neuroblastoma biology and highlight the therapeutic potential of chronotherapy approaches for improved treatment efficacy.

## INTRODUCTION

Circadian clocks are inheritable timekeepers that have evolved among diverse life forms in response to daily fluctuations in light and temperature.<sup>1,2</sup> In mammals, a master pacemaker located in the suprachiasmatic nucleus (SCN) of the hypothalamus coordinates the overall rhythm of the organism, while peripheral tissue clocks maintain their own intrinsic oscillations.<sup>3,4</sup> Hence, circadian rhythms can be detected from the level of the entire organism down to individual cells, underscoring their fundamental biological importance.<sup>3</sup>

At the cellular level, the generation of intracellular rhythms relies on interconnected transcriptional-translational feedback loops (TTFLs).<sup>5</sup> Central to this process are heterodimers formed by BMAL1 and CLOCK, which bind to E-box elements in the promoters of *Period* (*Per*) and *Cryptochrome* (*Cry*) genes, thereby promoting their transcription. In turn, PER and CRY proteins inhibit the activity of the BMAL1-CLOCK heterodimers, effec-

tively closing the negative feedback loop. Complementary feedback loops, involving genes such as *Reverb*, *Ror*, and *Dbp*, further adjust the period, amplitude, and phase of circadian oscillations, contributing to the system's flexibility and resilience.<sup>6</sup>

Circadian rhythms regulate approximately 40% of protein-coding genes,<sup>7</sup> orchestrating crucial physiological processes such as cell cycle progression,<sup>8</sup> metabolism,<sup>9</sup> and DNA repair.<sup>10</sup> This widespread influence underscores the clock's integral role in maintaining cellular homeostasis and its impact on various pathophysiological conditions.<sup>11</sup> While the disruption of circadian rhythms has been implicated with diverse cancer types,<sup>12</sup> a growing body of research shows that rhythmicity can persist in cancer cells to varying degrees.<sup>13–17</sup> In cancer therapy, circadian rhythms can be effectively leveraged to time treatments with the patient's natural biological cycles, potentially enhancing drug efficacy and reducing side effects, a treatment concept referred to as chronotherapy.<sup>18</sup> Despite these promising insights, the circadian clock status remains poorly understood in

many cancers, including neuroblastoma (NB), the most prevalent cancer in infancy, accounting for over 10% of childhood cancer-related deaths.<sup>19</sup> This pediatric tumor arises from fetal neural crest cells and is marked by considerable biological and clinical heterogeneity. Approximately 50% of patients are classified as high risk, with 5-year survival rates falling below 40%.<sup>20</sup> The aggressiveness of the disease is closely linked to a range of genetic alterations, including the amplification of the proto-oncogene MYCN, rearrangements at the TERT locus, inactivating mutations in ATRX and the activation of ALK.<sup>21</sup>

To investigate circadian properties in neuroblastoma, we conducted deep circadian phenotyping<sup>13,22</sup> across 12 distinct NB cell models. We combined long-term high-resolution bioluminescence assays of core clock genes with an in-depth computational characterization of the circadian signals, which revealed widespread but heterogeneous circadian oscillations. Integrating gene expression data, we identified circadian and NB-specific signatures distinguishing strongly rhythmic from weakly rhythmic models. Analysis of public drug sensitivity datasets uncovered compounds whose efficacy correlated with circadian gene activity, and complementary time-of-day assays with lorlatinib, cisplatin, and doxorubicin revealed distinct time-of-day sensitivity that was more pronounced in circadian-competent lines. Together, this systematic profiling establishes a resource linking circadian heterogeneity to genetic background and drug response, providing a foundation for circadian-aligned therapies in neuroblastoma.

## RESULTS

### Circadian phenotypes in neuroblastoma cell models

To record circadian signals in a wide range of neuroblastoma cell lines, we engineered them to stably express luciferase (Luc) reporters of two key circadian clock genes, *Bmal1* and *Per2*. We then generated high-resolution 5-day bioluminescence recordings of the reporter cell lines (Figure 1A), revealing considerable variability among them (Figure 1B and S1A, B; see Table S1 for clinical features of the cell models). For instance, while SKNSH showed robust oscillations for 5 days, GIMEN exhibited clear but rapidly damping rhythms, SH-SY5Y oscillated with extended periods, while CHP212 did not display detectable rhythmicity (Figure 1B). Interestingly, the *Bmal1* and *Per2* signals in GIMEN cells were nearly anti-phasic, indicative of a functional circadian clock network, whereas in SKNSH cells they displayed a pronounced phase shift.

To better characterize circadian rhythmicity, we applied discrete wavelet-based multiresolution analysis (MRA; see STAR Methods), decomposing detrended signals into noise (1–4 h), ultradian (4–16 h), circadian (16–32 h), and infradian (32–256 h) components. This revealed that 76.8% of the GIMEN-*Bmal1* signal lies within the circadian range, with minimal contribution of noise (0.3%; Figure 1C). However, an appreciable 18.8% of the signal resided in the infradian band, suggesting the presence of additional oscillatory dynamics. Extracting the circadian component across various NB models enabled us to rank them by rhythmic strength. Instead of a binary division into rhythmic or arrhythmic, the analysis revealed a continuum of rhythmicity (Figure 1D), consistent with our earlier findings in breast cancer models.<sup>13</sup>

Given the diverse clinical backgrounds of the patients from whom each NB cell line was derived (Table S1), we performed an exploratory analysis to investigate whether circadian components retained any association with basic clinical features such as patient age, biological sex, or ALK mutation status. Stratification by clinical features suggested an association whereby cell lines from patients older than two years tended to exhibit stronger circadian components (Figure S2A). Furthermore, female-derived and ALK-mutated samples tended toward higher rhythmicity compared to male-derived and ALK wild-type samples, respectively (Figures S2B and S2C). These trends are consistent with reported age- and sex-dependent variation in circadian regulation in humans.<sup>23,24</sup> However, given the limited sample size and the multiple biological differences of established cell lines from primary tumors, these associations should be interpreted with caution. We therefore focused subsequent analyses on mechanistic links within the cell lines themselves.

Next, we explored the presence of circadian phenotypes in neuroblastoma by conducting a principal component analysis (PCA) on the four coarse-grained MRA frequency components: noise, ultradian, circadian, and infradian. PCA revealed four distinct clusters, consistent across combined *Bmal1/Per2* data (Figure 1E) and reporter-separate analyses (Figures S3A and S3B), which supports the presence of intrinsic circadian subtypes. Loadings indicated that all but the ultradian component contributed substantially to variance (Figures S3C and S3D). To refine this classification, we therefore applied *k*-means clustering (*k* = 4) on noise, circadian, and infradian components. This analysis assigned each sample to a cluster defined by predominant variance in either of these patterns or a mixed pattern that fell between the circadian and infradian ranges (Figures 1F, 1G, S3E, and S3F; see Table S2 for detailed results).

In summary, our integrative framework revealed that samples from three specific models (SKNSH, NGP, and GIMEN) consistently fell within the circadian cluster, affirming the existence of stable circadian phenotypes. In contrast, most of the cell lines exhibited patterns that were either mixed circadian or infradian, with two models only (SH-SY5Y and CHP212) showing a complete absence of circadian rhythmicity. This highlights the diverse and complex nature of the circadian clock within neuroblastoma cell lines.

### Circadian signal stability and variability in neuroblastoma

Building on the observed circadian phenotypes, we next characterized signal parameters using two complementary approaches: harmonic regression, fitting a stochastic damped oscillator to each detrended trace to capture time-averaged properties, and continuous wavelet transform (CWT) to reveal time-dependent changes in non-stationary signals.<sup>25</sup> Importantly, we focused our analyses on recordings that classified as circadian or mixed circadian (Figure 1G).

Harmonic regression of detrended signal traces (Figure 2A) revealed predominantly prolonged signal periods of up to 36 h (Figure 2B). Only NGP-, SKNAS-, and GIMEN-*Bmal1* cells exhibited periods close to a 24-h cycle (Figure 2B). All cell lines showed damped oscillations (Figure S1), though the degree varied: LAN5 and SKNAS decayed within one cycle, whereas most

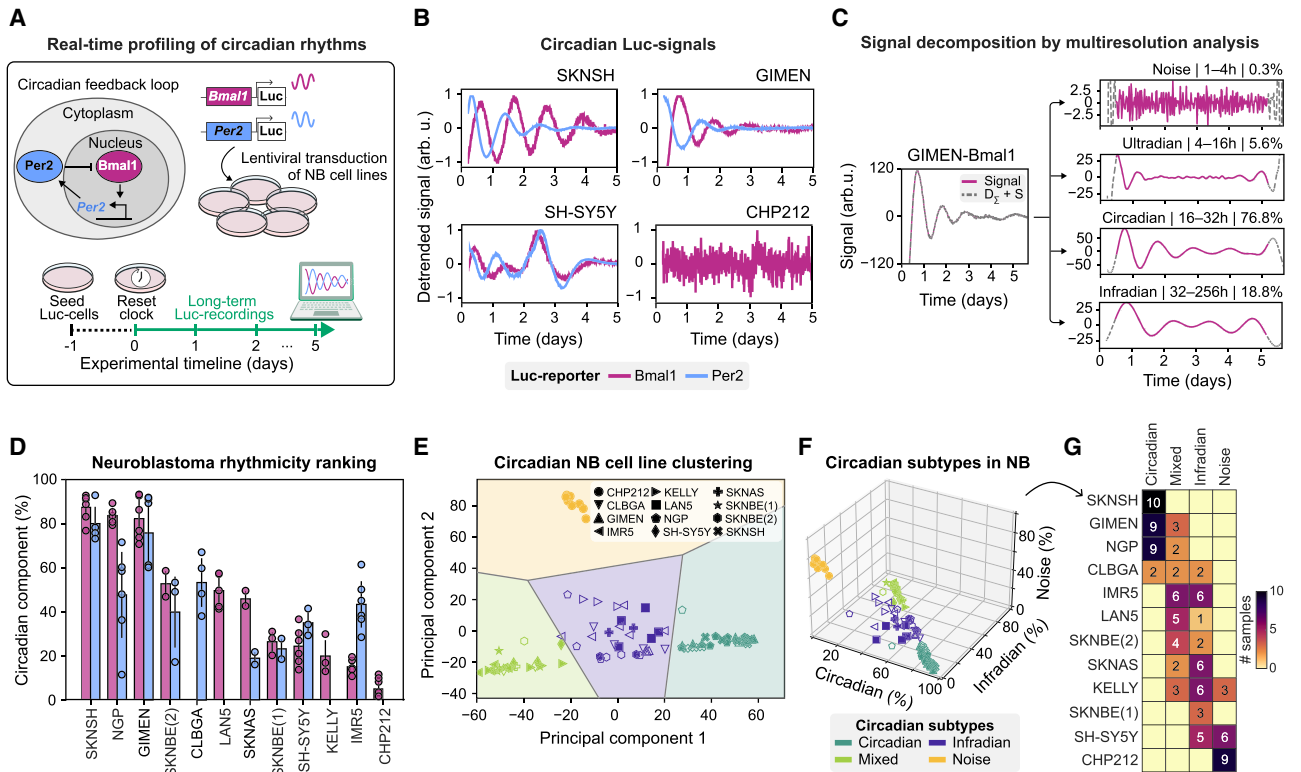


**Figure 1. Real-time profiling of circadian rhythms in neuroblastoma cell lines**

(A) Schematic of the experimental strategy to monitor circadian rhythms in neuroblastoma (NB) cell lines. NB cell lines stably expressing luciferase (Luc) reporters for *Bmal1* and *Per2* were generated via lentiviral transduction, enabling real-time expression monitoring. Following a circadian clock reset, Luc signal from cell populations was recorded over multiple days.

(B) Overlay of detrended *Bmal1* and *Per2* signal traces (color-coded) of four NB cell lines.

(C) Multiresolution analysis (MRA) of detrended GIMEN-*Bmal1* signal, breaking it down into four frequency components, with each component's percentage representing its share of the total signal.

(D) Bar plot ranking cell lines by their MRA circadian component, grouped and color-coded for *Bmal1*- and *Per2* signals. Data represent the mean  $\pm$  SD across individual samples (see exact numbers below).

(E) Principal component analysis (PCA) biplot showing the distribution of all *Bmal1*- and *Per2*-Luc samples ( $n = 106$ ) along the first two PCs, calculated from the four MRA frequency components. Cell models are distinguished by markers. PCA clusters are outlined and color-coded for clarity.

(F) 3D scatterplot depicting the distribution of all *Bmal1*- and *Per2*-Luc samples ( $n = 106$ ) along the MRA circadian, infradian, and noise axes. Clusters, determined by the dominant signal components, are color-coded for clarity.

(G) Heatmap showing the number of samples for each cell line (row) per circadian cluster (columns), corresponding to (F).

Data shown in (D)–(G) are derived from two biological replicates and technical triplicates ( $n = 6$  samples per Luc reporter). NGP-*Bmal1* and SH-SY5Y-*Per2* were assayed in technical duplicates in one experiment ( $n = 5$ ). CHP212-*Bmal1* was assayed in three biological replicates and technical triplicates ( $n = 9$ ). SKNSH-*Per2* was assayed in a single sample in one experiment ( $n = 4$ ). SKNAS-*Per2* was assayed in a single experiment in technical duplicates ( $n = 2$ ). SKNBE(1) and SKNBE(2) samples were assayed in a single experiment in technical triplicates ( $n = 3$ ).

retained half their amplitude beyond the first oscillation (Figure 2C). Interestingly, period length and damping were correlated, with slower decay linked to longer periods ( $R^2 = 0.48$ , Spearman  $r = -0.77$ ,  $p = 0.021$ ). These coupled signatures of amplitude loss and period prolongation suggest rapid desynchronization and weak extracellular coupling, processes that may promote tumor growth.<sup>26,27</sup>

To assess how circadian features change over time, we next applied CWT, which generates a time-period power spectrum, thereby illustrating the range and relative power of oscillatory components within a specific period range (Figure 2E). Tracking the main oscillatory component (“ridge”) revealed time-dependent variation in period and amplitude. In GIMEN-*Bmal1* cells,

rhythms remained stable for  $\sim 3.5$  days before decaying and lengthening to  $\sim 30$  h (Figure 2F), indicative of a loss of population synchrony. By quantifying the ridge length as a proxy for circadian clock strength, with longer, continuous ridges indicating robust signals, we observed a gradual ranking across models, where SKNSH displayed the longest ridge (Figure 2G). This finding aligns with its high ranking in the circadian component analysis and its clustering outcomes (see Figures 1D–1G).

We next aggregated continuous periods across replicates to assess potential variability (Figure 2H). Consistent with the stationary analysis (Figure 2B), periods ranged from short to extended, with circadian-clustered models closest to 24 h. LAN5, despite short periods in harmonic regression, averaged

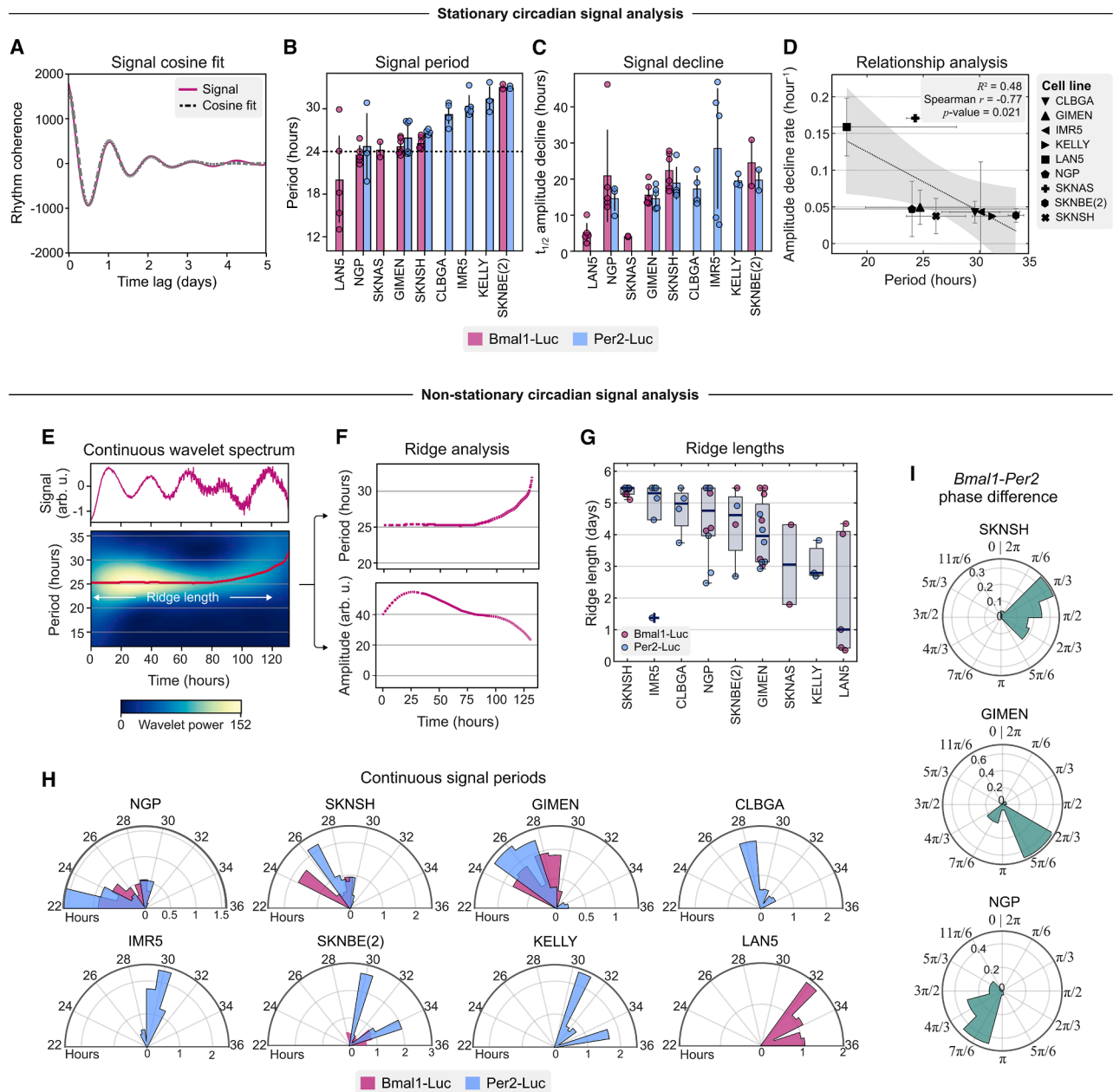


**Figure 2. Deep circadian phenotyping across neuroblastoma cell line models**

(A) Non-linear least squares fitting (dashed gray curve) to GIMEN-*Bmal1*-Luc signal (pink curve).

(B) Bar plot of NB cell lines ranked by mean signal periods, determined via non-linear least squares fitting and color-coded for *Bmal1*- or *Per2* signals. Data represent the mean  $\pm$  SD across individual samples. Dashed line = 24 h. Note that one NGP-*Per2* sample (period = 41.1 h) is cut from the axis but contributed to the mean  $\pm$  SD.

(C) See (B) but shown for mean amplitude decline half-life ( $t_{1/2}$ ). The order follows the same scheme as in (B).

(D) Relationship between amplitude decay rates and circadian periods across NB cell lines ( $n = 7$ , distinguished by markers), as determined by nonlinear least squares fitting. The gray area denotes the 95% confidence interval, with model accuracy shown by  $R^2$  values. Spearman's correlation coefficient ( $r$ ) and its  $p$  value are noted in the legend. Data represents the mean  $\pm$  SD across individual samples across Luc-reporters. Sample sizes in (B)–(D) per available reporter are LAN5, NGP-*Bmal1*, and IMR5 ( $n = 5$ ); SKNAS and SKNBE(2) ( $n = 2$ ); GIMEN and SKNSH-*Bmal1* ( $n = 6$ ); NGP-*Per2*, SKNSH-*Per2*, and CLBGA ( $n = 4$ ); and KELLY ( $n = 3$ ).

(E) Continuous wavelet transform (CWT) on detrended and normalized GIMEN-*Bmal1* signal (top). The corresponding wavelet spectrum (bottom) displays time-resolved periods, with the primary oscillatory component (*ridge*) highlighted in red.

(F) Ridge readout of continuous periods (top) and amplitudes (bottom), corresponding to the CWT analysis in (E).

(G) Boxplot displaying CWT ridge lengths from *Bmal1*-/*Per2* signals across cell lines. The box edges indicate the 25<sup>th</sup> and 75<sup>th</sup> percentiles, with whiskers extending to values within 1.5 times the interquartile range. The median is shown as a dark blue horizontal line.

(legend continued on next page)

~34 h here, likely due to excluding traces with ridges too short to track, underscoring the value of time-resolved analysis. Building on the insights into temporal dynamics of both period and signal stability, we further assessed the *Bmal1-Per2* phase differences over time for the three most circadian NB cell models: SKNSH, GIMEN, and NGP. Despite their overall circadian behavior, their phase relationships diverged: SKNSH showed a ~4 h lag ( $\pi/3$ ), GIMEN ~8–9 h, and NGP ~14 h (Figure 2I). Notably, the ~8 h lag resembles that reported for U2OS and MCF10A cells,<sup>13</sup> two highly circadian cell models,<sup>14,15</sup> suggesting that similar circadian clock timings may extend across different cell types.

To explore how circadian parameters relate to functional outputs, we further characterized the growth dynamics of the neuroblastoma cell line panel by long-term live-cell imaging (see STAR Methods). We first parametrized the normalized confluence data with a logistic function to obtain cell line-specific growth rates (Figure S4A). Next, we examined these growth rates in relation to circadian parameters derived from our deep phenotyping analysis (Figure S4B).

This revealed two significant associations: a negative correlation with the circadian component ( $R^2 = 0.57$ ,  $r = -0.75$ ,  $p = 0.012$ ; Figure S4C) and a positive correlation with the circadian period ( $R^2 = 0.27$ ,  $r = 0.52$ ,  $p = 0.152$ ; Figure S4D). These findings suggest that faster proliferating models display disrupted circadian rhythms, characterized by either weaker rhythms or prolonged periods.

In summary, our analysis reveals heterogeneous circadian properties in neuroblastoma cell models, with most cell lines exhibiting prolonged periods, variable damping and distinct *Bmal1-Per2* phase relationships. Time-resolved analyses revealed differences in signal stability that enabled ranking of circadian robustness. Importantly, weaker or lengthened rhythms link with faster cellular proliferation, suggesting that circadian impairment is functionally connected to tumor growth.

### Linking circadian phenotypes to gene expression

Building upon the circadian phenotyping results, we next sought to understand how the rhythmic patterns of the NB cell lines relate to gene expression profiles by analyzing their molecular profiles from the Cancer Cell Line Encyclopedia (CCLE) DepMap 2022-Q2 (<https://sites.broadinstitute.org/ccle/datasets>).<sup>28</sup> Using both circadian and NB-specific genes, we classified cell models by their circadian component defined from deep circadian phenotyping. We first tested all circadian or NB-specific genes, then iteratively examined gene combinations to identify optimal predictive sets (Figure 3A). Core clock genes were defined as those essential for TTFL regulation whose disruption impairs rhythmicity,<sup>5,29</sup> while NB-specific genes were those commonly mutated or dysregulated in neuroblastoma.<sup>30,31</sup>

Cluster analysis of raw expression values for the circadian genes classified eight NB cell models, whose gene expression data were available, into two overarching clusters (Figure S5A). However, each cluster contained cell models with both high and low circadian oscillation components. Linear discriminant

analysis (LDA) confirmed the poor predictive power of the full gene set, achieving only 25% accuracy by leave-one-out cross-validation (LOOCV) (Figures 3B and S5B). We therefore hypothesized that the circadian phenotype of each cell model might be more accurately predicted by a specific combination of genes. To test this, we systematically screened all possible gene combinations, from single genes up to sets of 15, and evaluated their classification performance. Both separation metrics, the ratio of between-class distance (BCD) to within-class distance (WCD; see Figure 3A), and LOOCV accuracy revealed a similar trend: the predictive power increased with the number of genes up to about 5–6, after which performance declined (Figures 3C and S5C). Notably, only combinations of 3–5 circadian genes consistently achieved high accuracy and well separation in the LDA space, indicating that small but specific subsets of circadian genes are sufficient to capture the circadian phenotype (Figures 3D, S5B, and S5D). Here, *Bmal1*, *Clock*, and *Rev-erb $\alpha$*  consistently appeared among the top-ranking genes.

Parallel analysis of NB-specific genes showed that while the full 11-gene panel separated models better than circadian genes (Figure 3E), it achieved 0% prediction accuracy (Figure S5E). Testing all 2,047 subsets revealed peak performance with 3–5 genes, after which accuracy declined (Figure 3F). These small subsets consistently reached 100% accuracy (Figures S5E and S5F), with *Phox2b* and *Ntrk2* emerging as most informative genes, frequently accompanied by *Atrx* (Figures 3G and S5G). Thus, as with circadian genes, a smaller number of NB-specific genes proved sufficient to classify circadian phenotypes.

These findings reveal that both circadian and NB-specific genes can be used to classify circadian phenotypes in the panel of neuroblastoma cell models, suggesting a potential interaction between oncogenic neuroblastoma pathways and circadian regulation.

### Circadian gene expression and treatment timing shape drug responses in neuroblastoma cell models

Having linked circadian phenotypes to gene expression, we next examined how circadian regulators relate to drug sensitivity. Here, circadian regulators may influence cellular processes underlying drug response, potentially serving as biomarkers for therapeutic efficacy.

Using CCLE data from NB models with matched availability on expression and drug sensitivity data, linear regression and Spearman analysis revealed multiple correlations between circadian genes and drug activity (ActArea; Figure 4A; refer to Table S3 for the drugs' clinical relevance in NB). Negative regulators such as *Cry2* and *Per2* tended to anticorrelate with drug sensitivity, while positive regulators such as *Clock* and *Npas2* showed positive correlations (Figures 4A and 4B), suggesting that core network relationships are preserved. After Bonferroni correction, four associations remained significant: *Per2*-topotecan, *Rev-erb $\alpha$* -paclitaxel, *Clock*-PF2341066, and *Rory $\gamma$* -PLX4720 (Figures 4A and 4C). Analyses of IC<sub>50</sub> and EC<sub>50</sub> data identified

(H) Probability-normalized, cell line-specific polar histograms of continuous signal periods for each Luc reporter (color-coded). Sample sizes in (G) and (H) are as described for (B)–(D), except for IMR5 ( $n = 6$ ).

(I) Probability-normalized polar histograms of *Bmal1-Per2* phase differences for the specified cell lines, averaged over multiple combinations: SKNSH ( $n = 25$ ), GIMEN ( $n = 36$ ), and NGP ( $n = 26$ ).

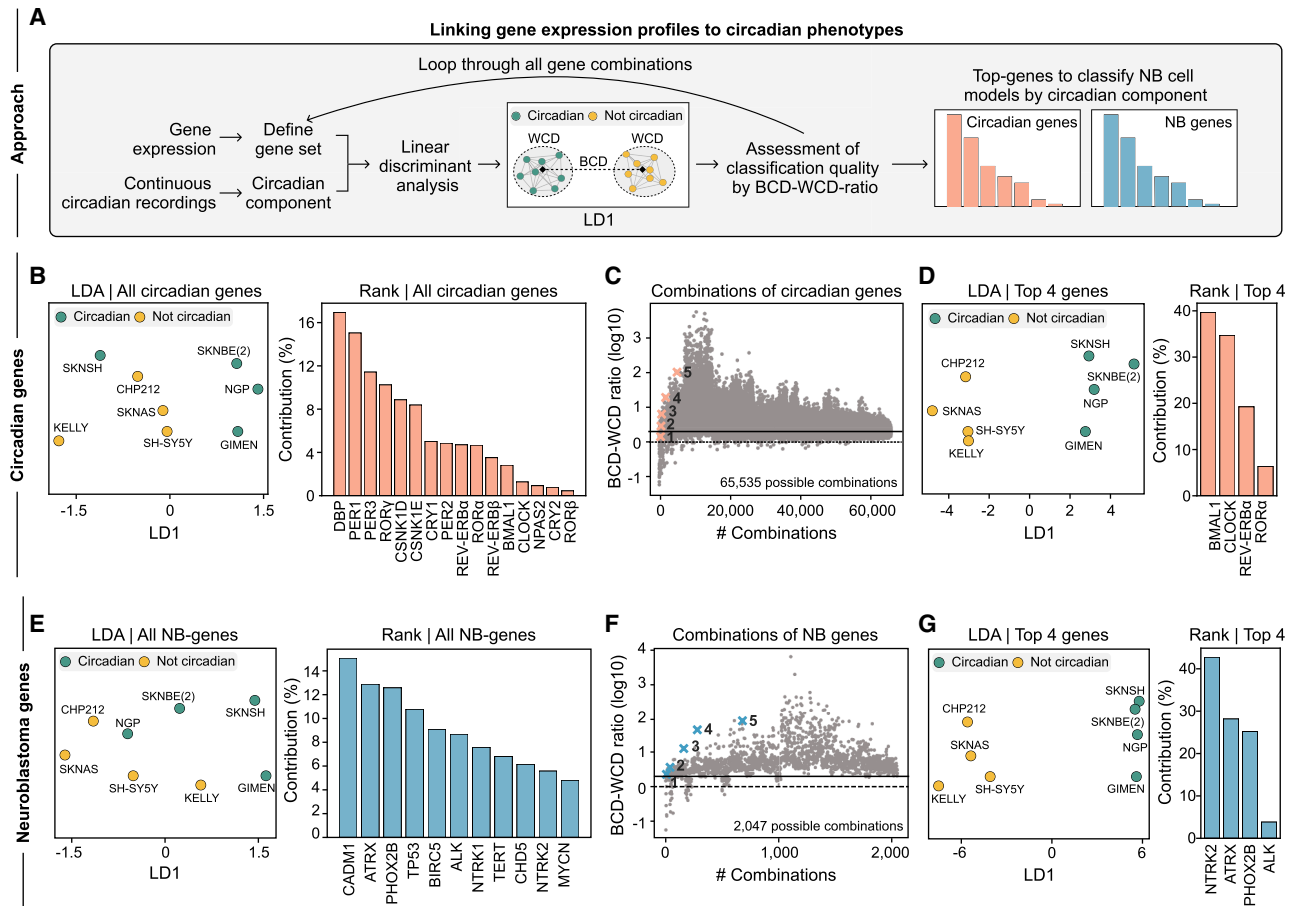


**Figure 3. Linking gene expression levels to circadian phenotypes in neuroblastoma**

(A) Overview of the linear discriminant analysis (LDA)-based approach used to investigate how circadian or neuroblastoma (NB)-specific genes influence circadian phenotypes across NB cell models. Each gene list was tested in various combinations to identify the subset of genes that most accurately predict circadian phenotypes. NB cell models were initially classified based on their characterized circadian component, determined through deep circadian phenotyping.

(B) *Left panel*: LDA on median-binarized circadian components (determined via MRA), using all 16 circadian genes as predictors. Cell models with circadian component values below or above the median are shown in yellow and green, respectively. The x axis represents the first linear discriminant (LD1), reflecting the greatest variance between these two groups. *Right panel*: bar plot ranking the 16 circadian genes by their individual contribution to the discriminative power of the LDA model.

(C) All possible combinations of circadian genes plotted against their corresponding log<sub>10</sub> ratio of between-cluster distance (BCD) to within-cluster distance (WCD), an LDA-based metric of separation quality. The best-performing combinations up to five genes are marked with an X.

(D) See (B), here shown for LDA using the top 4 performing circadian genes as predictors.

(E) See (B), here shown for LDA using all 11 NB-specific genes.

(F) See (C), here shown for NB-specific genes.

(G) See (B), here shown for LDA using the top 4 performing NB-specific genes as predictors.

additional links, including *Dbp*-topotecan, *Per1*-TAE684, and *Clock*-panobinostat (Figures S6A and S6B). Together, these results highlight topotecan and ALK inhibitors as consistently associated with circadian gene expression, though effect direction varied by sensitivity metric. This shows that, despite the small sample sizes, topotecan consistently shows significant correlations with specific clock genes, while the direction of these associations (positive or negative) depends on the drug sensitivity metric employed.

We next sought to directly test whether neuroblastoma cell models exhibit time-of-day (ToD)-dependent drug responses.

To do so, we performed ToD sensitivity assays using our established *in vitro* pipeline,<sup>22</sup> selecting five neuroblastoma cell lines from different ranges of the circadian rhythmicity spectrum: GIMEN and SKNSH (strong rhythmicity), SKNBE(2) (intermediate), and SH-SY5Y and CHP212 (weak rhythmicity). Following an established resetting-treatment protocol,<sup>22</sup> cells were treated at six circadian timepoints with three clinically relevant drugs: lorlatinib (ALK inhibitor), cisplatin (DNA crosslinker), and doxorubicin (DNA synthesis inhibitor; Figure 4D). GIMEN cells showed pronounced and consistent ToD-dependent responses across all tested drugs (Figure 4E, left), with lorlatinib eliciting the highest

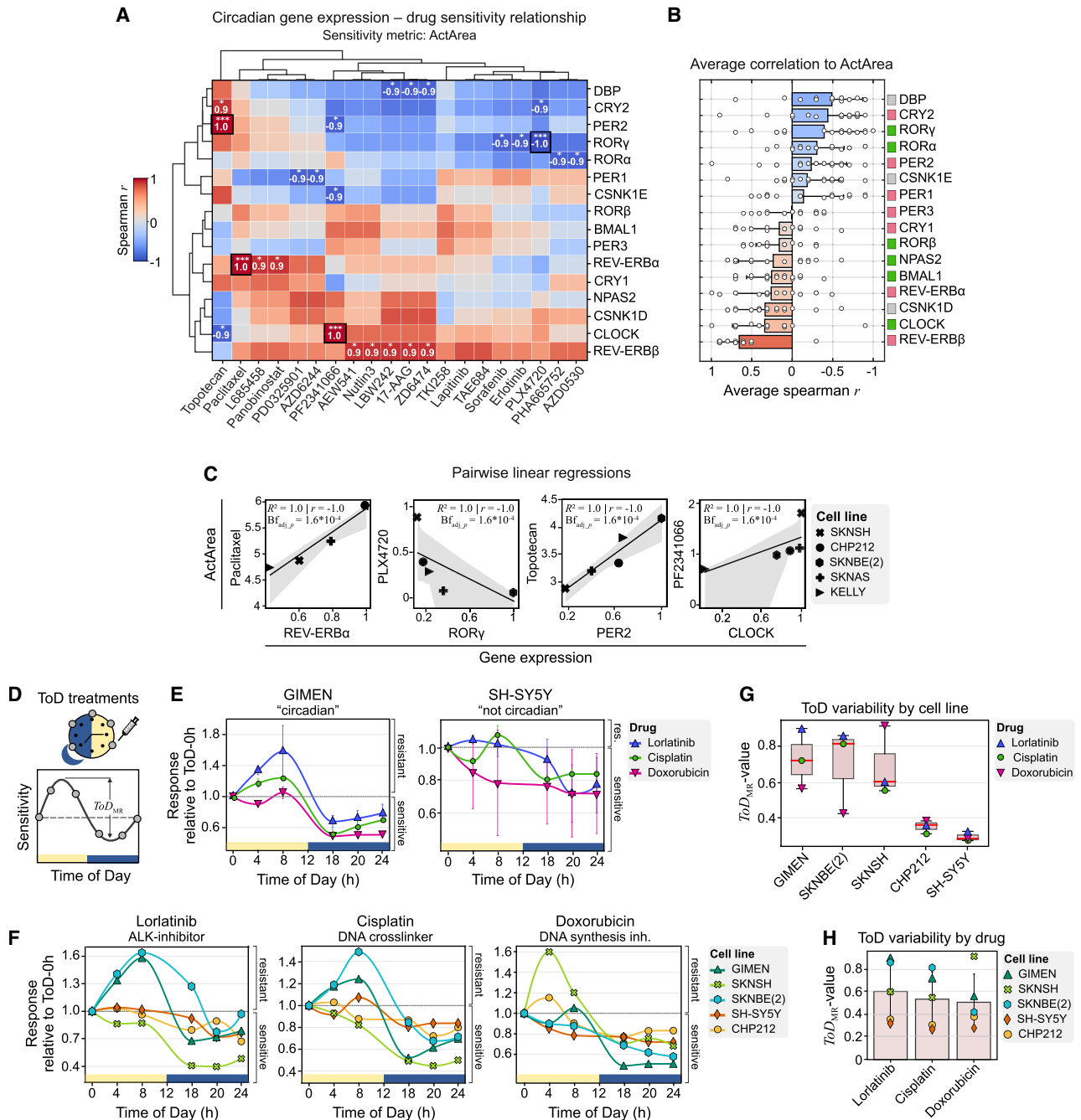


**Figure 4. Correlation analysis of drug sensitivity and circadian gene expression in neuroblastoma cell lines**

(A) Cluster map of Spearman correlation coefficients between ActArea values for multiple drugs and circadian gene expression across 6 NB cell lines, based on CLE data. Significant correlations (two-sided *t* test with no adjustments made) are indicated by stars (\*  $p = 0.037$ , \*\*\*  $p = 1.4 \times 10^{-24}$ ). Correlations remaining significant after Bonferroni correction ( $B_{f,adj,p} = 1.6 \times 10^{-4}$ ) are outlined in black.

(B) Bar diagrams of average Spearman correlations between ActArea values ( $n = 20$  drugs) and circadian gene expression, ranked by circadian genes in ascending order. Bars represent the mean  $\pm$  SD, with individual ActArea-gene correlations overlaid as white circles. Only one-sided error bars are shown for clarity. Bar colors match the heatmap in (A). Gene colors: green = positive regulators; red = negative regulators; gray = stabilizing/modulating/output genes of the circadian clock network.

(C) Linear regression of Bonferroni-significant ActArea-gene pairs, with the shaded area representing the 95% confidence interval.  $R^2$  values indicate model fit ( $n = 6$  cell models).

(D) Schematic of time-of-day (ToD) drug treatments and resulting variability in responses across the day. Arrows indicate the maximum ToD response range ( $ToD_{MR}$ ).

range in ToD responses between the most and least sensitive timepoints ( $ToD_{MR}$ ) (2.3-fold differences). By contrast, weakly rhythmic SH-SY5Y cells exhibited only minimal and inconsistent ToD variation across all three drugs (Figure 4E, right).

When we examined ToD responses across all cell models, each drug generated distinct temporal dynamics (Figures 4F and S6C). While sensitivity generally increased at later circadian times, the magnitude and pattern of modulation varied considerably between drugs and cell lines. This heterogeneity became further apparent when ranking models by their average  $ToD_{MR}$  value, which revealed a clear stratification where circadian-competent lines consistently showed higher temporal modulation compared to weakly rhythmic models (Figure 4G). Supporting this pattern, the weakly rhythmic cell lines CHP212 and SH-SY5Y also exhibited greater inter-experimental variability, indicating less reproducible ToD sensitivity profiles (Figure S6D). Among the three drugs tested, lorlatinib emerged as the most promising chronotherapeutic candidate, achieving the highest average  $ToD_{MR}$  value of  $0.61 \pm 0.27$  (Figure 4H). This cell line- and drug-specific variation in ToD sensitivity is consistent with our previous findings in breast cancer models<sup>22</sup> and reinforced the need for individualized chronotherapeutic assessment.

These experiments provide direct experimental evidence that circadian competence may shape ToD-dependent drug sensitivity in neuroblastoma, highlighting its potential as a determinant of chronotherapeutic efficacy.

## DISCUSSION

Circadian clocks are well known to influence cancer progression and treatment response,<sup>18,32,33</sup> yet their function in many tumor types remains unclear. Recently, it has been shown that altered expression of clock genes contribute to tumor development and progression in glioblastoma,<sup>34</sup> which raises questions about circadian regulation in other neural-derived cancers. Neuroblastoma, a highly aggressive pediatric cancer of neural crest origin,<sup>19</sup> represents a particularly relevant context for studying clock function given its severity and developmental origins. Using real-time *Bmal1*- and *Per2* reporters in 12 NB cell models, we uncovered striking heterogeneity in circadian rhythmicity across the cell line panel: most cell lines showed weak or damped rhythms, while only SH-SY5Y and CHP212 were arrhythmic (Figure 2). To our knowledge, these NB cell models have not been evaluated for circadian functionality before, except for GIMEN and SH-SY5Y, which were characterized in our preceding studies.<sup>22</sup> Our findings indicate that complete

loss of circadian function is rare. Notably, neither circadian gene expression levels (Figure S5A) nor mutations in core clock genes (none identified across the cell line panel) explains the arrhythmic phenotype, indicating that it may arise from mechanisms including weak intercellular coupling<sup>27</sup> or post-translational and epigenetic regulation of clock proteins.<sup>35</sup> In addition, we observed marked variability in circadian classification across replicates of certain cell lines (Figures 2E–2G), which may be influenced by factors such as the seeding density and synchronization strength.<sup>27,36</sup> We also noted that *Bmal1*- and *Per2* reporter signals sometimes yielded distinct circadian properties within the same cell line, likely reflecting their regulation by different promoter elements and positions within the circadian network, though technical factors such as reporter design may also contribute to these differences. To overcome these limitations of population-based recordings, single-cell approaches using circadian fluorescent reporters<sup>37,38</sup> combined with coupling analyses could offer deeper and more direct insights into the cellular dynamics that underlie circadian regulation in each cell model. In parallel, proteomic approaches focused on post-translational modifications and stability of core clock proteins may reveal molecular defects that contribute to arrhythmic phenotypes.

While intriguing, our exploratory correlations between circadian phenotypes in neuroblastoma cell lines and basic patient characteristics such as age or sex should be interpreted with caution (Figure S2), as long-established cell lines diverge from their parental tumors and lack the microenvironmental cues that shape circadian regulation *in vivo*.<sup>39</sup> Combined with the small sample size, this limits the clinical relevance of such associations. Future studies using patient-derived organoids or xenografts with linked clinical data will be necessary to determine whether circadian phenotypes retain diagnostic value.

Our deep circadian phenotyping approach, employing harmonic regression combined with continuous wavelet transform, revealed significant variability in period, amplitude decay, and overall stability in the circadian signals over time. This is in line with an earlier study where we characterized the circadian clock landscape across numerous breast cancer cell models,<sup>13</sup> suggesting that circadian regulation may be similarly heterogeneous across different cancer types.

It would be valuable to examine circadian behavior in non-malignant, neural crest-derived cells such as trunk neural crest cells (tNCCs), which represent the developmental origin of neuroblastoma. Although we did not identify suitable sources for tNCC cultures for circadian recordings, robust oscillations

(E) Time-of-day response curves (ToD-RCs) for GIMEN (left) and SH-SY5Y (right) cells treated with lorlatinib (triangle), cisplatin (circle), or doxorubicin (inverted triangle). Responses at each treatment time point are shown relative to treatment at 0 h. The relative response was calculated by dividing the confluency measured 4 days post-treatment by the corresponding confluency of the 0 h treatment. Data points represent the mean  $\pm$  SD across two independent experiments, each based on 9 images per well.

(F) ToD-RCs for lorlatinib (left), cisplatin (middle), and doxorubicin (right) across five neuroblastoma cell models. Curves show relative responses to ToD 0 h, as described in (E). Cell line markers: GIMEN = triangle; SKNSH = cross; SKNBE(2) = hexagon; SH-SY5Y = diamond; CHP212 = circle. Data points represent the mean across two independent experiments.

(G) ToD variability by cell line, sorted in descending order by average  $ToD_{MR}$  values. Points represent individual drug-cell line combinations (drug markers as in (E)). The box edges indicate the 25<sup>th</sup> and 75<sup>th</sup> percentiles, with whiskers extending to values within 1.5 times the interquartile range. The median is shown as a red horizontal line.

(H) ToD variability by drug, sorted in descending order by average  $ToD_{MR}$  values. The data represent the mean  $\pm$  SD  $ToD_{MR}$  values across cell lines for lorlatinib, cisplatin, and doxorubicin (cell line markers as in (F)).

have been documented in other normal neural cells, including SCN neurons<sup>40</sup> and astrocytes.<sup>41</sup> Direct comparisons between NB and tNCC cells could clarify whether the variable rhythms we detected represent a loss of normal circadian function or mirror a natural diversity potentially present in neural crest progenitor cells.

To assess whether the rhythmic properties of the cell lines have functional growth consequences, we examined their relationship to cell growth parameters. Analysis of the live-cell imaging recordings showed that faster-proliferating lines tended to have weaker or lengthened rhythms (Figure S4), consistent with evidence that clock restoration can act tumor-suppressively in neuroblastoma.<sup>42</sup> Thus, circadian impairment is not only a marker of heterogeneity but seems also to be functionally linked to growth dynamics.

We further asked whether circadian oscillation signatures relate to the cell lines' genetic profiles. Gene expression and LDA analyses showed that small subsets of circadian or NB-specific genes classified phenotypes with high accuracy, whereas larger sets performed poorly. *Bmal1* and *Clock* consistently emerged among circadian predictors, while *Phox2b* and *Ntrk2* stood out among NB-specific ones. However, the precise mechanistic roles of these genes remain unclear, and their predictive value should be validated in larger panels and, ultimately, in patient-derived and *in vivo* models.<sup>43</sup> If confirmed, this approach could enable the determination of a neuroblastoma tumor's circadian clock status from a simple snapshot of gene expression, using either circadian clock genes or neuroblastoma-specific markers. Ultimately, this would have significant implications for patient stratification and the assessment of the benefit from chronotherapeutic strategies.

Finally, given the well-established impact of circadian rhythms in cellular metabolism,<sup>44</sup> proliferation,<sup>45</sup> and drug responsiveness,<sup>46–48</sup> we explored the link between circadian gene expression and drug sensitivity in NB cell lines. Previous work showed that activating the core clock component ROR $\alpha$  enhances *Bmal1* expression and increases chemotherapy sensitivity in NB cells.<sup>42</sup> In line with this, our analysis identified several significant correlations between circadian regulators and drug sensitivity (Figure 4A). Notably, topotecan exhibited robust associations across sensitivity metrics, suggesting a circadian-dependent mechanism which is consistent with our earlier findings in breast cancer cell models.<sup>13</sup> Among targeted agents, ALK inhibitors (PF2341066 and TAE684) showed significant associations with circadian genes, highlighting their promise for chronotherapeutic application in neuroblastoma. Furthermore, 17-AAG displayed opposing correlations with *Cry2* and *Clock*, aligning with prior reports of its circadian timing-dependent efficacy<sup>46</sup> and indicating phase-specific relationships within the circadian feedback loop. To validate these findings, future studies should extend drug testing to additional NB models using dynamic assays (e.g., growth rate inhibition with live imaging<sup>49</sup>) and in more complex cancer models such as patient-derived organoids and mouse models. It will also be important to assess whether clinical features (e.g., patient age) or mutation status (e.g., ALK) modulate circadian-drug sensitivity, as our limited dataset suggests that genotype alone does not fully explain the observed variability.

To move beyond correlative evidence, we tested whether circadian competence translates into functional differences in drug response through time-of-day sensitivity assays. Our experiments demonstrate that circadian-competent neuroblastoma models exhibit pronounced temporal variation in drug sensitivity to the ALK inhibitor lorlatinib, the DNA crosslinker cisplatin, and the DNA synthesis inhibitor doxorubicin, while weakly rhythmic lines showed minimal ToD-dependent responses to these drugs. Notably, the relationship between circadian strength and chronotherapeutic potential does not seem to be strictly linear, since the intermediate circadian line SKNBE(2) ranked higher in overall ToD sensitivity than the strongly rhythmic SKNSH (Figure 4G). This suggests that factors beyond circadian component strength influence temporal drug responses, a complexity likely reflecting the interplay of multiple cellular characteristics, including overall drug sensitivity and growth dynamics, which we have previously shown to modulate chronotherapeutic potential in breast cancer models.<sup>22,50</sup> Interestingly, lorlatinib emerged as the most promising chronotherapeutic candidate, which is consistent with our previously identified correlations between circadian gene expression and sensitivity to ALK inhibitors such as PF2341066 (Figure 4A). Taken together, the evidence from both the correlation analyses and the functional experiments highlights the potential of using circadian timing to improve ALK inhibitor therapy in neuroblastoma. Here, validation in patient-derived organoids and *in vivo* models will be essential to better recapitulate tumor temporal dynamics and establish clinically relevant treatment schedules.

While our functional assays demonstrate that circadian heterogeneity is linked to growth dynamics and shapes time-of-day drug sensitivity, further mechanistic studies remain an important future direction. Dissecting how specific circadian gene expression programs translate into rhythmic outputs at the protein and pathway level and clarifying how individual circadian regulators modulate drug responses will be critical to fully understand circadian vulnerabilities in neuroblastoma. Such analyses will likely require single-cell reporter approaches, proteomic profiling of core clock proteins, and expanded time-resolved drug testing in patient-derived models.

In summary, we mapped circadian heterogeneity across neuroblastoma models and showed its relevance for both proliferation and drug response. By linking clock properties to gene expression and drug sensitivity and showing distinct time-of-day drug response dynamics, we establish a framework that underscores the importance of circadian regulation in neuroblastoma. Incorporating circadian profiling into neuroblastoma therapy may enhance efficacy while reducing toxicity,<sup>33</sup> opening new avenues to improve outcomes in this high-risk disease.

#### Limitations of the study

Our analyses are based on established neuroblastoma cell lines. While these models enable systematic and controlled profiling, they lack important physiological cues present *in vivo* that can influence circadian regulation. This limits the direct clinical relevance of associations between our circadian phenotypes and patient characteristics. While our functional assays demonstrate clear links between circadian competence and time-of-day dependent drug sensitivity, they do not fully resolve the

underlying molecular mechanisms which should be addressed in future mechanistic studies. Arrhythmic phenotypes remain incompletely explained and would benefit from complementary approaches such as single-cell recordings or proteomic profiling of core clock proteins to capture intercellular dynamics and post-translational regulation. Finally, using more complex tumor models will be essential to confirm the translational relevance of our findings and to establish how circadian heterogeneity influences neuroblastoma growth and treatment response in more physiological settings.

## RESOURCE AVAILABILITY

### Lead contact

Further information and requests should be directed to the lead contact, Adrián E. Granada ([adrian@granadalab.org](mailto:adrian@granadalab.org)).

### Materials availability

This study did not generate new unique reagents.

### Data and code availability

- Experimental data have been deposited at Figshare and are publicly available as of the date of publication. Accession numbers are listed in the [key resources table](#).
- All original code has been deposited at GitHub and is publicly available at <https://doi.org/10.5281/zenodo.18032430> as of the date of publication.
- Any additional information required to reanalyze the data reported in this paper is available from the [lead contact](#) upon request.

## ACKNOWLEDGMENTS

We are thankful to Annika Winkler for assistance with sample preparation as well as to Anna-Marie Finger and Astrid Grudziecki for guidance in the bioluminescence recordings. This work is part of a project backed by the German Federal Ministry of Education and Research (BMBF) through the e:Med Juniorverbund DeepLTNBC TP3-01ZX1917C. C.S. received support from the DFG-SCHM 3362/4-1 project number 511886499. J.D. acknowledges support by the Luxembourg National Research Fund (FNR) under the PRIDE program (PRIDE17/12252781).

## AUTHOR CONTRIBUTIONS

C.E., C.S., and A.E.G. conceived and planned the study. C.E. performed the experiments. C.E., C.S., J.D., and S.D.L. analyzed the data. A.K. provided resources for the bioluminescence recordings. C.E. wrote the manuscript. A.E.G. acquired funding, supervised the study, and edited the manuscript. All authors contributed to the interpretation of the results, provided critical feedback, and helped shape the research and manuscript.

## DECLARATION OF INTERESTS

The authors declare no competing interests.

## STAR★METHODS

Detailed methods are provided in the online version of this paper and include the following:

- [KEY RESOURCES TABLE](#)
- [EXPERIMENTAL MODEL AND STUDY PARTICIPANT DETAILS](#)
  - Cell culture
  - Influence of sex and gender
  - Cell line authentication
- [METHOD DETAILS](#)

- Generation of luciferase reporter cell lines
- Circadian bioluminescence recordings
- Long-term live cell imaging
- Time-of-day drug treatments
- Experimental design
- [QUANTIFICATION AND STATISTICAL ANALYSIS](#)
  - Profiling of circadian signals
  - Principal component analysis-based cluster analysis
  - Expression analysis of circadian genes
  - Linear discriminant analysis
  - Correlation analysis and pairwise linear regression
  - Growth dynamics analysis
  - Parametrization of time-of-day drug response curves

## SUPPLEMENTAL INFORMATION

Supplemental information can be found online at <https://doi.org/10.1016/j.celrep.2026.116975>.

Received: March 19, 2025

Revised: October 15, 2025

Accepted: January 14, 2026

## REFERENCES

1. Rosbash, M. (2009). The Implications of Multiple Circadian Clock Origins. *PLoS Biol.* 7, e1000062. <https://doi.org/10.1371/journal.pbio.1000062>.
2. Nikhil, K.L., Korge, S., and Kramer, A. (2020). Heritable gene expression variability and stochasticity govern clonal heterogeneity in circadian period. *PLoS Biol.* 18, e3000792. <https://doi.org/10.1371/journal.pbio.3000792>.
3. Chaix, A., Zarrinpar, A., and Panda, S. (2016). The circadian coordination of cell biology. *J. Cell Biol.* 215, 15–25. <https://doi.org/10.1083/jcb.201603076>.
4. Golombek, D.A., Bussi, I.L., and Agostino, P.V. (2014). Minutes, days and years: molecular interactions among different scales of biological timing. *Philos. Trans. R. Soc. Lond. B Biol. Sci.* 369, 20120465. <https://doi.org/10.1098/rstb.2012.0465>.
5. Takahashi, J.S. (2017). Transcriptional architecture of the mammalian circadian clock. *Nat. Rev. Genet.* 18, 164–179. <https://doi.org/10.1038/nrg.2016.150>.
6. Akman, O.E., Rand, D.A., Brown, P.E., and Millar, A.J. (2010). Robustness from flexibility in the fungal circadian clock. *BMC Syst. Biol.* 4, 88. <https://doi.org/10.1186/1752-0509-4-88>.
7. Zhang, R., Lahens, N.F., Ballance, H.I., Hughes, M.E., and Hogenesch, J.B. (2014). A circadian gene expression atlas in mammals: implications for biology and medicine. *Proc. Natl. Acad. Sci. USA* 111, 16219–16224. <https://doi.org/10.1073/pnas.1408886111>.
8. Chakrabarti, S., and Michor, F. (2020). Circadian clock effects on cellular proliferation: Insights from theory and experiments. *Curr. Opin. Cell Biol.* 67, 17–26. <https://doi.org/10.1016/j.celb.2020.07.003>.
9. Neufeld-Cohen, A., Robles, M.S., Aviram, R., Manella, G., Adamovich, Y., Ladeux, B., Nir, D., Rousso-Noori, L., Kuperman, Y., Golik, M., et al. (2016). Circadian control of oscillations in mitochondrial rate-limiting enzymes and nutrient utilization by PERIOD proteins. *Proc. Natl. Acad. Sci. USA* 113, E1673–E1682. <https://doi.org/10.1073/pnas.1519650113>.
10. Sancar, A., Lindsey-Boltz, L.A., Kang, T.H., Reardon, J.T., Lee, J.H., and Ozturk, N. (2010). Circadian clock control of the cellular response to DNA damage. *FEBS Lett.* 584, 2618–2625. <https://doi.org/10.1016/j.febslet.2010.03.017>.
11. Roenneberg, T., and Merrow, M. (2016). The Circadian Clock and Human Health. *Curr. Biol.* 26, R432–R443. <https://doi.org/10.1016/j.cub.2016.04.011>.

12. Fortin, B.M., Mahieu, A.L., Fellows, R.C., Kang, Y., Lewis, A.N., Ead, A.S., Lamia, K.A., Cao, Y., Pannunzio, N.R., and Masri, S. (2025). The diverse roles of the circadian clock in cancer. *Nat. Cancer* 6, 753–767. <https://doi.org/10.1038/s43018-025-00981-8>.
13. Ector, C., Didier, J., De Landtsheer, S., Nordentoft, M.S., Schmal, C., Keilholz, U., Herzel, H., Kramer, A., Sauter, T., and Granada, A.E. (2025). Circadian clock features define novel subtypes among breast cancer cells and shape drug sensitivity. *Mol. Syst. Biol.* 21, 315–340. <https://doi.org/10.1038/s44320-025-00092-7>.
14. Lellupitiyage Don, S.S., Lin, H.H., Furtado, J.J., Qraitem, M., Taylor, S.R., and Farkas, M.E. (2019). Circadian oscillations persist in low malignancy breast cancer cells. *Cell Cycle* 18, 2447–2453. <https://doi.org/10.1080/15384101.2019.1648957>.
15. Maier, B., Wendt, S., Vanselow, J.T., Wallach, T., Reischl, S., Oehmke, S., Schlosser, A., and Kramer, A. (2009). A large-scale functional RNAi screen reveals a role for CK2 in the mammalian circadian clock. *Genes Dev.* 23, 708–718. <https://doi.org/10.1101/gad.512209>.
16. Relógio, A., Thomas, P., Medina-Pérez, P., Reischl, S., Bervoets, S., Gloc, E., Riemer, P., Mang-Fatehi, S., Maier, B., Schäfer, R., et al. (2014). Ras-Mediated Deregulation of the Circadian Clock in Cancer. *PLoS Genet.* 10, e1004338. <https://doi.org/10.1371/journal.pgen.1004338>.
17. Qu, M., Zhang, G., Qu, H., Vu, A., Wu, R., Tsukamoto, H., Jia, Z., Huang, W., Lenz, H.-J., Rich, J.N., and Kay, S.A. (2023). Circadian regulator BMAL1::CLOCK promotes cell proliferation in hepatocellular carcinoma by controlling apoptosis and cell cycle. *Proc. Natl. Acad. Sci. USA* 120, e2214829120. <https://doi.org/10.1073/pnas.2214829120>.
18. Mormont, M.-C., and Levi, F. (2003). Cancer chronotherapy: Principles, applications, and perspectives. *Cancer* 97, 155–169. <https://doi.org/10.1002/cncr.11040>.
19. Louis, C.U., and Shohet, J.M. (2015). Neuroblastoma: molecular pathogenesis and therapy. *Annu. Rev. Med.* 66, 49–63. <https://doi.org/10.1146/annurev-med-011514-023121>.
20. Bosse, K.R., and Maris, J.M. (2016). Advances in the translational genomics of neuroblastoma: From improving risk stratification and revealing novel biology to identifying actionable genomic alterations. *Cancer* 122, 20–33. <https://doi.org/10.1002/cncr.29706>.
21. Ackermann, S., Cartolano, M., Hero, B., Welte, A., Kahlert, Y., Roderwieser, A., Bartenhagen, C., Walter, E., Gecht, J., Kerschke, L., et al. (2018). A mechanistic classification of clinical phenotypes in neuroblastoma. *Science* 362, 1165–1170. <https://doi.org/10.1126/science.aat6768>.
22. Ector, C., Schmal, C., Didier, J., De Landtsheer, S., Finger, A.-M., Müller-Marquardt, F., Schulte, J.H., Sauter, T., Keilholz, U., Herzel, H., et al. (2024). Time-of-day effects of cancer drugs revealed by high-throughput deep phenotyping. *Nat. Commun.* 15, 7205. <https://doi.org/10.1038/s41467-024-51611-3>.
23. Yalçın, M., and Relógio, A. (2023). Sex and age-dependent characterization of the circadian clock as a potential biomarker for physical performance: A prospective study protocol. *PLoS One* 18, e0293226. <https://doi.org/10.1371/journal.pone.0293226>.
24. Talamanca, L., Gobet, C., and Naef, F. (2023). Sex-dimorphic and age-dependent organization of 24-hour gene expression rhythms in humans. *Science* 379, 478–483. <https://doi.org/10.1126/science.add0846>.
25. Schmal, C., Mönke, G., and Granada, A.E. (2022). Analysis of Complex Circadian Time Series Data Using Wavelets. In *Circadian Regulation: Methods and Protocols*, G. Solanas and P.S. Welz, eds. (Springer US), pp. 35–54. [https://doi.org/10.1007/978-1-0716-2249-0\\_3](https://doi.org/10.1007/978-1-0716-2249-0_3).
26. Huber, A.L., Papp, S.J., Chan, A.B., Henriksson, E., Jordan, S.D., Kriebbs, A., Nguyen, M., Wallace, M., Li, Z., Metallo, C.M., and Lamia, K.A. (2016). CRY2 and FBXL3 Cooperatively Degrade c-MYC. *Mol. Cell* 64, 774–789. <https://doi.org/10.1016/j.molcel.2016.10.012>.
27. Gutu, N., Nordentoft, M.S., Kuhn, M., Ector, C., Möser, M., Finger, A.-M., Heltberg, M.S., Jensen, M.H., Keilholz, U., Kramer, A., et al. (2025). Circadian coupling orchestrates cell growth. *Nat. Phys.* 21, 768–777. <https://doi.org/10.1038/s41567-025-02838-4>.
28. Barretina, J., Caponigro, G., Stransky, N., Venkatesan, K., Margolin, A.A., Kim, S., Wilson, C.J., Lehár, J., Kryukov, G.V., Sonkin, D., et al. (2012). The Cancer Cell Line Encyclopedia enables predictive modelling of anticancer drug sensitivity. *Nature* 483, 603–607. <https://doi.org/10.1038/nature11003>.
29. Ko, C.H., and Takahashi, J.S. (2006). Molecular components of the mammalian circadian clock. *Hum. Mol. Genet.* 15 Spec No 2, R271–R277. <https://doi.org/10.1093/hmg/ddl207>.
30. Lerone, M., Ognibene, M., Pezzolo, A., Martucciello, G., Zara, F., Morini, M., and Mazzocco, K. (2021). Molecular Genetics in Neuroblastoma Prognosis. *Children* 8, 456. <https://doi.org/10.3390/children8060456>.
31. Niemeyer, C., and Eggert, A. (2017). Pädiatrische Hämatologie und Onkologie, 2 Edition (Springer Berlin). <https://doi.org/10.1007/978-3-662-43686-8>.
32. Sulli, G., Lam, M.T.Y., and Panda, S. (2019). Interplay between Circadian Clock and Cancer: New Frontiers for Cancer Treatment. *Trends Cancer* 5, 475–494. <https://doi.org/10.1016/j.trecan.2019.07.002>.
33. Lévi, F., Okyar, A., Dulong, S., Innominato, P.F., and Clairambault, J. (2010). Circadian Timing in Cancer Treatments. *Annu. Rev. Pharmacol. Toxicol.* 50, 377–421. <https://doi.org/10.1146/annurev.pharmtox.48.113006.094626>.
34. Petkovic, M., Yalçın, M., Heese, O., and Relógio, A. (2023). Differential expression of the circadian clock network correlates with tumour progression in gliomas. *BMC Med. Genomics* 16, 154. <https://doi.org/10.1186/s12920-023-01585-w>.
35. Pacheco-Bernal, I., Becerril-Pérez, F., and Aguilar-Arnal, L. (2019). Circadian rhythms in the three-dimensional genome: implications of chromatin interactions for cyclic transcription. *Clin. Epigenetics* 11, 79. <https://doi.org/10.1186/s13148-019-0677-2>.
36. Finger, A.-M., Jäschke, S., del Olmo, M., Hurwitz, R., Granada, A.E., Herzel, H., and Kramer, A. (2021). Intercellular coupling between peripheral circadian oscillators by TGF- $\beta$  signaling. *Sci. Adv.* 7, eabg5174. <https://doi.org/10.1126/sciadv.abg5174>.
37. Nagoshi, E., Saini, C., Bauer, C., Laroche, T., Naef, F., and Schibler, U. (2004). Circadian gene expression in individual fibroblasts: cell-autonomous and self-sustained oscillators pass time to daughter cells. *Cell* 119, 693–705. <https://doi.org/10.1016/j.cell.2004.11.015>.
38. Gabriel, C.H., del Olmo, M., Zehtabian, A., Jäger, M., Reischl, S., van Dijk, H., Ulbricht, C., Rakhymzhan, A., Korte, T., Koller, B., et al. (2021). Live-cell imaging of circadian clock protein dynamics in CRISPR-generated knock-in cells. *Nat. Commun.* 12, 3796. <https://doi.org/10.1038/s41467-021-24086-9>.
39. Zaaier, S., Groen, S.C., and Sanjana, N.E. (2021). Tracking cell lineages to improve research reproducibility. *Nat. Biotechnol.* 39, 666–670. <https://doi.org/10.1038/s41587-021-00928-1>.
40. Abe, M., Herzog, E.D., Yamazaki, S., Straume, M., Tei, H., Sakaki, Y., Menaker, M., and Block, G.D. (2002). Circadian Rhythms in Isolated Brain Regions. *J. Neurosci.* 22, 350–356. <https://doi.org/10.1523/JNEUROSCI.22-01-00350.2002>.
41. Brancaccio, M., Edwards, M.D., Patton, A.P., Smyllie, N.J., Chesham, J.E., Maywood, E.S., and Hastings, M.H. (2019). Cell-autonomous clock of astrocytes drives circadian behavior in mammals. *Science* 363, 187–192. <https://doi.org/10.1126/science.aat4104>.
42. Moreno-Smith, M., Milazzo, G., Tao, L., Fekry, B., Zhu, B., Mohammad, M.A., Di Giacomo, S., Borkar, R., Reddy, K.R.K., Capasso, M., et al. (2021). Restoration of the molecular clock is tumor suppressive in neuroblastoma. *Nat. Commun.* 12, 4006. <https://doi.org/10.1038/s41467-021-24196-4>.
43. Rosselot, A.E., Park, M., Kim, M., Matsu-Ura, T., Wu, G., Flores, D.E., Subramanian, K.R., Lee, S., Sundaram, N., Broda, T.R., et al. (2022). Ontogeny and function of the circadian clock in intestinal organoids. *EMBO J.* 41, e106973. <https://doi.org/10.15252/emboj.2020106973>.

44. Bass, J., and Takahashi, J.S. (2010). Circadian Integration of Metabolism and Energetics. *Science* 330, 1349–1354. <https://doi.org/10.1126/science.1195027>.
45. Matsuo, T., Yamaguchi, S., Mitsui, S., Emi, A., Shimoda, F., and Okamura, H. (2003). Control mechanism of the circadian clock for timing of cell division in vivo. *Science* 302, 255–259. <https://doi.org/10.1126/science.1086271>.
46. Lee, Y., Fong, S.Y., Shon, J., Zhang, S.L., Brooks, R., Lahens, N.F., Chen, D., Dang, C.V., Field, J.M., and Sehgal, A. (2021). Time-of-day specificity of anticancer drugs may be mediated by circadian regulation of the cell cycle. *Sci. Adv.* 7, eabd2645. <https://doi.org/10.1126/sciadv.abd2645>.
47. Ye, Y., Xiang, Y., Ozguc, F.M., Kim, Y., Liu, C.-J., Park, P.K., Hu, Q., Diao, L., Lou, Y., Lin, C., et al. (2018). The Genomic Landscape and Pharmacogenomic Interactions of Clock Genes in Cancer Chronotherapy. *Cell Syst.* 6, 314–328.e2. <https://doi.org/10.1016/j.cels.2018.01.013>.
48. Dallmann, R., Brown, S.A., and Gachon, F. (2014). Chronopharmacology: New Insights and Therapeutic Implications. *Annu. Rev. Pharmacol. Toxicol.* 54, 339–361. <https://doi.org/10.1146/annurev-pharmtox-011613-135923>.
49. Hafner, M., Niepel, M., Chung, M., and Sorger, P.K. (2016). Growth rate inhibition metrics correct for confounders in measuring sensitivity to cancer drugs. *Nat. Methods* 13, 521–527. <https://doi.org/10.1038/nmeth.3853>.
50. Gutu, N., Ishikuma, H., Ector, C., Keilholz, U., Herzel, H., and Granada, A.E. (2025). A combined mathematical and experimental approach reveals the drivers of time-of-day drug sensitivity in human cells. *Commun. Biol.* 8, 491. <https://doi.org/10.1038/s42003-025-07931-1>.
51. Balsalobre, A., Brown, S.A., Marcacci, L., Tronche, F., Kellendonk, C., Reichardt, H.M., Schütz, G., and Schibler, U. (2000). Resetting of Circadian Time in Peripheral Tissues by Glucocorticoid Signaling. *Science* 289, 2344–2347. <https://doi.org/10.1126/science.289.5488.2344>.
52. Berlak, M., Tucker, E., Dorel, M., Winkler, A., McGearey, A., Rodriguez-Fos, E., da Costa, B.M., Barker, K., Fyle, E., Calton, E., et al. (2022). Mutations in ALK signaling pathways conferring resistance to ALK inhibitor treatment lead to collateral vulnerabilities in neuroblastoma cells. *Mol. Cancer* 21, 126. <https://doi.org/10.1186/s12943-022-01583-z>.
53. Xu, Z., Sun, Y., Wang, D., Sun, H., and Liu, X. (2020). SNHG16 promotes tumorigenesis and cisplatin resistance by regulating miR-338-3p/PLK4 pathway in neuroblastoma cells. *Cancer Cell Int.* 20, 236. <https://doi.org/10.1186/s12935-020-01291-y>.
54. Lautz, T.B., Jie, C., Clark, S., Naiditch, J.A., Jafari, N., Qiu, Y.-Y., Zheng, X., Chu, F., and Madonna, M.B. (2012). The Effect of Vorinostat on the Development of Resistance to Doxorubicin in Neuroblastoma. *PLoS One* 7, e40816. <https://doi.org/10.1371/journal.pone.0040816>.
55. Mönke, G., Sorgenfrei, F.A., Schmal, C., and Granada, A.E. (2020). Optimal time frequency analysis for biological data - pyBOAT. Preprint at bioRxiv. <https://doi.org/10.1101/2020.04.29.067744>.
56. Leise, T.L., and Harrington, M.E. (2011). Wavelet-based time series analysis of circadian rhythms. *J. Biol. Rhythms* 26, 454–463. <https://doi.org/10.1177/0748730411416330>.
57. Myung, J., Schmal, C., Hong, S., Tsukizawa, Y., Rose, P., Zhang, Y., Holtzman, M.J., De Schutter, E., Herzel, H., Bordyugov, G., and Takumi, T. (2018). The choroid plexus is an important circadian clock component. *Nat. Commun.* 9, 1062. <https://doi.org/10.1038/s41467-018-03507-2>.
58. Westermark, P.O., Welsh, D.K., Okamura, H., and Herzel, H. (2009). Quantification of Circadian Rhythms in Single Cells. *PLoS Comput. Biol.* 5, e1000580. <https://doi.org/10.1371/journal.pcbi.1000580>.
59. Schmal, C., Herzog, E.D., and Herzel, H. (2018). Measuring Relative Coupling Strength in Circadian Systems. *J. Biol. Rhythms* 33, 84–98. <https://doi.org/10.1177/0748730417740467>.

STAR★METHODS

KEY RESOURCES TABLE

| REAGENT or RESOURCE  | SOURCE   | IDENTIFIER  |
|--|--|---|
| <b>Bacterial and virus strains</b>   |  |   |
| Lentivirus for transduction  | This paper. From HEK293T cells using pAB-mBmal1:Luc-Puro or plenti6-mPer2:Luc-Blas together with psPAX2 and pMD2G (see section “Recombinant DNA”). | –   |
| <b>Chemicals, peptides, and recombinant proteins</b>   |  |   |
| RPMI-1640 medium   | Gibco  | Cat #21875091   |
| Fetal Bovine Serum (FBS)   | Gibco  | Cat #10270106   |
| Penicillin-Streptomycin (Pen-Strep)  | Gibco  | Cat #15140122   |
| FluoroBrite DMEM medium (phenol red free)  | Gibco  | Cat #A1896701   |
| L-Glutamine (200 mM)   | Gibco  | Cat #25030-024  |
| HEPES (1 M)  | Gibco  | Cat #15630056   |
| Lipofectamine 3000   | Invitrogen   | Cat #L3000001   |
| Protamine sulfate (10 G)   | Sigma  | Cat #P3369  |
| PBS pH 7.4   | Gibco  | Cat #10010056   |
| Blasticidin S HCl  | Adooq  | Cat #A14212   |
| Puromycin  | Gibco  | Cat #A1113803   |
| Dexamethasone  | Sigma  | Cat #D4902  |
| D-Luciferin  | Abmole   | Cat #M9053  |
| Lorlatinib   | Sigma  | Cat #PZ0039   |
| Cisplatin  | Sigma  | Cat #232120   |
| Doxorubicin  | Hözlzel  | Cat #A14403-100   |
| Dimethyl sulfoxide (DMSO)  | Sigma  | Cat #D8418  |
| <b>Deposited data</b>  |  |   |
| Circadian luciferase data  | This paper   | Figshare: <a href="https://doi.org/10.6084/m9.figshare.30815522">https://doi.org/10.6084/m9.figshare.30815522</a> |
| Growth and time-of-day-dependent drug response data  | This paper   | Figshare: <a href="https://doi.org/10.6084/m9.figshare.30815537">https://doi.org/10.6084/m9.figshare.30815537</a> |
| Drug sensitivity data  | Cancer Cell Line Encyclopedia (CCLE), 2022-Q2  | CCLE: <a href="https://sites.broadinstitute.org/ccle/datasets">https://sites.broadinstitute.org/ccle/datasets</a> |
| Gene expression data   | Cancer Cell Line Encyclopedia (CCLE), 2022-Q2  | CCLE: <a href="https://sites.broadinstitute.org/ccle/datasets">https://sites.broadinstitute.org/ccle/datasets</a> |
| <b>Experimental models: Cell lines</b>   |  |   |
| Neuroblastoma cell lines (CHP212, CLBGA, GIMEN, IMR5, KELLY, LAN5, NGP, SH-SY5Y, SKNAS, SKNBE(1), SKNBE(2), SKNSH) | Johannes Schulte, Universitätsklinikum Tübingen, Clinic for Pediatrics and Adolescent Medicine, Germany  | N/A   |
| HEK293T  | Galit Lahav, Harvard Medical School, Department of Systems Biology, USA  | N/A   |
| Bmal1-Luc reporter cell lines  | This paper   | N/A   |
| Per2-Luc reporter cell lines   | This paper   | N/A   |
| <b>Recombinant DNA</b>   |  |   |
| pAB-mBmal1:Luc-Puro  | Achim Kramer, Laboratory of Chronobiology, Charité – Universitätsmedizin Berlin, Germany   | N/A   |

(Continued on next page)

**Continued**

| REAGENT or RESOURCE                 | SOURCE   | IDENTIFIER  |
|-------------------------------------|--|---|
| plenti6-mPer2:Luc-Bias              | Achim Kramer, Laboratory of Chronobiology, Charité – Universitätsmedizin Berlin, Germany | N/A   |
| psPAX2                              | Addgene  | ID 12260  |
| pMD2G                               | Addgene  | ID 12259  |
| <b>Software and algorithms</b>      |  |   |
| Analysis pipelines                  | This paper   | <a href="https://doi.org/10.5281/zenodo.18032430">https://doi.org/10.5281/zenodo.18032430</a>           |
| Python v3.9.7                       | N/A  | N/A   |
| Python Spyder v5.4.5                | N/A  | N/A   |
| pyBOAT (Python package)             | Mönke et al. <sup>51</sup>   | <a href="https://github.com/tensionhead/pyBOAT">https://github.com/tensionhead/pyBOAT</a>               |
| pywt                                | Lee et al. <sup>52</sup>   | <a href="https://github.com/PyWavelets/pywt">https://github.com/PyWavelets/pywt</a>                     |
| seaborn v0.13.2                     | Waskom et al. <sup>53</sup>  | N/A   |
| statsmodels v0.13.2                 | Seabold et al. <sup>54</sup>   | <a href="https://github.com/statsmodels/statsmodels">https://github.com/statsmodels/statsmodels</a>     |
| SciPy v1.13.1                       | Virtanen et al. <sup>55</sup>  | <a href="https://github.com/scipy/scipy">https://github.com/scipy/scipy</a>                             |
| Scikit-Learn v1.1.1                 | Pedregosa et al. <sup>56</sup>   | <a href="https://github.com/scikit-learn/scikit-learn">https://github.com/scikit-learn/scikit-learn</a> |
| PyCharm Community Edition v2021.2.2 | N/A  | N/A   |
| Incucyte software                   | Essen BioScience   | N/A   |
| MATLAB v2024b                       | N/A  | N/A   |
| Anaconda Navigator v2.5.0           | N/A  | N/A   |
| <b>Other</b>                        |  |   |
| LumiCycle luminometer               | Actimetrics  | N/A   |
| Incucyte SX5                        | Essen BioScience   | N/A   |

**EXPERIMENTAL MODEL AND STUDY PARTICIPANT DETAILS**

**Cell culture**

All neuroblastoma cell lines (CHP212, CLBGA, GIMEN, IMR5, KELLY, LAN5, NGP, SH-SY5Y, SKNAS, SKNBE(1), SKNBE(2), SKNSH) were kindly provided by the Schulte lab (Universitätsklinikum Tübingen, Clinic for Pediatrics and Adolescent Medicine, Germany). Clinical characteristics of the patients from whom each cell line was derived were as follows [CELL LINE: age (years) | gender (Male/Female)]: CHP212: 1.8y |M; CLBGA: 4y |M; GIMEN: 3.5y |F; IMR5: 1.1y |M; KELLY: 1y |F; LAN5: 0.4y |M; NGP: 2.6y |M; SH-SY5Y: 4y |F; SKNAS: 8y |F; SKNBE(1): 1.7y |M; SKNBE(2): 2.2y |M; SKNSH: 4y |F. Patient ages at sample collection ranged from 0.4 to 8 years (median 2.4 years). Five cell lines were derived from female patients and seven from male patients. The cell lines exhibited diverse genetic backgrounds including MYCN amplification status (amplified  $n = 9$ , normal  $n = 3$ ) and various mutations in ALK, TP53, PHOX2B and ATRX genes. All clinical information can be derived from Table S1. All twelve cell lines were included in the circadian rhythm profiling experiments and no experimental groups were allocated.

Cells were cultured in RPMI-1640 medium (Gibco) supplemented with 10% fetal bovine serum (FBS, Gibco) and 1% penicillin-streptomycin (Pen-Strep, Gibco). For bioluminescence measurements, the medium was switched to a phenol red-free FluoroBrite DMEM medium (Gibco), supplemented with 10% FBS, 300 mg/L L-glutamine (Gibco) and 1% Pen-Strep. Cell cultures were maintained at 37°C with 5% CO<sub>2</sub>.

**Influence of sex and gender**

Circadian rhythms exhibit sex- and age-dependent variation in humans. Biological sex influences circadian clock function through hormonal regulation and sex-specific gene expression patterns.<sup>23,24</sup> Age-related changes in circadian regulation have also been documented,<sup>24</sup> however, the retention of such associations in long-established cancer cell lines cultured *in vitro* remains uncertain, as these models lack the hormonal and microenvironmental contexts present *in vivo*.

**Cell line authentication**

All cell lines were routinely tested for mycoplasma contamination by PCR and tested negative. The cell lines have not been explicitly authenticated, i.e., by short tandem repeat profiling, by the authors.

## METHOD DETAILS

### Generation of luciferase reporter cell lines

HEK293T cells (kindly provided by the Lahav lab, Harvard Medical School, Department of Systems Biology, USA) at approximately 80% confluency were maintained in RPMI-1640 medium supplemented with 10 mM HEPES and transfected using a mixture that included 8.4  $\mu\text{g}$  of a lentiviral expression plasmid (either pAB-mBmal1:Luc-Puro or plenti6-mPer2:Luc-Blas), 6  $\mu\text{g}$  of psPAX2 (Addgene #12260) and 3.6  $\mu\text{g}$  of pMD2G (Addgene #12259) to generate lentivirus encoding circadian luciferase reporters. Transfection was conducted with Lipofectamine 3000 (Invitrogen) following the manufacturer's protocol. Viral particles were collected and filtered through 0.45  $\mu\text{m}$  Millipore filters at both 48- and 72-h post-transfection. For the transduction process, target cells at around 70% confluency were exposed for 6 h to a mixture containing 1 mL of the lentivirus-containing supernatant, 8  $\mu\text{g}/\text{mL}$  protamine sulfate (Sigma) and 10  $\mu\text{M}$  HEPES (Gibco). After incubation, cells were washed with PBS (Gibco) and maintained in their standard culture medium. Two days later, antibiotic selection was initiated by adding either 5  $\mu\text{g}/\text{mL}$  blasticidin (Adooq) or 2  $\mu\text{g}/\text{mL}$  puromycin (Gibco), according to the resistance marker encoded in the lentiviral vector.

### Circadian bioluminescence recordings

*Bmal1* or *Per2* luciferase reporter cell lines were seeded into 35-mm dishes (Nunc) so that they reached confluence by the following day. To synchronize the circadian rhythms across individual cells, a 1  $\mu\text{M}$  dose of dexamethasone<sup>36,51</sup> (Sigma, prepared in EtOH) was applied. After a 30-min incubation, the cells were rinsed once with PBS and imaging medium containing 250  $\mu\text{M}$  D-Luciferin (Abmole) was added. The dishes were then sealed with parafilm to prevent evaporation during the bioluminescence recording period. Measurements were taken every 10 min for up to 6 days using an incubator-embedded luminometer (LumiCycle, Actimetrics).

### Long-term live cell imaging

Live-cell imaging experiments were performed using cells expressing the *Bmal1*-Luc reporter where available. Cells were seeded in 48-well plates (Falcon) at densities reaching confluence by experiment termination. One day post cell seeding, long-term imaging was conducted using an Incucyte live-cell widefield microscope (Essen BioScience) with environmental control. Brightfield images were acquired at 10 $\times$  magnification from 9 fields per well at 2-h intervals over 5 days. Confluency detection was performed using integrated Incucyte software, with subsequent data analysis in Python.

### Time-of-day drug treatments

Cells were seeded at densities reaching confluence by experiment termination and allowed to adhere overnight. The following day, live recordings were initiated as described above. To generate distinct circadian populations, independent resetting steps were performed every 4 h over an 8-h window, yielding cohorts at 0, 4 and 8 h circadian time. Each group was subsequently treated with the same drug concentration, corresponding to the approximate half-maximal effective concentration ( $\text{EC}_{50}$ ) to appreciate response differences, either 32 or 48 h after the initial reset and cell growth was monitored for 4 days to determine sensitivity. This setup enabled simultaneous assessment of six circadian stages (0, 4, 8, 16, 20 and 24 h). Drug concentrations were selected based on literature values and partially adjusted in the second experiment to reduce toxicity. In the first experiment, lorlatinib (Sigma) was applied at 50 nM,<sup>52</sup> cisplatin (Sigma) at 1.5  $\mu\text{M}$ <sup>53</sup> and doxorubicin (Hözel) at 20 nM.<sup>54</sup> In the second experiment, lorlatinib was increased to 100 nM for GIMEN, SKNBE(2) and CHP212, while SH-SY5Y and CHP212 were treated with 1  $\mu\text{M}$  cisplatin and 10 nM doxorubicin. All drugs were administered in 0.18% DMSO (Gibco) as solvent.

### Experimental design

Unless stated otherwise all experiments were performed using 2–3 biological replicates with 2–3 technical replicates per condition. Exact numbers of biological and technical replicates and total sample sizes for each cell line and reporter are specified in the corresponding figure legends. Sample sizes were based on prior circadian bioluminescence studies demonstrating adequate power to detect rhythm changes in e.g., phase shifts and amplitude changes and practical constraints including experimental throughput. Data acquisition and analysis were not performed blinded due to the nature of the experimental setup and predefined reporter and treatment conditions. For time-of-day treatment assays, randomization was not applied as treatment groups were defined by fixed circadian time points and cell line identity.

## QUANTIFICATION AND STATISTICAL ANALYSIS

### Profiling of circadian signals

#### Data pre-processing

Each individual time series was trimmed to a length of 136 h and 10 min (i.e., approx. 5.67 days) so that all recordings were of equal size for a better quantitative comparability. Due to strong non-linear baseline-expression trends the trimmed time series were subsequently detrended by a sinc-filter with cutoff period  $T_c = 48$  h using the *sinc\_smooth* function of the Python package *pyBOAT* as previously described.<sup>25,55</sup> Due to a strong startle response at the beginning of the recordings, the first 5 h of the recordings are neglected throughout the whole time series analysis.

### Multiresolution analysis

A discrete wavelet transform based multiresolution analysis (MRA) was applied to determine the circadian rhythmicity of the detrended time series as previously described.<sup>56,57</sup> Here, the original signal is decomposed into its contributions at different period bands, termed details. The sum of all details equals the original signal. By this means, the MRA partitions the variance of the signal along the difference details, i.e., period bands. Thus, the portion of the variance corresponding to the part of the signal within the circadian range can be quantified and has been used as a measure of circadian rhythmicity.<sup>56,57</sup> We implemented the MRA using a Daubechies 20 wavelet (*db20*) of the Python *pywt* library and deconstructed the original signal into 7 details. To obtain a detail with a proper circadian period range between [16h, 32h], detrended time series have been down sampled from  $dt = 10$  to  $dt = 30$  min.

### Nonlinear least square fitting

To determine the damping coefficients together with the period, initial amplitude and noise strength of the oscillations, we fitted a stochastic linearly damped oscillator to the individual time-detrended time series using an autocorrelation approach as described previously.<sup>58,59</sup> In a nutshell, the autocorrelation function of a stochastic linearly damped oscillator can be determined analytically and this analytically obtained function is fitted to the autocorrelation of the experimentally obtained time series.<sup>59</sup> The autocorrelation of the experimental time series is obtained via the *acovf* function of the *statsmodels* Python library. The non-linear least squares fit of autocorrelation function of the stochastic linearly damped oscillator model to the experimentally obtained autocorrelation has been done by means of the *curve\_fit* function of the Scientific Python (*Scipy*) module. Only traces classified as *circadian* or *mixed* in the preceding multiresolution analysis were included. To ensure circadian relevance, time series with fitted periods  $>36$  h were excluded.

### Continuous wavelet transform

To determine non-stationary properties of the experimental time series, we applied a continuous wavelet transform (CWT) as implemented within the *pyBOAT* Python package.<sup>25,55</sup> Periods, phases and amplitudes are evaluated along the connected line of points of maximal power, termed *ridge*. For ridge detection, a threshold of 20 (arbitrary units of the CWT power spectrum) was applied to filter out low-amplitude fluctuations and ensure that only robust oscillatory components are considered.<sup>55</sup> Periods and phases were extracted by analyzing the amplitude-normalized signal within the continuous wavelet transform (CWT) power spectrum, while amplitudes and ridge lengths were evaluated from amplitude-unnormalized signals. Only traces classified as *circadian* or *mixed* in the preceding multiresolution analysis were analyzed.

### Principal component analysis-based cluster analysis

A principal component analysis (PCA)-based dimensionality reduction was done via the *Scikit-Learn* class *PCA*. Values of the first two principal components were used to group the data into four clusters using the k-means algorithm, implemented via the *Scikit-Learn* class *KMeans*. Based on this classification, we selected only the samples within the mixed or circadian clusters for further analysis, even when samples of the same cell line fell into different clusters, e.g., mixed and infradian.

### Expression analysis of circadian genes

Gene expression data of core circadian clock genes were retrieved from the CCLE (DepMap 2022-Q2): <https://sites.broadinstitute.org/ccle/datasets>. Cell models were clustered according to their expression levels of core circadian clock genes using the *clustermap* function from the *seaborn* Python library, applying *Euclidean distance* and *complete linkage* for clustering.

### Linear discriminant analysis

Linear discriminant analysis was performed on the min-max scaled gene expression of 16 circadian clock genes and 11 NB-related genes, reducing the data complexity to a single dimension. The continuous target drug sensitivity vectors for this supervised approach were binarized in respect to their median sensitivities. The *LinearDiscriminantAnalysis* class from the *scikit-learn* Python library was used with default tolerance parameter of 0.0001. Beyond the full sets of 16 circadian and 11 NB-related genes, LDA was applied to multiple gene subsets and evaluated using the log10-transformed ratio of between-to within-cluster-distances (BCD/WCD). The robustness of each model was further assessed by leave-one-out cross-validation (LOOCV), implemented with the *model\_selection* module of *scikit-learn* (Python v3.9.7) in PyCharm Community Edition (v2021.2.2).

### Correlation analysis and pairwise linear regression

Spearman's rank correlation was used to assess the relationship between circadian gene expression and the drug sensitivity parameters ActArea, IC<sub>50</sub> and EC<sub>50</sub>. The correlations were clustered using the *clustermap* function from the *seaborn* Python library, applying *Euclidean distance* and *complete linkage* for clustering. Statistical significance of correlations was determined using a two-sided *t* test with no adjustments made for multiple comparisons in the initial analysis. Significance levels are indicated by asterisks: \* *p*-value = 0.037, \*\*\* *p*-value =  $1.4 \times 10^{-24}$ . To control for multiple comparisons, the Bonferroni correction method was applied, leaving four significant correlations with  $Bf_{adj,p} = 1.6 \times 10^{-4}$ . Pairwise linear regression was performed to visualize significant correlations between single gene expression and drug sensitivity using the *lplot* and *regplot* functions from the *seaborn* Python library with a confidence interval of 95%.

### Growth dynamics analysis

One day after seeding, cell proliferation was monitored by long-term live-cell imaging of confluency as described above. Raw confluency trajectories were averaged across 9 images per well, smoothed with a Savitzky-Golay filter (window = 5 frames, polynomial order = 2), normalized to the initial timepoint, and truncated to 92 h. These processed growth curves were fitted with a logistic growth function:

$$\text{Growth}(t) = \frac{L}{1 + e^{-k(t-t_0)}} \quad (\text{Equation 1})$$

where  $L$  is the carrying capacity,  $k$  is the growth rate constant, and  $t_0$  is the inflection point. Non-linear least squares optimization (`curve_fit`, SciPy v1.7.1) was used to extract growth parameters. For correlation analyses, growth rates were systematically compared with circadian parameters obtained from MRA, CWT and ACoF. Pearson correlation coefficients were computed and significant associations were visualized using linear regression fits. Two cell lines were excluded from growth dynamics analysis: LAN5 due to compromised cell viability post-thaw and KELLY due to poor plate adherence that resulted in an insufficient cell density for reliable growth quantification.

### Parametrization of time-of-day drug response curves

Drug response data from the time-of-day treatment experiments were averaged across nine images per well. The final confluency, measured four days after treatment (“final response”), was normalized to the confluency at the respective treatment timepoint. Time-of-day response curves (ToD-RCs) were generated by averaging the final responses of each treatment timepoint across two independent experiments (Figure 4), normalizing them to the 0 h response and interpolating the resulting values using piecewise cubic hermite interpolation (PCHIP). In Figure S6C, ToD-RCs are shown separately for each experiment to illustrate reproducibility. To quantify temporal modulation, the maximum ToD response range ( $ToD_{MR}$ ) was calculated as the difference between the highest and lowest relative responses across circadian timepoints. To quantify inter-experimental variability for each cell line, the coefficient of variation (*coeff. var.*) was calculated at each timepoint across both experiments, then aggregated by drug and subsequently by cell model.

## **Appendix A5: Systems Biology**

Review title: **Challenges and opportunities in systems biology education**

Contributions: Study line program collection

Interpretation of results

Manuscript writing and revision

Table 1; S1

DOI link: <https://doi.org/10.1530/ERC-25-0024>

Published in: Endocrine-Related Cancer

## REVIEW

# Challenges and opportunities in systems biology education

Jeff Didier<sup>1,2</sup>, Sophia Croce<sup>1</sup>, Salma Bayoumi<sup>1</sup>, Elena Valceschini<sup>1,2</sup>, Hugues Escoffier<sup>1</sup>, Evelyn Gonzalez<sup>1,2</sup>, Ali Kishk<sup>1</sup>, Apurva Badkas<sup>1</sup>, Sébastien De Landtsheer<sup>1</sup> and Thomas Sauter<sup>1</sup>

<sup>1</sup>Department of Life Sciences and Medicine, University of Luxembourg, Belvaux, Luxembourg

<sup>2</sup>Regional Student Group Luxembourg a.s.b.l., Student Council, International Society for Computational Biology, Esch-sur-Alzette, Luxembourg

Correspondence should be addressed to T Sauter: [thomas.sauter@uni.lu](mailto:thomas.sauter@uni.lu)

This paper forms part of the themed collection Systems Biology Approaches in Hormone Dependent Cancer Research. The Guest Editors were Moray Campbell and Robert Clarke.

## Abstract

Systems biology requires combining deep understanding in biology with technological methods and computational approaches to acquire new insights. Accordingly, students need to gain knowledge in very different disciplines and their integration to succeed in this truly interdisciplinary field. This review summarizes a variety of study lines at the master's level and uses student and alumni feedback to highlight the main challenges and useful teaching approaches. Education in systems biology needs to be carefully designed to deliver deep knowledge in core aspects while still giving a broad overview of others. Teachers will need to find a good balance here. Integrated experimental and computational courses, as well as active learning approaches, can be key components of successful curricula. Training native systems biologists needs commitment by teachers and institutions and should start as early as possible.

Keywords: systems biology; higher education; master studies; alumni

## Introduction

Systems biology is a growing field of biological and biomedical research, driven by advancements in high-throughput sequencing technologies and the rapid rise of bioinformatics capabilities and machine learning. These advancements have enabled the collection and analysis of new types of biological data, allowing the completion of large-scale studies and, in turn, the formulation of new hypotheses. This development is reflected in a growing number of publications in the field, from 6,400 in 2003 to more than 35,000 in 2023 (scholar search, input 'systems biology'). In recent years, the landscape of biomedical research was marked by many significant contributions such as the discovery of new RNA species functions (Memczak *et al.* 2013, Conn *et al.* 2015), the large-scale identification of protein structures

(Jumper *et al.* 2021), and unprecedented insights into genomic and epigenetic regulation (Bujold *et al.* 2016).

This rapidly evolving landscape presents both opportunities and challenges for educational institutions. Beyond classical textbooks, traditional lab techniques, and standard analytical tools, both academic and industrial research increasingly demands not only the mastery of advanced biological concepts and computational skills, but also the capability to integrate these together in a 'big picture'. Students and educators might be poorly prepared to materialize this type of systems thinking, given the qualitative nature of traditional biology courses and the scarcity of applied biology-related content in computer science curricula.

Addressing these needs, several scholars have proposed educational frameworks that integrate biology and advanced computational and modeling courses to adequately prepare students for the need of conceptualizing living systems in terms of their components, interactions, and emerging properties (Cvijovic *et al.* 2016, Anton Feenstra *et al.* 2018, Attwood *et al.* 2019, Jungck *et al.* 2020, Dale & Craig 2022, Momsen *et al.* 2022, Smith *et al.* 2022, Tamir *et al.* 2023). Some of them provide course structures or course design ideas, and most point to the fundamental difficulty of fostering mastery of complex biological phenomena, advanced computational techniques, and the ability to analyze systems as a whole beyond the sum of their components.

Several works have discussed the issues of systems biology education. For example, the Bulletin of Mathematical Biology discussed the challenges of cross-disciplinary educational requirements of math and biology students (Jungck *et al.* 2020). Feenstra *et al.* shared course structure and its evolution, learnings, and guidance for teachers based on the systems biology course conducted jointly by the Vrije Universiteit, Amsterdam, and the University of Amsterdam (Anton Feenstra *et al.* 2018). Momsen *et al.* discussed the systems framework that can translate classical biology instructions toward a systems biology approach, conceptualizing living systems in terms of their building blocks, underlying structure and function, along with their interactions with the environment, resulting in both outcomes and evolution of interacting entities ('emergence') (Momsen *et al.* 2022). In a preprint, Dale and Craig describe a successful combination of a study of a biochemical experiment (enzyme kinetics) with a coding exercise to demonstrate the applicability of modeling (Dale & Craig 2022).

More recent perspectives have broadened the vision of systems biology education, for example, advocating for expansion beyond biology into public health and computer science (Voit 2022), calling for more comprehensive computational goals and public outreach (Cvijovic *et al.* 2016, Voit *et al.* 2023), or summarizing developments in modeling approaches (Zupanic *et al.* 2020). While these works provide valuable high-level insight or conceptual guidance, they often focus on single institutional models, broad future agendas, or theoretical perspectives.

In this review, we aim to complement this literature by offering a grounded, comparative view of how systems biology education is currently implemented across a variety of institutions. We present a curated overview of program structures, highlight challenges based on direct input from students and alumni, and explore practical issues such as skill diversity, course prerequisites, interdisciplinary integration, AI tool adoption, and student well-being. Our goal is to bridge theory and practice, offering concrete recommendations

that support a more adaptive and inclusive future for systems biology education.

## Examples of study lines

Most universities offer systems biology courses at the master's level (Vilaprinoyo *et al.* 2011), with a small but growing number of initiatives aimed at stimulating students' interest in the discipline at the undergraduate level, especially during the COVID-19 period. Such initiatives include (hybrid) workshops, crash courses, or the introduction of Bachelor's programs toward computational and systems biology offered by university departments, partnering societies, and graduate students (Mulder *et al.* 2018, LaTourrette *et al.* 2021). A variety of systems biology-oriented master's programs are offered globally, either as specialization tracks or as fully entitled study lines. The main descriptive characteristics of these (offered for the academic year 2024/2025) have been sampled for multiple universities from European, North American, and Caribbean countries (Table 1). The term 'systems biology' is often hidden behind more complex program names, sometimes including the terms 'bioinformatics', 'molecular', 'biochemistry', or 'computational biomedicine'. Other study lines directly refer to 'systems biology', either as a specialized track or as a fully titled program. The necessary credits and duration of the study lines are similar across most European countries with 120 ECTS over a 2-year period (corresponding to approximately 60 US semester credit hours or 240 CATS). There are some variations in countries such as France, England, the USA, and Cuba due to different educational systems, e.g., independent M1 and M2 levels in France over a 1-year period with 60 ECTS each, or 90 ECTS/180 CATS over the same period in England. The program structures typically focus on interdisciplinary approaches combining biology, bioinformatics, and computational methods. They focus on the inclusion of both theoretical and practical components while emphasizing individual research work and a thesis toward the end of the program duration. Nonetheless, the presented study lines show large variations in the way the programs are formatted. While some of them prefer problem- or project-based learning as a means of teaching, others offer a mix of lectures and seminars, including mandatory and elective units. As such, some programs can offer more flexibility in scheduling and thesis options, while others have a rather fixed curriculum and thesis track. The specialization tracks vary as well, with some study lines offering systems biology as a specialization, and others providing deeper specialization tracks such as cardiovascular, dynamic, neuro, or synthetic systems.

More detailed information on each study line, including the tuition fees, entry and language requirements, and application evaluations, can be reviewed in

**Table 1** Examples of systems biology master's programs in European, North American, and Caribbean countries. The main characteristics of the different study lines leading to a Master's degree in Systems Biology are displayed. MSc: Master of Science; ECTS: European Credit Transfer and Accumulation System; M2: second year in the French Master's program system; and CATS: Credit Accumulation and Transfer Scheme.

| Program name (degree)   | Credits (duration)           | Program structure  | Specialization tracks  |
|---|------------------------------|--|--|
| <b>University of Luxembourg (Esch-sur-Alzette, Luxembourg)</b>                              |                              |  |  |
| Molecular and Computational Biomedicine (MSc)   | 120 ECTS (2 years)           | <ul style="list-style-type: none"> <li>- Four semesters with around 15 weeks of full-time courses, plus additional time required for the exam preparation</li> <li>- The first semesters are course-based, mainly with block-courses of 2 weeks</li> <li>- The last 8 months individual research work is performed</li> <li>- The course content is around 1/3 lectures in biology and bio-medicine, 1/3 experimental and 1/3 computational practicals</li> </ul> <a href="https://www.uni.lu/fstm-en/study-programs/master-in-molecular-and-computational-biomedicine">https://www.uni.lu/fstm-en/study-programs/master-in-molecular-and-computational-biomedicine</a>  | <ul style="list-style-type: none"> <li>- Systems Biology</li> <li>- Biomedicine</li> </ul>   |
| <b>Maastricht University (Maastricht, Netherlands)</b>                                      |                              |  |  |
| Systems Biology (MSc)   | 120 ECTS (2 years)           | <ul style="list-style-type: none"> <li>- Year 1, periods 1 and 2: problem-based learning followed by compulsory courses, depending on background: biology and physiology or mathematics of biological systems</li> <li>- Mandatory courses: systems biology, modeling biosystems, experimental design and data management</li> <li>- Periods 3 and 6: project I and project II</li> <li>- Periods 4 and 5: elective choices among omics, cardiovascular systems biology, or dynamical systems and non-linear dynamics, fundamental and systems neuroscience, modeling metabolism, or machine learning and multivariate statistics</li> <li>- Year 2, period 1: two elective courses from computational neuroscience, network biology, scientific programming, or commercialization and entrepreneurship</li> <li>- Periods 2–6: Master's thesis</li> </ul> <a href="https://curriculum.maastrichtuniversity.nl/education/master/systems-biology">https://curriculum.maastrichtuniversity.nl/education/master/systems-biology</a> | <ul style="list-style-type: none"> <li>- Omics</li> <li>- Cardiovascular Systems Biology</li> <li>- Dynamical Systems &amp; Non-Linear Systems</li> <li>- Fundamental &amp; Systems Neuroscience</li> <li>- Modeling Metabolism</li> <li>- Machine Learning &amp; Multivariate Statistics</li> </ul> |
| <b>Ghent University (Ghent, Belgium)</b>  |                              |  |  |
| Bioinformatics (MSc)  | 120 ECTS (2 years)           | <ul style="list-style-type: none"> <li>- Common package (33 ECTS) of applied bioinformatics, including theoretical deepening and data analytical/ problem-solving skills</li> <li>- Systems biology specialization module (28 ECTS)</li> <li>- Applied mathematics and informatics module (20 ECTS)</li> <li>- Optional courses (9 ECTS)</li> </ul> <a href="https://studiekiezer.ugent.be/2023/master-of-science-in-bioinformatics-systems-biology-en">https://studiekiezer.ugent.be/2023/master-of-science-in-bioinformatics-systems-biology-en</a>  | <ul style="list-style-type: none"> <li>- Systems Biology</li> <li>- Bioscience Engineering</li> <li>- Engineering</li> </ul>   |
| <b>Université Paris-Saclay/Université d'Evry-Val-d'Essonne (Evry-Courcouronnes, France)</b> |                              |  |  |
| Systems and Synthetic Biology (M2 level) (MSc)  | 60 ECTS (1 year)             | <ul style="list-style-type: none"> <li>- Five core compulsory modules</li> <li>- Five selection modules (among 11)</li> <li>- Six-month research internship</li> </ul> <a href="https://www.mssb.fr">https://www.mssb.fr</a>   | <ul style="list-style-type: none"> <li>- Systems Biology</li> <li>- Synthetic Biology</li> </ul>   |
| <b>Technical University of Denmark (Copenhagen, Denmark)</b>                                |                              |  |  |
| Bioinformatics and Systems Biology (MSc)  | 120 ECTS (2 years)           | <ul style="list-style-type: none"> <li>- Polytechnical foundation courses (5 ECTS)</li> <li>- Program specific courses (55 ECTS, of which five in innovation courses, ten in mandatory courses, 40 in chosen program-specific courses)</li> </ul> <a href="https://www.dtu.dk/english/education/graduate/msc-programmes/bioinformatics-and-systems-biology">https://www.dtu.dk/english/education/graduate/msc-programmes/bioinformatics-and-systems-biology</a>  | <ul style="list-style-type: none"> <li>- Biomedical Bioinformatics</li> <li>- Infectious Disease Health Informatics</li> <li>- Bioinformatic Methods in Life Sciences</li> </ul>   |
| <b>Imperial College London (South Kensington, UK)</b>                                       |                              |  |  |
| Bioinformatics and Theoretical Systems Biology (MSc)  | 90 ECTS or 180 CATS (1 year) | <ul style="list-style-type: none"> <li>- Composed of two core modules: bioinformatics and theoretical systems biology, and mathematics and computing</li> <li>- Computing project reinforcing programming skills through</li> </ul>  | No specialization tracks   |

(Continued)

**Table 1** Continued.

| Program name (degree)   | Credits (duration)        | Program structure   | Specialization tracks  |
|---|---------------------------|---|--|
|   |                           | <ul style="list-style-type: none"> <li>group project over 11 weeks</li> <li>- Bioinformatics and systems biology project applying course skills in research environment over 22 weeks</li> <li>- Lectures, computing labs, practical classes, presentations and seminars, group work</li> <li>- 30% projects; 70% examinations and coursework</li> <li>- Coursework, written exams, dissertation, computer and mathematics assignments</li> <li>- Individual research project, presentations, group report, and oral exam</li> </ul> <p><a href="https://www.imperial.ac.uk/study/courses/postgraduate-taught/bioinformatics">https://www.imperial.ac.uk/study/courses/postgraduate-taught/bioinformatics</a></p>   |  |
| <b>Karolinska Institute (Stockholm, Sweden)</b><br>Molecular Techniques in Life Science (MSc)   | 120 ECTS<br>(2 years)     | <ul style="list-style-type: none"> <li>- First year advanced level courses in genetics and genomics, translational medicine, applied communication, and molecular life science methods, as well as the foundations of biostatistics, programming, bioinformatics, and comparative genomics</li> <li>- Second year mandatory courses in applied gene technology with bioinformatics analysis of large-scale data, and applied proteomics</li> <li>- The second half of the autumn semester offers three courses, of which the student should select two: systems biology, drug development, and a project course</li> <li>- During the spring semester, the individual degree project is performed</li> </ul> <p><a href="https://education.ki.se/programme/5mt23-masters-programme-in-molecular-techniques-in-life-science">https://education.ki.se/programme/5mt23-masters-programme-in-molecular-techniques-in-life-science</a></p> | <ul style="list-style-type: none"> <li>- Systems Biology</li> <li>- Drug Development</li> </ul>  |
| <b>University of Turku (Turku, Finland)</b><br>Molecular Systems Biology (MSc)  | 120 ECTS<br>(2 years)     | <ul style="list-style-type: none"> <li>- Common courses</li> <li>- Track-specific major subject studies</li> <li>- Selectable studies</li> <li>- Master's thesis</li> </ul> <p><a href="https://www.utu.fi/en/study-at-utu/masters-degree-programme-in-biosciences-molecular-systems-biology">https://www.utu.fi/en/study-at-utu/masters-degree-programme-in-biosciences-molecular-systems-biology</a></p>  | <ul style="list-style-type: none"> <li>- Molecular Systems Biology</li> <li>- Evolutionary Biology</li> </ul>  |
| <b>University of Ottawa (Ottawa, Canada)</b><br>Biology (MSc)   | 60 ECTS (1 year)          | <ul style="list-style-type: none"> <li>- Multiple lecture and seminar available (63 in total) giving each 3 units/credits</li> <li>- No clear structure requirement given</li> <li>- Possible course components: lecture, theory and laboratory, magistral courses, and seminars</li> </ul> <p><a href="https://catalogue.uottawa.ca/en/graduate/master-science-biology-specialization-bioinformatics">https://catalogue.uottawa.ca/en/graduate/master-science-biology-specialization-bioinformatics</a></p>  | <ul style="list-style-type: none"> <li>- Bioinformatics</li> </ul>   |
| <b>George Washington University School of Medicine and Health Sciences – Graduate School of Columbian College of Arts and Sciences (Washington, DC, USA)</b><br>Bioinformatics and Molecular Biochemistry (MSc) | 30 credits<br>(1–2 years) | <ul style="list-style-type: none"> <li>- Thesis and non-thesis tracks</li> <li>- Eleven credits in required courses, 6 credits in required track, and 13 credits of electives (non-thesis option) or 6 credits in thesis and 7 credits of electives (thesis option)</li> <li>- Schedule flexibility, with 1-year or 2-year program option</li> <li>- Hands-on experience in a myriad of laboratories and research initiatives</li> <li>- Diverse elective course pool to choose from</li> </ul> <p><a href="https://bulletin.gwu.edu/arts-sciences/biochemistry-molecular-medicine/ms-bioinformatics-molecular-biochemistry">https://bulletin.gwu.edu/arts-sciences/biochemistry-molecular-medicine/ms-bioinformatics-molecular-biochemistry</a></p>  | <ul style="list-style-type: none"> <li>- Cancer Biology</li> <li>- Inflammation</li> <li>- Pathobiology</li> <li>- Computational Genomics</li> </ul> |

(Continued)

**Table 1** Continued.

| Program name (degree)                      | Credits (duration)              | Program structure   | Specialization tracks  |
|--|---------------------------------|---|--|
| <b>University of Havana (Havana, Cuba)</b> |                                 |   |  |
| Biochemistry (MSc)                         | 60 credits<br>(3 years, hybrid) | <ul style="list-style-type: none"> <li>- Basic mandatory courses: biomolecules, enzymology, immunology, biochemical method, metabolic biochemistry, research work</li> <li>- Research work evaluation: two research seminars in 4th and 5th semesters (8 credits each), pre-defense act before scientific council for thesis endorsement and writing (8 credits), remaining credits awarded upon thesis defense (8 credits)</li> <li>- Credit accumulation: minimum of 60 total credits required, maximum 24 credits per course (18 mandatory, 6 optional), 32 credits for research work, minimum 4 credits for non-lecture activities</li> </ul> <a href="https://serviciosacademicos.fundacion.uh.cu/slides/maestria-en-bioquimica-91">https://serviciosacademicos.fundacion.uh.cu/slides/maestria-en-bioquimica-91</a> | <ul style="list-style-type: none"> <li>- Biochemistry and Systems Biology</li> <li>- Immunology</li> <li>- Biotechnology</li> <li>- Molecular Biology</li> </ul> |

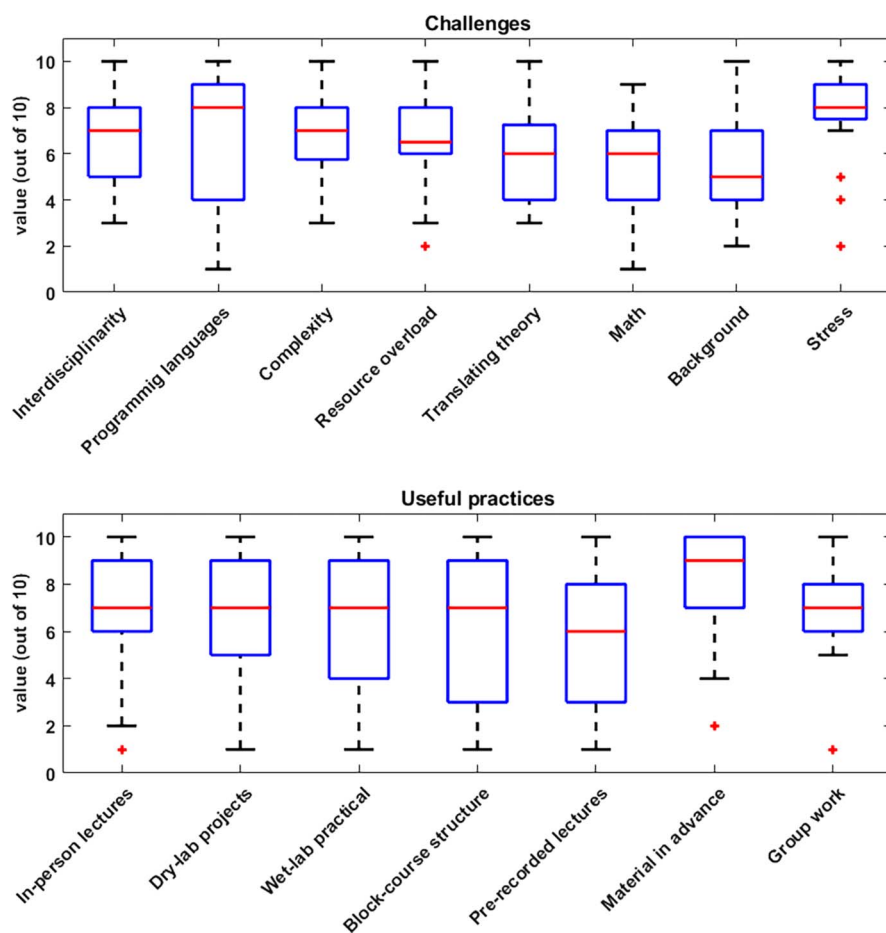
Supplementary Table S1 (see section on [Supplementary materials](#) given at the end of the article). Most strikingly among them, the total tuition fees accumulated over the study line period vary widely between national and international applicants, ranging from free in Sweden and Finland to around £15,000 GBP (€17,500 Euro) in England for national students, and from around €800 Euro in Luxembourg to nearly £37,000 GBP (€43,000 Euro) in England for international students. European universities typically have separate tuition fees for national and international students, while North American and Caribbean countries generally have higher tuition fees regardless of nationality. Entry requirements generally include a Bachelor's degree from an accredited institution in life sciences or related fields, with a strong background in bioinformatics, for example, experience in coding, statistical analysis, work with large datasets, data visualization, or reproducibility practices. Some programs require a specific minimum number of credits in mathematics, molecular biology, and computer programming. Rarely, entry requirements may be linked to the student's Bachelor's passing grade (e.g., Ottawa, Canada, requiring at least 70% average score). Language requirements usually include a minimum CEFR English level of B1 to C1.

## How current students at University of Luxembourg see their studies

To also include student opinions in this review, we reached out to our students of the Master's in Integrated Systems Biology (MISB) and of the International Master's in Biomedicine (IMBM) at the University of Luxembourg. The MISB is currently renamed and slightly reoriented to the Master's in Molecular and Computational Biomedicine (MMCB, [Table 1](#)). Both study lines – MISB/MMCB and IMBM – offer a 2-year full-time education consisting of 120 ECTS. All students spend the

first semester together at the University of Luxembourg and receive experimental and computational training on genomics, transcriptomics, proteomics, and R programming, in addition to lectures on biology, biomedicine, and systems biology. We thereby follow a block-course structure of 2-week blocks per topic; see, for example, our project-based learning course on metabolic network modeling ([Sauter \*et al.\* 2022](#)). The use of 2-week thematic modules allows students to immerse themselves deeply in a focused topic, promoting both conceptual understanding and hands-on skill acquisition. One of the key motivations for this 2-week block-course structure is that it allows for regular laboratory practicals, which often require several uninterrupted hours and cannot be accommodated within traditional 90 min class slots. Moreover, it also facilitates close interaction with faculty and guest researchers and helps students see the integration of theory and practical application in a short, intensive timeframe. While the IMBM students then move to the partner universities in Strasbourg, France, and Mainz, Germany, for more training in biomedical and clinical research, the MISB/MMCB students stay in Luxembourg to deepen their knowledge in systems biology, other omics techniques, and molecular medicine. In addition, to specifically help biologists learn programming languages such as R, we use scaffolded exercises that start with biological questions and datasets familiar to them, progressively introducing statistical and scripting concepts. This is complemented by peer-assisted learning, interactive coding platforms, and workshop-style teaching where coding is integrated with data interpretation.

In total, 21 students responded to the sent-out questionnaires ([Fig. 1](#)). When reporting about their main challenges, the feedback was quite heterogeneous, indicating more student-specific challenges rather than general issues. As most of our students are entering the master's with training in biology, learning programming languages (starting with R) is challenging.

**Figure 1**

Feedback of current students of the Master's in Integrated Systems Biology and the International Master's in Biomedicine of the University of Luxembourg. Questionnaires were sent out to students in early 2024. The bar plots show the answers to the questions listed in Supplementary File S2.

In addition, the complexity of biological systems in general and the required interdisciplinarity and background, including in mathematics, were sometimes felt to be challenging. Together with an overload of available resources and topics to study, this often resulted in a very stressful start to the studies. This usually stabilizes when completing the coursework after the first year of the programs and when moving to the individual research-based second study year. But taking this feedback into account, the first semester is now simplified by making some courses optional and by adding two lecture-free weeks for digesting the studied material.

In addition, in terms of the useful practices, the student responses were heterogeneous (Fig. 1). Students appreciated most classical in-person lectures, computational dry-labs including project-based learning, and especially receiving the study material in advance, allowing them to prepare the courses in advance. Interestingly, pre-recorded lectures and group work in general were not always seen positively, the latter often due to very different backgrounds and learning paces of the group members. In addition, the block-course structure of our studies is sometimes seen critically as not allowing enough time to recap.

To furthermore focus on the challenges of students in bioinformatics when moving to research (e.g., master's thesis), we organized within the ISCB-SC RSG Luxembourg association (International Society for Computational Biology Student Council's Regional Student Group, see <https://www.uni.lu/life-en/social-life/student-associations-clubs/rsg/>) a dynamic graduate networking event titled 'Struggles in Bioinformatics Education' mostly with University of Luxembourg master's and PhD students. As a result, the discussions highlighted a diverse landscape of challenges and opportunities for graduate students. These range from navigating the UNIX environment or a variety of programming languages, where Python emerges as a favored choice, to grappling with complex concepts such as Singularity containers or understanding the purpose and versatility of tools such as R Markdown. In terms of teaching methodologies, this extends to a clear preference for project-based learning, offering hands-on experience. However, students expressed concerns about the overwhelming workload, exacerbated by limited programming courses in Bachelor's programs, which can make catching up difficult in master's programs. In addition, questions arose about the availability of courses focusing on

transferable skills, such as ‘good scientific practice’, ‘data visualization with python’, or ‘science communication’, that are only available to PhD students at the University of Luxembourg, highlighting a need for broader curriculum offerings.

## How alumni of University of Luxembourg assess their previous studies

To also get an overview of the long-term impact of the systems biology education, we reached out with a questionnaire to the alumni of the two master’s study lines at the University of Luxembourg connected to systems biology (Fig. 2). Most alumni who responded work in academia, with a few who moved to industry, teaching, or administration. Most found a job already before graduation and at the latest within 7–12 months after graduation. Most of the alumni considered the systems biology and bioinformatics aspects of their studies to be of high importance for their smooth transition to their current job. A vast majority of our alumni are currently using respective computational methods very often or at least sometimes, further underlying the high relevance of systems biology

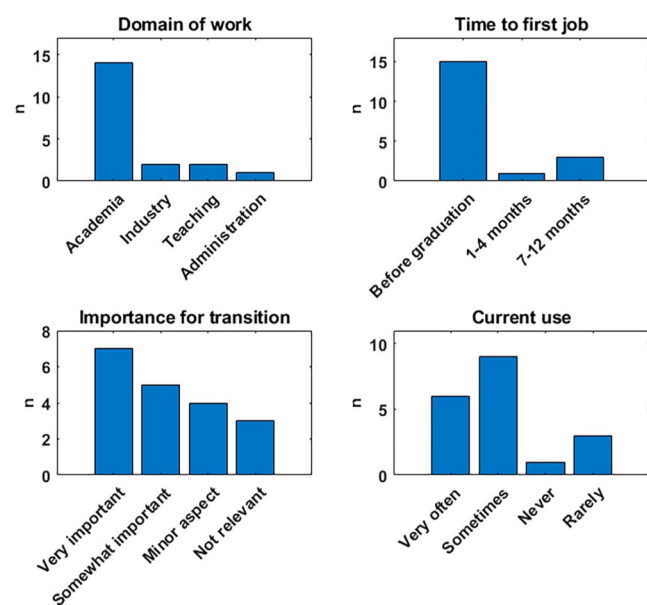


**Figure 2**

Feedback of alumni of the Master’s in Integrated Systems Biology and the International Master’s in Biomedicine of the University of Luxembourg. Questionnaires were sent out to alumni in 2024. The bar plots show the answers to the following questions (top left to bottom right): i) In which field are you working now? ii) How long did it take you to find your first employment after graduation? iii) How important were the systems biology/bioinformatics study courses for reaching your current job? iv) How often are you using systems biology/bioinformatics now?

training. Interestingly, when assessing which methods are used by the alumni, a wide variety was indicated, ranging from analyzing different omics data types, images, and clinical data to metabolic and protein network modeling, dynamical pharmacokinetic modeling, and machine learning, as well as statistical approaches. In addition, programming in different languages such as R, Python, and MATLAB was mentioned. Programming in R is, for example, also used by alumni now teaching in schools and thus reaching pupils very early in their education, as well as other teachers. This overview illustrates the need for a broad introduction covering multiple subjects and methods in systems biology and bioinformatics. On the other hand, various topics were mentioned where deeper knowledge would be needed, ranging from programming to statistics, mathematics in general, and machine learning.

## Conclusions: challenges and opportunities

First, when reaching out to students via the course director or via student representatives, we have seen some differences in the feedback obtained. The emotionally more challenging points were mostly reported via the student representatives. As such, the student representatives form a vital link between students and institutions. They fulfill responsibilities such as relaying information, advocating for students, collecting feedback, and collaborating on solutions to enhance the overall student experience. Despite the importance of honest feedback, students may hesitate to provide it to their educators, opting instead to share more openly with their peers. This reluctance could stem from concerns about how expressing unfavorable feedback might impact their grades and assessments. In addition, the formal nature and inherent reverence in educator-student relationships may hinder students’ willingness to offer criticism. The possibility of providing feedback to peers in a less formal environment is very important.

From the feedback of students and alumni, as well as our own experience as teachers and study director, several key challenges in systems biology education can be identified and are summarized in the following sections.

## Interdisciplinarity

Systems biology at the master’s level attracts students of various disciplines – biology, biotechnology, pharmacy, as well as physics, engineering, and computer science, among other fields. While this is important to build up the needed interdisciplinarity, given such broad backgrounds, designing a curriculum and bringing everyone on a common ground is challenging. This has

been recognized already in the literature on systems biology education, and several authors have provided guidelines and inputs for designing the courses. For example, Feenstra *et al.* have highlighted the need for depth and focus on core topics along with an overview of multiple related fields (Anton Feenstra *et al.* 2018). It is necessary to balance introducing core skills and competencies with fostering the ability to translate between different disciplines. Accordingly, it remains also an open question how and when the integration of students from different backgrounds is performed. It might be useful to have background-specific courses in the beginning, such as ‘math for biologists’ or ‘molecular biology for engineers’. Developing such foundational interdisciplinary courses can, however, be limited by faculty availability and expertise. Some institutions address this through co-teaching models, hiring interdisciplinary staff, or fostering collaborations between departments to pool expertise across domains. One approach adopted in other interdisciplinary programs to address varying student backgrounds is the use of pre-matriculation ‘boot camps’, typically held in the summer, which offer foundational training in key disciplines such as mathematics, biology, or computer science. These preparatory courses could be a valuable strategy for systems biology programs to help incoming students achieve baseline competency before formal coursework begins.

Establishing sustainable systems biology programs requires adequate infrastructure and teaching resources. While many computational tasks can be handled with standard laptops, more advanced analyses benefit from high-performance computing, reliable internet, and institutional IT support. Open-source software and cloud-based platforms can ease some of these challenges. Thus, some institutions do provide publicly available repositories with up-to-date teaching material and exercises. As an example, our systems biology curriculum includes a GitHub-based resource for the metabolic modeling course (<https://github.com/sysbiolux/ISB705MetabolicNetworkModeling>). Such resources not only reduce barriers to entry but also promote collaborative learning and curriculum development across institutions.

## Pre-requisites

On top of this, setting clear prerequisites for systems biology programs remains a challenge, particularly for students from non-quantitative backgrounds. At the University of Luxembourg, for example, while no strict coding threshold is enforced at admission, basic familiarity with a scripting language such as R or Python is highly recommended. To address varying entry levels, introductory programming sessions and self-paced resources are provided early in the

curriculum, and some institutions have implemented preparatory boot camps to bridge foundational gaps.

During the above-mentioned RSG graduate networking event, participants also discussed potential solutions for some of these challenges. Pre-semester preparation, involving crash courses using Jupyter Notebooks, was highlighted to familiarize students with key concepts before the first semester. To promote deeper engagement, methods to encourage active learning were considered (Sauter *et al.* 2022, Sauter & Albrecht 2023) and avoiding superficial approaches, such as relying on prefilled scripts. In addition, there were proposals for workshops and training sessions aimed at providing foundational skills earlier in the academic journey, with interest in recording these sessions for accessibility. A yearly competition was also suggested to incentivize learning and collaboration through group projects, with potential prizes for participants. These proactive measures signify a commitment to enhance the learning experience and to prepare students for the rigors of bioinformatics.

## Systems medicine and translational research

A related question is how interdisciplinarity can be achieved. As Melissa Aikens stressed, ‘authentic problems are not simply putting a mathematics or physics problem in a biological context but rather applying principles from another discipline or bridging interdisciplinary concepts to solve questions that biologists answer’ (Jungck *et al.* 2020). This needs to start with the teachers, and even before, in the research environment of the institution. Compared to the early days of systems biology some 25 years ago, a lot has been achieved here already. Many research institutes and research projects are truly interdisciplinary and provide a great environment for the students to learn and become native systems biologists. Teaching also needs to become truly interdisciplinary. We need more integrated courses combining state-of-the-art knowledge with experimental and computational approaches. Students should seamlessly generate their own data, analyze these with computational approaches, and interpret the results in the context of the latest literature. This will not go without effort from the teacher’s side, but it is needed to foster interdisciplinarity. A notable development that reflects this interdisciplinary maturity is the emergence of systems medicine, where systems biology concepts are directly applied to clinical research and patient care. Programs such as those developed by the Institute for Systems Biology (<https://isbscience.org/education-initiatives/systems-medicine-education/>) and Georgetown University (<https://systemsmedicine.georgetown.edu/>) exemplify this shift, offering graduate-level training at the interface of biology,

computation, and medicine. As the healthcare field increasingly incorporates systems-level approaches, it is likely that medical professionals will also require foundational knowledge in systems biology, presenting another dimension of opportunity – and responsibility – for systems biology education. In some European contexts, governmental support has been instrumental in developing and fostering such interdisciplinary programs, either through targeted funding initiatives, digitalization strategies, or infrastructure investment. For instance, national and EU-level grants have supported the creation of interdisciplinary graduate schools and infrastructure for data-intensive biology. However, the extent and type of support vary significantly across countries and institutions and are often influenced by national political priorities, such as investment in innovation, STEM education, or healthcare modernization. As such, the development and recruitment success of systems biology programs can be shaped by broader political agendas.

## Assessment challenges

Another challenge related to interdisciplinary learning is the difficulty of its assessment and the evaluation of systems thinking in students. As courses are typically graded by one final note, it is important to consider multiple techniques to ensure constructive evaluation across the disciplines involved. This can include rubrics for systems thinking by breaking down the exercises or projects into the specific disciplines and individually evaluating them (e.g., mathematics, coding, biological interpretation, critical thinking, and presentation skills). Another method would be peer evaluation and portfolio assessments of the students, where project progress is being documented and discussed. As an example, in our study line, students will be engaged in peer-evaluated project pitches and result presentations, but also classical exams, quizzes, and final assignments. Besides these methodologies of evaluating interdisciplinary learning, it remains important as a teacher to offer actionable feedback to the students and to make them aware of these opportunities.

## Standardization

It is also important to acknowledge that educational systems can vastly differ across countries, particularly when comparing the EU and the US. Undergraduate education in the US, for example, tends to be broader and more flexible, while European systems are often more specialized from early on. These differences can influence how systems biology programs are structured and what kind of preparation students bring with them. While most of the programs we listed are based in Europe, we also included examples from the US and tried to reflect these broader trends. Despite structural

differences, a shared curriculum is still possible if it focuses on key competencies and learning outcomes, rather than enforcing a one-size-fits-all model. This would allow flexibility for institutions to adapt to the content while ensuring that core systems biology skills are covered.

## AI in systems biology education

Systems biology is a rapidly evolving field, and as our alumni mentioned, it is attractive and diverse in its applications (Fig. 2). This brings up the challenge of how to avoid being overwhelmed by the diversity and complexity of data and methods. Which resources to choose for learning, and how to condense and focus teaching? More specifically, it has often been shown to be challenging for students to learn new content within a course while at the same time learning how to write the necessary code. There must be enough time to deepen the knowledge. For this matter, the emergence of AI tools such as GitHub Copilot, ChatGPT, or other generative models has begun to influence coding education, including within systems biology. While we have not yet formally integrated these tools into the curriculum, students are increasingly using them informally to support coding tasks. This raises both opportunities – for personalized learning and error correction – and challenges, including overreliance or misuse. Further study is needed to define the best practices for integrating AI responsibly into scientific training, especially in systems biology education. On the other hand, for teachers, it might be challenging to include the fast evolution and development of new techniques. How to deal with this always-moving finishing line? One of the aspects here will be to start systems biology training during the Bachelor's study or even earlier. As mentioned, some of our alumni are now teaching in school and thereby using R coding within their biology classes at the junior high-school level. This inspiring feedback points in the right direction.

## Big picture learning

And similarly, but in a longer perspective, how to develop and transmit a mindset of life-long learning? And how to balance study efforts and well-being? For example, at the University of Luxembourg, there is a growing effort of providing useful information and offers to the students toward improving mental health and well-being, including great self-help material (<https://www.uni.lu/life-en/mental-health-wellbeing/>). While it is important to see this emerge, it will be even more important in the long run to have these integrated within the studies from the beginning, not only when problems arise. Teachers will once again have to adopt it themselves first to be able to transmit it to their students.

Finally, despite systems biology being well received in the transition to the job market (Fig. 2), the gap between academia and industry might also be an issue, since the private sector typically uses more proprietary, unpublished methods and practices. Academic projects are typically limited, and often students need to be trained in long-term thinking in terms of public deliverables, as well as corporate practices and economics. This gap can be reduced by active academia-industry collaborations, also in the context of teaching.

In the face of these multifaceted challenges, the future of systems biology education lies in turning fragmentation into integration across disciplines, methodologies, and sectors to build a truly translational and future-ready educational paradigm. Embracing these challenges as opportunities will not only strengthen systems biology education but also ensure its relevance and resilience in a rapidly evolving scientific and societal landscape.

---

#### Supplementary materials

This is linked to the online version of the paper at <https://doi.org/10.1530/ERC-25-0024>.

---

#### Declaration of interest

The authors declare that there is no conflict of interest that could be perceived as prejudicing the impartiality of the work reported.

---

#### Funding

This work was supported by the Luxembourg National Research Fund (FNR) under Grant Nos. PRIDE17/12252781/DRIVEN, PRIDE21/16763386/CANBI02, and PRIDE21/16749720/NEXTIMMUNE2.

---

#### Author contribution statement

TS designed the review. JD, SDL, AB, and TS contributed to the writing of the manuscript. All authors were involved in the collection and assessment of the data and approved the final version of the manuscript.

---

## References

- Anton Feenstra K, Abeln S, Westerhuis JA, *et al.* 2018 Training for translation between disciplines: a philosophy for life and data sciences curricula. *Bioinformatics* **34** i4–i12. (<https://doi.org/10.1093/bioinformatics/bty233>)
- Attwood TK, Blackford S, Brazas MD, *et al.* 2019 A global perspective on evolving bioinformatics and data science training needs. *Brief Bioinform* **20** 398–404. (<https://doi.org/10.1093/bib/bbx100>)
- Bujold D, Morais DADL, Gauthier C, *et al.* 2016 The international human epigenome consortium data portal. *Cell Syst* **3** 496–499.e2. (<https://doi.org/10.1016/j.cels.2016.10.019>)
- Conn SJ, Pillman KA, Toubia J, *et al.* 2015 The RNA binding protein quaking regulates formation of circRNAs. *Cell* **160** 1125–1134. (<https://doi.org/10.1016/j.cell.2015.02.014>)
- Cvijovic M, Höfer T, Aćimović J, *et al.* 2016 Strategies for structuring interdisciplinary education in systems biology: an European perspective. *NPJ Syst Biol Appl* **2** 16011. (<https://doi.org/10.1038/npjbsa.2016.11>)
- Dale R & Craig S 2022 Integrating math modeling, coding, and biology in a CURE lab (preprint). *bioRxiv*. (<https://doi.org/10.1101/2022.01.20.477155>)
- Jumper J, Evans R, Pritzel A, *et al.* 2021 Highly accurate protein structure prediction with AlphaFold. *Nature* **596** 583–589. (<https://doi.org/10.1038/s41586-021-03819-2>)
- Jungck JR, Robeva R & Gross LJ 2020 Mathematical biology education: changes, communities, connections, and challenges. *Bull Math Biol* **82** 117. (<https://doi.org/10.1007/s11538-020-00793-0>)
- LaTourrette K, Stengel A & Clarke J 2021 Student-led workshops: filling skills gaps in computational research for life scientists. *Nat Sci Educ* **50** e20052. (<https://doi.org/10.1002/nse2.20052>)
- Memczak S, Jens M, Elefsinioti A, *et al.* 2013 Circular RNAs are a large class of animal RNAs with regulatory potency. *Nature* **495** 333–338. (<https://doi.org/10.1038/nature11928>)
- Momsen J, Speth EB, Wyse S, *et al.* 2022 Using systems and systems thinking to unify biology education. *CBE Life Sci Educ* **21** es3. (<https://doi.org/10.1187/cbe.21-05-0118>)
- Mulder N, Schwartz R, Brazas MD, *et al.* 2018 The development and application of bioinformatics core competencies to improve bioinformatics training and education. *PLoS Comput Biol* **14** e1005772. (<https://doi.org/10.1371/journal.pcbi.1005772>)
- Sauter T & Albrecht M 2023 *Introduction to Systems Biology: Workbook for Flipped-Classroom Teaching*, 1st edn Cambridge, UK: Open Book Publishers. (<https://doi.org/10.11647/OBP.0291>)
- Sauter T, Bintener T, Kishk A, *et al.* 2022 Project-based learning course on metabolic network modelling in computational systems biology. *PLoS Comput Biol* **18** e1009711. (<https://doi.org/10.1371/journal.pcbi.1009711>)
- Smith RW, Garcia-Morales L, Martins Dos Santos VAP, *et al.* 2022 Research-driven education: an introductory course to systems and synthetic biology. *Front Syst Biol* **2** 981800. (<https://doi.org/10.3389/fsysb.2022.981800>)
- Tamir R, Ben-Zvi Assaraf O & Maman S 2023 System-thinking progress in engineering programs: a case for broadening the roles of students. *Front Educ* **8** 1138503. (<https://doi.org/10.3389/educ.2023.1138503>)
- Vilaprinyo E, Alves R & Sorribas A 2011 Teaching systems biology. *IET Syst Biol* **5** 131–136. (<https://doi.org/10.1049/iet-syb.2010.0032>)
- Voit EO 2022 Systems biology beyond biology. *Front Syst Biol* **2** 987135. (<https://doi.org/10.3389/fsysb.2022.987135>)
- Voit EO, Shah MA, Olivença D, *et al.* 2023 What's next for computational systems biology? *Front Syst Biol* **3** 1250228. (<https://doi.org/10.3389/fsysb.2023.1250228>)
- Zupanec A, Bernstein HC & Heiland I 2020 Systems biology: current status and challenges. *Cell Mol Life Sci* **3** 379–380. (<https://doi.org/10.1007/s00018-019-03410-z>)

## **Appendix A6: Example of course material**

Book chapter: **Drug Target Prediction Using Context-Specific Metabolic Models  
Reconstructed from rFASTCORMICS**

Contributions: Code revision

Test operability of material for different operating systems

Method section adaptation

DOI link: [https://doi.org/10.1007/978-1-0716-2513-2\\_17](https://doi.org/10.1007/978-1-0716-2513-2_17)

Published in: Cancer Drug Resistance: Methods and Protocols

# Drug target prediction using context-specific metabolic models reconstructed from rFastcormics

Tamara Bintener<sup>1</sup>, Maria Pires Pacheco<sup>1</sup>, Ali Kishk<sup>1</sup>, Jeff Didier<sup>1</sup>, Thomas Sauter<sup>1\*</sup>

<sup>1</sup>Department of Life Sciences and Medicine, University of Luxembourg, Esch-Alzette, Luxembourg

\*Corresponding Author: Thomas Sauter (thomas.sauter@uni.lu)

## Abstract

Metabolic modelling is a powerful computational tool to analyse metabolism. It has not only been used to identify metabolic rewiring strategies in cancer but also to predict drug targets and candidate drugs for repurposing. Here, we will elaborate on the reconstruction of context-specific metabolic models of cancer using rFASTCORMICS and the subsequent prediction of drugs for repurposing using our drug prediction workflow.

**Keywords** Metabolic Modelling, Cancer, Drug prediction, Drug repurposing

## Introduction

De novo drug discovery is expensive and time-consuming. On average, from the discovery of a new compound to the approval of a drug, 14 years pass, and the approval rates are still dismal while the necessary investments are increasing. Drug repurposing, on the other hand, requires fewer resources while searching for new indications of already approved drugs. As the drug profiles are already established, the first clinical trial phases can be skipped, greatly reducing the costs and approval times **(1)**.

Computational and systems biology approaches have been developed to predict novel drug targets, their mechanisms of action as well as their interaction that can be depicted via gene regulatory **(2)**, protein interaction **(3, 4)**, signalling **(5)**, and metabolic networks **(6–8)**.

For example, genome-scale metabolic networks are a computational representation of metabolism and describe the relationship between genes, proteins, reactions, and the involved metabolites. Metabolic models have many applications that enabled, among others, predicting biomarkers for inborn errors of metabolism (9), identifying metabolic changes and mechanisms in cancer (10, 11), and cancer-specific drug targets (6–8, 12–14).

Model-building algorithms, such as the FASTCORE family (14–16), extract a subnetwork from a generic metabolic reconstruction that best reflects the input experimental data by maximizing the inclusion of reactions under the control of expressed genes and the exclusion of reactions associated with inactive genes. Therefore, it is possible to reconstruct context-specific models that are specific for a tissue, cancer type, or even patient.

By reconstructing and comparing the metabolism between cancer-specific and healthy models, metabolic vulnerabilities and drug targets can be discovered and exploited for drug repurposing using the here explained drug target and repurposing workflow that has previously been used to identify drugs for colorectal cancer (14) and melanoma (17). But the drug repurposing workflow based on rFASTCORMICS for RNA-seq data can be applied without modifications to find, analyse, and overcome drug resistance mechanisms in other cancers and diseases, given the appropriate experimental data is provided.

Within the drug repurposing workflow, in silico gene knockouts are performed to simulate the inhibiting effects of drugs as gene knockouts can be a surrogate for drug effects. Even though there exist options to perform single, double, and multiple knockouts in metabolic models, we have slightly altered the original code to only delete those genes that are inhibited by a drug. As such, the input of the in silico deletion is no longer genes but drugs.

## Materials

*Please download and install the following programs and toolboxes on your computer.*

### 1.1. Matlab and toolboxes

rFASTCORMICS was developed for Matlab (MathWorks) and requires the Statistics and Machine Learning Toolbox as well as the Curve Fitting Toolbox. Both toolboxes can be downloaded from the “Add-On Explorer” within Matlab.

Additionally, a compatible IBM CPLEX installation is needed (or an equivalent solver). A free academic version of the IBM ILOG CPLEX Optimization Studio can be requested for university staff and students from <https://www.ibm.com/products/ilog-cplex-optimization-studio>.

The COBRA (COntstraint-Based Reconstruction and Analysis) Toolbox (**18**) is available at <https://opencobra.github.io/cobratoolbox/stable/> and needs to be installed according to the respective tutorial. The COBRA toolbox is a community effort to collect computational scripts that allow performing quantitative predictions on the metabolism that include flux balance analysis, in silico knockouts, and robustness analysis, among others.

Detailed manuals for these installations on Windows and macOS are provided at <https://github.com/sysbiolux/rFASTCORMICS>.

## 1.2. rFASTCORMICS

rFASTCORMICS for RNA-seq can be downloaded from [https://www.en.uni.lu/research/fstm/dlsm/research\\_areas/systems\\_biology/software/rfastcormics](https://www.en.uni.lu/research/fstm/dlsm/research_areas/systems_biology/software/rfastcormics) or <https://github.com/sysbiolux/rFASTCORMICS> and needs to be added to the working path of Matlab (see Note 1).

## 1.3. Input Model

Any genome-scale reconstruction can be taken as an input model as long as it is in a COBRA-compatible format. Note that different input models have different gene identifiers. For example, the Recon family reconstructions use NCBI gene identifiers, whereas HMR 2 and Human 1 use Ensembl identifiers. Therefore, a gene conversion file (dictionary) is needed to map the genes from the expression data onto the metabolic model. For the following example, this file is provided with rFASTCORMICS and contains the official gene symbols as well as ENTREZ Gene IDs to allow mapping between the gene expression data and the input model. In general, the conversion file can be compiled using the Ensembl Biomart tool available at <https://m.ensembl.org/biomart/martview/>.

## 1.4. Expression data

Whereas FASTCORMICS was designed for microarray data, rFASTCORMICS was designed to take RNA-seq data as input. So far, rFASTCORMICS was tested with unfiltered

FPKM transformed RNA-seq data. The data can be provided in any readable format for Matlab (Excel, text file).

## Methods

A running example script (*Molecular\_Biology\_Bintener\_et\_al\_181121.m/mlx*) for the model reconstruction as described in detail here is provided with the download of rFASTCORMICS (<https://github.com/sysbiolux/rFASTCORMICS>).

### 1.5. Expression data input

1. Start Matlab and make sure all needed files and toolboxes are properly installed and added to the Matlab path, see Note 1.
2. Import the gene expression data into Matlab. Make sure to get three distinct variables
  - colnames: cell array with as many columns as samples
  - rownames: cell array with as many genes as measured
  - fpkm: measurements per gene and sample. The provided fpkm\_BRCA\_cancer.txt contains 10 breast cancer samples from the TCGA and fpkm\_BRCA\_control.txt 10 breast control samples and will be loaded separately into Matlab and merged afterwards.

If your data comes in a single text format, you can use

```
data = readtable('fpkm.txt', "ReadRowNames", true);
```

As we have two different example files, we use

```
data_cancer = readtable('fpkm_BRCA_cancer.txt',  
"ReadRowNames", true);
```

```
data_control = readtable('fpkm_BRCA_control.txt',  
"ReadRowNames", true);
```

to combine the data:

```
data = [data_cancer, data_control];
```

followed by

```
fpkm = table2array(data);
```

```
rownames = data.Properties.RowNames;
```

```
colnames = data.Properties.VariableNames;
```

3. With the data loaded, we can proceed with the discretization step that will determine if a gene is expressed (value of 1), not expressed (value of -1), or if the gene has an unknown expression status (value of 0). For this we use

```
discretized = discretize_FPKM(fpkm, colnames, 1);
```

The output will be an array with -1, 0, or 1 for each gene in each sample. Setting the third argument of the discretized\_FPKM function to 1 will enable the generation of figures that show the gene expression distribution per sample as well as the discretization threshold (see Figure 1). These figures will be saved automatically in the Figures folder in your working directory. It is always advised to check the density plots, sometimes the density plot is too skewed and some slight adjustment needs to be made, see Note **Error! Reference source not found**. In case this function is used in MATLAB's command window with the figure argument set to 1, it is important to let all the figures pop-up first, as closing these windows during the process will lead to an error.

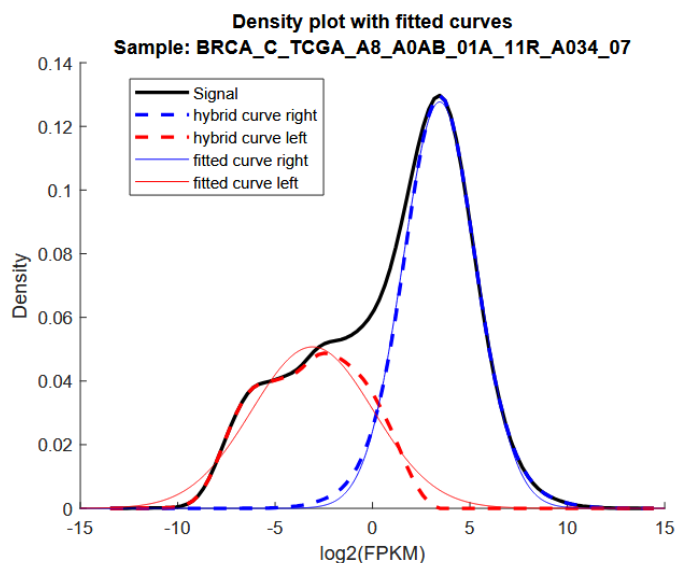


**Figure 1: Density plot showing the log<sub>2</sub>(FPKM) gene expression distribution of one sample.** In black, the original gene expression is shown. In blue and red, the left and right half-Gaussians are shown, respectively. For more information on these steps, please refer to the material an methods section of rFASTCORMICS (14).

## 1.6. Context-specific model reconstruction

1. Here we are using the human reconstruction Recon 2.04 that can be downloaded from <https://www.vmh.life/files/reconstructions/Recon/2.04/Recon2.v04.mat.zip>. Unzip the compressed archive and add it to your working path in Matlab. Load the reconstruction with:

```
load Recon2.v04.mat
```

2. To reconstruct a context-specific model, the input model must be consistent. To achieve this, we use `fastcc` (included in the rFASTCORMICS download) on the loaded generic reconstruction whose variable is called `modelR204` as follows:

```
A = fastcc_4_rfastcormics(modelR204, 1e-4,0);  
consistent_model = removeRxns(modelR204,  
modelR204.rxns(setdiff(1:numel(modelR204.rxns),A)))
```

Here, `consistent_model` is the flux consistent part of the input reconstruction which means that every reaction can carry a non-zero flux

3. Before reconstructing the models based on the expression data via rFASTCORMICS, a few parameters need to be set:
  - a. **dico**: a file that allows mapping gene identifiers between the input data and the model. An example is provided with the rFASTCORMICS download:

```
load dico_ML.mat
```

- b. **medium**: if the cells have been grown in a specific media it can be defined here to further constrain the model. The medium variable contains the identifiers of the metabolites that are allowed to be taken up by the model and hence are present in the medium.

```
load medium_example.mat
```

- c. **already\_mapped\_tag**: 1 if the data has previously been mapped to the model identifier and 0 if the mapping was not done yet.

```
already_mapped_tag = 0
```

- d. **consensus\_proportion**: in case consensus models are built, this variable defines the fraction of samples required to have expressed a gene or to not have expressed a gene to consider the gene and associated reaction to be expressed (1) and not expressed (-1), respectively. Genes that do not reach the consensus proportion are tagged with unknown expression status (0).

`consensus_proportion = 0.9`

- e. **epsilon**: flux threshold to distinguish active from non-active reactions. Usually, epsilon is a small number close to 0 such as 0.0001 to avoid numerical issues with the solver.

`epsilon = 1e-4`

- f. **biomass\_rxn**: the biomass reaction ID in the model which will be used as an objective reaction by the `fastcormics_RNAseq` function.

`biomass_rxn = {'biomass_reaction'};`

- g. **optional\_settings** is an object that can contain the following fields:  
unpenalized systems:

- **unpenalizedSystems**: systems (also called pathways) for which the inclusion of reactions is not penalized. The inclusion of reactions that are associated with genes of unknown status is penalized to favour the inclusion of reactions under the control of expressed genes. It is however possible to define an unpenalized set of reactions that will not be forced in the reconstruction but would be favoured over non-core reactions.
- **func**: also called objective function. These are reactions that have to be included as they are optimized for during the analysis. Often the biomass and ATP maintenance are set as objective functions in a model.
- **not\_medium\_constrained**: metabolites that are not in the medium but, due to shortcomings of the model, they have to be taken up to allow the objective function(s) to carry a flux.
- **medium**: a list of metabolites identifiers that can be taken up by the model according to the medium composition.

`unpenalizedSystems = {'Transport, endoplasmic reticular'; 'Transport, extracellular'; 'Transport, golgi apparatus'; 'Transport, mitochondrial'; 'Transport, peroxisomal'; 'Transport, lysosomal'; 'Transport, nuclear'};`

```

unpenalized =
consistent_model.rxns(ismember(consistent_model.subSystems,unpenalizedSystems));

optional_settings.unpenalized = unpenalized;

optional_settings.func = {'DM_atp_c_';'biomass_reaction'};

not_medium_constrained = 'EX_tag_hs(e)';

optional_settings.not_medium_constrained = not_medium_constrained;

optional_settings.medium = medium_example;

```

4. The command to reconstruct a context-specific model looks as follows:

```

[model_out, A_final] = fastcormics_RNAseq(consistent_model, discretized,
rownames, dico, biomass_rxn, already_mapped_tag,
consensus_proportion, epsilon, optional_settings)

```

In general, the variable `model_out` is not saved because the generated models can take up a lot of memory. Hence, if many models are created, `model_out` should be replaced with `~`. The variable `A_final` (or `A_keep`) contains the indices of reactions that have to be included in the model and can later be used to quickly reconstruct the context-specific model.

5. We can further distinguish between two scenarios during the model reconstruction process with `rFASTCORMICS`.

We can reconstruct a model for each sample:

```

for i = 1:numel(colnames)

[~, A_keep{i}] = fastcormics_RNAseq(consistent_model, discretized(:,i),
rownames, dico, biomass_rxn, already_mapped_tag,
consensus_proportion, epsilon, optional_settings)

end

```

or we can reconstruct a consensus model for each condition. Only reactions that are active in at least 90% of the samples will be included for the reconstruction of the consensus model. As we have 10 cancer samples:

```
[model_cancer, A_final_cancer] = fastcormics_RNAseq(consistent_model,
discretized(:,1:10), rownames, dico, biomass_rxn, already_mapped_tag,
consensus_proportion, epsilon, optional_settings)
```

and 10 control samples:

```
[model_control, A_final_control] = fastcormics_RNAseq(consistent_model,
discretized(:,11:20), rownames, dico, biomass_rxn, already_mapped_tag,
consensus_proportion, epsilon, optional_settings)
```

6. The variable "A\_keep" saves the indices of active reactions and can be saved in a more comparable array, called models\_keep. Here, for the sample-specific models:

```
models_keep = zeros(numel(consistent_model.rxns), numel(colnames));
for i=1:numel(colnames)
    models_keep(A_keep{i},i) = 1;
end
```

Similarly, for the consensus models that will be saved in a different variable called models\_keep\_consensus:

```
models_keep_consensus = zeros(numel(consistent_model.rxns), 2);
models_keep_consensus(A_final_cancer,1) = 1
models_keep_consensus(A_final_control,2) = 1
```

## 1.7. Basic model and pathway analysis

Based on the models\_keep variables, basic analyses based on the reaction presence can be performed.

1. Firstly, the similarity between the two models can be assessed via the Jaccard similarity index. Generally speaking, the Jaccard similarity index compares the intersection of two sets over their union:

$$\frac{M1 \cap M2}{M1 \cup M2}$$

In Matlab the Jaccard similarity score is calculated using:

```
J = squareform(pdist(models_keep','jaccard'));
```

The results can be represented in a clustergram. See Note **Error! Reference source not found.** for the altcolor colorcode or use any other available colormap.

```
cgo_J = clustergram(1-J,...
'RowLabels', colnames,...
'ColumnLabels', colnames,...
'ColumnLabelsRotate',270, ...
'Cluster', 'all', ...
'symmetric','False',...
'Colormap', altcolor)

addTitle(cgo_J,{'Model similarity based on Jaccard
distance','models_keep'})
```

Here, each model is represented on the x and the y axis and compared with every model. On the diagonal, a model is compared with itself which results in a similarity score of 1, represented by the dark colour. The darker the colour, the higher the similarity. Using the clustergram, we can determine models with a high similarity that also form clusters as can be observed by the dendrogram (see Figure 2).

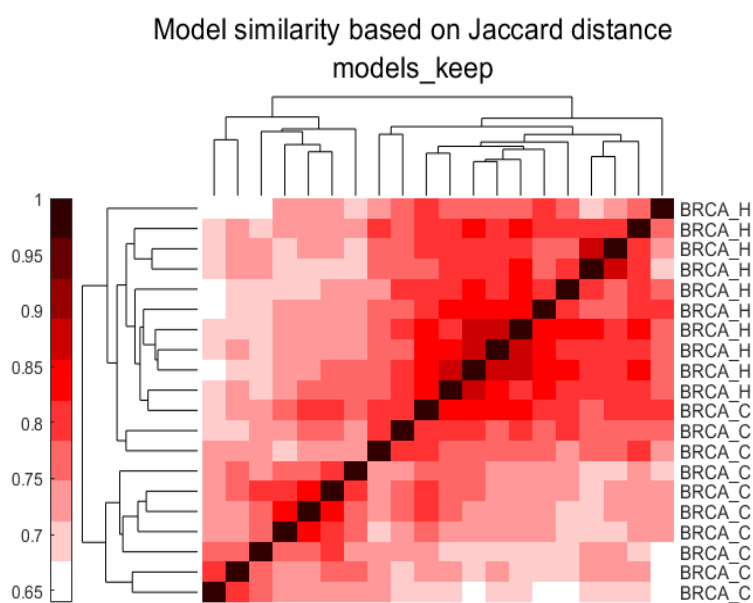


**Figure 2: Clustergram showing the model similarity for 10 breast cancer samples (BRCA\_C) and 10 control samples (BRCA\_H).** Because each of the 20 models has been compared with each other, the darker diagonal line describes the case in which a model was compared with itself and is completely similar (score of 1). A relatively homogeneous cluster can be observed for BRCA\_H whereas BRCA\_C is

more heterogeneous.

2. Pathway analysis can be performed by analysing the number of reactions present per pathway in the context-specific model in comparison to the input model. A score of 0.5 means that half of the reactions of the input model are present in the context-specific model for a given pathway. Within the model, pathways are often noted as “subsystems”. First, we will extract the number of reactions per pathway from the input model and compile the information in a table:

```
Pathways = table(unique(consistent_model.subSystems));  
[pathways, ~, ub] = unique(consistent_model.subSystems);  
path_counts = histc(ub, 1:length(pathways));  
T = table(pathways, path_counts);  
[I, ia, ib] = intersect(Pathways.Var1, T.pathways);  
Pathways.consistent(ia) = T.path_counts(ib);  
Pathways.Properties.VariableNames{1}='Pathways';
```

3. Then we can add the same pathway information for the consensus models:

```
[pathways, ~, ub] =  
unique(consistent_model.subSystems(find(models_keep_consensus(:,1))))  
;  
path_counts = histc(ub, 1:length(pathways));  
T = table(pathways, path_counts);  
[I, ia, ib] = intersect(Pathways.Pathways, T.pathways);  
Pathways.Var2(ia) = T.path_counts(ib);  
Pathways.Properties.VariableNames{3} = 'cancer_consensus';  
[pathways, ~, ub] =  
unique(consistent_model.subSystems(find(models_keep_consensus(:,2))))  
;  
path_counts = histc(ub, 1:length(pathways));  
T = table(pathways, path_counts);  
[I, ia, ib] = intersect(Pathways.Pathways, T.pathways);
```

```

Pathways.Var2(ia) = T.path_counts(ib) ;

Pathways.Properties.VariableNames{4} = 'control_consensus';

```

and the sample-specific models:

```

for i=1:numel(colnames)

    [pathways, ~, ub] =
    unique(consistent_model.subSystems(find(models_keep(:,i))));

    path_counts = histc(ub, 1:length(pathways));

    T = table(pathways, path_counts);

    [I, ia, ib] = intersect(Pathways.Pathways, T.pathways);

    Pathways.Var2(ia) = T.path_counts(ib);

    Pathways.Properties.VariableNames{4+i} = colnames{i}

end

```

4. The pathway activity rates can also be represented by dividing each sample by the number of reactions in the consistent input model:

```

PathwayActivity = Pathways;

for i=3:size(PathwayActivity,2)

    PathwayActivity(:,i) =
    array2table(table2array(PathwayActivity(:,i))./table2array(PathwayA
ctivity(:,2)));

end

```

5. If only 2 conditions or samples are compared, the pathway activity can be represented in a scatter plot. Here we will compare the consensus models saved in column 3 and 4 in the PathwayActivity variable. First, pathways with a difference higher than 20% will be identified for later plotting.

```

diff_idx = find(abs(table2array(PathwayActivity(:,3))-
table2array(PathwayActivity(:,4))) > 0.2)

```

6. All the pathways will be plotted in gray and surrounded by a black circle if the difference is higher than 20% and the pathway name will be added:

```
figure

hold on

scatter(table2array(PathwayActivity(:,3)),table2array(PathwayActivity(:,4)),'filled','MarkerFaceColor',[0.9 0.9 0.9])

scatter(table2array(PathwayActivity(diff_idx,3)),table2array(PathwayActivity(diff_idx,4)), 'black')

ylabel('cancer consensus model')

xlabel('control consensus model')

title('Pathway presence rate in the consensus models')

line([0 1], [0,1],'Color','k')

line([0 0.8], [0.2,1],'Color','k','LineStyle','--')

line([0.2 1], [0,0.8],'Color','k','LineStyle','--')

legend({'All pathways','>20%'},"Location","best")

text(table2array(PathwayActivity(diff_idx,3)),table2array(PathwayActivity(diff_idx,4)), PathwayActivity.Pathways(diff_idx))
```

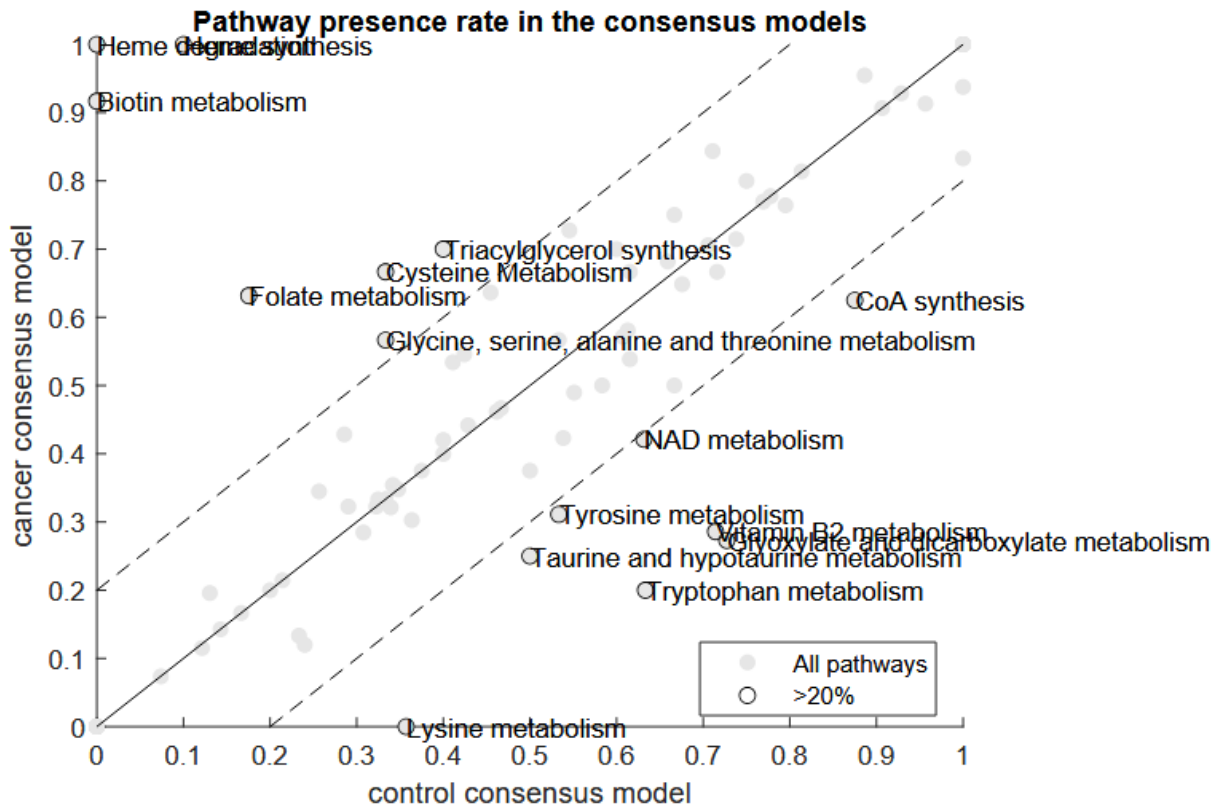


**Figure 3: Pathway presence rate in the consensus models.** Pathways whose activity difference is higher than 20% in either model are highlighted with a dark circle.

7. Alternatively, if several samples are compared, a heatmap can be useful. Here the consensus models are also included for completeness.

```

cgo = clustergram(table2array(PathwayActivity(:,3:end)),...
'RowLabels', PathwayActivity.Pathways,...
'ColumnLabels', PathwayActivity.Properties.VariableNames(3:end),...
'ColumnLabelsRotate',270, ...
'Cluster', 'column', ...
'symmetric','False',...
'Colormap', altcolor)

h = plot(cgo); set(h,'TickLabelInterpreter','none');

colorbar(h)

title(h,'Pathway activity')

```

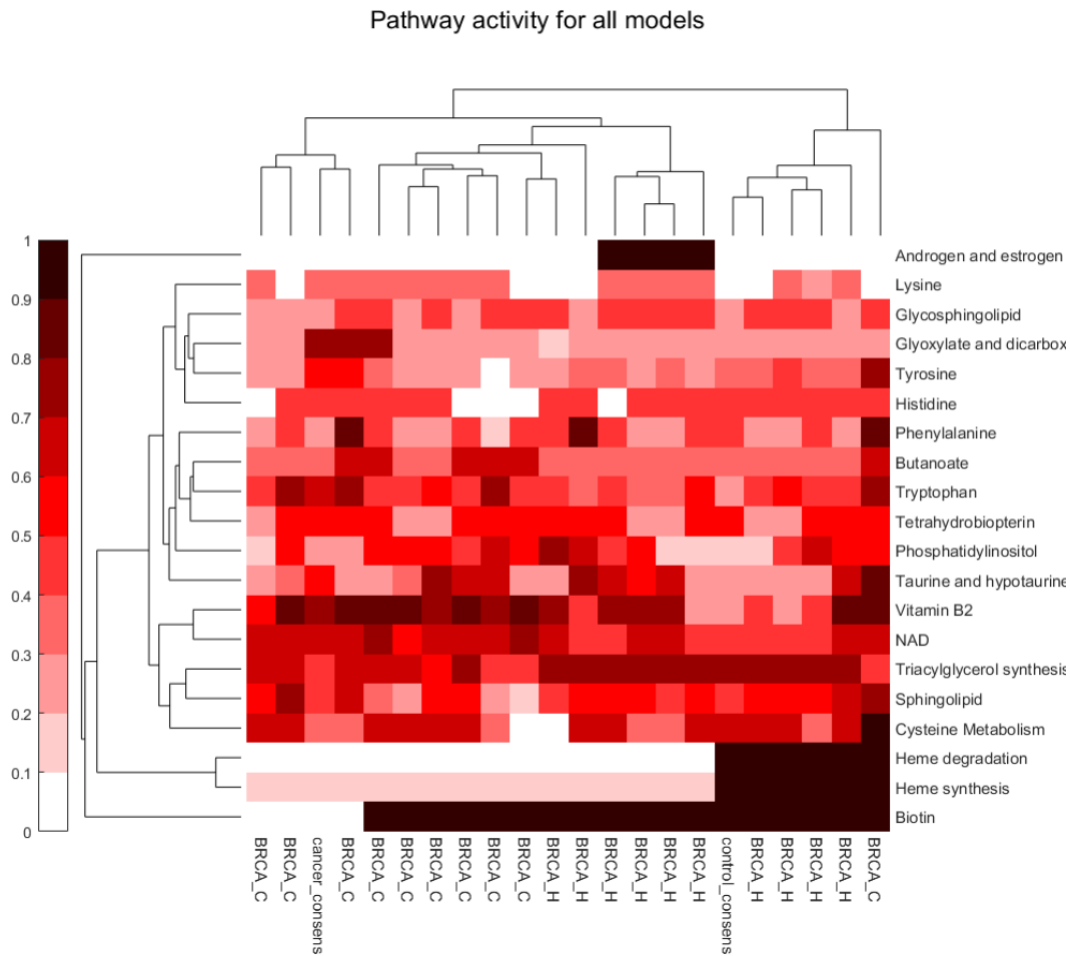


**Figure 4: Pathway presence rates for all models in a heatmap clustergram.** Note that the number of shown pathways was reduced to 20 for a better representation.

### 1.8. In silico gene deletion and essential genes

After the context-specific model reconstruction, we can proceed with the in silico gene deletion. To this aim, an objective function needs to be set for the model. Generally, the biomass\_reaction is used to describe quickly proliferating cells such as cancer cells. For healthy cells, the ATP demand reaction is considered here. Then, for each gene in the model, the corresponding reaction fluxes are set to zero and the flux through the objective function is calculated.

1. The objective function is set via the changeObjective function from the COBRA toolbox. To set the biomass reaction as objective function:

```
model_out = changeObjective(consistent_model,'biomass_reaction')
```

To set the ATP demand as objective function:

```
model_out = changeObjective(consistent_model,'DM_atp_c_')
```

It can be verified with with the checkObjective function from the COBRA toolbox

```
checkObjective(model_out)
```

2. To perform the in silico gene deletion for every model for both objective functions, we first need to initialize the solver

```
changeCobraSolver('ibm_cplex')
```

3. Then we can run the single gene deletion adapted from the COBRA toolbox for the sample-specific models:

```
for i=1:size(models_keep,2)

    ind = find(~cellfun(@isempty, regexp(consistent_model.rxns,
    'DM_atp_c_')));

    model_out =
    removeRxns(consistent_model,consistent_model.rxns(setdiff(1:nu
    mel(consistent_model.rxns),find(models_keep(:,i)))));

    model_out =
    changeObjective(model_out,consistent_model.rxns(ind));

    [grRatio, grRateKO, grRateWT, hasEffect, delRxns, fluxSolution] =
    singleGeneDeletion_rFASTCORMICS(model_out,'FBA',[,],0,1);

    grRatio_ATP(:,i)= grRatio;

    grRateKO_ATP(:,i) = grRateKO;

    grRateWT_ATP(:,i) = grRateWT;

    ind = find(~cellfun(@isempty, regexp(consistent_model.rxns,
    'biomass_reaction')));

    model_out =
    removeRxns(consistent_model,consistent_model.rxns(setdiff(1:nu
    mel(consistent_model.rxns),find(models_keep(:,i)))));

    model_out =
    changeObjective(model_out,consistent_model.rxns(ind));
```

```

[grRatio, grRateKO, grRateWT, hasEffect, delRxns, fluxSolution,
genelist] =
singleGeneDeletion_rFASTCORMICS(model_out,'FBA',[],0,1);

grRatio_biomass(:,i) = grRatio;

grRateKO_biomass(:,i) = grRateKO;

grRateWT_biomass(:,i) = grRateWT;

end

```

The main outputs from this part are grRatio\_ATP and grRatio\_biomass. For both variables, the rows represent genes and the columns represent samples. grRatio stands for growth ratio and gives information on how much the gene deletion affects the objective function. Further information can be taken from the original COBRA documentation.

4. For the next analysis, it is easier to convert the geneList of ENTREZ IDs into Gene symbols using the dictionary:

```

[B, ia, ib] = intersect(genelist,dico.ENTREZ)

genelist(ia, 2) = dico.SYMBOL(ib)

```

5. For the determination of essential cancer genes, we use a growth ratio of 0.5 as a cut-off. Additionally, the gene deletion should affect at least half of the samples. For the control samples, a more stringent cut-off is used; the ATP maintenance should only be minimally affected and not be below 0.9 in at least 10% of the control samples. This means that a gene whose deletion reduces the biomass production below 50% in at least half of the samples compared to the wild type are considered to be essential. We can use the following code to find the essential genes for the cancer and control samples:

```

essential_cancer_genes = genelist (sum(grRatio_biomass(:,1:10) < 0.5,2)
> 5,2)

essential_control_genes = genelist (sum(grRatio_ATP(:,11:20) < 0.9,2) >
1,2)

```

6. To find genes essential in cancer only:

```
cancer_specific_genes = setdiff(essential_cancer_genes,  
essential_control_genes)
```

As a follow up for the predicted essential genes, an enrichment test can be performed by using experimentally validated essential genes from CRISPR Cas9 data with a hypergeometric test. Additionally, these genes can be looked up in several databases such as the DrugBank to potentially find drugs that allow inhibiting the protein product from the essential gene.

### 1.9. In silico drug deletion and drugs for repurposing

Instead of performing gene deletion, one can directly estimate the effect of a drug if the information on the gene-drug relation is available. For example, if a drug inhibits one or multiple gene products, these genes can be knocked down and the effect on the objective function can be measured. Therefore, we have modified the single gene deletion script to take as input a model and a list of drugs to be simulated.

1. Before starting the drug deletion, we need to define a list of drugs whose effect will be evaluated on the models. To this aim, we can use the provided gene-drug list called GeneDrugRelations to extract a list of drugs from the DrugBank. 1175 unique inhibiting drugs can be tested:

```
load GeneDrugRelations.mat  
  
DrugList = unique(GeneDrugRelations.DrugName)
```

2. The DrugDeletion script is used in the same way as the singleGeneDeletion for rFASTCORMICS. First, the model is reconstructed from the models\_keep variable, then the objective function is set and the analysis is run:

```
for i=1:size(models_keep,2)  
  
    ind = find(~cellfun(@isempty, regexp(consistent_model.rxns,  
    'DM_atp_c_')));  
  
    model_out =  
    removeRxns(consistent_model,consistent_model.rxns(setdiff(1:nu  
    mel(consistent_model.rxns),find(models_keep(:,i)))));
```

```

model_out =
changeObjective(model_out,consistent_model.rxns(ind));

[grRatio, grRateKO, grRateWT] =
DrugDeletion(model_out,'FBA',DrugList);

Drug_grRatio_ATP(:,i) = grRatio;

Drug_grRateKO_ATP(:,i) = grRateKO;

Drug_grRateWT_ATP(:,i) = grRateWT;

ind = find(~cellfun(@isempty, regexp(consistent_model.rxns,
'biomass_reaction')));

model_out =
removeRxns(consistent_model,consistent_model.rxns(setdiff(1:nu
mel(consistent_model.rxns),find(models_keep(:,i))))));

model_out =
changeObjective(model_out,consistent_model.rxns(ind));

[grRatio, grRateKO, grRateWT] =
DrugDeletion(model_out,'FBA',DrugList);

Drug_grRatio_biomass(:,i) = grRatio;

Drug_grRateKO_biomass(:,i) = grRateKO;

Drug_grRateWT_biomass(:,i) = grRateWT;

end

```

3. Finding drugs for repurposing in cancer is similar to finding cancer-specific essential genes:

```

cancer_drugs = DrugList(sum(Drug_grRatio_biomass(:,1:10) < 0.5,2) > 5)
control_drugs = DrugList(sum(Drug_grRatio_ATP(:,11:20) < 0.9,2) > 1)
cancer_specific_drugs = setdiff(cancer_drugs, control_drugs)

```

## Conclusions

The hereby presented workflow for the reconstruction of context-specific models coupled with a drug repurposing workflow allows for the discovery of interesting drugs for repurposing. After the drug prediction, additional information on the drugs should be sought to determine their feasibility in in vitro validation experiments. For example, the availability, solubility, and concentration of the compounds are of high importance to perform sensible follow-up experiments.

Additionally, by comparing models from different conditions such as therapy-resistant and therapy-responding cells, metabolic mechanisms and rewiring strategies that play a role in the resistance can be discovered and possibly overcome in the future.

## Notes

1. To add a folder to your Matlab working path use `addpath('directory')`. To add all subfolder from the current folder use `addpath(genpath(pwd))`.
2. If you get an error “Error: The input was too complicated or too big for MATLAB to parse” add feature `astheightlimit 2000` to the beginning of your code
3. If the peak of the distribution is shifted towards the left side, i.e. if the leftmost peak is higher than the rightmost curve, use the provided `discretize_FPKM_skewed` function.
4. Altcolor code: `altcolor = [255 255 255;255 204 204; 255 153 153; 255 102 102; 255 51 51; 255 0 0; 204 0 0; 152 0 0; 102 0 0; 51 0 0]/255;`

## References

1. Nosengo N (2016) Can you teach old drugs new tricks? *Nature* 534:314–316
2. Landsheer S De, Trairatphisan P, Lucarelli P, et al (2017) FALCON: a toolbox for the fast contextualization of logical networks.
3. Zoraghi R and Reiner NE (2013) Protein interaction networks as starting points to identify novel antimicrobial drug targets. *Curr Opin Microbiol* 16:566–572

4. Badkas A, Landtsheer S De, and Sauter T (2020) Topological network measures for drug repositioning. *Brief Bioinform* 00:1–13
5. Mistro G Del, Lucarelli P, Müller I, et al (2018) Systemic network analysis identifies XIAP and I $\kappa$ B $\alpha$  as potential drug targets in TRAIL resistant BRAF mutated melanoma. *npj Syst Biol Appl* 4:39
6. Folger O, Jerby L, Frezza C, et al (2011) Predicting selective drug targets in cancer through metabolic networks. *Mol Syst Biol* 7:501
7. Frezza C, Zheng L, Folger O, et al (2011) Haem oxygenase is synthetically lethal with the tumour suppressor fumarate hydratase. *Nature* 477:225–228
8. Turanli B, Zhang C, Kim W, et al (2019) Discovery of therapeutic agents for prostate cancer using genome-scale metabolic modeling and drug repositioning. *42:386–396*
9. Shlomi T, Cabili MN, and Ruppin E (2009) Predicting metabolic biomarkers of human inborn errors of metabolism. *Mol Syst Biol* 5:263
10. Resendis-Antonio O, Checa A, and Encarnación S (2010) Modeling core metabolism in cancer cells: Surveying the topology underlying the warburg effect. *PLoS One* 5:e12383
11. Yizhak K, Gaude E, Dévédec S Le, et al (2014) Phenotype-based cell-specific metabolic modeling reveals metabolic liabilities of cancer. *Elife* 3:1–23
12. Agren R, Mardinoglu A, Asplund A, et al (2014) Identification of anticancer drugs for hepatocellular carcinoma through personalized genome-scale metabolic modeling. *Mol Syst Biol* 10:721
13. Diener C and Resendis-Antonio O (2016) Personalized Prediction of Proliferation Rates and Metabolic Liabilities in Cancer Biopsies. *Front Physiol* 7:1–11
14. Pacheco MP, Bintener T, Ternes D, et al (2019) Identifying and targeting cancer-specific metabolism with network-based drug target prediction. *43:98–106*
15. Vlassis N, Pacheco MP, and Sauter T (2014) Fast Reconstruction of Compact Context-Specific Metabolic Network Models. *PLoS Comput Biol* 10:e1003424
16. Pacheco MP, John E, Kaoma T, et al (2015) Integrated metabolic modelling reveals cell-type specific epigenetic control points of the macrophage metabolic network. *BMC Genomics* 16:809
17. Bintener T, Pacheco MP, Kulms D, et al Melanoma in silico drug target prediction

across patients and cell lines using metabolic modelling approaches. Under preparation.

18. Heirendt L, Arreckx S, Pfau T, et al (2019) Creation and analysis of biochemical constraint-based models using the COBRA Toolbox v.3.0. *Nat Protoc* 14:639–702